OPTIMIZATION AND CHARACTERIZATION OF BULK HEXAGONAL BORON NITRIDE SINGLE CRYSTALS GROWN BY THE NICKEL-CHROMIUM FLUX METHOD

by

TIM HOFFMAN

B.S., Kansas State University, 2012

AN ABSTRACT OF A DISSERTATION

submitted in partial fulfillment of the requirements for the degree

DOCTOR OF PHILOSOPHY

Department of Chemical Engineering
College of Engineering

KANSAS STATE UNIVERSITY
Manhattan, Kansas

2016

Abstract

Hexagonal boron nitride (hBN) is a wide bandgap III-V semiconductor that has seen new interest due to the development of other III-V LED devices and the advent of graphene and other 2-D materials. For device applications, high quality, low defect density materials are needed. Several applications for hBN crystals are being investigated, including as a neutron detector and interference-less infrared-absorbing material. Isotopically enriched crystals were utilized for enhanced propagation of phonon modes. These applications exploit the unique physical, electronic and nanophotonics applications for bulk hBN crystals.

In this study, bulk hBN crystals were grown by the flux method using a molten Ni-Cr solvent at high temperatures (1500°C) and atmospheric pressures. The effects of growth parameters, source materials, and gas environment on the crystals size, morphology and purity were established and controlled, and the reliability of the process was greatly improved. Single-crystal domains exceeding 1mm in width and 200μm in thickness were produced and transferred to handle substrates for analysis. Grain size dependence with respect to dwell temperature, cooling rate and cooling temperature were analyzed and modeled using response surface morphology. Most significantly, crystal grain width was predicted to increase linearly with dwell temperature, with single-crystal domains exceeding 2mm in at 1700°C.

Isotopically enriched ^{10}B and ^{11}B hBN crystal were produced using a Ni-Cr-B flux method, and their properties investigated. ^{10}B concentration was evaluated using SIMS and correlated to the shift in the Raman peak of the E_{2g} mode. Crystals with enrichment of 99% ^{10}B and >99% ^{11}B were achieved, with corresponding Raman shift peaks at 1392.0 cm^{-1} and 1356.6 cm^{-1}, respectively. Peak FWHM also decreased as isotopic enrichment approached 100%, with widths as low as 3.5 cm^{-1} achieved, compared to 8.0 cm^{-1} for natural abundance samples.

Defect selective etching was performed using a molten NaOH-KOH etchant at 425°C-525°C, to quantify the quality of the crystals. Three etch pit shapes were identified and etch pit width was investigated as a function of temperature. Etch pit density and etch pit activation energy was estimated at 5×10^{7} cm^{-2} and 60 kJ/mol, respectively. Screw and mixed-type dislocations were identified using diffraction-contrast TEM imaging.

OPTIMIZATION AND CHARACTERIZATION OF BULK HEXAGONAL BORON NITRIDE SINGLE CRYSTALS GROWN BY THE NICKEL-CHROMIUM FLUX METHOD

by

TIM HOFFMAN

B.S., Kansas State University, 2012

A DISSERTATION

submitted in partial fulfillment of the requirements for the degree

DOCTOR OF PHILOSOPHY

Department of Chemical Engineering
College of Engineering

KANSAS STATE UNIVERSITY
Manhattan, Kansas

2016

Approved by:

Major Professor
James H Edgar

Copyright

Abstract

Hexagonal boron nitride (hBN) is a wide bandgap III-V semiconductor that has seen new interest due to the development of other III-V LED devices and the advent of graphene and other 2-D materials. For device applications, high quality, low defect density materials are needed. Several applications for hBN crystals are being investigated, including as a neutron detector and interference-less infrared-absorbing material. Isotopically enriched crystals were utilized for enhanced propagation of phonon modes. These applications exploit the unique physical, electronic and nanophotonics applications for bulk hBN crystals.

In this study, bulk hBN crystals were grown by the flux method using a molten Ni-Cr solvent at high temperatures (1500°C) and atmospheric pressures. The effects of growth parameters, source materials, and gas environment on the crystals size, morphology and purity were established and controlled, and the reliability of the process was greatly improved. Single-crystal domains exceeding 1mm in width and 200μm in thickness were produced and transferred to handle substrates for analysis. Grain size dependence with respect to dwell temperature, cooling rate and cooling temperature were analyzed and modeled using response surface morphology. Most significantly, crystal grain width was predicted to increase linearly with dwell temperature, with single-crystal domains exceeding 2mm in at 1700°C.

Isotopically enriched ^{10}B and ^{11}B hBN crystal were produced using a Ni-Cr-B flux method, and their properties investigated. ^{10}B concentration was evaluated using SIMS and correlated to the shift in the Raman peak of the E_{2g} mode. Crystals with enrichment of 99% ^{10}B and >99% ^{11}B were achieved, with corresponding Raman shift peaks at 1392.0 cm^{-1} and 1356.6 cm^{-1}, respectively. Peak FWHM also decreased as isotopic enrichment approached 100%, with widths as low as 3.5 cm^{-1} achieved, compared to 8.0 cm^{-1} for natural abundance samples.

Defect selective etching was performed using a molten NaOH-KOH etchant at 425°C-525°C, to quantify the quality of the crystals. Three etch pit shapes were identified and etch pit width was investigated as a function of temperature. Etch pit density and etch pit activation energy was estimated at 5×10^{7} cm^{-2} and 60 kJ/mol, respectively. Screw and mixed-type dislocations were identified using diffraction-contrast TEM imaging.

Table of Contents

List of Figures

List of Tables

Acknowledgements

This dissertation is the culmination of several years of work, accomplished not through just my work, but through the expertise and effort of many people. I want to thank several people who made this work possible, both directly and indirectly. First, I want to thank Dr. James Edgar; without his mentoring, patience and ideas, this project would have never begun. I hope that this work has helped to benefit him and future researchers interested in hBN. Next, I want to thank my undergraduate assistants, Yichao Zhang and Xiu Wang, who showed initiative to pursue research early in their careers and did vital work for this project. Thanks to my committee members, who sacrificed their time and energy to help provide useful feedback in improving this work and furthering my education. I also want to heavily thank the graduate students in the Edgar group, as well as all the graduate students in the KSU Chemical Engineering department, who gave up their time to assist on this project without complaint and acted in a spirit of community and respect. I want to thank researchers who I collaborated with outside of the department, including Dr. Jeffrey Geuther and Tyrel George of the KSU Nuclear Engineering Department, who collaborated on making hBN neutron detectors, Dr. Neelam Khan of Georgia Gwinnett College, who did AFM analysis on hBN samples, Dr. Jingyu Lin and Dr. Hongxing Jiang of Texas Tech University, who performed photoluminescence measurements, and Drs. Josh Caldwell, Kurt Gaskill, Nabil Bassim, Mark Twigg and associates at the US Naval Research Laboratories, who collaborated on numerous projects and did a lot of analysis to my benefit. Final thanks go to the companies and agencies that provided vital funding for this project, the NSF, Department of Homeland Security, the Domestic Nuclear Detection Office and the II-VI Foundation. Without their contributions, this project and my educations would not have been possible. A hearty thanks to all!

Dedication

I dedicate this work to my family, my friends and most importantly, my wife. Without your support and encouragement, none of this would have been possible. Thank you.

Chapter 1 - Motivation

Hexagonal boron nitride (hBN) is a wide bandgap III-V semiconductor that has seen new interest due to the development of other group III nitride devices and the advent of graphene and other 2-D materials. It shares some similarities with other group III nitrides (AlN and GaN), such as its wide bandgap (5.8 eV). However, its structure is unique: it has an anisotropic, van der Waals (2-D) structure which mimics the behavior of graphite. Its wide bandgap, anisotropic structure and elemental composition have made it attractive for new applications, such as deep UV LEDs, substrates for 2-D materials, nanophotonic devices and solid-state neutron detectors.

These new applications for hBN take advantage of its electronic and optical properties, as opposed to older applications which utilize its chemical stability and mechanical properties (i.e.: a high temperature graphite replacement) and for which fine grain powders and hot pressed ceramics are suitable. To maximize performance, these new applications require high purity, defect-free bulk hBN single crystals. The major challenge for evaluating these hBN applications has been in producing large single crystal domains, due to the extreme conditions required to grow hBN from liquid or vapor BN and/or boron sources.

Its physical properties make conventional melt or sublimation-condensation growth techniques difficult to implement for hBN. Solution growth techniques are much more practical, but are less developed relative to other conventional growth methods used to produce other bulk crystals (such as the Czochralski process for silicon). However, they can produce high quality crystals under readily achieved growth conditions.

This dissertation investigates the growth of bulk hBN crystals using the Ni-Cr flux method, a solution growth method originally demonstrated by Kubota *et al* [1]. Key advantages of this method include its ability to growth large hBN crystals at atmospheric pressures (compared to similar techniques which require high pressure and high temperature operation). The Ni-Cr flux growth process was improved through experimentation and the implementation of statistical optimization. Conclusions are reached as to the best conditions of temperature and time profiles for maximizing the crystal size. Furthermore, the process was advanced so hBN crystals could be grown using elemental boron as a primary source material, which enabled the growth of isotopically-enriched hBN crystals. Analysis of the synthesized hBN crystals is presented, illustrating the size, and quality of bulk hBN crystals produced by this method. Several studies using these bulk hBN crystals to demonstrate neutron detector and nanophotonic device performance are also considered. This work validates that the Ni-Cr flux process is a viable technique for producing the device-grade hBN bulk crystals necessary to pursue these new optoelectronic applications and explore its new uses of nanophotonics and semiconductor physics.

Chapter 2 - Background

Hexagonal boron nitride (hBN) is a synthetic compound- semiconductor material, which has received attention due to the success of other group III-nitrides and wide bandgap semiconductors, such as GaN, AlN and SiC. It has a long history of use and a variety of applications; the development of other group III-nitride LEDs, the discovery of graphene and the need for new neutron detector materials have opened up new purposes for hBN. This dissertation presents the research preformed to understand and optimize the growth of hBN by the Ni-Cr flux method to enable production of high quality, large bulk hBN crystals. These new applications require single crystal hBN to maximize charge carrier mobilities and minority carrier lifetimes and minimize non-radiative recombination of electrons and holes for their successful execution.

To understand the methods pursued in this work, the basic properties of hBN are described, including its chemical and physical properties, as well as its crystal structure and related allotropes. The most common methods of hBN formation, chemical vapor deposition (CVD) and bulk growth via flux, will be identified and contrasted. Future applications of hBN as a solid-state neutron detector, a substrate and dielectric for graphene, and a deep ultra-violet (UV) light source will also be described.

2.1 Basic Properties of BN

Boron nitride is commonly used in industry due its softness, high chemical stability, and resistance to oxidation [2-5]. This high chemical stability is due to the strong B-N bond, which is isoelectronic to the carbon-carbon bond but less likely to oxidize or react chemically with other compounds. This similarity with the carbon-carbon bond results in analogous crystal structures and mechanical properties between polymorphs of BN and carbon compounds. BN forms three main crystalline phases with long-range order: hexagonal (hBN), cubic (cBN) and wurtzitic (wBN) boron nitride.

hBN is analogous to graphite and consists of stacked planes of sp^2 hybridized boron and nitrogen with strong in-plane bonding and weak van der Waals plane-to-plane bonding. This difference in bond strength produces anisotropic mechanical properties, giving hBN a very low interlayer shear stress and making it a soft material (1.6 on the Mohs scale). This anisotropy also allows isolation of an hBN monolayer, similar to graphene. Due to this 2-D nature, wide bandgap and similar a-plane lattice constants (1.6% mismatch) hBN is suitable as a substrate for graphene [6].

cBN and wBN do not have planar structures. Instead, each B atom is bonded strongly to four N atoms in sp^3 hybridization (and vice versa for N atoms). cBN and wBN are corollaries to the carbon allotropes diamond and lonsdaleite (hexagonal diamond), respectively, and do not share the strongly anisotropic nature of hBN. Both of these forms of BN are noted for their superior hardness and density; the hardness of cBN surpassed only by that of diamond. However, growth of these phases has been limited due to the high pressures (>1 GPa) required for their synthesis [7]. This difficulty in formation of cBN currently disqualifies it from semiconductor applications, based on the BN phase diagram developed by Solozhenko *et al* [8] with assistance from previous work by Bundy, Wentorf and Corrigan [9-10].

2.2 Growth Methods for hBN

There are two primary methods for the growth of structurally ordered hBN: chemical vapor deposition (CVD) of hBN films and bulk growth of hBN crystals. Historically, CVD has been the predominant method for synthesis due to its ability to produce both highly-ordered epitaxial hBN and less-ordered pyrolytic boron nitride (pBN) films [2,4,11-12]. The recent focus of hBN CVD techniques is the selection of growth conditions and substrates for the formation of a few-layer or monolayer hBN, typically for use as a substrate for hBN/graphene heterostructure devices [13].

Several metal substrates have been investigated for hBN monolayers and hBN/graphene heterostructure synthesis, including nickel [14-15], chromium [16], cobalt [17], and copper [18]. These growth methods can produce hBN monolayers with wrinkle-free surfaces and low surface roughness, which are nearly transparent under optical microscopy and, on Ni and Cu (111) surfaces, produce hBN crystals with a triangular habit. The formation of this triangular morphology, as opposed to a more hexagonal form, is theorized to be due to preferential edge termination in N atoms to lower the interface energy in the crystal [19].

While CVD growth of hBN is viable for some applications, it tends to produce stacking disorders in crystal planes, causing degradation in crystal grain size and thickness [20]. Therefore, bulk growth methods are needed when larger crystal grains and higher crystalline quality are required. Bulk hBN crystals cannot be grown by traditional melt growth techniques due to the high melting temperature (>3000°C) and low vapor pressure of BN [21]. Instead, crystals must be formed using a flux-growth technique, in which hBN is dissolved in a solvent at high temperature, and then slowly cooled to cause precipitation [22]. Many different fluxes have been investigated for the growth of both hBN and cBN crystals, but the highest degree of success has been demonstrated using silicon, sodium, lithium and LiBr, barium, copper, nickel, nickel-molybdenum and nickel-chromium solutions [1,23-31].

Among these fluxes, the Ni-Cr system has shown the most promise in producing hBN crystals of sufficient size for device fabrication and can be operated at atmospheric pressures, reducing the expense of equipment needed [1,29-31]. Ni and Cr were used as an alloy by Kubota *et al* [1] due to their high solubility for boron and nitrogen, respectively [32-36]. Clear hBN crystals with hexagonal habit were reported to have formed on the top surface of the Ni-Cr flux [1].

hBN crystal growth at Kansas State was previously investigated by Ben Clubine, a Master's student working under Dr. Edgar (graduated May 2012). He investigated the grown of hBN crystals using a Ni-Cr flux using a pair of resistively-heated vertical graphite and tungsten furnaces, growing crystals at atmospheric pressures and high temperature (1500-1700°C) under N_2 [37-38]. Clubine was able to identify operating parameter space for hBN crystal formation, as well as demonstrate the ability to control the size and thickness as a function of growth temperature. Crystal grains as large as 5mm were formed using growth temperatures up to 1700°C. Crystal thickness varied inversely with growth temperature. At lower temperatures, the crystals exhibited a thicker, more hexagonal shape, with growth rates roughly equal in the *a* and *c* directions. At higher temperatures, the crystals had a more triangular habit and preferred to grow wider and thinner. This difference in shape may be due to preferential termination of the crystal edge with either N or B atoms, maximizing exposure of one set of dangling bonds and increasing crystal stability [19,39].

2.3 hBN Applications

Conventional applications for boron nitride, typically in powder or hot-pressed form, range from use as fillers in plastic and cosmetics, coatings, high-temperature lubricants and refractory materials due to its mechanical softness, high chemical stability, resistance to oxidation and its ability to be sintered into a hot-pressed form that can be easily machined [2-5]. In many ways, these uses resulted from the applications that required the performance of graphite, but in chemical environments and at temperatures where graphite was unsuitable. This use led to hBN commonly being referred to as “white graphite”.

Modern applications for hBN look to leverage its unique structural and optoelectronic properties. These applications include neutron detection, 2-D material, deep UV optical devices and nanophotonics, as will be discussed below. However, the main similarity of these applications is the requirement for single-domain, high purity defect-free hBN crystals, due to its enhanced grain size and improved transport properties.

2.3.1 hBN Devices for Neutron Detection

Among the many potential applications of bulk hBN crystals is neutron detection. Effective detection of neutrons is vital for national defense and nuclear non-proliferation, as special nuclear materials (including ^{235}U and ^{239}Pu) undergo spontaneous fission, releasing neutrons into the surrounding environment [40]. Currently, ^{3}He gas detectors are the most established neutron-detecting technology. Unfortunately, the global supply of ^{3}He, a side-product of tritium decay produced from nuclear weapons production, is scarce due to the worldwide reduction in nuclear weapons [41]. Due to this diminishing supply, replacement neutron detection technologies must be investigated to ensure national defense and nonproliferation.

Boron has a long history as a neutron-detecting material due to the large thermal neutron capture cross-section of the ^{10}B isotope (approximately 3800 barns) [42]. Upon neutron capture, ^{10}B undergoes one of two nuclear reactions, both of which result in the emission of a ^{7}Li ion and alpha particle. The most common reaction pathway (occurring 94% of the time) also emits an additional gamma ray from the ^{7}Li nucleus. Figure 2.1 illustrates these two reaction pathways and their emitted high energy particles.

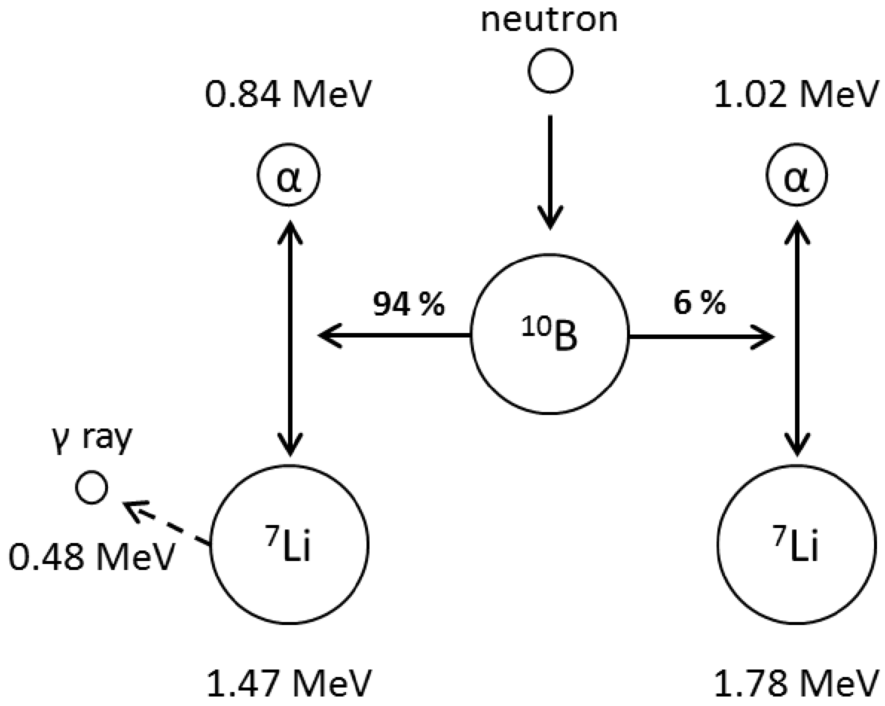

Figure 2.1: A diagram of the products and energies of the two neutron capture reactions for ^{10}B. The gamma ray is not considered in the total energy calculation of the 94% path, as it is likely to escape the detector volume without depositing its energy.

Boron has been incorporated as a neutron conversion material in several neutron detector designs, the simplest being a planar boron-coated silicon detector. In this detector geometry, neutrons are captured in the boron layer, producing an alpha particle and ^{7}Li ion, which travel in opposite directions. One of these two highly energetic particles may scatter into the silicon layer, causing ionization and charge carrier generation and allowing for the indirect measurement on the incident neutron [43]. Due to this structure, a sufficiently thick layer of boron is necessary to maximize neutron capture and form charged particles; however, increasing the boron layer thickness leads to self-absorption of the charged particles within the boron layer. These phenomena and device structure result in an optimal thickness of the boron layer, and makes the device efficiency for this detector geometry low (4%) [42-44]. This type of heterogeneous neutron detector can be improved by using three-dimensional structures, such as pillar-structured ^{10}B-backfilled geometries, but the maximum efficiency can only be increased to approximately 50% [45]. Additionally, these heterogeneous devices require complex pillar-etching techniques, as well as methods to effectively backfill structures detection material (^{7}Li or ^{10}B compounds).

The benefit of hBN as a neutron detector is the combination of the neutron conversion and charge collection in the same volume (Figure 2.2). Because of this, hBN detectors may achieve high detector efficiencies, theoretically approaching 100% with crystal thickness up to 1mm, as simulated by Yazbeck in his Master's thesis [46]. Additionally, hBN has several properties which make it suitable as a solid-state neutron detector, including elements with low atomic numbers resulting in high gamma ray discrimination, and a high dielectric strength capable of supporting a high bias voltage which improves charge collection [47]. Some success has been demonstrated with fabrication of devices from pyrolytic BN, both by McGregor *et al* [48] and Li *et. al* [49]. The study by McGregor *et al* [48] reported a neutron response, independent of the gamma signal, observed over the background noise. However, the full neutron interaction spectrum expected for ^{10}B was not resolved; likely due to low device efficiency from poor charge collection caused by the small grain size and high dislocation densities in pBN. The study by Li *et al* [49] reported an increase in device current under the presence of thermal neutrons; however, they did not provide a count spectrum or compare this to a gamma-only condition, making it difficult to conclusively conclude that the device was reacting to neutrons. Bulk hBN crystals are anticipated to have improved charge carrier properties and reduced density of trapping states resulting from their highly ordered structure and larger grain size.

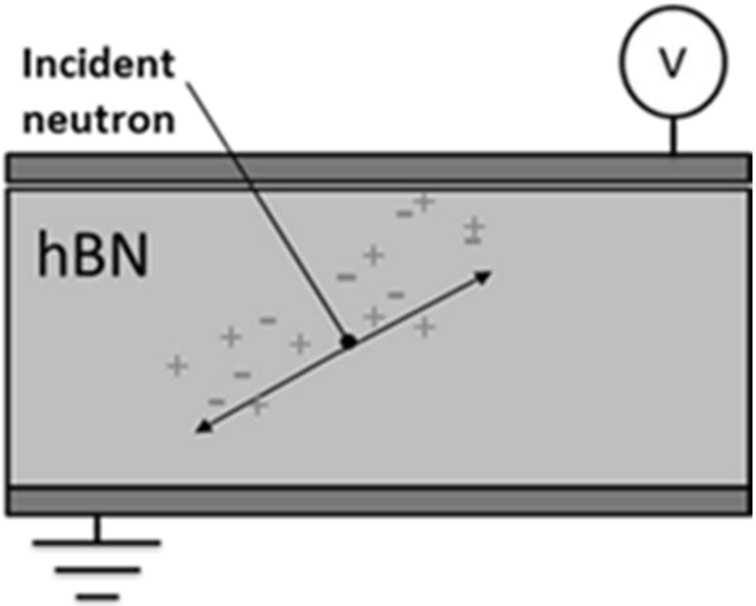

Figure 2.2: Simple schematic of a planar hBN neutron detector. Incident neutrons penetrate the thin metal contact layer, are captured in the crystal bulk and cause the generation of a large amount of electron-hole pairs, which are collected by an applied voltage.

2.3.2 hBN for 2-D Heterostructures

hBN has been proposed as a substrate for atomically-thin 2-D materials, particularly graphene, due to its planar structure, wide bandgap and its ability to form a flat, insulating and inert surface [13]. Graphene has recently attracted much attention and study based on its unique mechanical and electrical properties, such as its high mechanical strength and stiffness and very high electrical and thermal conductivity [50-54]. However, its planar nature causes its electrical transport properties to be substrate-dependent; the highest room-temperature electron mobility for graphene supported by any material was on hBN single crystals (140,000 $cm^{2}\cdot V^{-1}\cdot s^{-1}$). The electron mobility of graphene from the same source placed on SiO_2 was nearly 2.5 times lower [55]. The high value of room temperature electron mobility for graphene on hBN is near to that of suspended graphene, allowing for high mobility graphene devices with less architectural limitations [13,55-59].

hBN substrates for graphene and other 2-D materials have been prepared using CVD-grown thin films or exfoliating layers from bulk crystals [13,55-60]. hBN layers exfoliated from bulk crystals have the highest electron mobility in graphene on hBN, superior to that of CVD-grown hBN layers due to larger grain size and lower surface roughness. However, CVD-grown hBN may become a route to producing large area hBN substrates if optimal growth conditions can be determined, particularly if graphene layers can be grown directly on top hBN by CVD [18-19]

Beyond simply supporting graphene on hBN for mobility measurements, heterostructures composed of stacked layers of hBN, graphene and other 2-D materials have been investigated to synthesize novel devices. Wang et al. [61] demonstrated a simple graphene field-effect transistor (GFET) composed of an hBN/bi-layer graphene/hBN structure, with hBN acting as both the substrate and gate dielectric. This device performed with superior electron mobility and carrier velocities than a conventional GFET on a SiO_2 substrate and Al_2O_3 gate dielectric and demonstrated an hBN/graphene high-frequency transistor. Many more novel designs leveraging the compatibility of hBN and graphene have been demonstrated in recent literature, including a high-frequency graphene transistor for RF applications [62], an hBN-supported thin graphene interconnect replacement for Cu on-chip wiring [63] and a process for developing monolayer circuits consisting of selectively grown strips of hBN and graphene [64], as well as several other devices [65-70]. Due to the large number of new 2-D materials being discovered and investigated, vertically-stacked heterostructure devices can be fabricated to create designer optoelectronic devices for an enormous range of potential applications.

2.3.3 hBN Deep UV LEDs

While much of the focus of recent research on hBN has been for its potential use as a substrate for graphene, hBN has also received attention for its optical properties. Like other group III-nitride semiconductors, such as AlN and GaN, hBN is notable for its light-emitting properties [6]. hBN is similar to other III-V compounds, such as AlN, in its wide bandgap energy (5.8 eV), resulting in band-edge light emission near 215 nm in the deep ultra-violet (DUV) spectrum upon excitation [71]. Cathodoluminescence spectra for hBN crystals grown by Watanabe *et al* [72] show an intense DUV peak at 215 nm, produced by both high pressure (Ba-BN flux) and atmospheric pressure (Ni-Cr flux) conditions. Additionally, hBN single crystals can have significantly higher luminescence intensity compared to other wide bandgap materials; compared to AlN, hBN has intensities 500x higher at low temperature (10K) and 100x higher at room temperature [73].

There are several potential applications for high efficiency solid state DUV lasers or LEDs, including medical or water sterilization systems or as a laser-reader in the next generation of optical media [74-75]. Conventional light sources in the DUV range are typically mercury, argon or excimer gas-discharge lamps, which are bulky, unstable, energy-intensive, short-lived and potentially toxic in event of containment failure [75-76]. Development of a compact LED or laser hBN device would allow for a safe, energy-efficient DUV light source without the issues associated with these conventional lamps.

Implementation of hBN LED devices requires improved hBN crystal quality and grain size, in order to maximize band-edge luminescence intensity, as well as allow for device fabrication and handling. New cathodoluminescence and photoluminescence studies of hBN band properties are needed, as its behavior as either a direct or indirect bandgap semiconductor remains in dispute [71-77]. Analysis of high purity, defect-free hBN crystals will enable these debates to be resolved.

2.3.4 hBN Nanophotonic Devices

hBN is an exciting new 2-D nanophotonic metamaterial, along with graphene, MoS_2 transition metal dichalcogenides and other new 2-D materials [78]. Using single or few layers of these materials, potentially in composite layered-heterostructures (as discussed in Section 2.3.2), these materials allow for strongly enhanced light-matter interactions and may enable new types of optoelectronic sensors and devices.

hBN is also notable not only as a 2-D dielectric for these materials, but also for its own specific nanophotonic applications. It displays hyperbolic optical response, due to its highly anisotropic structure [79]. This means that the real permittivity about its orthogonal crystal planes have opposite signs, so that it shows both metallic and dielectric optical behavior simultaneously [80]. Such behavior is of interest for a wide array of potential applications, such as super-resolution imaging (ultramicroscopy) and quantum nanophotonics in the mid-IR range [79-80] Additionally, hBN is also notable for its support of phonon-polaritons, which are collective modes originating from the coupling of photons with optical phonons in polar crystals [80]. The propagation of surface phonon-polariton waves in few-layer hBN was demonstrated by Dai *et al* [82]. This study proved that phonon-polariton wavelength and confinement was dependent on the number of hBN layers, allowing for tunable devices. The combination of these two properties allows for the propagation of hyperbolic phonon-polaritons in hBN, which allow for many near-field optical applications, such as sub-diffractional focusing and very large effective refractive indices (up to 86) [83-84].

Chapter 3 - Experimental Methodology

This chapter discusses the theory of the Ni-Cr flux growth process, as well as the major experimental and analytical techniques utilized by this study. A detailed description is provided of the furnace equipment and materials that was used for the hBN growth. Methods for crystal extraction and transfer are also discussed. Finally, the most significant microscopy and spectroscopy techniques used for hBN crystal analysis are discussed, including both their previous applications in literature and their implementations in this work.

3.1 Ni-Cr Flux Growth Method

Growth of hexagonal boron nitride crystals presents a unique challenge, compared to other semiconductor materials such as silicon or III-V materials (GaAs or GaN), as BN does not readily form liquid or vapor phase at reasonable temperatures and pressures. This inhibits typical melt-based crystal growth techniques, like the Czochralski process, or other methods like sublimation-recondensation growth and forces more complex methods to be pursued [6,85-86].

Unlike many semiconductor materials, boron nitride does not follow common phase transitions, such as melting into a liquid phase at elevated temperatures. Instead, boron nitride incongruently decomposes to solid or liquid boron and N_2, or sublimes from hBN to a vapor state at high temperatures and low pressures, depending on its environment. Like carbon, BN transitions from the hexagonal phase to a cubic phase at high temperatures and high pressures [8-10]. To work around these problematic phase transition problems, researchers investigated solution-based growth techniques as an alternative to conventional techniques to produce hBN single crystals, such as the flux method [1,22-31]. In this method, liquid-solid equilibrium is achieved by dissolving BN source material in a secondary flux, or solvent. This flux is heated to supersaturate the source material, and then is cooled to precipitate the desired crystals on the cooling flux surface.

To form crystals, BN powder is dissolved in a molten metal or metalloid flux. Several solutions have been investigated in literature; among these, the nickel-based solutions have produced the best results [1,29-31]. Taniguchi [29-30] originally selected a nickel solvent for production of cubic boron nitride (cBN) using a high pressure synthesis method, but eventually adapted the process for lower pressure growth of hBN [31]. The Ni flux was replaced with a Ni-Cr eutectic mixture to improve nitrogen solubility and was fully adapted to allow for growth of hBN at atmospheric pressures under nitrogen [1,31]. This atmospheric pressure operation is vital for the viability of this method, as it greatly reduces the cost and material demands for the growth temperatures required for this method.

Operating parameters for hBN growth using Ni-Cr flux were established based on work performed by Ben Clubine in his Master's Thesis work [37]. For his experiments, using a pair of vertical graphite and tungsten resistively-heated furnace, he found that large hBN crystal flakes (up to 5 mm in width) could be formed using dwell temperatures from 1450°C to 1700°C, dwell times of 24 to 48 hours. These crystals were characterized by x-ray diffraction (XRD) and Raman spectroscopy to analyze the quality, phase and strain of the hBN crystals. Their XRD pattern exhibited strong, narrow peaks for the (002), (004), and (006) planes, corresponding to stacked basal planes in the c-direction; however, some peaks consistent with non-basal planes in hBN, such as the (100),(101) and (102) peaks, were also present in the spectra, suggesting the presence of inter-crystalline grain boundaries and polycrystalline hBN within the samples [87-88]. Raman spectra of the hBN crystals showed single peak at 1366 cm^{-1}, corresponding to the E_{2g} vibration mode of hBN [89], with measured FWHM, 8.0 cm^{-1}. This was one of the narrowest peaks observed for hBN single crystals, compared to values of 9.1 cm^{-1} reported by Watanabe *et al* [31]. The presence of a single narrow peak confirms that these crystals exhibited low stress and high purity (*i.e.* no cubic BN) and was indicative of the quality of the crystals grown by this metal flux growth process.

3.2 Furnace Equipment

The horizontal flux growth methods pursued in this thesis are based on the work of Kubota *et al* [1,30-31]. In this process, hBN crystals are precipitated from Ni-Cr flux which is contained in a hot-pressed boron nitride (HPBN) boat, shown in Figure 3.1. Functionally, this HPBN boat serves as both the crucible for the flux and the BN source material during the growth process.

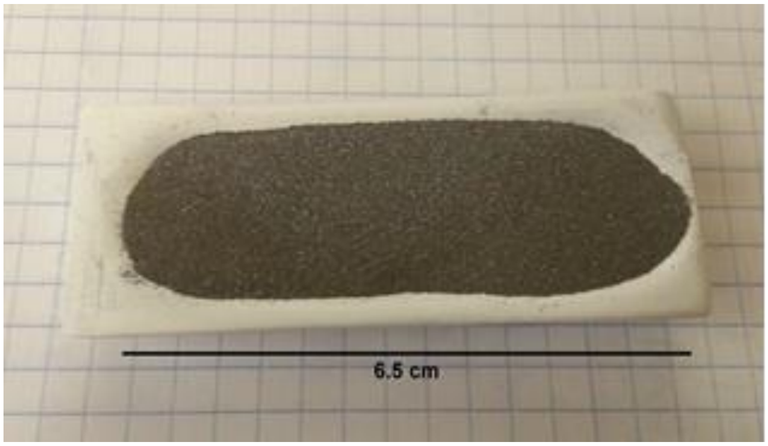

Figure 3.1: Optical micrograph of nickel and chromium powder loaded into a hot-pressed BN boat in preparation of ingot formation for hBN growth.

Two furnace systems were utilized for hBN flux growth over the course of my research. The first system was a CM Furnaces 1600 series single heating zone horizontal tube furnace, referred hereto as the “CM furnace”. The system was equipped to handle 1.5” OD alumina tubes, with a hot zone approximately 6 inches in length and an upper operating limit of 1600 °C. This furnace was used in preliminary studies for flux growth, as well as implementation of the response surface methodology (RSM) study of the flux process parameter space. The second furnace adapted for hBN flux growth was a Mellen Company TD16 series, four heating-zone (three hot, one cold), horizontal tube furnace, referred hereto as the “Mellen furnace”. It was equipped to handle a 2.5” OD alumina tube, with a total hot zone of approximately 18”, and was also capable of operating up to 1600°C. This system was used to scale-up the flux growth process to a larger Ni-Cr ingot mass, as well as investigate production-style growth refinement techniques. Each of these systems used U-shaped Super Kanthal $MoSi_2$ heating elements, with temperature measured by Type B thermocouples positioned within the hot zones of each furnace. These two furnace systems are shown below in Figure 3.2.

CM Furnace System

Mellen Furnace System

Figure 3.2: Micrographs showing (top-left) CM furnace system with sealed alumina tube, (bottom-left) wide-angle view showing CM furnace power supply and control system, (top-right) Mellen furnace system with sealed alumina tube and (bottom-right) Mellen furnace gas and temperature control system

These furnaces were operated in a similar fashion, but with a different size of alumina tubes and differently shaped HPBN boats. Boats for the CM furnace system were machined from a 1.125” diameter x 12” long BN rod, while boats for the Mellen furnace were shaped from 2”x 6”x 0.625” BN plates. The machined shapes for these boats are shown below in Figure 3.3. Source metals were weighed out on a 51 wt% Cr basis, thoroughly mixed and placed into the center of the bottom BN boat. The top and bottom boat were then stacked and loaded into the alumina tube installed in each respective furnace.

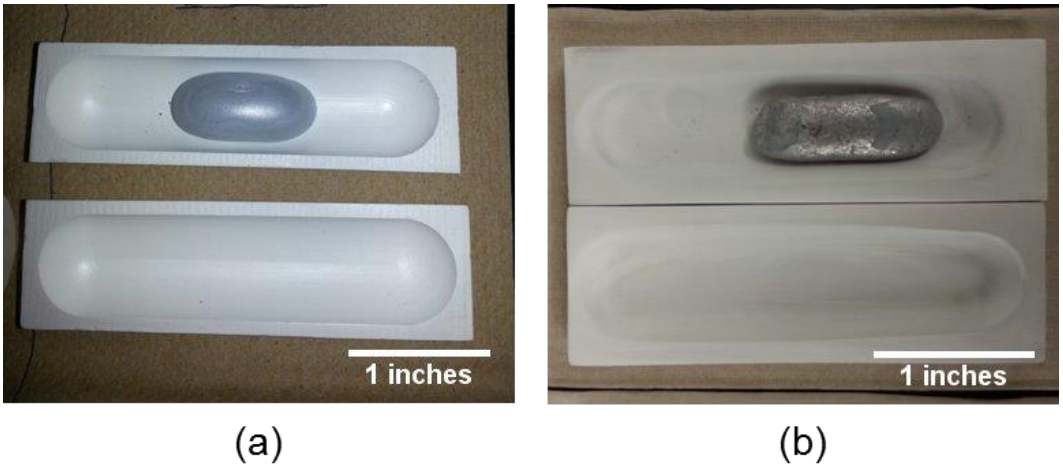

Figure 3.3: Optical micrographs of boats used for hBN crystal growth, machined from hot-pressed boron nitride (HPBN) (a) for the CM furnace system and (b) for the Mellen furnace system.

After centering the boat in the furnace hot zone, the alumina tubes were sealed using quick-connect fittings, which connected the furnace tube to the rest of the vacuum and gas flow system. Both N_2 and (in the Mellen system) forming gas (5% H_2 in Ar balance) was fed into the tube using a mass flow controller and pneumatic valve for each gas stream on the upstream side of the tube. Tube pressure was controlled by downstream rough and butterfly valves, alternatively feeding to a vacuum pump during gas purging cycles or to the fume hood exhaust during high temperature operation. Tube pressure was measured using a pressure transducer for high pressures (1-1000 torr) and thermocouple gauge for low pressures (0.001-1 torr), mounted at a T-junction near the upstream end of the alumina tube. During crystal growth, a positive pressure was maintained to prevent oxygen backflow during crystal growth at high temperatures. Diagrams of the vacuum and gas flow systems for the CM and Mellen furnaces are illustrated in Figure 3.4 and Figure 3.5.

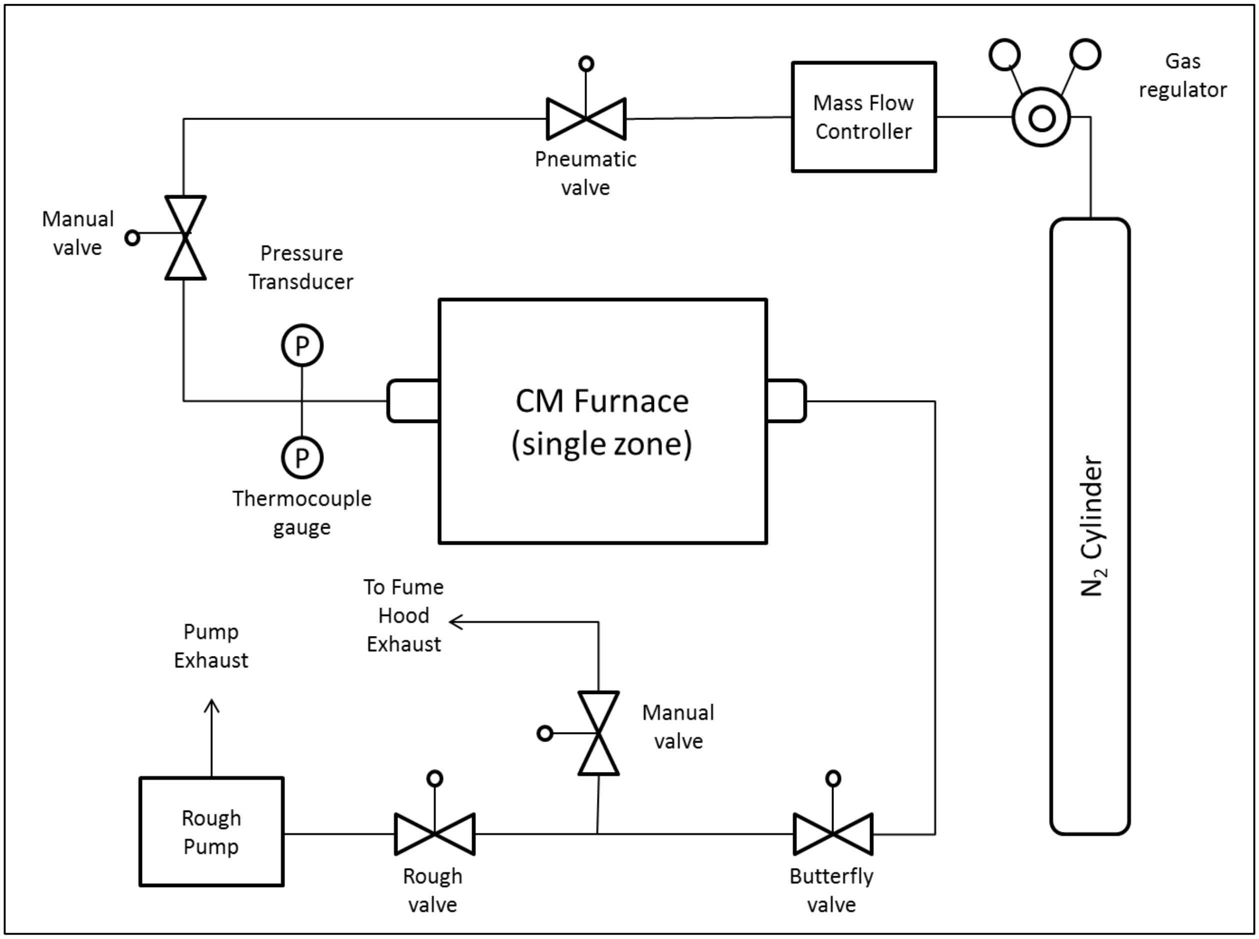

Figure 3.4: Generalized schematic of CM furnace and gas flow/vacuum system of hBN flux growth.

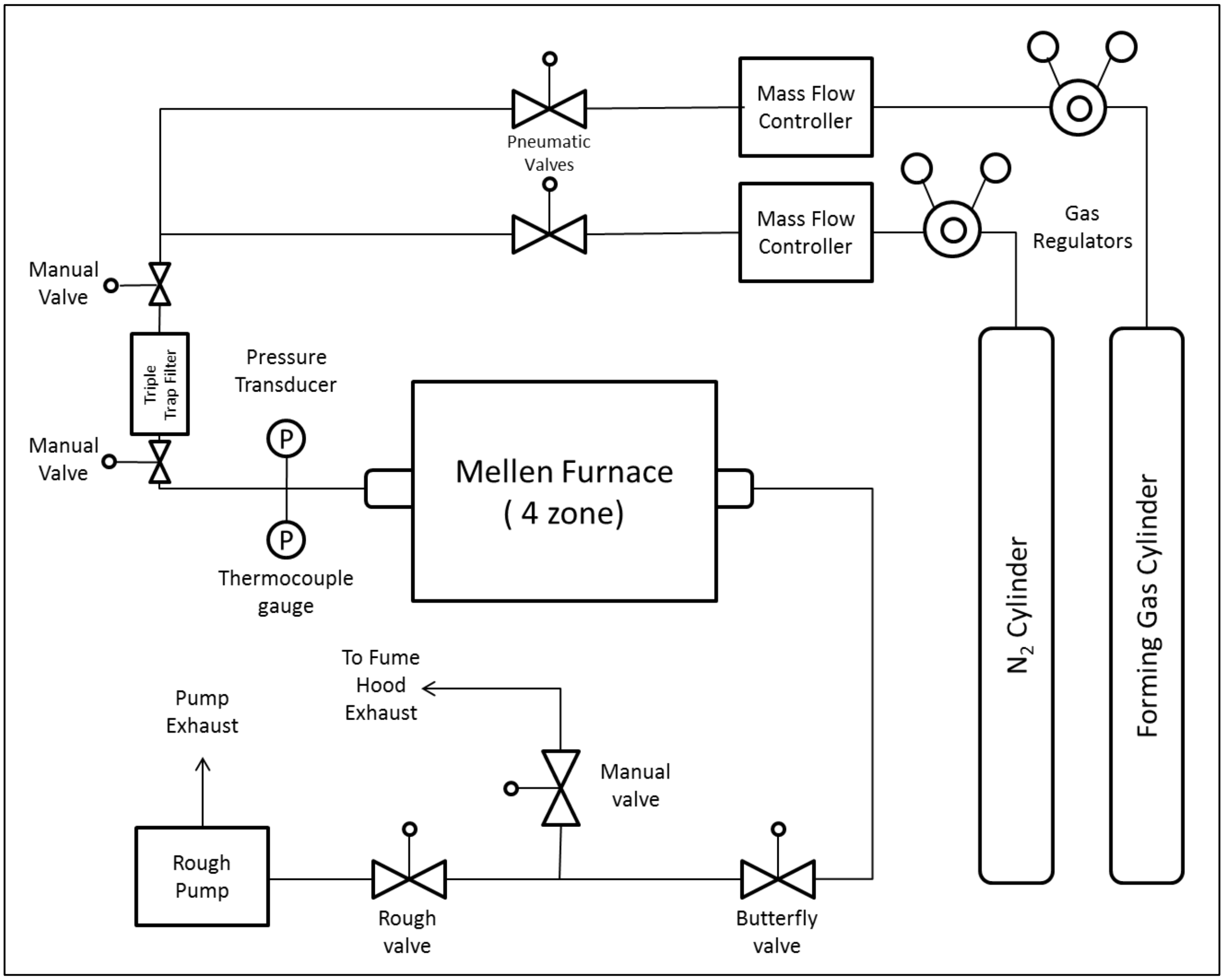

Figure 3.5: Generalized schematic of Mellen furnace and gas flow/vacuum system of hBN flux growth.

3.3 Experimental Materials

The materials of primary importance for this study were the nickel and chromium metal used for the flux, the gas flowed through the furnace chamber and the HPBN boats containing the molten metals. Ideally, crystal growth is performed with high purity materials, with particular focus toward the elimination of oxygen and carbon impurities, which can act as trapping sites and limit the formation of large crystals. This section enumerates the materials utilized for experimentation and their quality, in terms of size, form and specified purity.

Multiple sources of nickel and chromium were tested in the experiments; powder and bulk forms of both metals were employed. These metals sources were purchased from Alfa Aesar and are listed in Table 3.1, listing the materials, morphology (powder, etc.), purity and which furnace they were used for.

Table 3.1: List of standard nickel and chromium source materials used in CM and Mellen furnace experiments

Material	Particle size/mesh	Purity (metals Basis)	Vendor	Furnace
Nickel powder	-50+100 mesh	99.7%	Alfa Aesar	CM
Chromium powder	-100 mesh	99%	Alfa Aesar	CM
Nickel shot	2-25 mm	99.95%	Alfa Aesar	Mellen
Chromium pieces	2-12 mm	99.2%	Alfa Aesar	Mellen

Bulk metals were employed for the Mellen furnace experiment, as the larger boat enabled their use, while CM furnace boats were too small to hold the Ni shot and Cr pieces. These bulk materials were of slightly higher purity, due to their lower surface area. Oxygen and carbon impurity concentrations for the metal powders and resulting Ni-Cr ingots were assessed using LECO elemental analysis, listed below in Table 3.2.

Table 3.2: LECO analysis of carbon and oxygen impurity concentration for Alfa Aesar Ni and Cr powders (listed above in Table 3.1) and resulting Ni-Cr ingots

Analyzed Sample	**Carbon Concentration (ppm)**	**Oxygen Concentration (ppm)**	**Particle Size/Mesh**
Alfa Aesar Nickel powder	120	3200	-50+100 mesh
Alfa Aesar Chromium powder	180	>10	-100 mesh
Alfa Aesar Powder Ni-Cr Ingot	>100	>30	N/A

In addition to standard Ni-Cr flux growth, growth of isotopically enriched hBN was investigated in this study. To achieve this, ^{10}B and ^{11}B enriched metal powder was incorporated with nickel and chromium sources to form a Ni-Cr-B alloy. Two Ni-Cr-B alloy samples, each with composition of 46.76 wt.% Cr, 41.47 wt.% Ni and 11.78 wt% B, were prepared by Ames Laboratories using triple arc-melting on a water-cooled copper hearth plate under an argon environment. Source materials for the Ni-Cr-B alloy consisted of 99.998% purity electron beam melted nickel, 99.997% purity chromium, and two sources of enriched 99.999% purity boron from Ceradyne with isotope concentrations of 99.99 at.% ^{11}B and 92.64 at.% ^{10}B, respectively. The Ni and Cr source materials had low carbon and oxygen impurity concentrations; <75ppm and <35 ppm respectively, measured by glow discharge mass spectroscopy. These boron source materials were used for the high temperature synthesis and crystallization of hBN enriched in ^{11}B and ^{10}B isotopes, grown in alumina boats. An additional highly enriched ^{10}B powder source (>99% ^{10}B) was obtained from Ceradyne crystal growth of highly enriched h^{10}BN. This powder was mixed with the standard Ni and Cr source materials listed above (Table 3.1 and Table 3.2) to form a Ni-Cr-B flux, also grown in alumina boats.

The effect of oxygen and carbon impurities on the hBN growth process were evaluated with alternative nickel and chromium sources from ESPI Metals and Alfa Aesar. Details of these materials are listed below in Table 3.3. hBN was growth in the Mellen furnace system using these high purity metals (along with forming gas) to minimize oxygen and carbon impurities and produce high purity hBN crystals.

Table 3.3: List of alternative nickel and chromium source materials used in hBN growth experiments

Material	Vendor	Particle size/mesh	Purity (metals basis)	Carbon Concentration (ppm)	Oxygen Concentration (ppm)
Nickel powder	ESPI Metals	3.5 µm	99.995%	660	970
Chromium powder	ESPI Metals	2-5 mm	99.999%	15	220
Nickel powder	Alfa Aesar	-100 mesh	99.999%	<100	N/A
Chromium pieces	Alfa Aesar	2-3 mm	99.995%	N/A	N/A

High purity process gases were also employed for crystal growth to minimize the impurity incorporation. The nitrogen and forming gas were supplied by Matheson Tri-gas. Matheson Ultra High Purity grade N_2 gas (99.999% purity) had less than 2ppm oxygen, 2ppm carbon and 0.5 ppm total hydrocarbon concentration. Forming gas, made up of 5% H_2 in argon, was used as an additive gas in a 1 to 4 ratio with N_2 in the Mellen furnace system to reduce oxygen and carbon impurities present from metal and HPBN sources during furnace operation. Pure argon gas (99.9999%) was also used in place of N_2 for limited experiments investigating performance of hBN growth in a low nitrogen environment.

Hot-pressed boron nitride boats served both as the container for the flux and the BN source material. HBC-grade HPBN in both rod and plate form were obtained from Momentive and were machined to form the boats shown in Figure 3.3. This grade of HPBN was isothermally pressed and formed without the use of oxide binders to minimize carbon and oxygen impurities. Its impurity concentrations were less than 10,000 ppm carbon and 4000 ppm oxygen, as reported by the manufacturer.

The alumina tubes and boats used in the experiments were obtained from two providers, Coorstek and McDanel Advanced Ceramic Technologies. All alumina tubes and boats were 99.8% dense cast alumina and were capable of withstanding the temperatures and environments of the hBN flux growth process without degradation. Tubes were replaced approximately every 3-6 months and were subject to slight warping and red discoloration of the interior of the tube, as well as some embedding of Ni-Cr metal from evaporation over time.

3.4 Ni-Cr Flux Growth Process

The hBN Ni-Cr flux growth process was divided into two stages: an initial ingot formation cycle (used in most latter experiments) and a main experiment cycle. As the metal source materials (excluding the pre-formed enriched Ni-Cr-B alloys) were separate nickel and chromium, an ingot formation cycle was performed so that the metals could melt, mix and wet the HPBN boat to form a homogenous Ni-Cr ingot saturated in BN. Ni and Cr materials were weighed and loaded into the HPBN boat on a 51wt% Cr basis and well-mixed. The CM and Mellen furnace experiments were approximately 15g and 75g, respectively.

Following this, the loaded boat was centered into the hot zone of the furnace tube and the system was sealed. The tube was then evacuated and backfilled with N_2 (and forming gas) three times to sweep out and displace any residual oxygen and other gas contaminants present in the tube. On the third backfill, the tube pressure was increased to and maintained at 850 torr, by closing the rough valve to the pump and controlling the pressure through a butterfly valve which vented to the hood exhaust. The furnace was heated to 1500°C and held for 12 hours, then quenched to back ambient temperature at 200 °C/hr. This process resulted in the formation of a slightly rounded, shiny Ni-Cr ingot saturated in BN. In addition, during this step residual impurities migrated to the outer metal surface. After the cycle completed, the ingot was removed from the system, re-weighed and documented. It was then polished to remove these precipitated impurities, as well as hBN nuclei from the surface in preparation for the main experimental cycle. An example of the resulting polished Ni-Cr ingot is shown below in Figure 3.6.

Figure 3.6: Optical micrograph of Ni-Cr ingot after ingot formation cycle and polishing of precipitated impurities

After completing the ingot-formation cycle and polishing of the Ni-Cr ingot and HPBN boat, the main cycle experiment was performed. This process began with the weighing of boat and ingot. After these were recorded, the ingot and boat were again centered and sealed into the hot zone of the furnace tube, and the same triplicate evacuation–backfill cycle enumerated before was performed to remove oxygen impurities from the system. Following this, tube pressure was established and maintained at 850 torr, and the furnace was engaged in a set of four stages:

heating, dwelling, cooling, and quenching. Within these four stages, there are five process variables that can be tuned to control crystal growth: (1) dwell temperature, (2) dwell time, (3) cooling rate, (4) cooling temperature and (5) quench rate. Figure 3.7 illustrates these furnace stages and process variables in the hBN growth process.

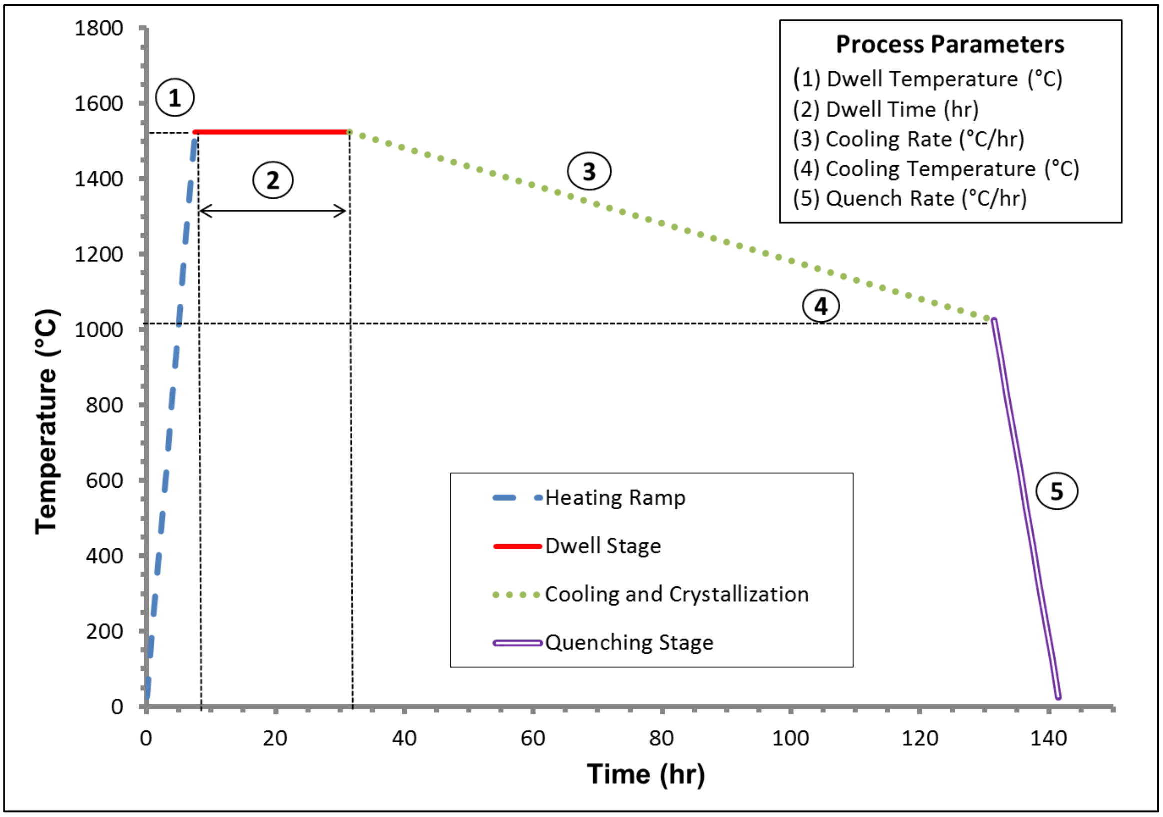

Figure 3.7: Diagram of furnace temperature profile during main cycle experiment and process variables that were controlled.

The crystal growth process began by rapidly heating the furnace at 200 °C/hr to the dwell temperature. It was then held at the dwell temperature for a specified dwell time. These first two stages allowed the Ni-Cr ingot to melt and re-wet the HPBN boat, saturating the metal with BN at the dwell temperature and allowing time for mixing. Next, the furnace was slowly cooled at a fixed cooling rate. In this stage, the driving force for hBN crystal nucleation was the reduction of BN solubility with the cooling Ni-Cr solution, causing hBN crystals to precipitate on the top and sides of the flux. hBN crystals continued to grow on the molten Ni-Cr as it slowly solidified. Once the mixture reached the specified cooling temperature, the furnace was quenched at 100-200 °C/hr to bring the tube to ambient temperature. Finally, the HPBN boat and metal ingot was removed from the furnace tube. Samples were weighed again following the experiment to ensure that there was no major mass lost during the run. A small amount of mass was lost (>5%) during most main cycle runs due to evaporation of the Ni and Cr at high temperature (at 1500°C, P_{vap} is 0.91 Pa for Ni, 2.06×10^4 Pa for Cr).

3.5 Crystal Transfer Methods

Following the hBN flux growth process, crystals were formed on the surface of the cooled Ni-Cr ingot. However, performing analysis of crystals while on the metal surface was difficult; therefore it was necessary to obtain freestanding crystals or transfer crystals onto a suitable handle substrate. Due to the high chemical stability of the Ni-Cr alloy, it was impractical to etch the metal away from the crystals. Instead, the mechanical softness and planar structure of the hBN was used as an advantage to allow for the dry transfer of crystals using thermal release tape.

Revalpha Thermal Release Tape[1] with 120°C and 150°C release temperature was obtained from Nitto Denko. hBN crystals were transferred by a method adapted from Caldwell *et at* [90] for the dry transfer of epitaxial graphene. First, the release tape was cut down to a suitable size, typically a 1cm^2 square. The Ni-Cr ingot was cleaned by sonication in acetone and allowed to dry to remove any dust or particulates from the crystal surface. Once dry, the release tape was contacted with the hBN crystals, and light manual pressure was applied for approximately one

---

[1] http://www.nitto.com/us/en/products/group/e_parts/electronic/001/

minute to provide a good tape-crystal interface. The tape was then slowly peeled from the surface, causing the hBN crystal to cleave about the basal plane and be removed with the tape. Finally, the crystal-tape complex was brought into contact with an arbitrary handle substrate. Manual pressure was used to ensure a good substrate-crystal interface, and then the tape-crystal-substrate complex was placed substrate side down onto a hot plate and heated to the tape release temperature. This caused the tape adhesive to release and the tape backing to peel away, transferring the hBN crystals on the handle substrate. Illustration of this transfer process as well as hBN crystals transferred onto glass handle substrate is shown in Figure 3.8(a) and (b), respectively. Alternatively, free-standing crystal flakes were obtained by following the above process, but washing crystals free of the release tape adhesive using acetone instead of bringing the flakes in contact with a handle substrate.

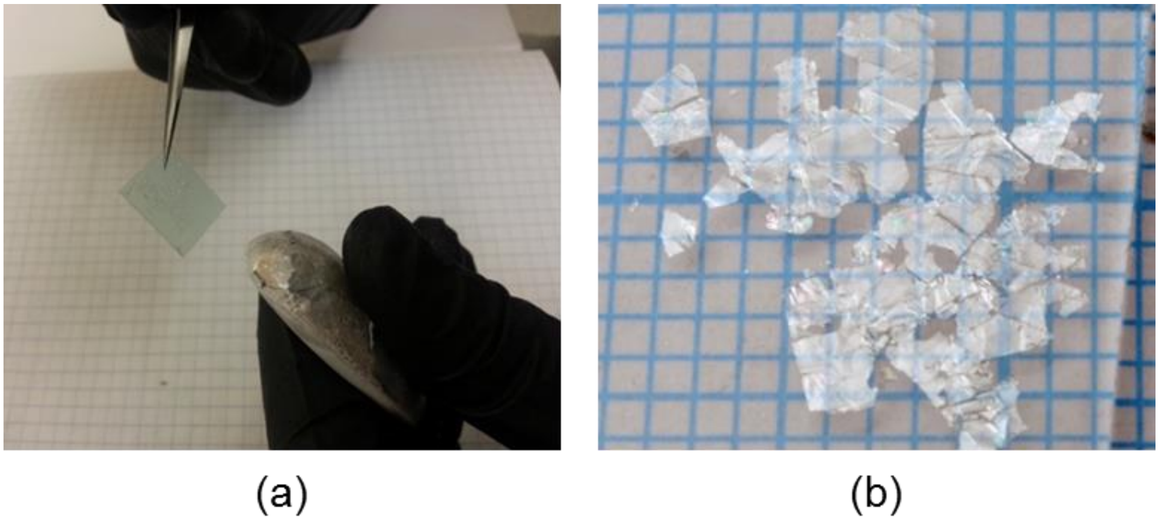

Figure 3.8: Optical micrograph showing (a) mechanical extraction of hBN crystals from the ingot surface using thermal release tape and (b) hBN crystals transferred onto glass substrate using thermal release tape process

Handle substrates for crystal transfer were chosen on the basis of the analysis techniques being utilized, including glass, quartz, sapphire and silicon. The thickness of hBN crystal layers transferred by this method was measured on the order of 10 μm.

3.6 Analysis Techniques

The hBN crystals grown by this study were characterized a number of analytical techniques to evaluate their physical, chemical and electrical properties. This section enumerates briefly on the theory and implementation of the main analytical techniques, including optical, electron and atomic force microscopy, x-ray diffraction, Raman and luminescence spectroscopy, and defect-selective etching.

3.6.1 Optical Microscopy

The most practical and important analytical technique employed in this study was optical microscopy. Using this technique, the width, thickness and quality of the crystal grown by the flux process was evaluated, as increasing crystal grain size is important to allow for easier device fabrication. Additionally, the thickness of grains formed is important, as increasing crystal thickness should increase the neutron absorption for hBN neutron detectors. An ideal crystal grain for a neutron detector would be over 1mm wide and 200μm thick.

The primary optical microscope utilized for analysis in this work was a Nikon LV100 series scope with magnification range from 50x up to 1000x. This system was equipped with an image capture system, allowing for the production and analysis of optical micrographs. Additionally, this system was also equipped with a Nomarski prism for differential interference contrast microscopy at higher magnification (500x-1000x) to enhance small textural features of samples. In addition to this microscope, a stereoscope system with image acquisition was also used for the analysis of larger samples at lower magnification. This system supported only standard optical microscopy setup up to approximately 50x magnification. Optical micrographs of these two systems are pictured below in Figure 3.9 and Figure 3.10.

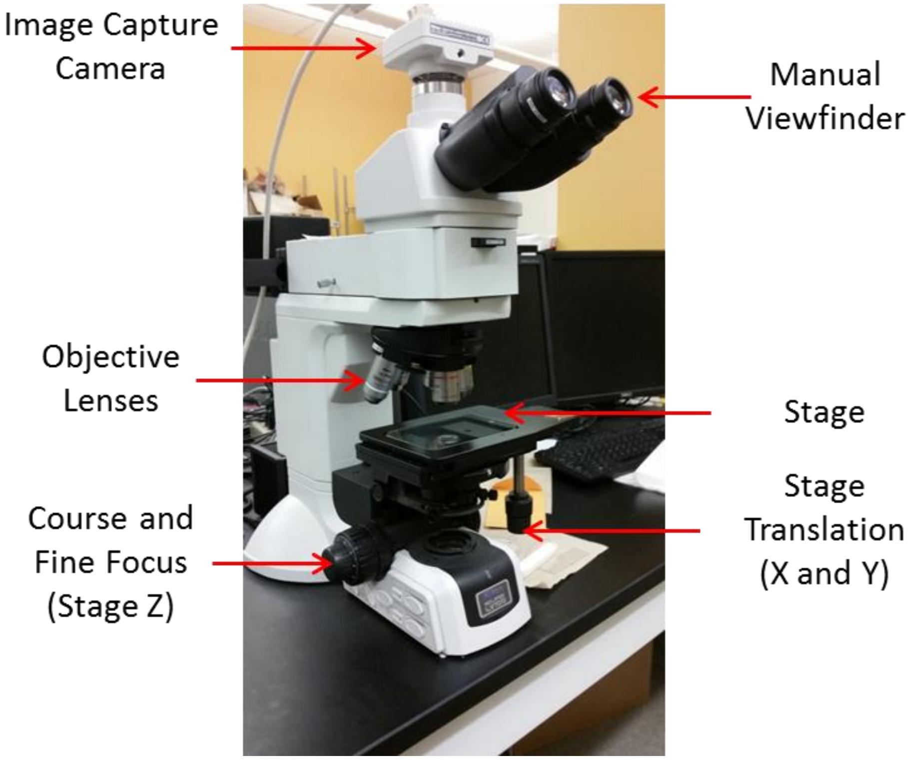

Figure 3.9: Labeled image of Nikon LV100 optical microscopy used for sample analysis and image capture.

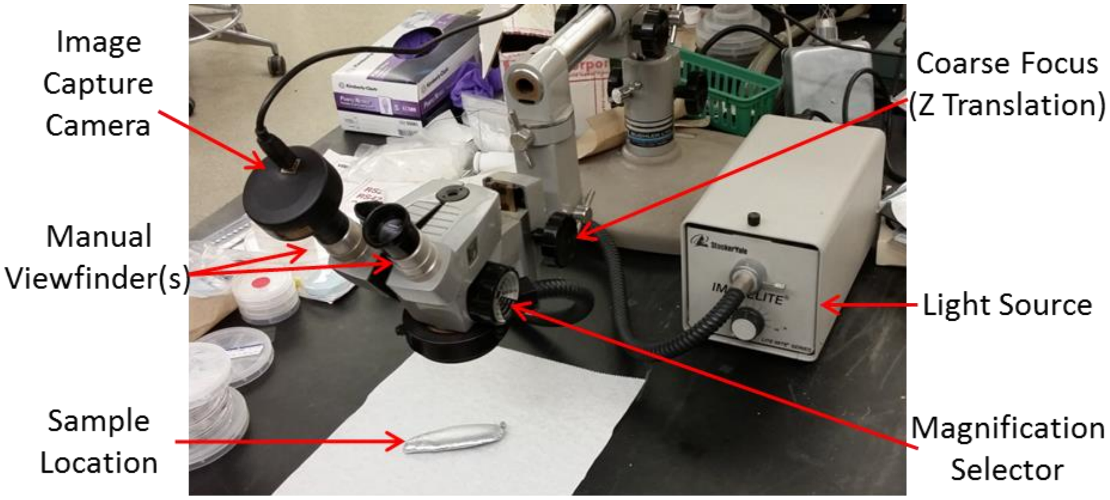

Figure 3.10: Labeled Image of Stereomicroscope system used for sample analysis and image capture.

Crystals were imaged while still on the Ni-Cr metal surface, after removal from the surface on release tape, as well as after transfer onto a handle substrate or free-standing. Crystals still on the metal surface were typically imaged with the stereoscope system. Otherwise, the Nikon system was preferred due to its higher magnification and improved image capture capabilities.

3.6.2 Electron Microscopy

In addition to optical microscopy, high-resolution electron microscopy techniques were employed for analysis of crystal microstructure features, most prominently scanning electron microscopy (SEM). In SEM, a beam of electrons, typically with energies between 1 and 30 keV, is focused onto a sample [91-92]. Electrons emitted from the sample are then collected and analyzed to form an image. Due to the short electron wavelength, SEM has superior resolution compared to optical microscopy.

The resulting electrons from the primary beam interacting with the sample are made up of two types: secondary electrons (SE) and backscattered electrons (BSE). Secondary electrons with energies below 50 eV, are typically produced through multiple collisions of the primary beam with the sample, while backscattered electrons have much higher energies (>50 eV) due to primary electrons scattering off the sample after only a few collisions. The production of these types of electrons is a function of atomic number (Z) in the sample material and the ratio of these electrons can provide contrast in the resulting image.

In addition to imaging information provided by SEs and BSEs, analytical information can be extracted from the sample from other sample interaction with the primary beam, such as characteristic x-rays. The energies of these x-rays can be analyzed to determine the elemental composition of samples, through techniques such as energy-dispersive x-ray spectroscopy

(EDS). An illustration of the information that can be extracted from SEM is shown below in Figure 3.11

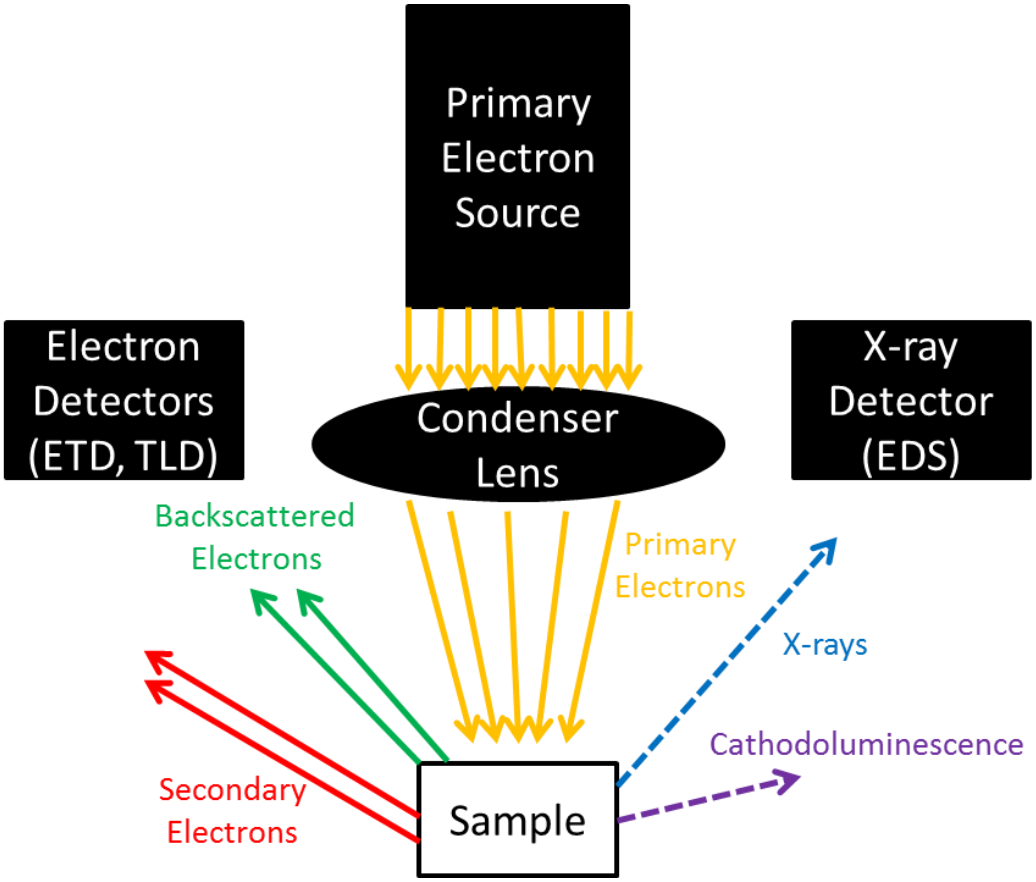

Figure 3.11: Generalized diagram of SEM operation. Primary electron beam is focused onto sample, producing backscattered and secondary electrons, x-rays, cathodoluminescence and other emissions which are collected via various detectors.

The SEM systems utilized for this work were the FEI Nova NanoSEM 430 at Kansas State University and a FEI Versa3D Dual Beam SEM/FIB at the University of Kansas Microscopy and Analytical Imaging (MAI) Laboratory. Typical accelerating voltages available for these systems' operation ranged from 1-30 kV, with an achievable minimum beam size of 0.8 nm at 30 kV. Detectors used for imaging included the standard Everhart-Thornley detector (ETD) and Through Lens detector (TLD), as well as the low voltage, high contrast vCD detector.

Both systems were also equipped with energy dispersive x-ray spectroscopy (EDS) detector systems, allowing for elemental characterization by the SEM system by analysis of characteristic x-rays.

Because hBN is an electrical insulator, charging of the crystals was a major problem which could distort the SEM image. To minimize these charging effects, samples were coated with a thin metal layer (10nm Au/Pd) before SEM analysis. This metal coating allowed for imaging of samples without charging artifacts.

3.6.3 Atomic Force Microscopy

The surface roughness and topography of the hBN crystals was analyzed by atomic force microscopy (AFM), with resolution down to the nanometer scale [93]. This technique uses a force probe, consisting of a cantilever and tip, paired with a focused laser and photodiode to evaluate surface height of a sample cause by measuring the upward or downward bending of cantilever. The sample is probed across a specified area, producing a 3-D topological map of the its surface.

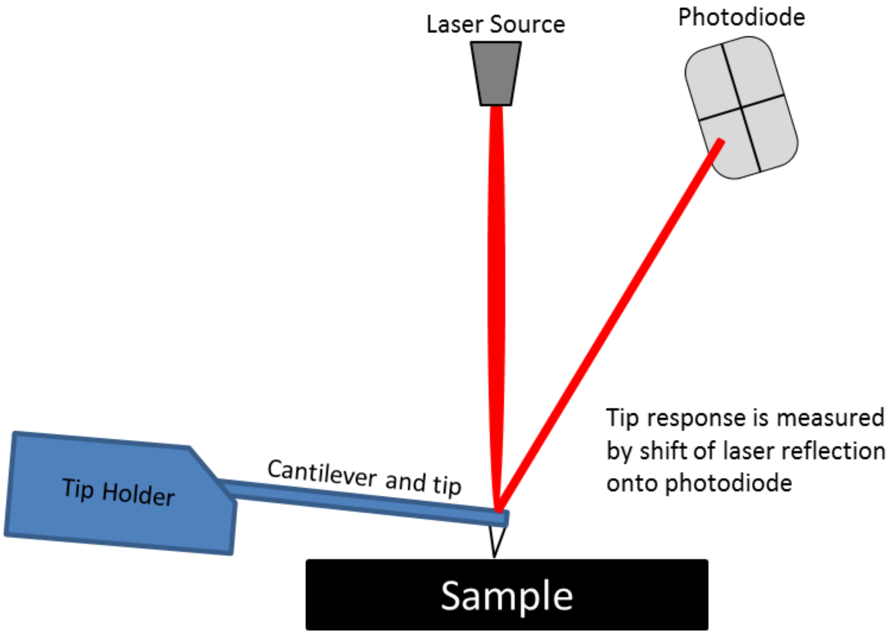

Figure 3.12: Schematic illustration of core components of AFM: cantilever and tip with holder, focused laser beam, photodiode detector. Tip response is actively probed by the reflected laser onto the photodiode.

Due to its 2-D nature, hBN crystals have exceptionally low surface roughness, approaching an atomically-smooth surface. This phenomenon has been characterized in work investigating hBN as a dielectric for ultrahigh mobility graphene [13] and graphene transistors [61], with RMS surface roughness values as low at 50 pm reported for 0.5x0.5 μm^2 areas. AFM can also evaluate the c-plane lattice parameter in hBN samples by measuring height difference of a single monolayer step [94].

AFM analysis performed in this study was done courtesy of Dr. Neelam Khan of Georgia Gwinnett College Department of Physics. Bulk hBN crystals were transferred onto suitable handle substrates (quartz) for analysis of surface roughness. Samples were measured in contact-mode using Innova AFM system and MSCT cantilevers.

3.6.4 X-ray Diffraction

X-ray diffraction (XRD) is an analytical technique which relies on Bragg diffraction of x-rays to characterize crystalline materials. Bragg diffraction occurs due to coherent and incoherent scattering of x-rays (or other particles, i.e. neutrons or electrons) passing through a crystal lattice at specific angles and wavelength and is described by Bragg's law:

$$n\lambda = 2dsin(\theta) \qquad \textit{Equation 1}$$

where *n* is an integer, λ is the wavelength of the incident wave, *d* is the lattice spacing and θ is the angle between the incident wave and the lattice plane [95]. An illustration of Bragg scattering is given in Figure 3.13.

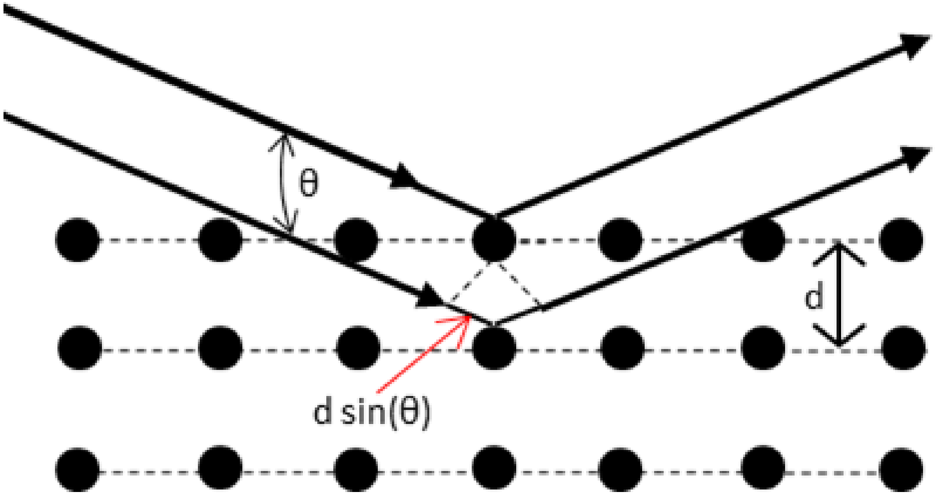

Figure 3.13: Visual representation of Bragg diffraction. Parallel lines show crystalline planes, while dots represent atoms. Scattering angle is a function of d-spacing and incident x-ray wavelength (λ).

XRD patterns have been employed extensively in powder and pyrolytic BN materials, to reveal their respective degrees of order. [11, 87-88,96]. Due to the hexagonal stacked nature of the material, the (002), (004) and (006) peaks dominate the spectra; other peaks, such as the (100), (101) and (102), are much less intense. Few spectra have been reported for bulk crystals, due to the difficulty of production and small size of these samples. Kubota *et al* [31] did report XRD pattern for crystals grown using a Ni-Mo flux method, similar to the one pursued in this study, after crushing the crystals into a fine powder. This pattern was dominated by the (002) peaks and its reflections, although many minor peaks were identifiable.

X-ray diffraction measurements provided quantitative information about the 3-D ordering and presence of stacking faults, plane slipping and polycrystallinity within samples. These measurements were performed using a Rigaku Miniflex II powder X-ray diffractometer with Cu $K\alpha_1$ X-ray source ($\lambda = 0.15456$ nm), pictured in Figure 3.14. The system was capable of performing coupled $\theta/2\theta$ scans with either a fixed or continually rotating sample. Scan range for the system was from 5° to 150° (2θ), with a scanning speed from 0.01°/min to 100°/min. To allow for scans to be complete with low noise in a reasonable time and without oversaturation of the detector, most scans were performed from 20° to 90° at a scanning speed of 1-2°/min Measurements were performed either on hBN crystals transferred onto glass or exfoliated onto release tape.

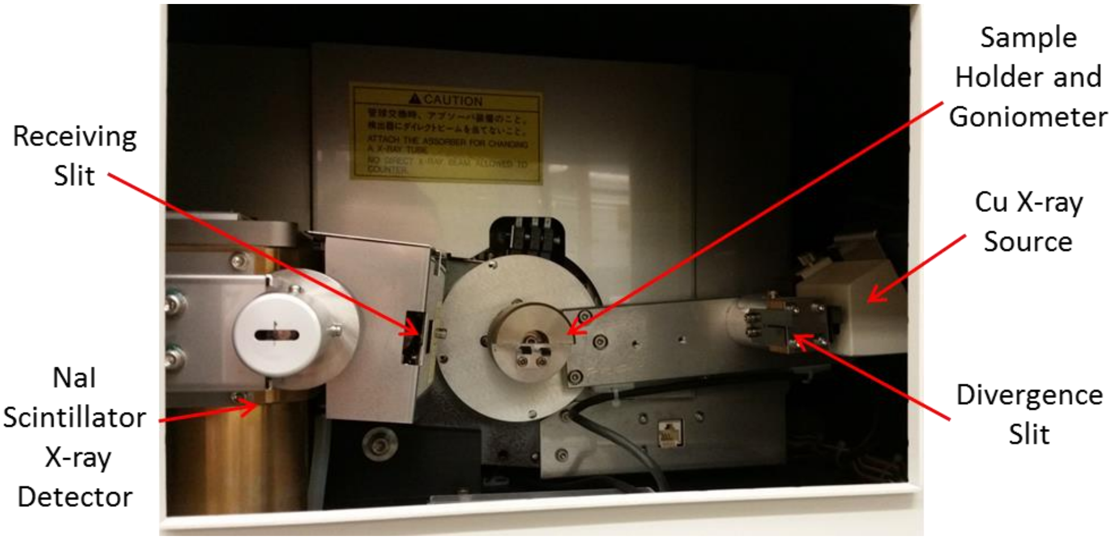

Figure 3.14: Labeled image of the interior of Rigaku Miniflex II powder x-ray diffractometer

The full width at half maximum (FWHM) of the (002) peak is a relevant figure of merit for assessing the quality of hBN bulk crystals, as its increase correlates to the presence of stacking faults, dislocations and other defects present in the crystal [88]. However, this measurement does not provide information on turbostratic disorder, the rotational misalignment of stacked basal planes in the [001] direction in the samples. Therefore, minor peaks, notably the (100), (101) and (102), are of interest to quantify the degree of this turbostratic disorder in crystals.

3.6.5 Raman Spectroscopy

Raman spectroscopy is a form of vibrational spectroscopy that utilizes inelastic scattering of a monochromatic light source as its principle mechanism for identifying vibrational modes in compounds [97]. The resulting spectra can be used as a "fingerprint", giving non-destructive identification on the physical properties of the material due to peak location, intensity and width. In crystalline materials, Raman spectra can be used to infer details on the presence of structural defects, identified by peak broadening, and on stress in the crystal lattice, which can shift the peak position several wavenumbers [98]. The primary Raman-active mode in hBN occurs near 1364-1370 cm^{-1}, determined experimentally by measurement on pyrolytic BN [89,99]. This vibrational mode is the E_{2g} phonon mode due to in-plane vibration of the B-N bond, similar to that observed in graphite.

Raman spectroscopy has been used successfully to analyze few-layer hBN, as the peak position shifts between mono and multi-layer samples, with the "bulk" peak occurring at approximately 1366 cm^{-1} and the monolayer peak occurring at 1369 cm^{-1} [94]. Few studies have been published that analyze Raman effects across bulk single crystal hBN due to their limited size and production. Kubota *et al* [31] reported a single Raman peak at 1365 cm^{-1} with a FWHM of 9.0cm^{-1} for an hBN bulk crystal grown using a Ni-Mo flux growth process. This measurement can serve as a benchmark for peak position and FWHM for single crystal bulk hBN standards. Comparatively, the Raman peak FWHM for pyrolytic BN films are on the order of 30 cm^{-1}, as reported by Geick and Perry [89].

Raman spectroscopy in this study was taken with a custom built system, courtesy of Dr. Bret Flanders at the Department of Physics at Kansas State. The system used a Nd:YAG frequency-doubled 532 nm laser source focused through a microscope and collected through a Horiba analyzer. This allowed focusing of the laser on the sample up to 1000x magnification. The Raman shift was calibrated using a Si standard based on its characteristic peak at 520 cm^{-1} [100]. Additional measurements were performed by Dr. Josh Caldwell and associates at the U.S. Naval Research Laboratories.

3.6.6 Photoluminescence Spectroscopy

Photoluminescence (PL) spectroscopy is a contactless, non-destructive, optical analytical technique used in semiconductor materials to probe their electronic structure and photoexcitation processes [101]. This method operates by exciting a material with light at energies above its bandgap, then observing the resulting photoemissions from the material as it relaxed to the ground state. A similar technique, cathodoluminescence (CL) spectroscopy, relies on similar principles but uses high-energy free electrons for excitation (often within an SEM system) [102]. Through these methods, spectra can be analyzed for the presence of impurities, dopants, structural defects and other trapping states, as well as investigate band structure [101-102]. Additional information may be gained by performing studies at low temperature or through time-resolved spectroscopy techniques.

For bulk hBN, PL and CL spectra have been reported in several studies by Watanabe *et al* for crystals grown using Ba-BN [71-72] and Ni-Mo [31] fluxes. These spectra evaluate room temperature band-edge luminescence at approximately 5.77 eV (215 nm wavelength) [71]. Through intrinsic fundamental absorption spectra analysis, Watanabe *et al* determined the experimental bandgap of hBN crystals to be 5.971 eV, with s-type exciton structure characteristic of a direct-bandgap material [71]. This bandgap measurement and structure has been disputed, however, with other studies reporting an indirect bandgap at 5.955 eV [77].

In addition to this main peak near 5.8 eV, luminescence spectra show several additional peaks. The first grouping of these occurs just below the main luminescence peak (from 5.8 eV – 5.4 eV) and corresponds to bound-exciton states attributed to stacking dislocations [103], Frenkel excitons [104] and donor-acceptor pair recombination [105]. A second grouping of mid-band states at approximately 4.5 eV- 4 eV was originally attributed to the presence of carbon and oxygen impurities within crystals [71], but recent study of 2-D hBN defect structure suggests these may also correlate to the presence of nitrogen vacancies and anti-site defects within the crystal lattice [106].

For the purpose of this study, PL spectra were used as a method to evaluate the quality of grown hBN crystals, both by peak intensity and width of the main luminescence peak near 5.8 eV (215 nm), as well as the presence of peak correlating to impurities and defects. Room temperature (300K) spectra were collected courtesy of Dr. Hongxing Jiang and Dr. Jingyu Lin of the Texas Tech University Nanophotonics Center, using a deep UV laser spectroscopy system consisting of a Ti/sapphire laser with excitation energy of 6.2 eV.

3.6.7 Defect-Selective Etching

Defect-selective etching (DSE) is a method to examine the defect structure and defect density of hBN crystals. In this technique, samples are etched at controlled conditions to produce etch pits propagating from defect sites within the material. Previous etching studies revealed that typical aqueous solution-based etching techniques at moderate temperatures (<100°C) were insufficient to etch chemically stable hBN. Instead, chemical and electrochemical methods using KOH and other hydroxide salts at high temperatures (>350°C) have been identified for successfully forming etch pits. The most conventional etching technique is a molten KOH or KOH/NaOH mixture [107-110].

Using DSE developed by prior studies on other materials (GaN, AlN and SiC), conditions for etching of bulk hBN crystals were developed using a 50 mol% KOH/NaOH molten mixture [107-112]. Crystals were etched using a canister-style furnace, placing the etchant in a vitreous carbon crucible centered in the furnace, as pictured in Figure 3.15. The etchant was heated to a molten state at the desired etching temperature, from 425-525°C. The hBN flake was introduced to the etchant and etched for one minute. Then the flake was removed and quenched in water to cool the sample, stop the etching process and remove the majority of the etchant on the flake surface. Following this, the flake was soaked overnight in a 30 vol% acetic acid solution to remove the residual hydroxide salts. Etch pits were then analyzed by optical microscopy, SEM and AFM to determine their size, topography, orientation and areal density as a function of etching temperature. Detailed analysis of this DSE study on hBN crystals is discussed in Chapter 7.

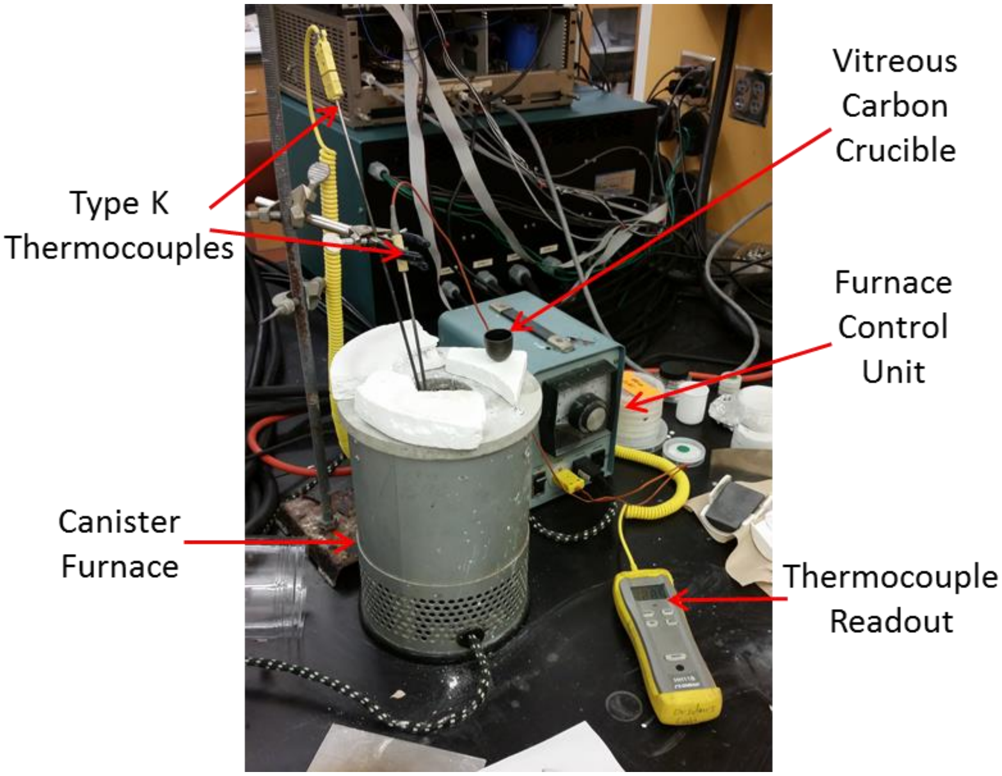

Figure 3.15: Labeled image of canister furnace setup used for defect selective etching of hBN flakes using molten KOH-NaOH etchant.

Chapter 4 - hBN Growth by Ni-Cr Flux Method

The initial experiments and study of the growth of bulk hBN crystals in this work were a continuation of the study done by Ben Clubine, [38]. These first experiments tested whether the hBN growth method, originally performed using vertical furnaces, could be adapted the horizontal CM furnace system. They investigated the effect of cooling rate on hBN crystal size and morphology, and were published in May 2013 in the *Journal of Crystal Growth* in combination with Mr. Clubine's work on similar experiments focused on the effects dwell time and temperature [39]. Then, several additional experimental studies were performed using both the CM and Mellen furnaces to further improve and refine the crystal growth process.

This chapter discusses the results and findings of these experiments, including the adaptation of hBN growth to the CM furnace, the study of cooling rate on crystal formation, the implementation of an ingot formation cycle to improve growth consistency, the process scale-up from the CM to the larger Mellen furnace, the study of how growth parameters effect crystal morphology, the use of forming gas to eliminate oxygen and carbon impurities, the effect of N_2 partial pressure of hBN formation and the use of high purity Ni and Cr sources. These studies go into the "sausage-making" of hBN crystal growth, enumerating the major findings, as well as the process minutiae which helped to incrementally improve process consistence and crystal quality.

4.1 Methods

Experiments discussed in this section were performed using a combination of the CM and Mellen furnaces to further understand and improve the Ni-Cr growth process. Different growth conditions, including cooling rate, the use of a "pre-melt" ingot formation cycle and different gas makeup mixture and high purity materials were investigated among several series of experiments to better control the hBN crystal growth process to yield large, defect and impurity free crystal grains. The furnace operation was described in Chapter 2. Source materials were Ni and Cr powder for the CM furnace runs and Ni shot and Cr pieces for the Mellen furnace runs, unless otherwise specified. Analysis of these samples was performed using optical microscopy, as well as SEM, XRD and photoluminescence spectroscopy. Additional details on the implementation of these techniques and others are further discussed within each study.

4.2 Results and Discussion

In this section, several procedures for improving hBN crystal growth using the Ni-Cr flux method are explored, including the implementation of the "pre-melt" ingot formation cycle, the scale up of BN boat and metal ingot size from the smaller CM furnace to the Mellen furnace, the impact of forming gas and the effect of N_2 partial pressure on hBN and ingot morphology and the use of high purity (low carbon and oxygen impurities) nickel and chromium sources. Additionally, different hBN crystal morphologies were investigated based on control of process parameters. These experiments are vital toward the qualitative and quantitative understanding of the Ni-Cr flux growth process, as well as moving it forward into a more reliable industrial growth process.

4.2.1 Cooling Rate Experiments

A set of hBN crystal growth experiments was performed to qualitatively understand how cooling rate affected the crystal morphology. These used the CM furnace, with Ni and Cr powders mixtures (without an ingot formation cycle) at a 51 wt% Cr composition in HPBN boats. Experiments operated following the standard four-stage heating cycle, illustrated in Figure 3.7, with dwell time and temperature held constant at 24 hr and 1500 °C, respectively. The cooling rate was varied from 2°C/hr to 10°C/hr, cooling to 1200 °C and causing the hBN to precipitate and crystallize on the surface of the flux. This was followed by a quench at 200°C/hr after cooling to 1200 °C to cool the system to ambient and allow for analysis.

Following these experiments, the hBN crystals formed on the Ni-Cr flux surface were analyzed by optical microscopy to determine the crystal morphology and size (Figure 4.1 and Figure 4.2). The quality of the hBN layers was highly dependent on the cooling rate. The crystalline morphology shifted from a fine grain, grey-white layer formed at a cooling rate of 10°C/hr to a sheet of clear crystals formed at 2°C/hr. The 4°C/hr cooling rate appeared to mark the transition cooling rate for the formation of optically clear, large (>500 µm) crystal grains. At this cooling rate, crystals tended to form as islands surrounded by white, fine-grain and powder-like hBN. The highest quality crystals were grown at 2°C/hr. They were clear and colorless, with some cracking within crystalline grains, presumably due to strain resulting from phase change within the metal flux during cooling, lattice mismatch and difference in coefficient of thermal expansion between the metal and crystals.

(a) *10 °C/hr cooling rate* **(b)** *4 °C/hr cooling rate* **(c)** *2 °C/hr cooling rate*

Figure 4.1: Macroscopic optical micrographs (taken by stereomicroscopy) illustrating differences in hBN crystal morphology grown at cooling rates of (a) 10°C/hr, (b) 4°C/hr and (c) 2°C/hr. hBN morphology transitions from a white-grey film (10°C/hr) to a clear crystal sheet with macroscopically visible grain size (2°C/hr) with decreasing cooling rate. Reproduced from Hoffman et al [38].

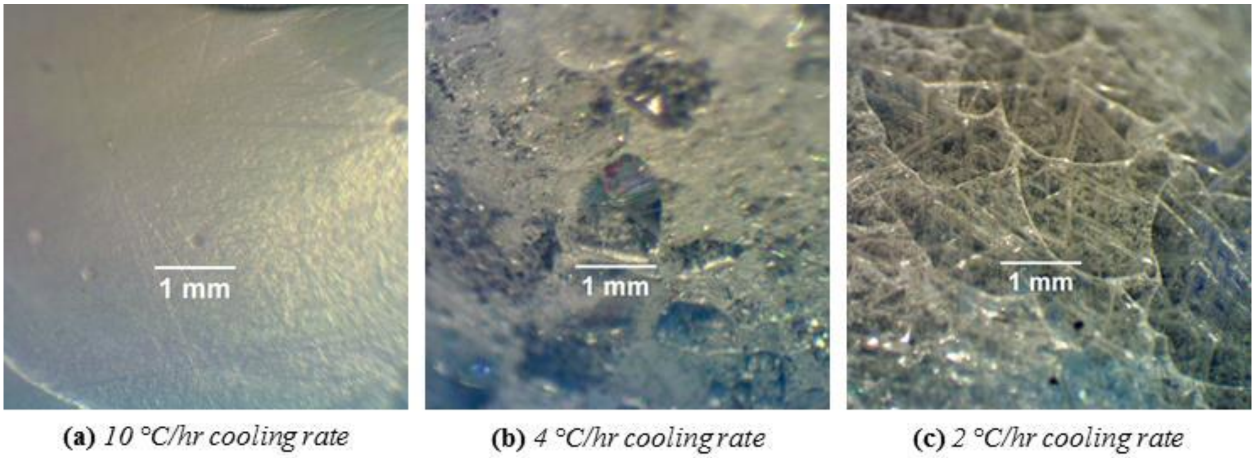

(a) *10 °C/hr cooling rate* **(b)** *4 °C/hr cooling rate* **(c)** *2 °C/hr cooling rate*

Figure 4.2: High magnification optical micrographs (taken by Nikon LV100) comparing hBN crystal grains grown at cooling rates of (a) 10°C/hr, (b) 4°C/hr and (c) 2°C/hr. hBN quality transitions from white-grey in color and very small grain size (10°C/hr) to clear crystals with macroscopically visible grain size (2°C/hr) with decreasing cooling rate. Reproduced from Hoffman *et al* [38].

The hBN flakes grown at 2°C/hr cooling rate were transferred onto a glass handle substrate via thermal release tape transfer. They were optically clear with single domain size on the order of 300 μm across (Figure 4.3). These flakes were then characterized by XRD, scanning from 20° to 90° (2θ). This diffraction pattern was compared to that produced by hBN powder ground off of the HPBN boats (Figure 4.4). The crystal samples were significantly more ordered than their source material, characterized by the narrowing of the (002) basal plane peak, from 0.63° for the powder to 0.18° for the crystal. Additionally, the (100) and (101) peaks seen in the powder sample were absent in the crystal sample, confirming that it was of single crystal orientation.

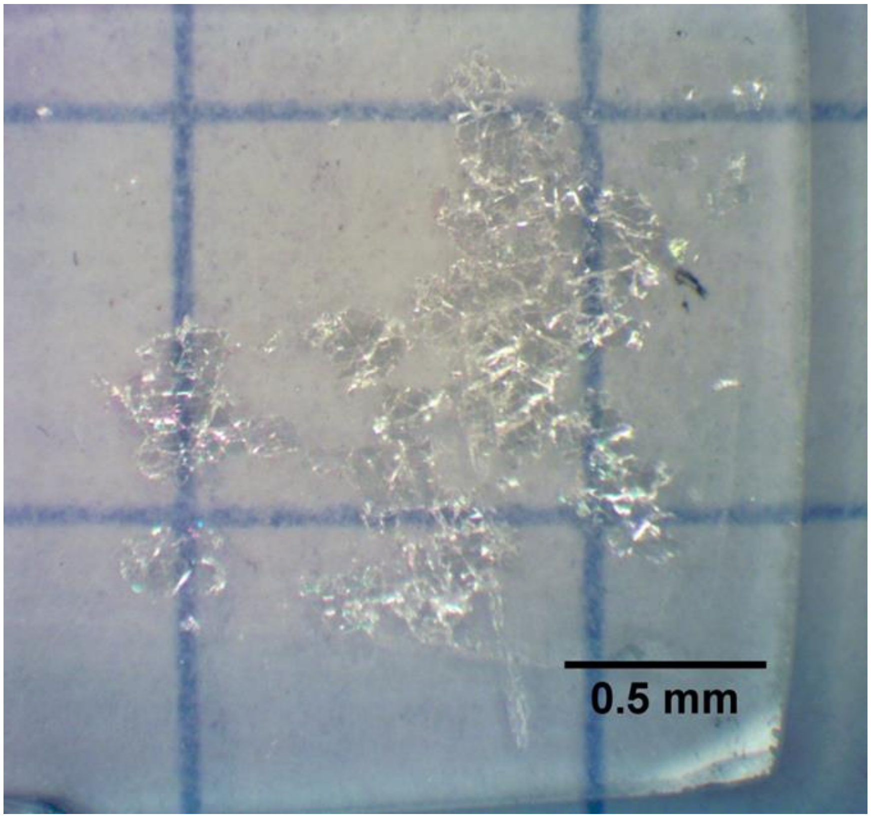

Figure 4.3: Optical micrograph of hBN crystals grown at 2°C/hr cooling rate transferred by release tape to a glass handle substrate for XRD and Raman analysis

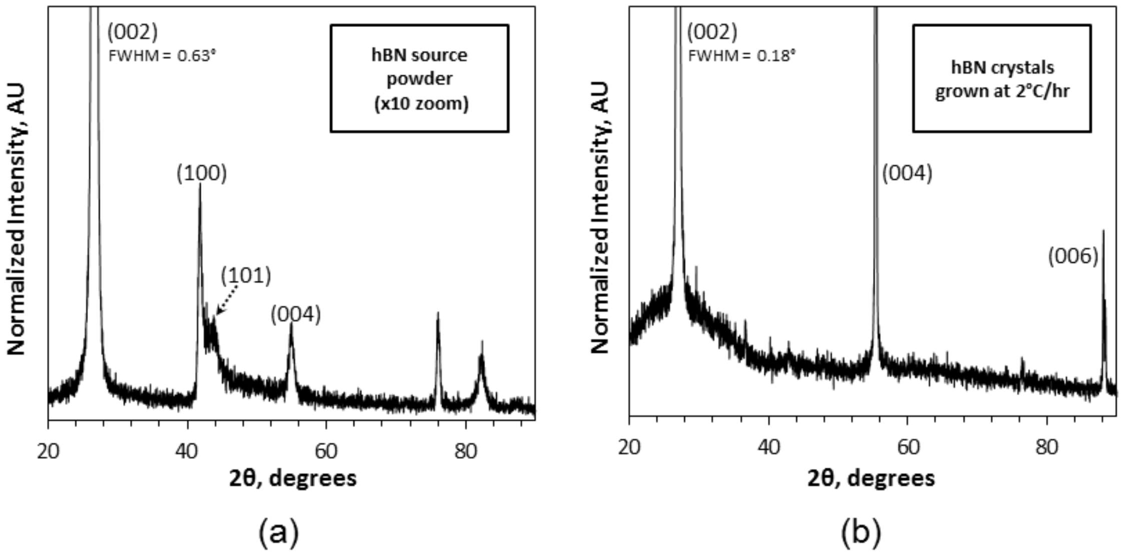

Figure 4.4: XRD spectra for (a) Momentive HBC grade BN powder (source material) and (b) hBN crystals grown at 2°C/hr cooling rate transferred onto glass handle substrate. Substantial (002) peak narrowing and suppression of satellite peaks, such as the (100) and (101) peaks, confirm crystals are well-ordered and of high quality.

The main Raman peak taken on these hBN flakes on glass was at 1366 cm^{-1} with a peak FWHM of 9.0 cm^{-1}, in agreement with Clubine [37] and Watanabe *et al* [31] for single crystal hBN (Figure 4.5). This confirmed that these crystals grown at 2°C/hr were hBN of high quality with low strain.

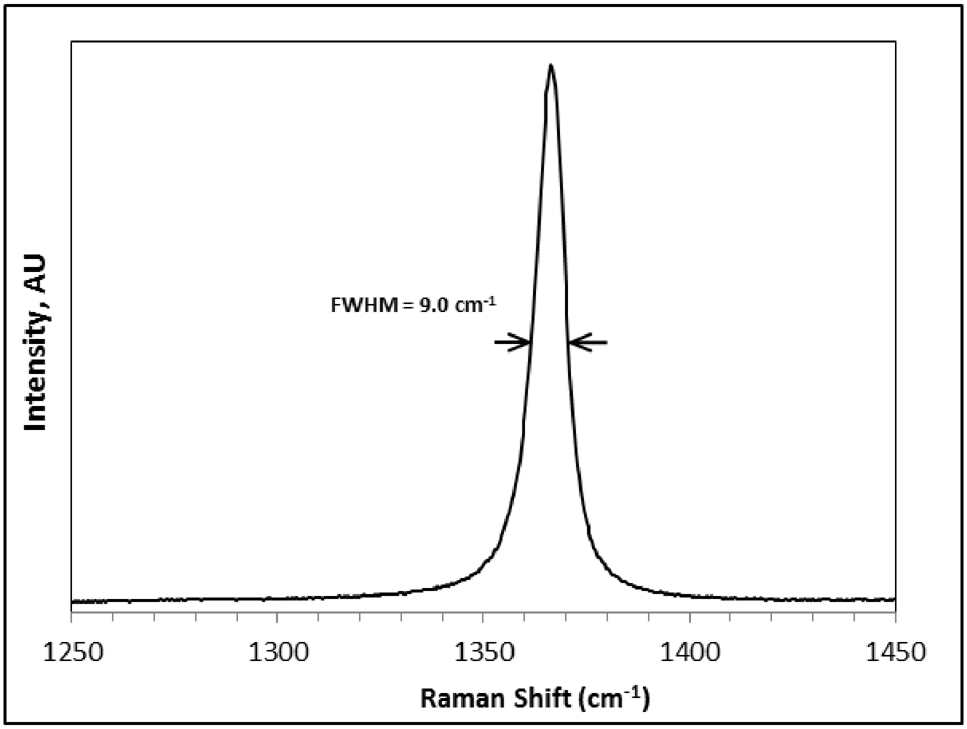

Figure 4.5: Raman spectra for hBN crystal grown at 2°C/hr cooling rate. The peak maximum was observed at 1366 cm^{-1} with FWHM of 9.0 cm^{-1} corresponds to the E_{2g} vibration mode for hBN and in agreement high quality crystals.

4.2.2 Effect of Ingot Formation Cycle on Growth Consistency

Early experiments were performed by starting from separate Ni and Cr sources with no pre-mixing. For these experiments, dwell temperatures and times of 1500-1525°C and 24-36 hours, respectively, and cooling rates between 2-4°C/hr, were investigated, mixing nickel and chromium source materials in the BN boat before loading into the CM furnace. Unfortunately, these experiments had a high rate of failure and run-to-run variability, often producing discolored or otherwise low quality non-crystalline BN layers. This poor production of hBN was believed to be caused by impurities present in the source metals, which migrated out of the molten flux, causing discoloration in the form of nickel and chromium oxide and serving as nucleation sites to produce large amounts of fine grain BN. The different types of experimental failures are shown in Figure 4.6.

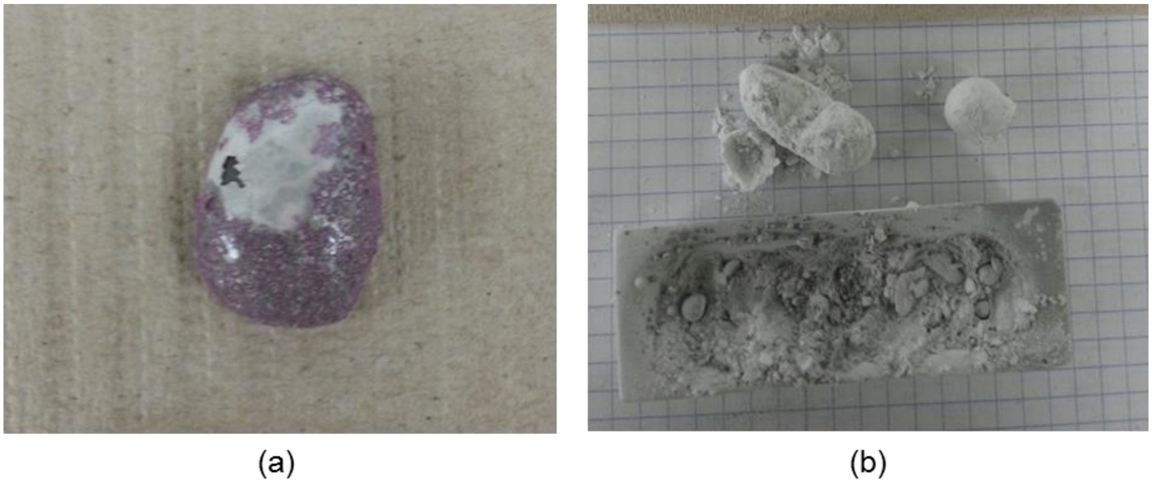
(a) (b)

Figure 4.6: Optical micrographs illustrating (a) migration of oxides to the ingot surface, causing red discoloration and (b) presence of impurities causing formation of fine grain, polycrystalline BN layers.

In searching for a solution to this problem, previously formed Ni-Cr ingots were re-used. These ingots were first thoroughly polished, removing all BN and oxide discoloration from its surface until shiny, and then reloaded into the furnace in a BN boat. hBN crystals were then grown on the recycled ingot using the process parameters listed above. A polished Ni-Cr ingot prepared for recycle experiment is shown in Figure 4.7.

Figure 4.7: Optical micrograph showing polished Ni-Cr ingot readied for recycle experiment

These recycled ingots produced high quality hBN crystals more reliably than experiments performed starting from separate Ni and Cr sources. This was due to two main reasons. First, reusing Ni-Cr ingots ensured that the molten flux produced would be fully saturated in BN and already well-mixed. Further, initial flux formation and cooling forced impurities from the Ni and Cr sources to precipitate on the surface; these were eliminated by polishing before subsequent experiments.

This impurity segregation phenomenon was confirmed by dicing an ingot used in a successful recycle experiment and performing elemental analysis on carbon, oxygen and nitrogen on the metal bulk through the LECO Corporation. Nickel and chromium source materials were also tested for comparison. From this analysis, the carbon and oxygen impurity concentrations in the recycled Ni-Cr ingot were less than 35 ppm, compared to 130 ppm and 3300 ppm, respectively, for the Ni source and 30 ppm and 200 ppm, respectively for the Cr source. Additionally, the nitrogen concentration for the recycled ingots was as high as 18,000 ppm, compared to <10 ppm for the Ni source and 20 ppm for the Cr source, showing the saturation of BN in the recycled ingot. These results are summarized below in Table 4.1.

Table 4.1: Summary of LECO elemental analysis of carbon, oxygen and nitrogen in recycled Ni-Cr ingot and Ni and Cr source materials

Sample	Carbon Conc. (ppm)	Oxygen Conc. (ppm)	Nitrogen Conc. (ppm)
Recycled Ni-Cr Ingot	35	35	18,000
Ni Source	130	3300	<10
Cr Source	30	200	20

Based on these findings, the standard experimental procedure was modified to include an ingot formation cycle before hBN crystal growth experiments (as explained in Chp 2). In this cycle, Ni and Cr source materials were loaded into the furnace, ramped to 1500°C, held for 12 hr, and then quenched to ambient temperature. This was a quick method to melt and mix the Ni and Cr source materials and saturate the ingot in BN, effectively simulating the recycle experiment conditions while efficiently using time. After this cycle, the ingot was removed from the furnace, polished to remove all surface impurities and prepared for the crystal growth cycle. This experimental structure (ingot formation → crystal growth cycle) was implemented for all future experiments (with exception of experiments re-using Ni-Cr ingots from prior runs). Additionally, this method showed that Ni-Cr ingots could be easily recycled for production-style hBN growth (particularly if the hBN crystals could be effectively separated from the ingot).

4.2.3 Scale Up of CM Furnace Methods to Mellen System

In an effort to grow larger hBN crystals, the Ni-Cr process was adapted from the smaller CM furnace (1.5” OD alumina tube) to the multi-zone Mellen furnace (2.5” OD alumina tube). The differences between these two systems were explained in Chapter 2. Growth with larger amounts of source material produced more hBN crystals per run (and thus per unit time) due to the larger cross-sectional area available in the 2.5” OD tube, as well as the increased hot zone width. Furthermore, the longer and wider BN boats used in the Mellen furnace decreased the curvature of the flux surface, inducing less stress on the hBN crystals.

Due to the change in the alumina tube size, a different BN boat configuration was used for the Mellen furnace experiments, shifting from the 3” (long) x 1.125” (diameter) trenched rod boats of the CM system to the 2” (wide) x 6”(long) x 0.625” (thick) trenched plate boats, shown in Figure 3.3. This change in boat shape allowed for a major increase in Ni-Cr ingot size, thus increasing the top surface area useable for hBN crystal formation from approximately 5-6 cm^2 to 18-20 cm^2 for typical successful samples. The difference in size between the ingots formed from these two furnaces is illustrated in Figure 4.8. Additionally, due to the larger size of the Mellen furnace, up to three of these samples can be grown simultaneously, increasing the effective total surface area for crystal growth up to tenfold.

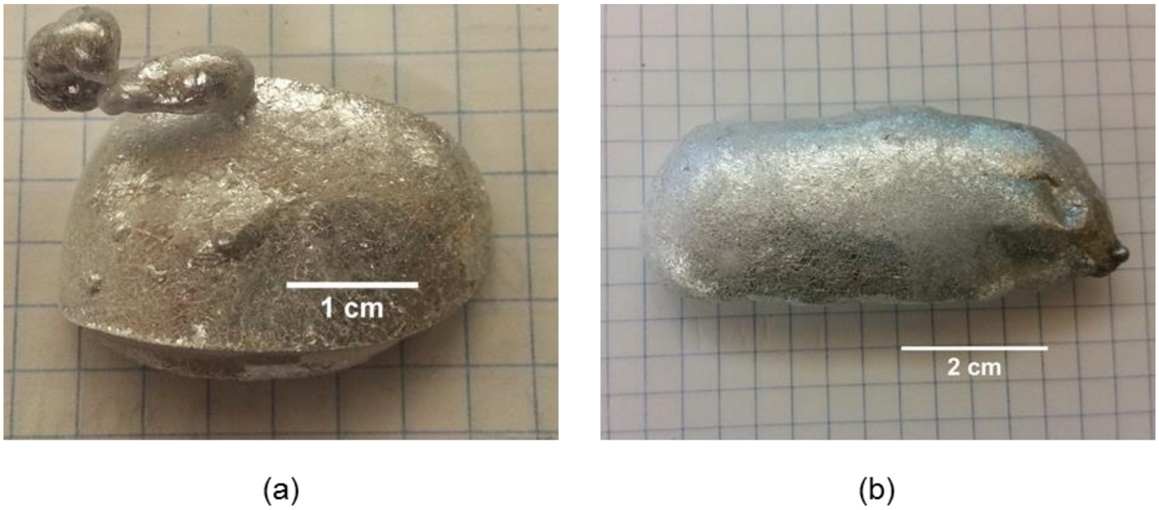

Figure 4.8: Optical micrographs of Ni-Cr ingot with hBN crystals formed on the surface produced from the (a) CM furnace and (b) Mellen furnace.

Scaling up this process to the Mellen furnace enabled the growth of large areas of high quality crystals, while freeing the CM system to use as a pilot furnace to explore the effects of process parameters on the growth process, as will be discussed in Chapter 5. Additionally, some of the larger hBN crystal grains (as large as 2 mm in width) were grown in the Mellen system, shown in Figure 4.9.

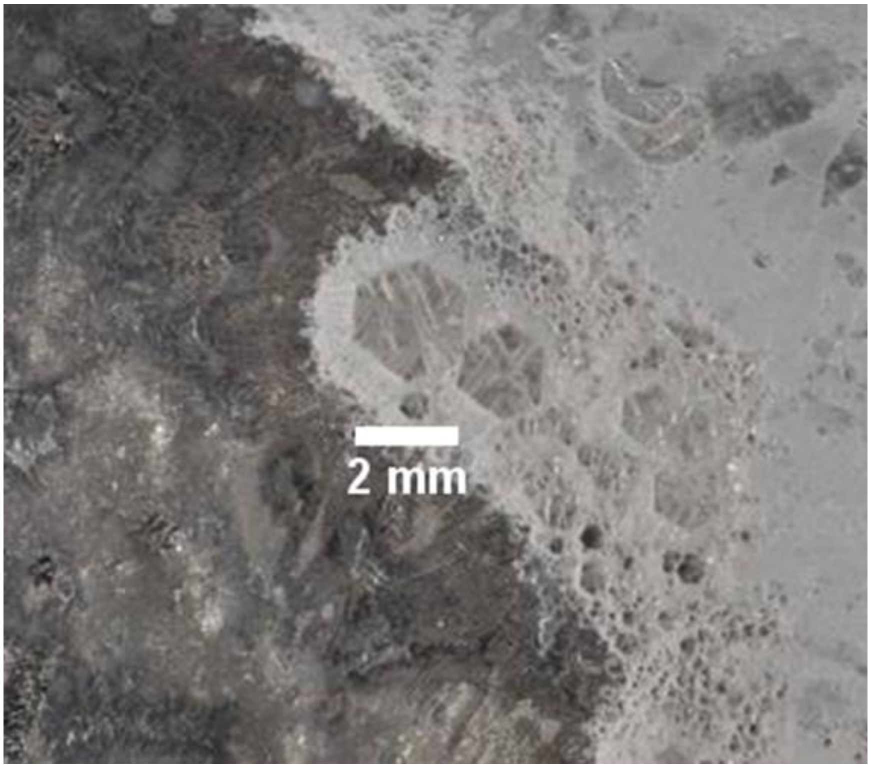

Figure 4.9: Optical micrograph showing large hexagonal hBN grain formed in Mellen furnace experiment

4.2.4 hBN Crystal Morphology

Two main hBN morphologies were formed by the Ni-Cr flux process: hBN platelets and prismatic crystals. The description of these two morphologies, their subcategories and conditions of their formation will be enumerated in this section, as well as the potential advantageous and applications for each type. Schematic sketches of these morphologies are illustrated in Figure 4.10.

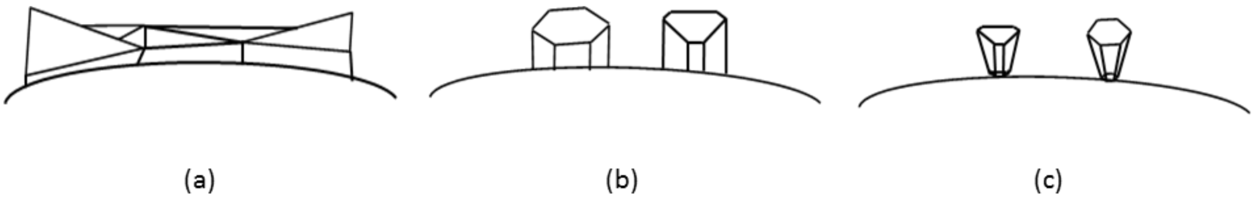

Figure 4.10: A schematic drawing showing cross-sectional view of hBN morphologies: (a) platelets, (b) prismatic-shaped crystals and (c) tapered needles

The hBN platelet morphology (Figure 4.10a) completely covered the Ni-Cr ingot surface with a water-clear, translucent crystal layer. This crystal layer was made up of domains with triangular, hexagonal, rounded or irregularly shaped habits, with grains growing into each other in a continuous polycrystalline sheet. For the best samples, the crystal sheet completely covered the entire ingot top surface, producing a very large area of viable hBN crystal grains (Figure 4.11).

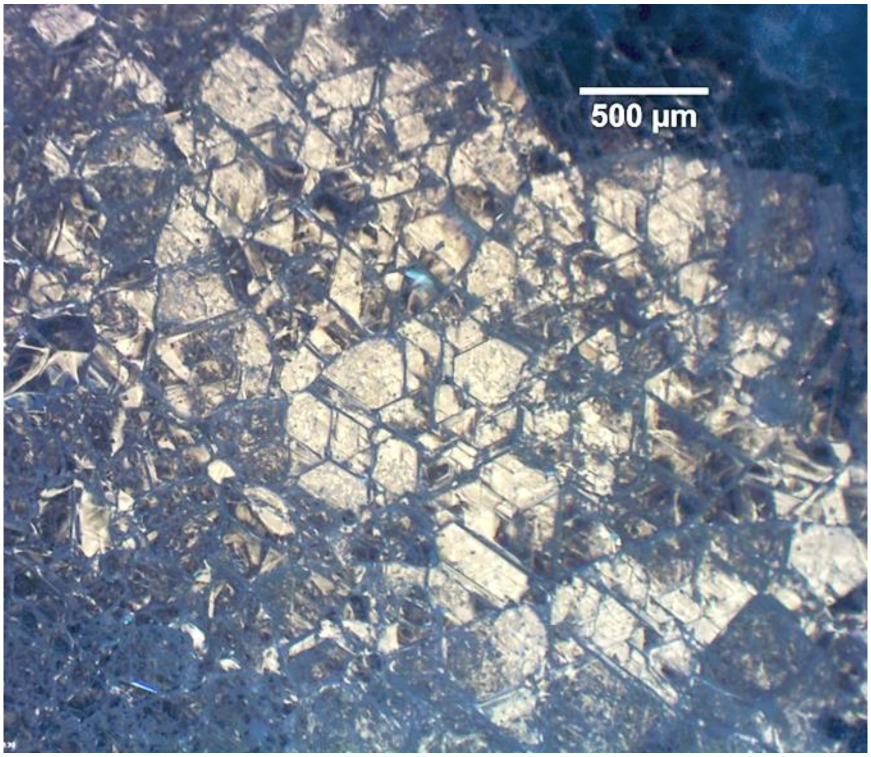

Figure 4.11: An optical micrograph showing Ni-Cr ingots covered by platelet-like hBN crystals with triangular and irregular domains in crystal sheet.

The platelet morphology formed most often by slow cooling rates (≤ 4°C/hr) and higher dwell temperature (≥1500°C). Under these conditions, crystal growth is most favorable in the a-direction, promoting wider but thinner crystal grains [19,37-39]. Due to the continuous nature of the crystal sheet, hBN flakes made up of several connected domains could be transferred onto handle substrates, with flake sizes as large as 5mm. Individual grains from these transferred crystal sheets exceeded 500 µm in width, with typical transferred grain thickness on the order of 10 µm. Examples of these transferred crystal sheet flakes are shown in Figure 4.12. These transferred crystal sheets are suitable for contact deposition and device fabrication due to their large area. Additionally, these flakes tend to be nearly atomically flat; their RMS roughness, as determined by AFM, was on the order of 0.042 nm for a 2x2 µm^2 scan area.

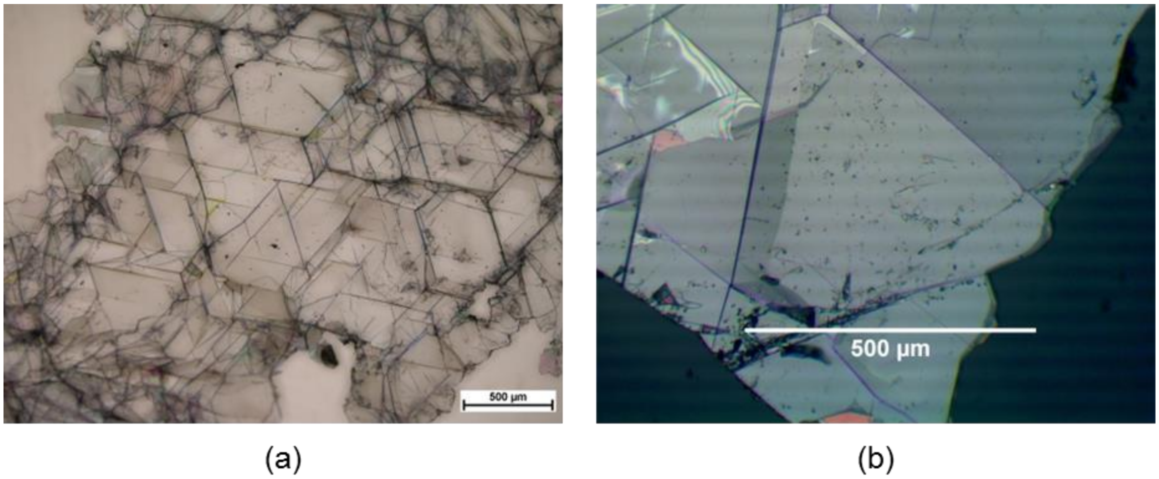

(a) (b)

Figure 4.12: Optical micrographs showing (a) a transferred hBN flake showing triangular domains with total width >3mm and (c) a transferred hBN flake with large triangular grain >500 um in width

The prismatic hBN crystals had hexagonal or truncated hexagonal (hexagonal with three shortened sides) cross-sectional area. This morphology could be split into two subsets: standard prismatic crystals (Figure 4.10b) and tapered needle-like crystals (Figure 4.10c). The standard hBN prisms were identified by their consistent basal plane width throughout their thickness (looking like a hexagonal prism), while the needle-like crystals had the widest dimension on the top surface and tapered to a smaller size at the hBN-metal interface. Both these prismatic grains were often embedded within powder-like BN layers and separated from the Ni-Cr ingot surface via a fine-grain BN buffer layer. In an ideal sample, these crystals are crack-free and clear, covering the entire ingot surface. Optical and SEM images of these prismatic and needle-like crystals are illustrated in Figure 4.13, Figure 4.14 and Figure 4.15.

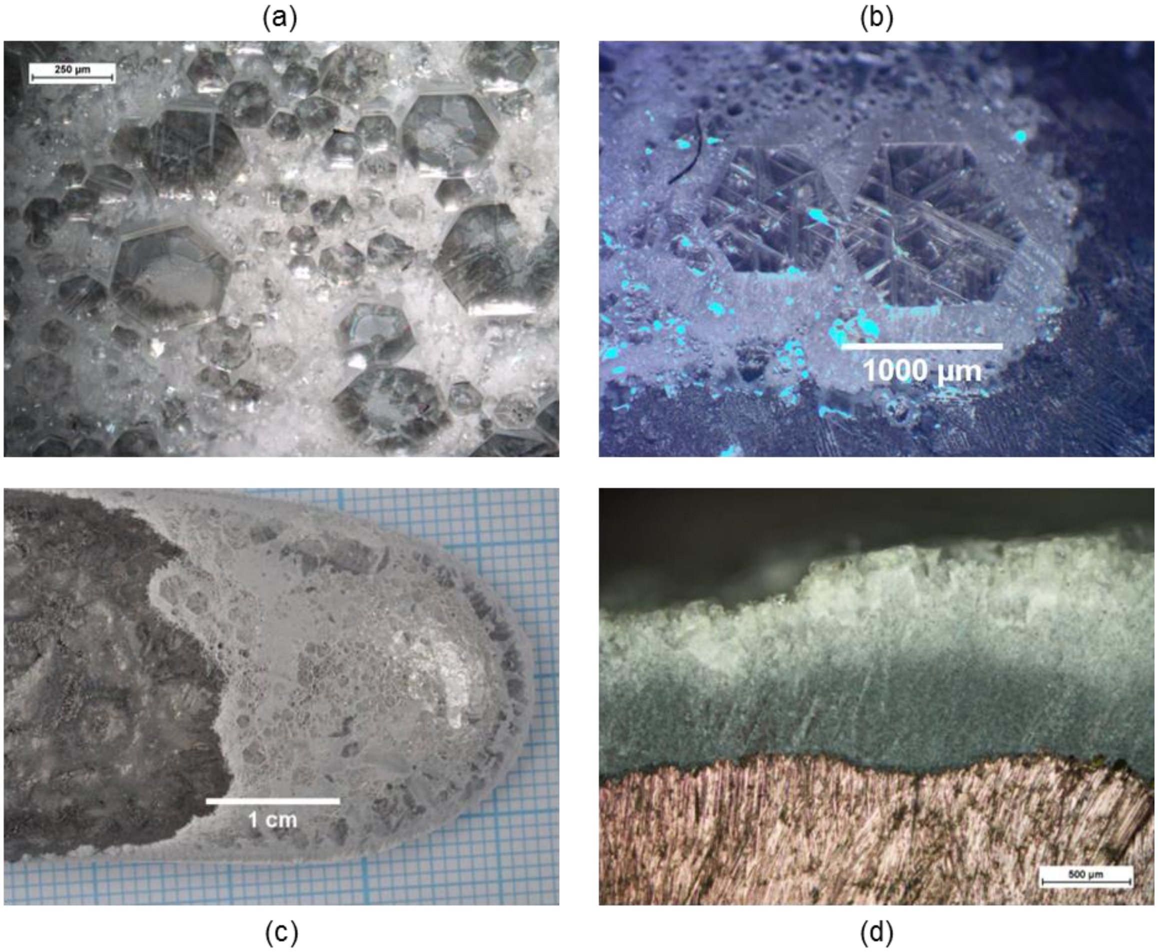

Figure 4.13: Optical micrographs of (a) prismatic hexagonal crystals embedded within fine-grain polycrystalline BN layer, (b) large, hexagonal hBN prisms (>1000µm across basal plane) with some cracking embedded within white BN amorphous layer, (c) macro-photograph of prismatic crystals on metal ingot surface, and (d) cross-sectional image showing prismatic hBN crystals formed on top of an BN buffer layer on the Ni-Cr surface.

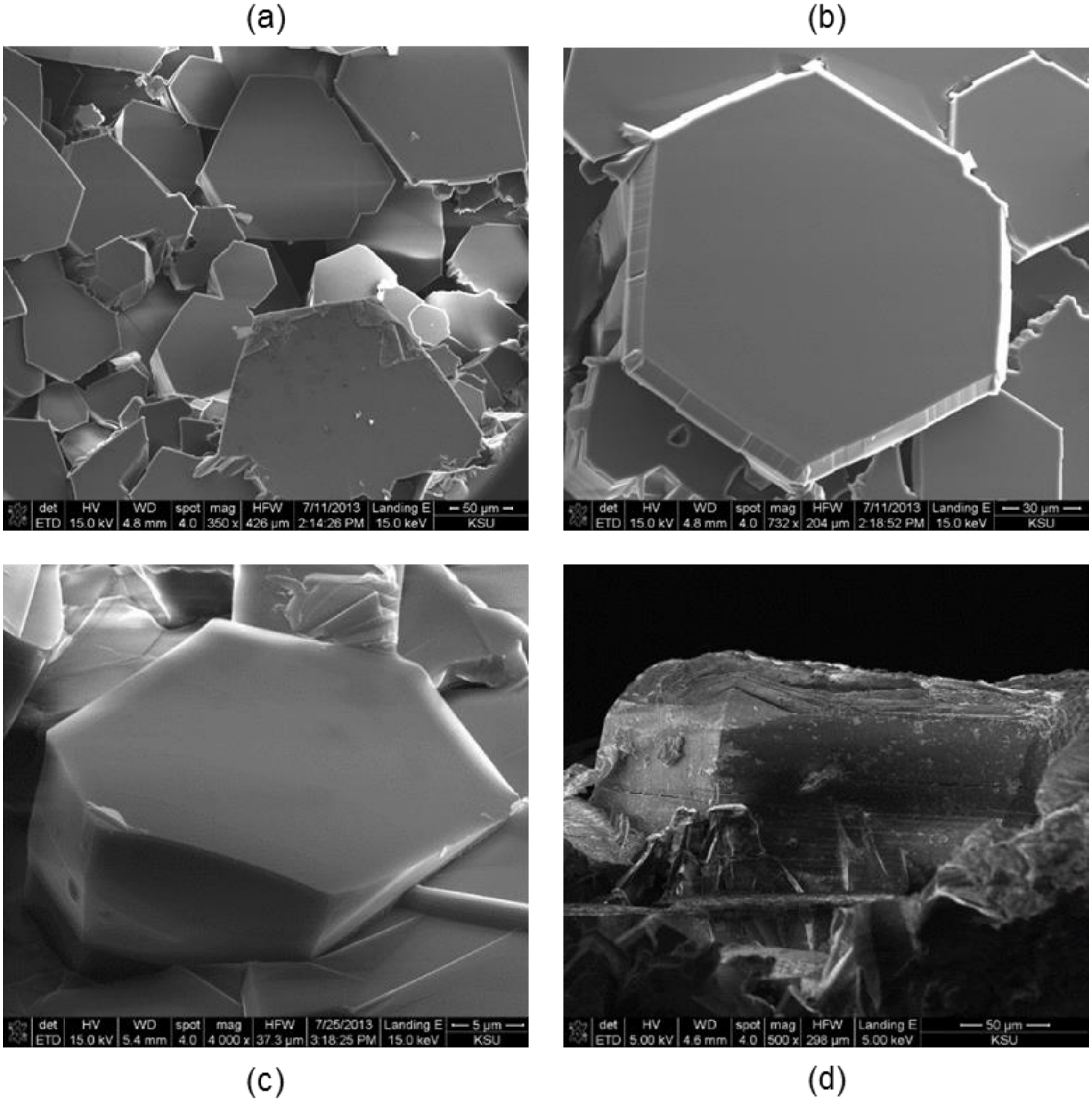

Figure 4.14: SEM images of hBN prisms: (a) grouping of hexagonal and truncated hexagonal platelets with well-defined basal planes 50µm to 200µm across, (b) large, well-defined hexagonal prism (150µm across basal plane) with an atomically smooth basal plane surface, (c) smaller hexagonal prism showing crystal thickness (>10µm) relative to the basal plane width, (d) side-view of hBN prism (imaged on cross-sectionally diced metal ingot) with a crystal thickness of >100µm sitting the Ni-Cr surface.

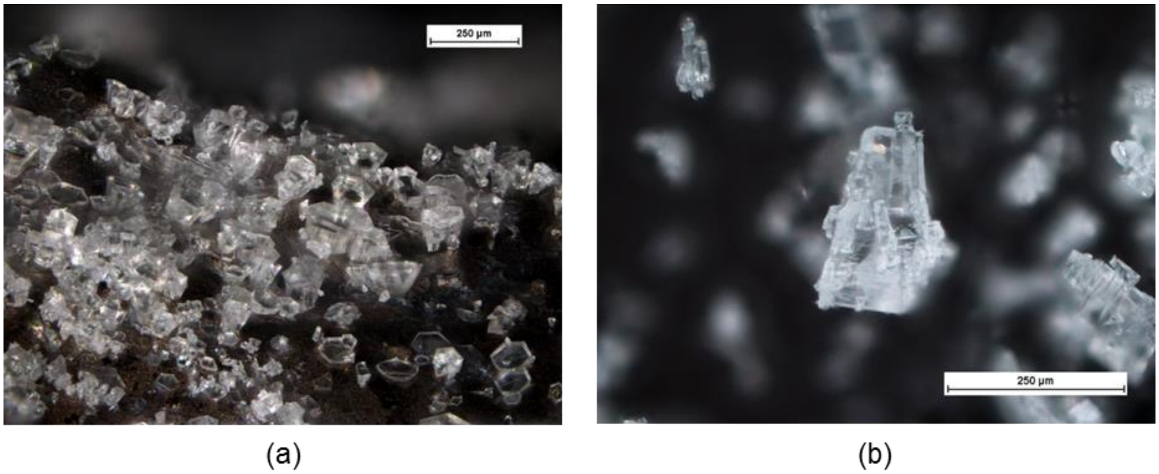

Figure 4.15: Optical micrograph of (a) clear, tapered hBN crystals attached to metal surface and (b) free-standing tapered hBN crystals scraped from the ingot surface.

hBN crystal prisms most often formed at higher cooler rates (4°C/hr) and lower dwell temperatures (<1500°C), although they also readily formed under identical conditions as the crystal sheet morphology. Tapered or needle-like crystals typically formed when the system was initially cooled at a controlled rate (2-4°C), then rapidly quenched while still at high temperature (>1300°C). This rapid quenching was often the result of unexpected furnace shutdown due to power loss or thermocouple failure mid-run, thus its growth conditions were difficult to precisely document. For both these morphologies, crystals formed as isolated domains with clearly defined geometric habit, unlike the crystal sheet morphology.

Like the platelet morphology, prisms and tapered crystals were extracted with thermal release tape. Additionally, these crystals often were isolated on the ingot surface, sometimes with side edges free from the metal surface. This allowed these crystals to be extracted from the metal surface manually via fine-tipped forceps with minimal damage. These freestanding flakes could then be placed onto a suitable handle substrate for analysis. One such hexagonal prism pair (connected in one corner at 90°) is pictured below in Figure 4.16. Tapered crystals were challenging to transfer onto substrates, as the tapered edges provided limited surface area for adherence.

(a) (b)

Figure 4.16: Optical micrographs showing (a) hexagonal prism attached at approximately 90° transferred by release tape onto handle substrate and (b) thickness measurement of perpendicular platelet (>60µm thick).

These different morphologies suggest different potential applications. The hBN platelet sheets are the most desired morphology, as it produces large areas of high quality hBN crystals with large domains. These domains are some of the largest, as they are formed under conditions which favor growth in the a-axis. These flakes are likely best for 2-D heterostructure devices and optoelectronic devices due to their large domain size. Prismatic crystals may have a niche application for neutron detection, where their thicker nature (>100µm) is favored to promote neutron absorption. Finally, tapered crystals are not expected to be useful for device fabrication and heterostructure systems. However, they form the thickest domains of all crystal morphologies and provide large a-axis cross-section, which may be useful for studying a-direction physical properties in hBN, such as thermal conductivity. These tapered crystals may also be useful for nanophotonic applications, utilizing the anisotropic optical properties of hBN.

4.2.5 Effect of Tube Gas Environment during Growth

Control of the gas environment during crystal growth was important to encourage the formation of large hBN crystals while also suppressing the formation of unwanted oxides, fine grain BN powder and other boron-rich phases. In early experiments, high purity N_2 gas was exclusively used, with a process pressure of 850 torr and a continuous gas flow (400 SCCM in CM system, 1 SLM in Mellen system). These conditions produced excellent hBN crystals; however, samples did occasionally produce a pink or reddish film (particularly in the Mellen system). This film was not hBN; instead it was a form of chromium oxide. This oxide was speculated to form due to impurities present within the nickel and chromium source material, as well as due to chromium replacement reaction with alumina in the tube (forming a "red ring" inside the center of the tube over its lifetime). The oxide film tended to cover a large portion of the metal surface, providing numerous nucleation sites to produce fine grain BN or covering the surface of hBN crystal sheets or platelets. Micrographs of samples produced under N_2 flow showing this oxide formation are shown in Figure 4.17 and Figure 4.18.

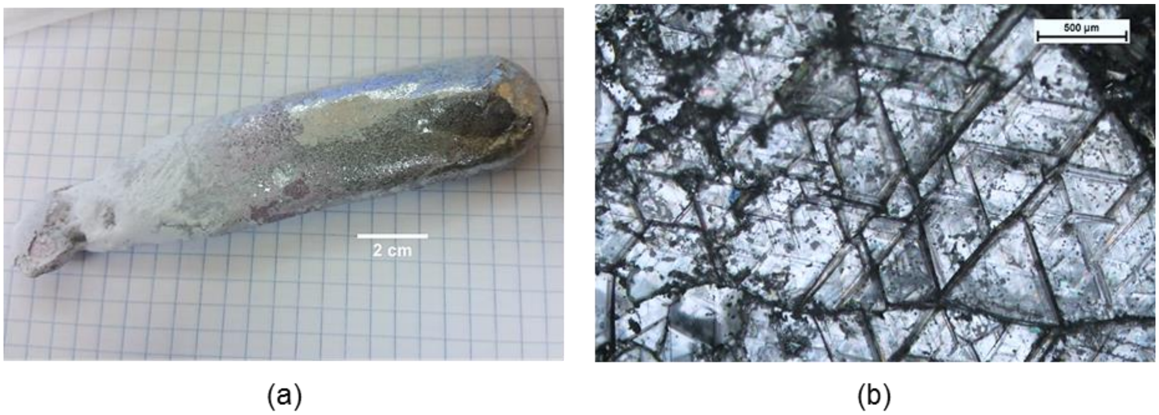

(a) (b)

Figure 4.17: Optical micrographs of (a) Ni-Cr ingot grown in the Mellen furnace under N_2 gas flow only partially covered with red oxide crystals and (b) triangular crystal grains on ingot which are partially covered by fine grain BN and red oxide powder.

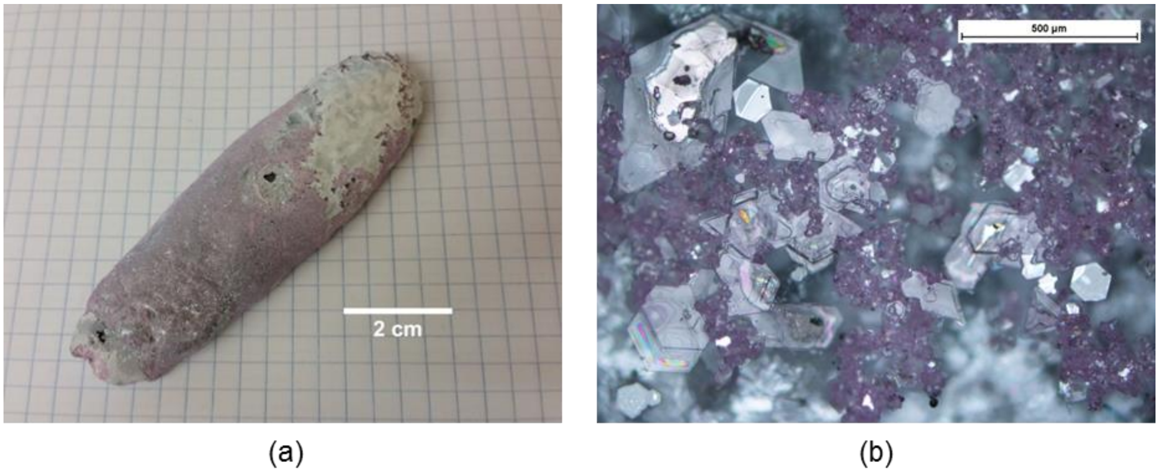

Figure 4.18: Optical micrographs of (a) Ni-Cr ingot grown in the Mellen furnace under N_2 gas flow only, covered with red oxide crystals and fine grain BN and (b) red oxide crystals which formed on top of hBN crystal platelets.

XRD was performed on the reddish powder formed on these ingots (Figure 4.19). The resulting pattern included peaks for hBN, as well as peaks which were identified as trigonal phases of Cr_2O_3 (eskolaite) and/or Cr-doped Al_2O_3 (synthetic ruby). Cr_2O_3 seemed to be the most sensible; however eskolaite has a dark green color inconsistent with the optical characterization of the powder. The synthetic ruby phase was consistent with the color of the oxide powder, and thus was assumed to make up the majority of this phase. Speculatively, the aluminum in this phase likely came from the alumina tube as a “red ring” formed on the inner surface of the tube after multiple experiments. Chromium from the flux may have vaporized and substituted for aluminum in the tube, forming this synthetic ruby phase and diffusing to the surface of the ingot.

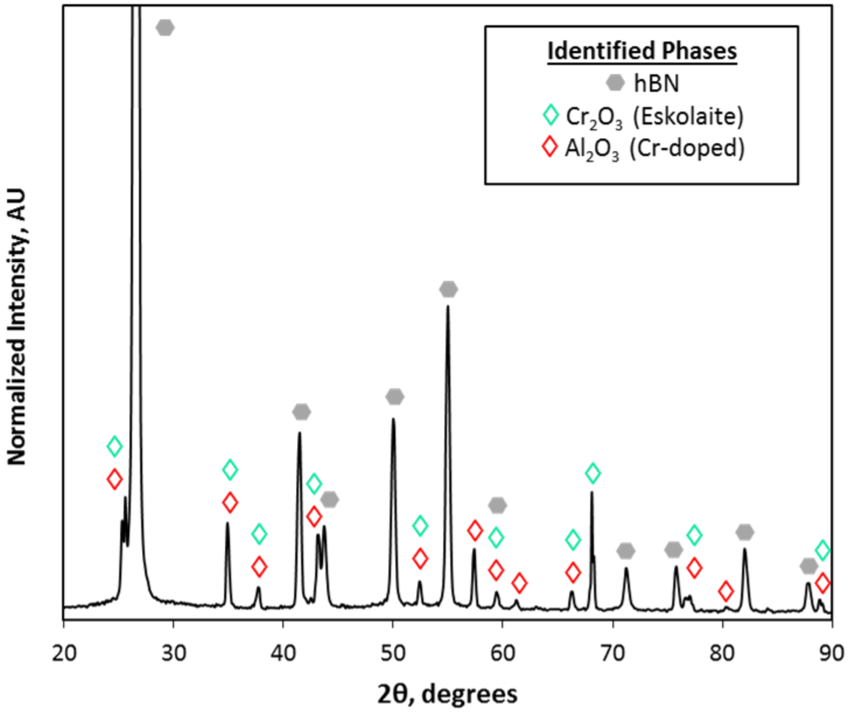

Figure 4.19: XRD pattern for BN and red oxide powder for sample grown under N2 gas flow only. In addition to hBN, peaks corresponding to trigonal Cr_2O_3 (eskolaite) and/or Cr-doped Al_2O_3 (synthetic ruby) phases were identified.

To eliminate this oxide film formation and impurities from the source material *in situ*, a small amount of forming gas (5% H_2 in argon) was added to the N_2. The H_2 in the gas caused volatilization of carbon and oxygen impurities from the source materials, so they are swept out of the tube. The argon balance was non-reactive at high temperatures in the tube, while ensuring that H_2 was below its lower explosive limit at all times to maintain safety, with or without N_2 in the gas makeup.

Initial experiments in the Mellen system flowed forming gas in a 2:1 ratio of forming gas to N_2, with otherwise identical growth conditions. These conditions produced excellent, oxide-free ingots entirely covered by water-clear hBN crystals. One such sample, which produced a crystal sheet with triangular domains, is illustrated in Figure 4.20. These experiments confirm that the addition of forming gas was effective to eliminate oxide impurities during growth. Furthermore, the fine-grain hBN growth was largely eliminated.

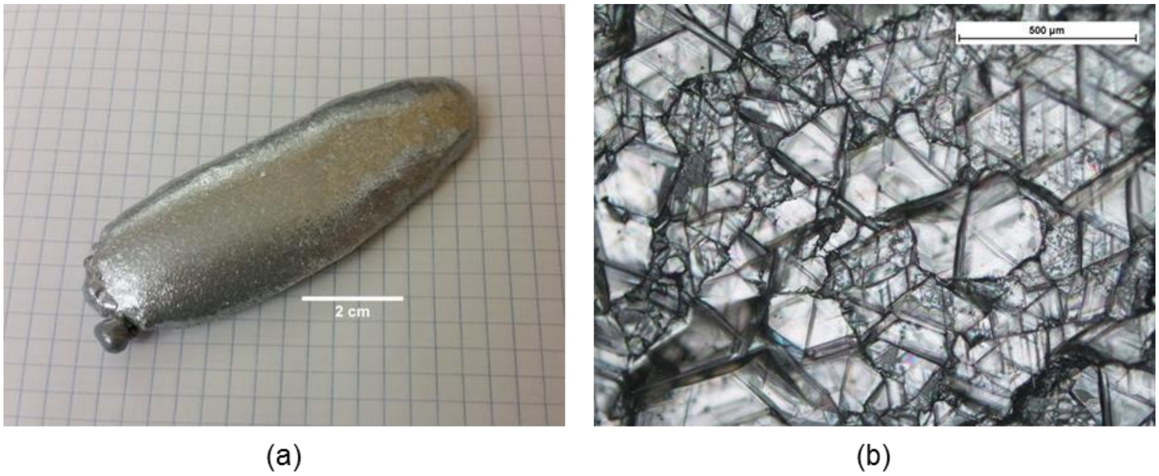

Figure 4.20: Optical micrographs of (a) Ni-Cr ingot grown in the Mellen furnace under N_2 and forming gas flow (2:1 ratio), with surface free from oxide layer and (b) water-clear hBN crystals with triangular and irregular shaped domains.

XRD of hBN crystals grown with this 2:1 forming gas to N_2 ratio confirmed they were highly crystalline (Figure 4.21) and well-ordered, with a (002) peak FWHM of 0.34°. All peaks corresponding to non-basal planes {(100), (101), …} from 40° to 90° were clearly resolved in this pattern, however, their peak intensity was less than 1% relative to the (002) peak. Thus, these crystals were of single-crystal orientation with minimal presence of polycrystalline BN or oxide impurities.

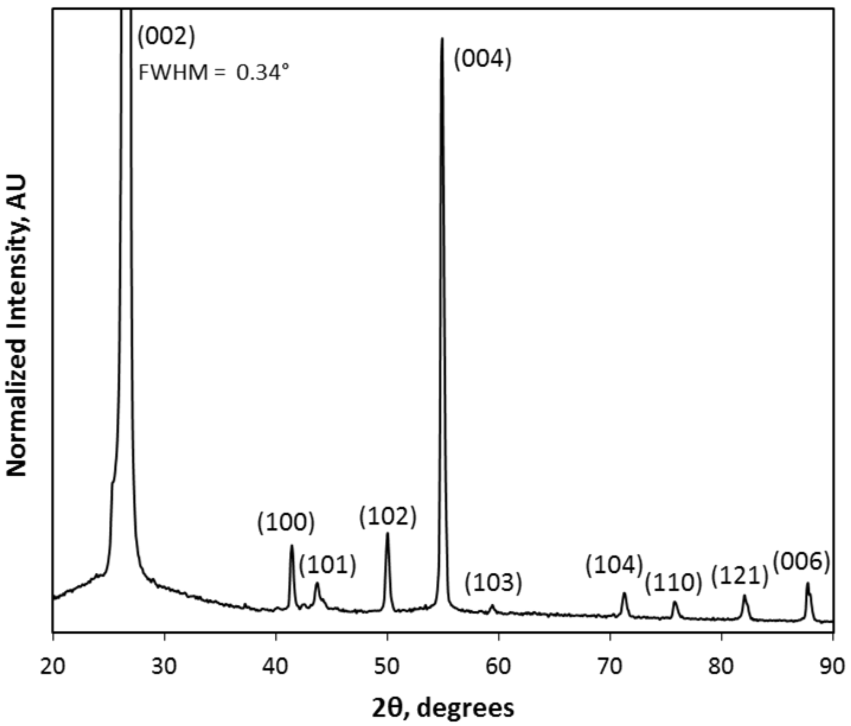

Figure 4.21: XRD pattern for clear hBN crystals grow under 2:1 N_2 to forming gas conditions. Identified peaks corresponding to the hBN crystal lattice are labeled accordingly. (002) peak FWHM was 0.34°, indicating highly crystalline hBN.

Additional runs were performed, studying the effect of gas composition on the hBN crystal morphology. With an N_2 to forming gas ratio of 1:1, illustrated in Figure 4.22, the ingot surface was significantly rougher, with vast peaks and valleys present, and substantially wetted the BN boat. Both heavily fractured hBN crystals, and an unidentified metallic phase, were present on the ingot surface, as shown in Figure 4.22(b). The XRD pattern for this metallic phase was identified as a combination of peaks from orthorhombic Cr_3B_4, Ni_4B_3 and Cr_3NiB_{12} phases (Figure 4.23). This phase can be generalized as $Cr_xNi_{1-x}B_4$ and likely forms due to concentration of boron in the flux exceeding the nitrogen concentration as a result of the lower N_2 partial pressure (approximately 425 torr, as compared to 565 torr for the 2:1 N_2 to forming gas run or 850 torr for N_2 only).

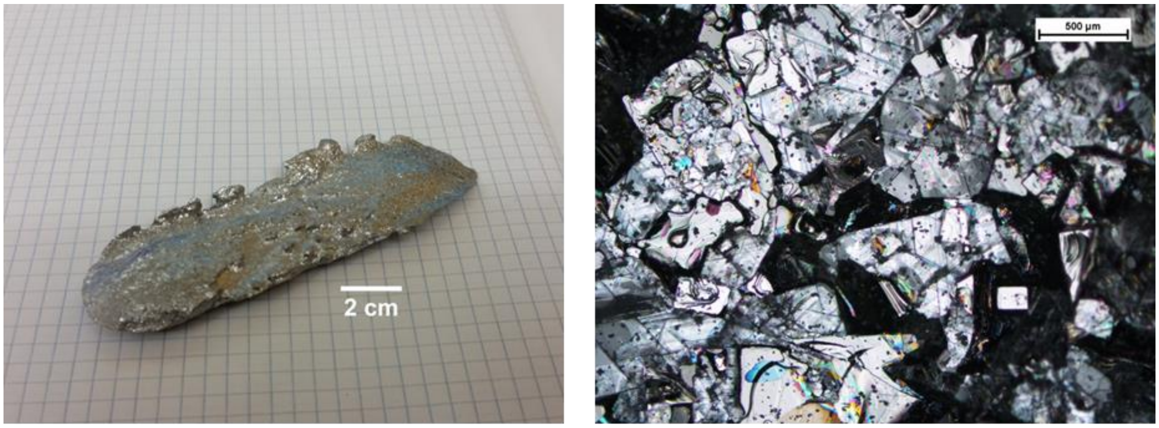

(a) (b)

Figure 4.22: (a) Photograph of Ni-Cr ingot grown in the Mellen furnace under N_2 and forming gas flow (1:1 N_2 to forming gas), with rough metal surface and (b) micrograph of heavily-fractured hBN crystals with irregular domains intermixed with unidentified boron-rich cubic metallic phase

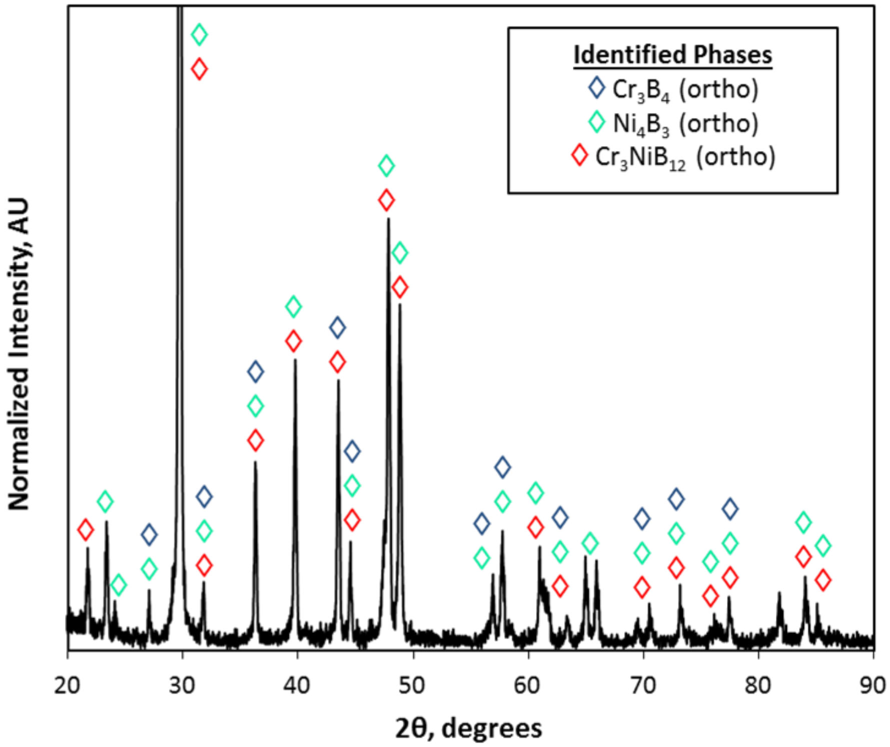

Figure 4.23: XRD pattern for metallic phase formed during growth under 1:1 N_2 to forming gas. Peaks were identified as a combination of orthorhombic Cr_3B_4, Ni_4B_3 and Cr_3NiB_{12} phases.

An additional experiment using pure argon gas and no N_2 or forming gas produced an ingot with an even rougher surface than the previous experiment, with the $Cr_xNi_{x-1}B_6$ phase dominating the surface and only a handful of heavily cracked hexagonal hBN crystals present (Figure 4.24).

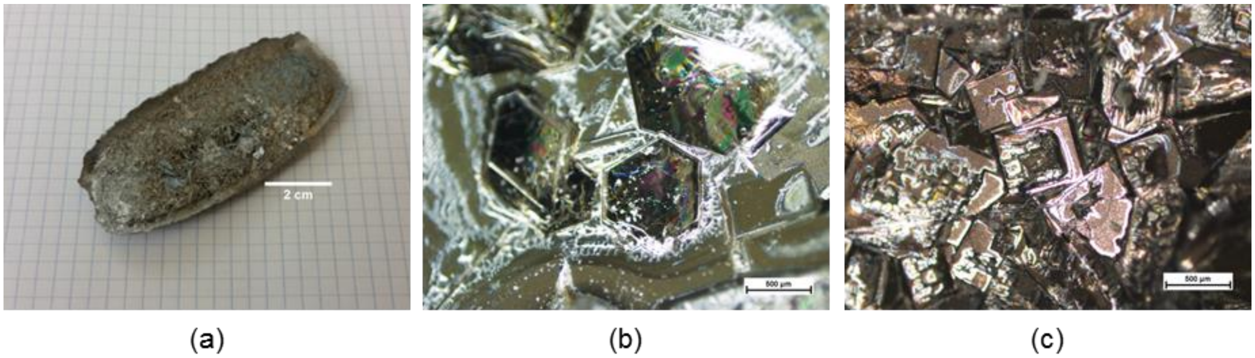

(a) (b) (c)

Figure 4.24: Optical micrographs of (a) Ni-Cr ingot grown in the Mellen furnace under Ar gas flow), with rough metal surface characterized by cubic metallic phase, (b) odd hexagonal hBN grains on ingot surface observed under dark field and (c) crystals of unidentified boron-rich metallic phase

With argon flow only, the metal ingot heavily wetted the BN boat, causing the metal spreading across the width of the boat, as opposed to typical behavior under N_2, where the ingot had a higher contact angle with the boat. This change in wetting behavior, coupled with the formation of an additional crystal phase, was believed to be caused by the decreased N_2 partial pressure in the tube during crystal growth (approximately 0 torr). Due to this decline, nitrogen dissolved in the Ni-Cr flux from the boat was postulated to have off-gassed during growth and swept out of the tube, leading to the continued wetting of the BN boat, accumulation of boron in the flux and formation of the boron-rich phase.

Based on the results of these experiments, forming gas was permanently implemented as a part of the gas makeup to the tube. The N_2 to forming gas ratio was increased to 4:1 for future experiments in the Mellen furnace to eliminate source material impurities while maintaining a sufficiently high N_2 partial pressure to promote hBN crystal formation. This resulted in the elimination of red oxide film formation during growth.

4.2.6 Growth with Alternative Ni-Cr Source Materials

The next set of experiments focused on further reducing carbon and oxygen impurities by growing crystals using alternative metal sources. Two sets of nickel and chromium sources were obtained from ESPI Metals and Alfa Aesar (enumerated in Section 2.3). These materials were used in standard experiments in the Mellen furnace to test whether the purity, size or shape of the crystals changed.

The first experiment was performed using the ESPI Metals source materials, which had lower oxygen impurity concentration compared to the standard metal sources but higher carbon impurity concentrations. The impurity concentrations for the Ni and Cr sources were 660 ppm carbon and 970 ppm oxygen for the Ni source and 15 ppm carbon and 220 ppm oxygen for the Cr source. This experiment was initially meant to be an ingot formation style run, with the system brought to 1500°C, dwelled for 12 hours, then rapidly quenched to ambient temperature at 200°C/hr. Surprisingly, the resulting ingot formed by this experiment was entirely covered by a clear sheet of triangular domains, as seen in Figure 4.25. The metal ingot was shiny and entirely free from any apparent oxides, impurities or fine grain BN. These results were similar to runs that were cooled at 4°C/hr with standard sources; however, this run only took two days of runtime (compared to 5+ days required for similar results with standard sources).These crystal flakes were then transferred via thermal release tape onto double-side polished sapphire handle substrates, as shown in Figure 4.25(c).

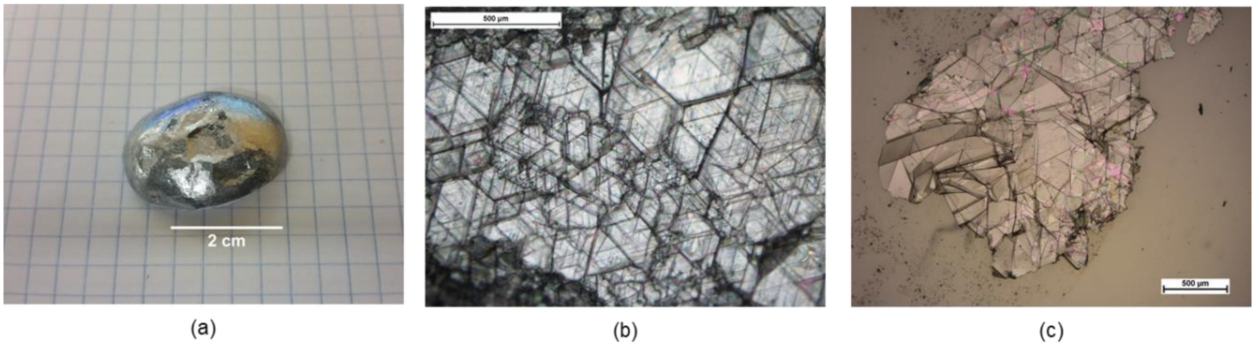

Figure 4.25: Optical micrograph of (a) Ni-Cr ingot from high purity run performed with ESPI Metals sources, cooling at 200C/hr from 1500C, (b) hBN crystal sheet with triangular grains on ingot top surface and (c) hBN flake from ingot transferred onto sapphire handle substrate

Following the success of this initial ESPI Metals ingot formation run, a subsequent and more standard run was performed, consisting of an ingot formation cycle followed by a main cycle consisting of a dwell at 1500°C for 12 hr, a 5°C/hr cool to 1200°C and a quench to ambient. This run produced very similar water-clear triangular grains all along the ingot surface, with these domains appearing on average to be slightly larger than the prior run, as shown in Figure 4.26. Flakes from this sample were transferred onto double-side polished sapphire, pictured in Figure 4.26(c), annealed at 500°C and then analyzed by photoluminescence spectroscopy, courtesy of Drs. Jiang and Lin of Texas Tech University.

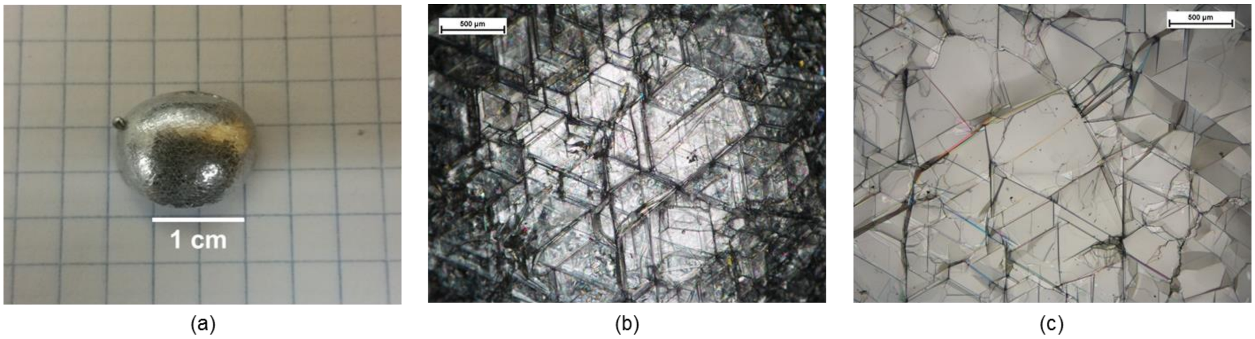

Figure 4.26: Optical micrograph of (a) Ni-Cr ingot from high purity run performed with ESPI Metals sources, cooling at 5C/hr from 1500C, (b) hBN crystal sheet with triangular grains on ingot top surface and (c) hBN flake from ingot transferred onto sapphire handle substrate and annealed at 500°C

Photoluminescence analysis of the ESPI Metals source hBN flakes revealed slight change in luminescence spectra compared to flakes grown using standard Ni-Cr sources (Figure 4.27). Band-edge luminescence peaks at 5.751 eV, as well as at approximately 5.62 eV and 5.50 eV, were better resolved and more intense for the high purity flake, indicating improved crystal quality. Intensity for energy bands responsible for defects and impurities, located around 4.3 eV and 2.9 eV, were also lower in relative intensity, confirming a slight reduction in their concentration in the flakes.

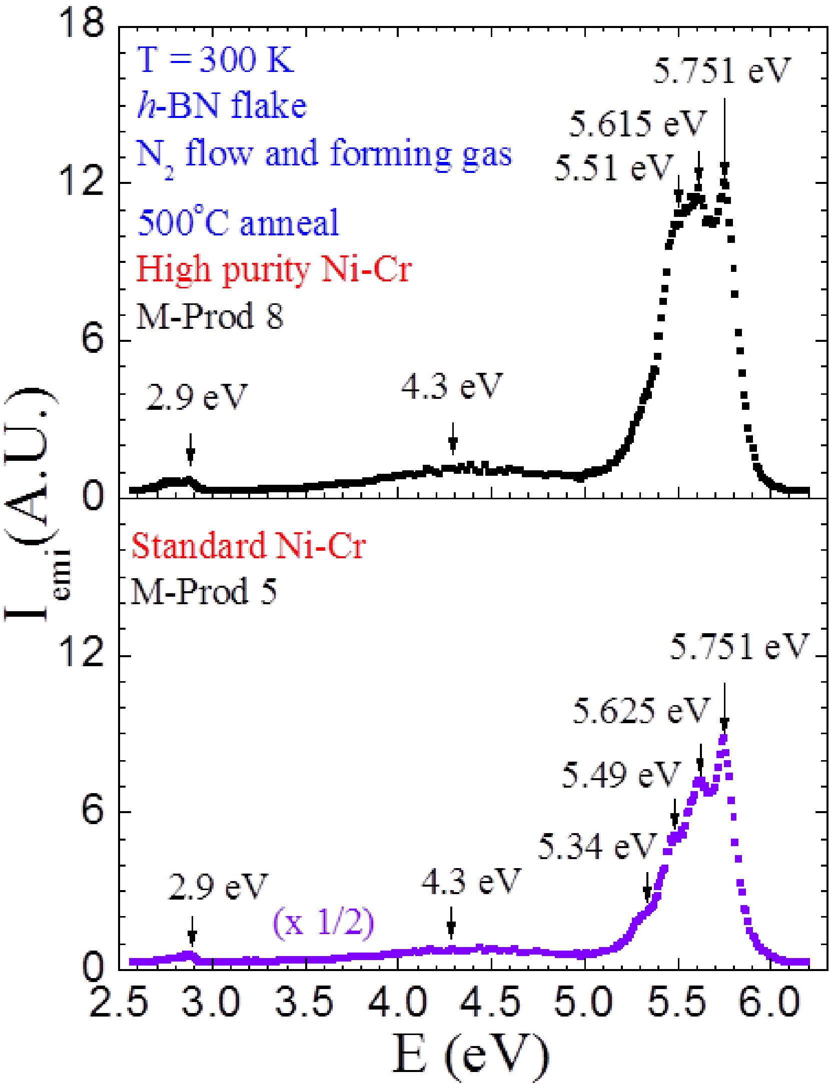

Figure 4.27: PL spectra comparing hBN crystals growth with (*top*) high purity ESPI Metals source and (bottom) standard Ni-Cr source. Both samples were grown under identical furnace conditions with N$_2$ and forming gas flow. Crystal were transferred onto sapphire substrates and annealed at 500°C before analysis. High purity source shows higher intensity band-edge luminescence peaks relative to peaks pertaining to defects at 4.3 and 2.9 eV, indicating lower impurity concentrations in hBN crystals.

An additional, high purity Ni and Cr source was obtained from Alfa Aesar, with the express purpose of growing hBN crystals using a very low carbon nickel source (<100 ppm). Using these Alfa Aesar sources, an experiment was performed using the same conditions as the second ESPI Metals experiment (ingot formation cycle, 1500°C dwell for12 hr, 5°C/hr cool to

1200°C). These conditions yielded a shiny Ni-Cr ingot covered in clear, low-defect, truncated hexagonal hBN platelets (Figure 4.28).

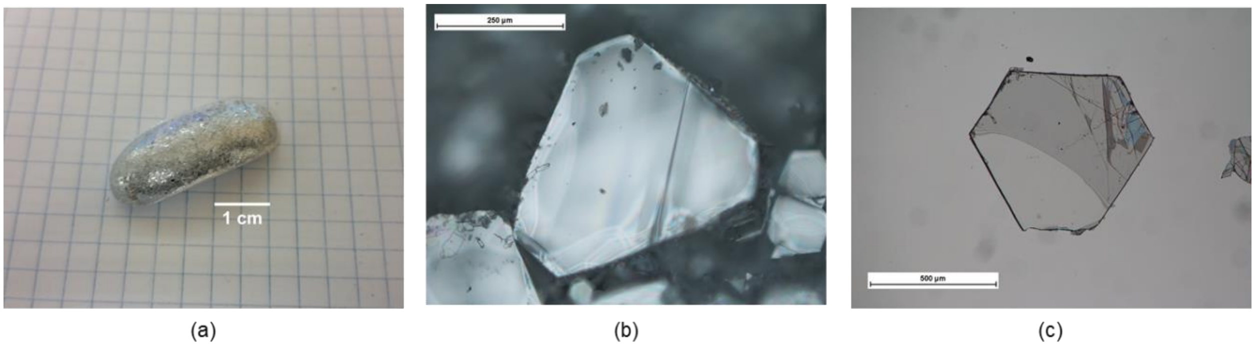

Figure 4.28: Optical micrograph of (a) Ni-Cr ingot from high purity run performed with Alfa Aesar low carbon sources, cooling at 5C/hr from 1500C, (b) hBN platelet with truncated hexagonal on ingot top surface and (c) hexagonal hBN platelet from ingot transferred onto sapphire handle substrate and annealed at 800°C

Based on the qualitative analysis of the hBN crystal clarity and defect density, as well as the change in photoluminescence spectra, these high purity runs showed that the impurity concentration and quality of grown crystals was improved. Elimination of these unwanted impurities is vital for the development of hBN optoelectronic devices, as these impurities act as trapping states which restrict free carrier transport. Use of high purity metal sources, in addition to use of forming gas can help to control these impurities and yield device-grade hBN material. Ideally, these high purity Ni and Cr sources would be able to be recycled for successive runs, helping to reduce the additional costs associated with their use.

4.3 Relevance of This Work

From the results of this study, the basic operating region for hBN crystal growth using Ni-Cr flux was able to be established. Lower cooling rates (< 4°C/hr) produced clear, well-ordered crystals, and the growth method demonstrated by Ben Clubine was successfully adapted to a horizontal tube furnace system The use of HPBN boats as sole BN source material for crystal growth was also demonstrated, allowing for growth of crystals without the presence of fine grain BN powder to serve as nucleation sites.

Following this first set of cooling rate experiments, the Ni-Cr flux growth process was continually and incrementally improved, increasing consistency of successful growth runs and the size and quality of hBN crystals. Key among these improvements are the implementation of the ingot formation cycle before the main cycle and the addition of forming gas to actively suppress oxide formation *in situ*. These two adjustments were applied to all future runs and have made a significant impact on growing large hBN crystals for collaborative research and device fabrication. Identification and control of hBN morphology may allow growth to be tuned to specific applications, such as growing thicker crystals for neutron detection. Finally, growing crystals from high purity materials is an important step towards obtaining device-grade crystals free from impurities. Growing hBN crystals free of these impurities and their resulting trapping states is required for the development of hBN-based deep UV optoelectronic devices.

Chapter 5 - Statistical Design of Experiments and Optimization of the Ni-Cr Flux Growth Process

Prior experiments (discussed in Chp 3) varied one parameter at a time to evaluate its effect on the size and quality of resulting hBN grains. Unfortunately, due to the long time required for each individual experiment (3-5 days), this mode of study was inefficient in the use of time and resources. To circumvent this inefficiency, a new study was performed using response surface methodology, a statistical technique based on the use of regression analysis and designed experiments, to perform a comprehensive study of all process parameters in the Ni-Cr flux growth process.

The main goal of this study was to identify process conditions producing large (< 1000 µm grain width and 100 µm thickness), low-defect density hBN bulk crystals ready for device fabrication, enabling their study as neutron detectors, deep UV emitters and other application. The following individual steps were taken to achieve this goal:

- Define an experimental region to be examined, consisting of process parameters such dwell temperature, dwell time, cooling rate, cooling temperature and quench rate, to model and control the size of hBN crystal grains.
- Model and identify process parameters with significant first-order (linear) effects with respect to crystal grain width and eliminate insignificant factors using a short set of screening experiments.
- Develop a comprehensive second-order model, including two-parameter interaction and quadratic terms, for both grain width and thickness responses using significant parameters from the screening in a complete factorial designed set of experiments.

This chapter discusses the motivation, methodology and results from this statistical study and the significance of these findings for the Ni-Cr flux growth process.

5.1 Motivation

Response surface methodology (RSM) is a statistical technique used in the design of industrial or research process optimization. It maximizes information from a minimum number of experiments and resources. By using a designed set of experiments, RSM can identify important factors and model their responses in processes. RSM is useful in studies with a large number of experimental factors or high experiment cost (or which are time-consuming) to treat factors one at a time. Experiments are designed to treat all factors simultaneously through the development of response surfaces, to understand both main and interaction effects [113].

While RSM is useful across a wide variety of industrial and research applications, studies in crystal growth are particularly good candidates, as experiments tend to last days to weeks and can involve several factors including time, temperature, cooling rate and system composition, which can greatly affect the resulting crystal structure and quality. Some examples of its use in literature include the investigation of $AlAs_ySb_{1-y}$ crystal growth by molecular beam epitaxy [114], which considered four parameters (growth temperature, growth rate, As_2-flux and Sb_2-flux) to develop an empirical model for of the resulting crystal composition, as well as the control of oxygen concentration in high purity silicon formed by a magnetic Czochralski process [115]. In both of these cases, investigators turned to RSM methods to model very complex processes dependent on multiple parameters (with parameter interactions) to robustly model the respective systems.

5.2 Methods

The goal of this RSM experiment study was to model the effect that the five process parameters (Figure 3.7) had on the hBN crystal grain width and thickness formed by the Ni-Cr flux process. Using these experiments, growth conditions would be identified to allow for the growth of hBN grains >1000 μm in width and >100 μm in thickness. Through this modeling, optimal growth conditions were identified, helping to direct the focus of future work in hBN growth. These five parameters were:

1) *Dwell temperature:* Maximum temperature that the furnace was heated to during the onset of the experiment
2) *Dwell time*: Amount of time that the system was held constant at the dwell temperature
3) *Cooling rate*: Rate at which the furnace was cooled following the completion of the dwell stage
4) *Cooling temperature*: Temperature at which the furnace transitioned from cooling at the cooling rate to the quench rate
5) *Quench rate*: Rate at which the furnace was rapidly cooled to ambient temperature to allow for the Ni-Cr ingot to be removed from the system.

Typically for processes with more than three process variables, experimental designs are split into two portions: a set of screening experiments to eliminate insignificant factors using a fractional factorial experiment, and a set of main experiments which employed more robust full factorial design, using the remaining significant factors to develop a second-order model for the process, including main and interactions effects [113].

These two experimental sets (screening and main) were created using two-level factorial design structure (plus center points). In this type of design, “upper” (+1), “lower” (-1) and “center” (0) values were defined for each process variable to correlate with the coded variables and to construct the screening and main experiment sets. The general relationship between these coded and “natural” variables is defined below.

$$Coded\ Variable = \frac{[Natural\ Variable -\ Center\ Value\ (0)]}{{}^{1}/_{2}\,[Upper\ Value\ (+1) - Lower\ Value(-1)]}$$

Equation 2

Using results from previous experiments (discussed in Chp 3), these upper and lower values were selected within a viable operability region to allow for a large difference between values for a factor, while still allowing for hBN crystal growth under all investigated conditions. “Center run” points, which used the average of the high and low values for each parameter , were added to each set of experiments to help with model stability, as well as providing some amount of replication in each set. Selection of these valuables did not need to be identical for both the screening and main experimental sets, so more conservative values were selected for the screening runs, while values were expanded to allow for maximum experimental region for the main experiments (values used for the screening and main experiments enumerated in Section 5.3.1 and 5.4.1, respectively).

Statistical analysis for this project, including the experimental design structure and RSM analysis of the screening run first-order (linear) only model and main experiment second-order model, was performed using the R software package and the Package ‘rsm’ library. R is an open source programming language and platform for computational analysis of statistics and graphical modeling [116]. Package ‘rsm’ is a program library for R developed by Russell Lenth at the University of Iowa for the use of response surface methodology in R, including both the computational design of orthogonal experiments and the analysis of designed experiment data to develop predictive models and response surfaces [117]. Numerous examples and documentation of using R and Package ‘rsm’ with model building and data analysis have been published by Lenth [117-119].

5.3 Screening Experiments

The region of interest for the five experimental parameters was defined and their first-order (linear) response was modeled using a limited number of experiments to identify significant parameters to carry over into the more comprehensive “main” set of experiments. This set sacrificed some degree of predictive power for the sake of time, so that a limited set of “important” parameters could be studied in greater detail in the second stage of this study. This section enumerates on how the screening experiment set was designed and executed, as well as the how resulting modeling and evaluation of parameter response was evaluated.

5.3.1 Design Structure of Screening Experiment Set

The first step in the development of the response surface for the flux growth process was to identify significant process parameters and eliminate factors which did not have a significant effect on how crystals are formed. Since this screening set eliminated parameters using a minimum amount of experiments and time, only one response was considered, the crystal grain width. To minimize the number of experiments, only first-order (linear) terms were considered. A generalized model of these linear effects and response for the screening experiments is represented as

$$y_{Grain\,Width} = \beta_0 + \beta_1 x_1 + \beta_2 x_2 + \beta_3 x_3 + \beta_4 x_4 + \beta_5 x_5 \qquad \textit{Equation 3}$$

with x_1 through x_5 corresponding to coded process variables, y corresponding to sample grain width, β's corresponding to fitted coefficients obtained using regression analysis in R. These coded variables and their corresponding factorial values for each parameter are listed in Table 5.1.

Table 5.1 Two-level factor and center point values for the five process variables Explored for screening experiment set

Process Variable	Units	Upper Value (+1)	Lower Value (-1)	Center Value (0)
Dwell Temperature (x_1)	°C	1500	1400	1450
Dwell Time (x_2)	hr	24	12	18
Cooling Rate (x_3)	°C/hr	9.0	4.0	6.5
Cooling Temperature (x_4)	°C	1250	1050	1150
Quench Rate (x_5)	°C/hr	150	70	110

Screening experiment set designs often use a fractional factorial design, as a full 2^5 factorial experiment set would have required 32 experiments. With experiments requiring around five days on average to complete, a full factorial set would require nearly six months to complete. Instead, a 2^{5-1} (half) or 2^{5-2} (quarter) fractional factorial design could be applied (requiring 16 and 8 experiments, respectively) to develop a first-order model to determine main effects. These two options each had tradeoffs; the half fraction required more experiments and time but allowed for better prediction of main effects, while the quarter fraction required the minimum number of experiments but had fewer degrees of freedom to estimate model lack of fit.

The selected design for the screening experiment was to compromise between these options and modify the 2^{5-2} (quarter) factorial design by adding two center points to make a ten run design. These center points increased the model degrees of freedom and allowed for some estimate of error via replication The final screening run experiment set design was constructed by using the following two 3-factor interactions as generating relationships, which, with the addition of their resulting 4-factor, form the complete defining relationship:

$$I = x_1 * x_3 * x_5 \qquad \textit{Equation 4}$$

$$I = x_1 * x_2 * x_4 \qquad \textit{Equation 5}$$

$$I = x_2 * x_3 * x_4 * x_5 \qquad \textit{Equation 6}$$

This structure caused the blocking factor (used to split the factorial design into quarters) to be confounded with these three and four-factor interactions. This confounding was acceptable, as these higher order interactions were assumed to be negligible. However, this design structure caused the main effects to be aliased with two-factor interactions for the screening set, as this was a Resolution III design [113]. This aliasing was unavoidable for this structure and could possibly cause false-significance of a main effect due to a strong two-factor interaction it is aliased with. However, this was an acceptable trade-off for limiting the number of experiments in the screening process and ensuring efficient use of time. Using R and the Package ‘rsm’ software, a randomized order of experiments was designed for the screening experiments (Table 5.2).

Table 5.2: Randomized run order of the 2^{5-2} (quarter) fractional factorial experiments and center runs(*) for the screening set.

Run Order	Dwell Temperature (°C)	Dwell Time (hr)	Cooling Rate (°C/hr)	Cooling Temperature (°C)	Quench Rate (°C/hr)
1	1500	12	9	1250	70
2	1500	12	4	1250	150
3	1500	24	4	1050	150
4	1400	24	4	1250	70
5	1400	12	4	1050	70
6*	1450	18	6.5	1150	110
7	1400	12	9	1050	150
8	1500	24	9	1050	70
9	1400	24	9	1250	150
10*	1450	18	6.5	1150	110

Following the completion of these experiments, the average width of hBN grains with the largest characteristic size within each sample was measured. Based on this, analysis of variance (ANOVA) was performed, in R were used to determine significance and allow the development of the second-order model [113,117-119].

5.3.2 Screening Experiments Results

After completing the set of ten experiments listed in Table 5.2, the average width of hBN grains of the largest characteristic size within each sample (referred to as "average grain width") was evaluated by extracting crystal grains from each sample onto thermal release tape. Multiple transfers were performed on each sample in an effort to reduce within-sample variance. Grain width was measured using optical microscopy, with length evaluated using the Nikon LV100 upright microscope and Nikon Elements image capture software (described in Section 2.6.1). Several (at least 5 per sample) of the largest crystal grains within each sample were measured to provide a consistent estimate of the average width of the largest crystals formed, as well as the within-sample variance (shown as error bars). An optical micrographs showing the measurement of one crystal grain selected from these samples, is illustrated in Figure 5.1. The average (characteristic) grain width ranged from 525μm to 31μm for these ten runs (the average grain width data for CM-Screen runs is presented in Table 10.2 in Appendix B).

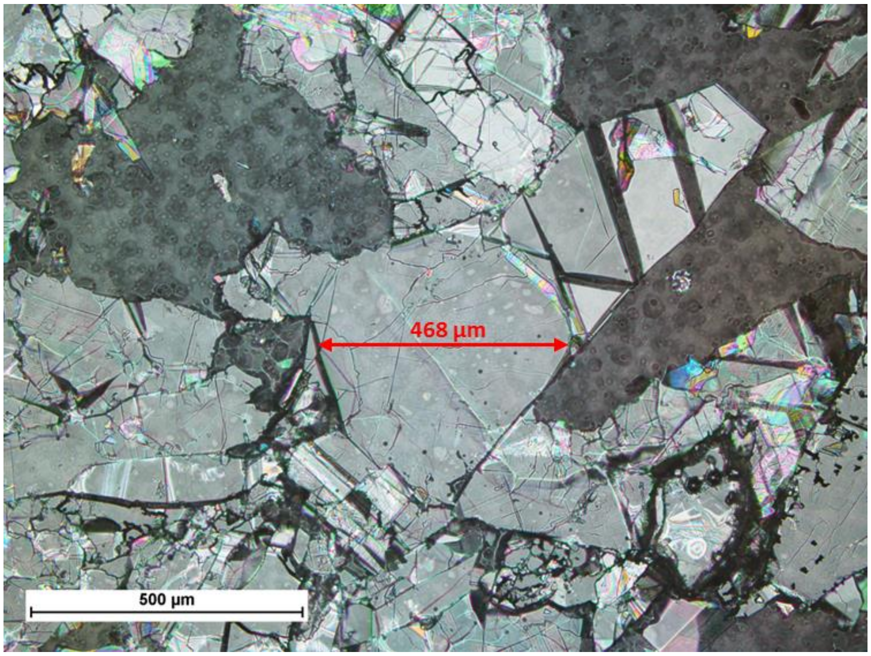

Figure 5.1: Optical image showing hBN flakes transferred onto thermal release tape and measurement of the width of characteristic grains for screening experiment analysis

Next, the screening runs were analyzed using response surface methodology and linear regression analysis in R. Before building the model, the data was first analyzed for any systemic problems which may have impacted the results of the experiments. The average grain width was plotted against the run order, to ensure that there was no trend due to experiment sequence (Figure 5.2). Fortunately, this data did not show a significant trend with respect to run order.

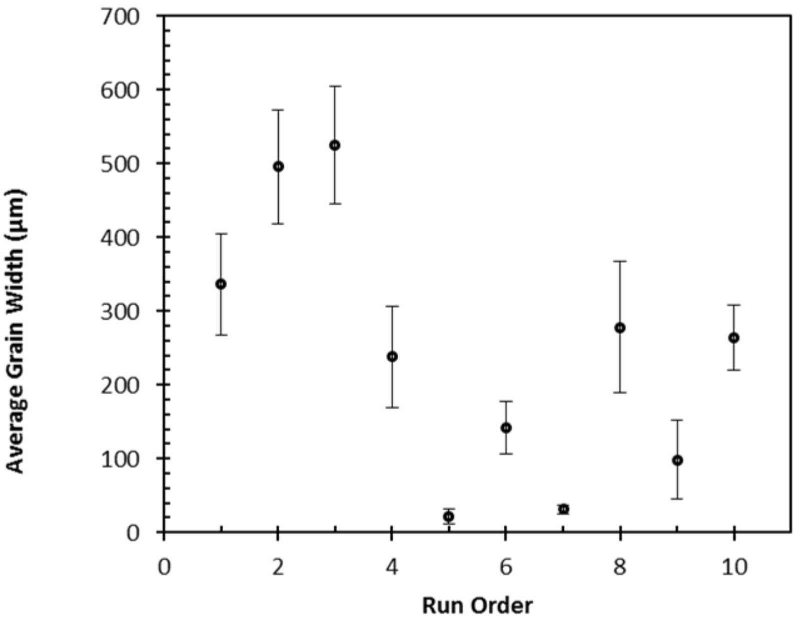

Figure 5.2: Scatterplot of average grain size against run order for screening run experiments. Grain size shows no dependence on experiment sequence, as confirmed by an R^2 value of 0.29.

The model was built to determine the most significant parameters in R (code for screening experiment analysis presented in Appendix D). Since the screening experiment set was a fractional factorial design (2^{5-2}), analysis was limited to first-order (linear) terms only. The first model that was investigated considered all five parameters. Analysis of variance (ANOVA) and lack of fit F-tests for this model (presented in Table 10.4 in Appendix C) showed that the significant terms for this model (p-value ≤ 0.05) were dwell temperature and cooling rate. Diagnostics for this model show a high R^2 value (> 0.7) and an insignificant lack of fit F-test (p-value > 0.05), which indicate excellent model fit. However, the adjusted R^2 value, which normalizes R^2 calculation based on the number of parameters in the model, indicated that this full five-parameter model was “inefficient” due to the presence of several insignificant terms.

To improve the parameter fit, a second model was built to determine the initial linear model based on the screening run results. This model included the two significant parameters from the first model, dwell temperature and cooling rate, as well as the next lowest p-value term, cooling temperature. This third term was retained despite its low significance, as it was anticipated to have significant second order terms with the remaining two parameters for the main experiment set (ANOVA and lack of fit F-test diagnostics for this truncated model are presented in Table 10.5 in Appendix C). This analysis confirmed the significance of the dwell temperature and cooling rate parameters, which have nearly identical F-test p-values as the prior model. Cooling temperature was still insignificant in this model (p-value $\approx 0.21 > 0.5$). R^2 and lack of fit F-test p-values decreased in this reduced model compared to the five parameter model, but only slightly, confirming that the majority of the "work" of the model was done by these three terms. This is illustrated by the adjusted R^2 value, which is greater than in the first model, showing a very efficient model fit without overfitting.

From the ANOVA analysis produced by R, the final linear model for average (characteristic) grain width as a function of growth parameters can be expressed as

$$\begin{aligned} y_{Grain\,Width}\ (\mu m) \\ &= \left(3.1\ {}^{\mu m}/_{\circ C}\right)T_{Dwell} - \left(27\ {}^{\mu m \cdot hr}/_{\circ C}\right)\ R_{Cool} \\ &+ \left(0.4\ {}^{\mu m}/_{\circ C}\right)\ T_{Cool} - 4550\ \mu m \end{aligned}$$

Equation 7

with T_{dwell} representing dwell temperature (in °C), R_{cool} the cooling rate (in °C/hr) and T_{cool} the cooling temperature (in °C).To demonstrate the fit of this model, average grain width data was plotted against each of the three parameters, with dwell temperature in Figure 5.3, cooling rate in Figure 5.4 and cooling temperature in Figure 5.5. For each plot, the respective linear component of the model was presented over the data as a red dashed line. The linear fit of the dwell temperature and cooling rate terms fall quite close to the trend of the data, while the fit of the cooling temperature is less significant.

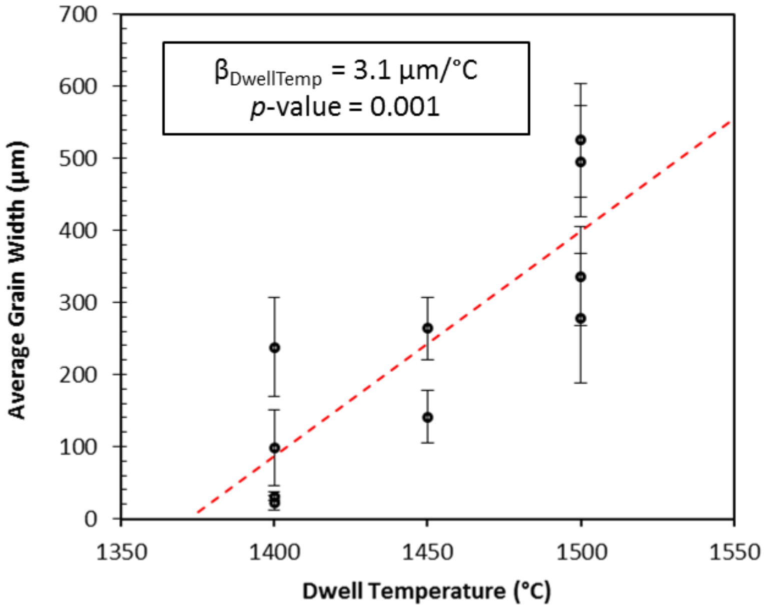

Figure 5.3: Scatterplot of average grain size against dwell temperature for screening run experiments (red dotted line highlights the linear trend of the parameter). Dwell temperature shows a strong linear correlation with grain size (*p*-value << 0.05), with grain size increasing with dwell temperature.

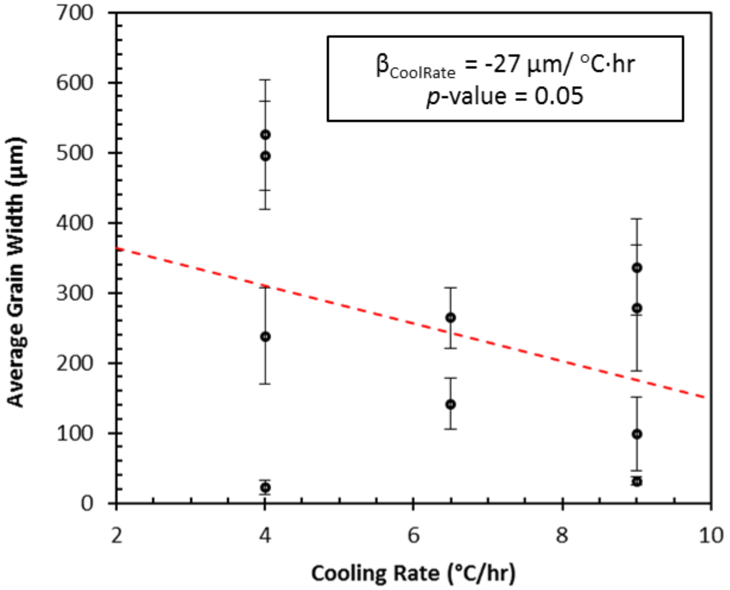

Figure 5.4: Scatterplot of average grain size against cooling rate for screening run experiments (red dotted line highlights the linear trend of the parameter). Cooling rate shows a significant linear correlation with grain size (*p*-value = 0.05), with lower cooling rates resulting in larger grain size.

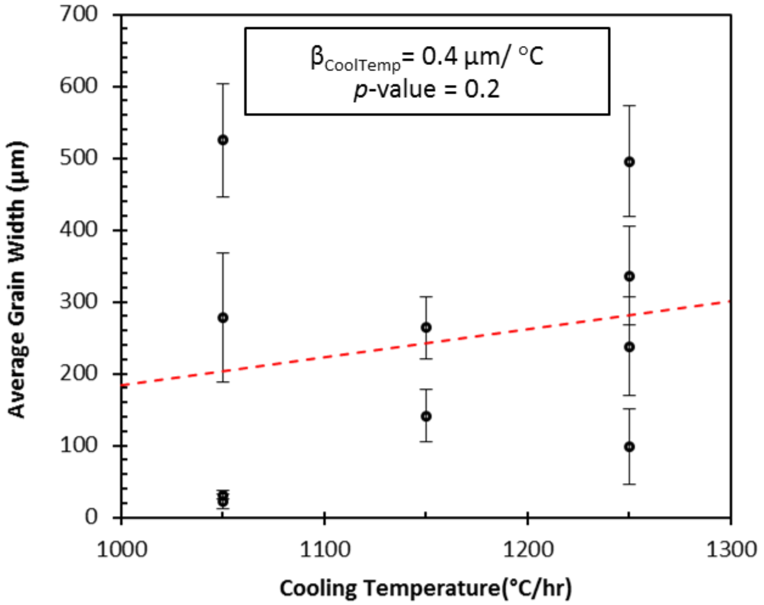

Figure 5.5: Scatterplot of average grain size against cooling temperature for screening run experiments (red dotted line highlights the linear trend of the parameter). Cooling temperature does not show a significant trend with grain size (*p*-value > 0.05); however it was retained for the main experiment set due to interest in potential interaction terms with dwell temperature and cooling rate.

These screening experiments and the resulting analysis and model fitting proved to be successful. The two most significant parameters (dwell temperature and cooling rate) were identified using a set of only ten experiments. Ultimately, these results were only the first stage in the analysis and optimization of this growth process, and largely served as a starting point toward the design and implementation of the main experiment set. This second set of experiments used a set of twenty of experiments on this reduced number of parameters to be able to build a more descriptive second-order model, as discussed below.

5.4 Main Experiments

The second stage of the study developed a comprehensive second-order model based on dwell temperature, cooling rate and cooling temperature. As the less important parameters had been removed from consideration, a more predictively-powerful model could be built by using a larger experimental design (as the number of experiments in the design scaled exponentially with number of parameters considered). Thus, the experiments utilized in this section were both efficient in modeling power as well as in time and resource use.

This section elaborates on how this “main” experiment set was designed and executed, as well as how the resulting modeling and parameter response was evaluated. The resulting second-order model then predicted the optimal regions of growth within the experimental parameter-space, identifying conditions which may yield improved growth performance.

5.4.1 Design Structure of Main Experiment Set

Following the results of the screening experiments, three process parameters were retained for investigation in the main experimental set: dwell temperature, cooling rate and cooling temperature. This main experiment set was used for response surface analysis using a second-order design, considering not only the first-order (linear) effects (as in the screening run model), but also two-parameter interaction terms and quadratic terms.

To effectively model these parameters' response, a particular type of experimental design, called the central composite design (CCD), was used. This design structure is constructed using a full set of factorial runs with additional center and axial points added to this structure to allow the evaluation of these interaction and quadratic terms. An illustration of this design for three parameters is shown in Figure 5.6.The main advantage of the CCD is its variance optimality due to its orthogonal structure and rotatability; thus it is useful in developing second-order models with high resource efficiency and accuracy [113].

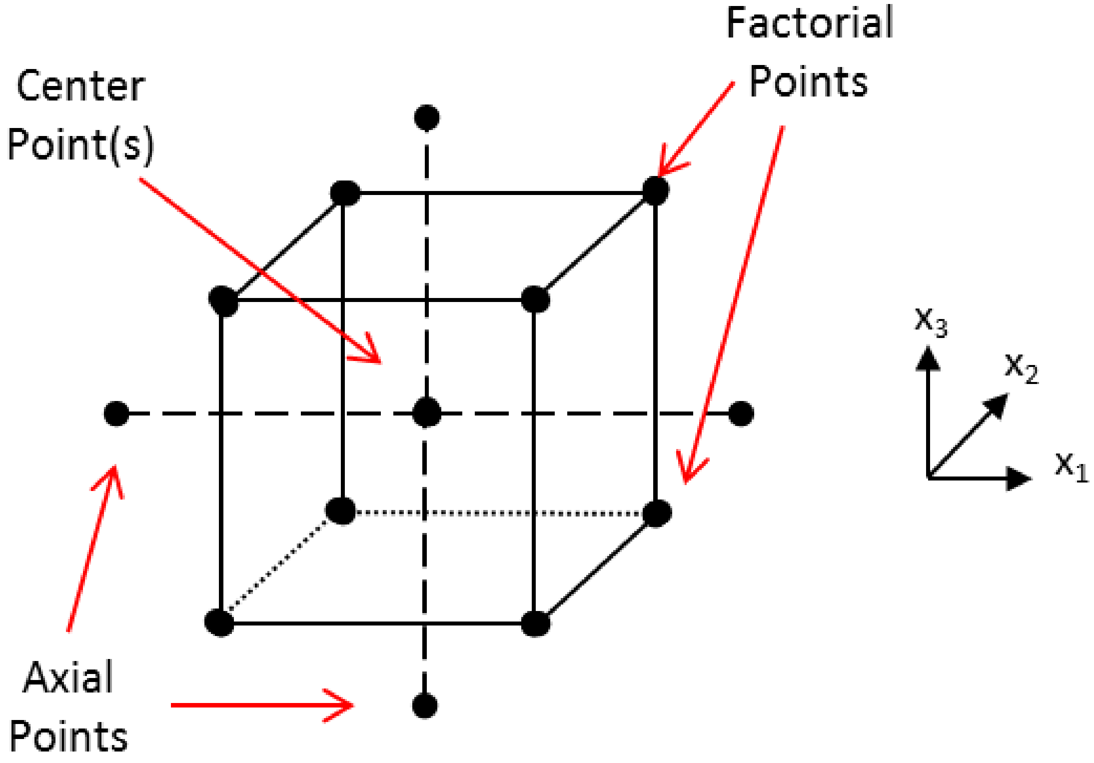

Figure 5.6: Diagram of three factor central composite design [113]. Alpha corresponds to the distance of the axial points from the design center (in coded values).

Using R, a three-factor (2^3) CCD was constructed, this time using slightly different values for the creation of the coded variables (Table 5.3. The change in coded variables expanded the region of interest for these experiments, placing the axial values at the extremes of past experimental study.

Table 5.3: Two-level factor and center point values remaining three parameters studied in main experiment set.

Process Variable	Units	Upper Value (+1)	Lower Value (-1)	Center Value (0)
Dwell Temperature (x_1)	°C	1500	1400	1450
Cooling Rate (x_2)	°C/hr	8.0	3.0	5.5
Cooling Temperature (x_3)	°C/hr	1250	1050	1150

For this type of CCD, the typical blocking scheme is to split the 2^3 factorial design points into two blocks, with the axial points in the third and two center points included in each block, making 20 total runs. Blocking was performed to help account for (and reduce) inhomogeneity between experiments over time, as the alumina tube and BN boats used in the experiment experience physical stress and corrosion due to the extreme heat and wetting of the molten Ni-Cr flux and must be exchanged. Table 5.4 shows the run order and coded variable values for this rotatable three factor CCD, which set axial point values at 1.68 to ensure design orthogonality and rotatability (axial points and factorial points all fall on the surface of a sphere with radius of 1.68), as well as minimize model variance.

Table 5.4: Blocking and run order for a three factor rotatable CCD with six center runs.

Block 1 (Factorial 1)				***Block 2 (Factorial 2)***				***Block 3 (Axial 1)***			
Run Order	**x_1**	**x_2**	**x_3**	**Run Order**	**x_1**	**x_2**	**x_3**	**Run Order**	**x_1**	**x_2**	**x_3**
1	1	1	-1	**1**	0	0	0	**1**	0	0	1.68
2	-1	1	1	**2**	-1	1	-1	**2**	0	0	0
3	-1	-1	1	**3**	0	0	0	**3**	1.68	0	0
4	0	0	0	**4**	-1	-1	-1	**4**	0	-1.68	0
5	1	-1	1	**5**	-1	-1	1	**5**	0	1.68	0
6	0	0	0	**6**	1	1	1	**6**	-1.68	0	0
								7	0	0	0
								8	0	0	-1.68

Following the completion of these experiments, the crystal grain width and thickness was measured. Based on this, ANOVA and F-tests for linear effects and lack of fit (LOF) in R were used to build second-order models for grain width and thickness with respect to these three parameters.

5.4.2 Main Experiment Results

The main experiments were performed in a set of three blocks, consisting of two half fraction factorial blocks made up of six experiments (four factorial points + two center points) and one axial block (six axial points + two center points), as described in Table 5.4. Average (characteristic) grain width analysis was performed in the same fashion as the screening runs, with crystals first extracted onto thermal release tape and measured using the optical microscope system. Crystal layer thickness measurement required the dicing of the metal ingots using a diamond wheel saw to allow access to a cross sectional view of the hBN layer. This thickness was also measured using the Nikon microscope system. Optical micrographs showing prepared ingot cross-sections and the layer measurement are shown below in Figure 5.7. Data for each of these measurements is presented in Table 10.3 of Appendix B.

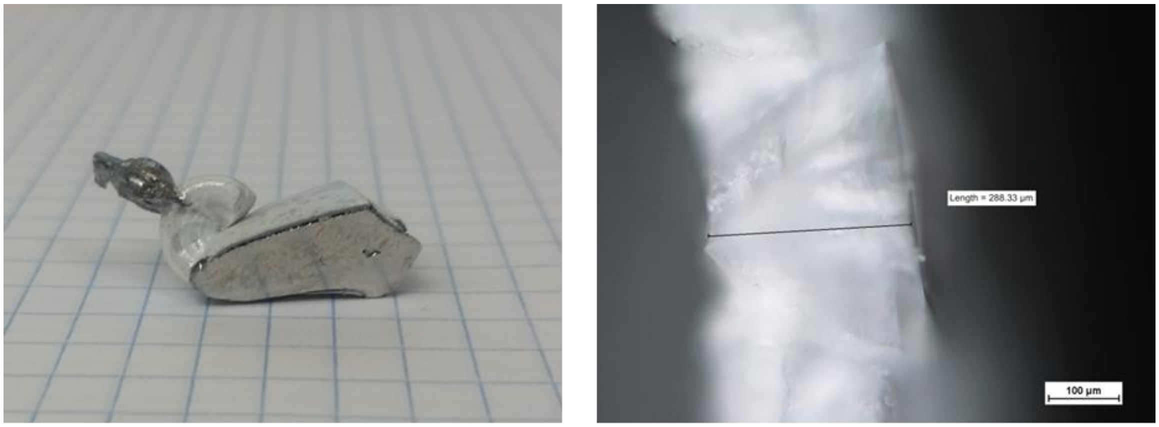

(a) (b)

Figure 5.7: (a) Macro photograph of diced ingot allowing for cross-sectional view of hBN crystal layer and (b) optical micrograph of thickness measurement of slightly tapered hBN crystals from main run experiment

The average (characteristic) grain width and crystal layer thickness measurements were plotted with respect to run order within each block to check for any systemic issues with the experiments, as done with the screening runs (Figure 4.8). These plots showed no concerning trends for either response, with R^2 values of 0.024 and 0.059 for the two plots, respectively.

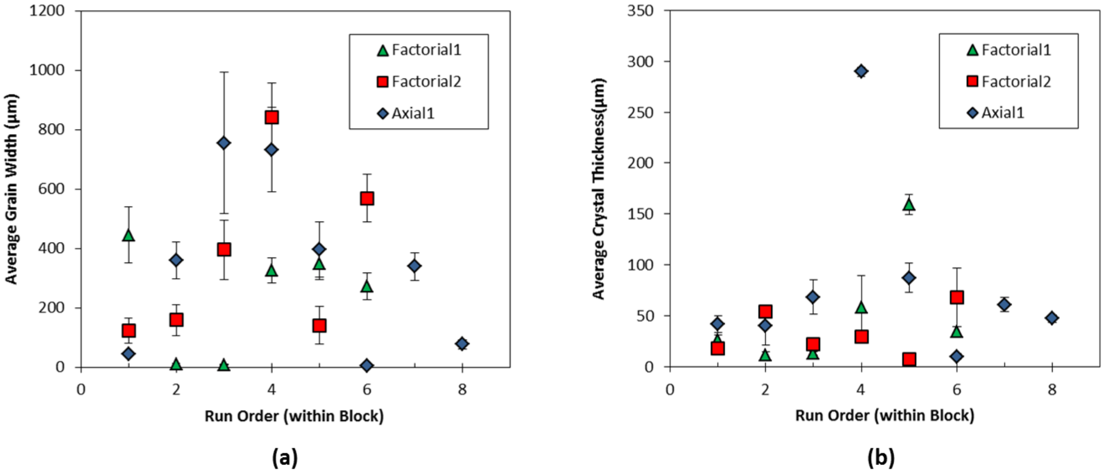

Figure 5.8: Scatterplots of average (a) grain width and (b) crystal thickness against run order within each block. For both plots, there was no trend was observed with respect to experiment sequence, showing no systemic issues with experiment order.

In addition to the run order plots, the larger number of center points (coded value = 0 for all parameters) in the main experiment set also justifies analyzing them. Due to the design structure, the only replicated experiments were these center runs, thus they were the best method for evaluating experimental error. For these plots, all six center point values (experiments run under identical conditions, two per block) were plotted, along with the center point average value (Figure 4.9). Error bars for each center point represent their within-sample variability, while the bars for the average value represent run-to-run variability. Within-sample variability for grain width was slightly less than that between samples, indicating that within-sample variation was not problematic. For crystal layer thickness, there was somewhat higher within-sample variability for a few measurements, however overall sample variability was acceptable.

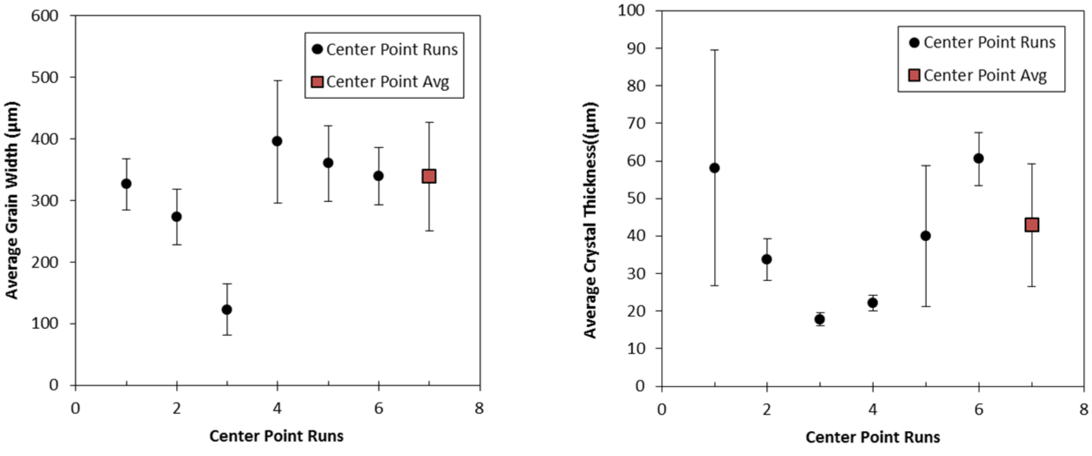

(a) **(b)**

Figure 5.9: Scatterplot of center run measurements and center run average for (a) average grain width and (b) average crystal layer thickness. Center point values are the only replicated runs within the main experiment set; therefore the center point average deviation represents run-to-run experimental error for each response.

Following these initial diagnostic tests, model building and analysis was performed for each response, starting with grain width. For the screening experiments, grain width had a strong correlation with dwell temperature and cooling rate. Before beginning the model fitting for this response, the raw data collected for experiments with respect to each parameter was plotted (Figure 5.10. From these plots, we see a clear linear correlation between grain width and dwell temperature, and a less clear trend with respect to cooling rate and no apparent trend with respect to cooling temperature. In order to fully evaluate these trends, regression analysis was performed using R.

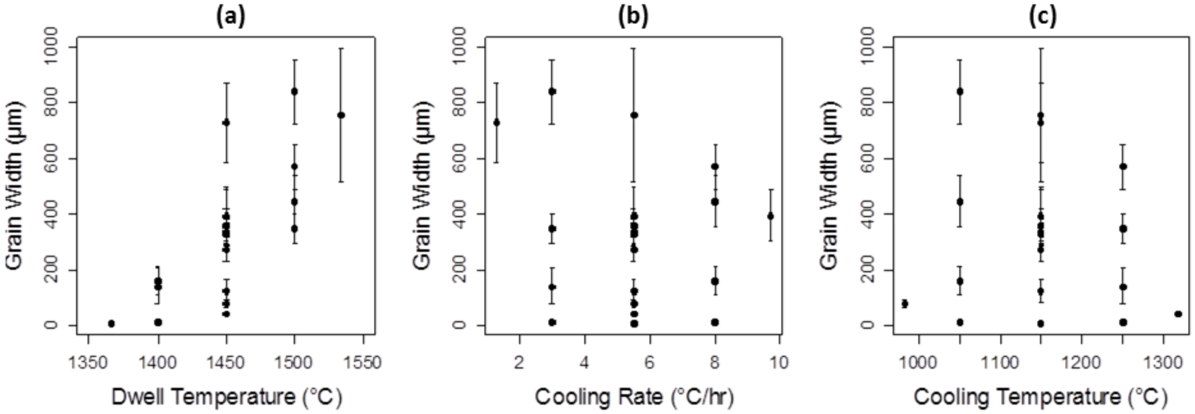

Figure 5.10: Scatterplots depicting average grain width plotted against (a) dwell temperature, (b) cooling rate and (c) cooling temperature.

Starting with the modeling process, the collected data was imported into R. Note that for RSM analysis, parameters must be converted from natural variables to normalized coded variables (x1, x2, and x3). The relationship between the coded variables used in the model and the natural variables are as follows:

$$x_1 = \frac{(Dwell\ Temperature - 1450℃)}{50℃} \qquad \textit{Equation 8}$$

$$x_2 = \frac{\left(Cooling\ Rate - 5.5\frac{℃}{hr}\right)}{2.5\frac{℃}{hr}} \qquad \textit{Equation 9}$$

$$x_3 = \frac{(Cooling\ Temperature - 1150℃)}{100℃} \qquad \textit{Equation 10}$$

Modelling and analysis was performed again using R (code for main experiments presented in Appendix D). Several successive models were developed to identify significant parameters for the grain width model (Table 5.5). A standard α = 0.05 level of significance (95% confidence level) was used for all parameter fit and lack of fit F-test evaluation. The first model fitted the first-order (linear) terms only. For this model, only the x_1 term (dwell temperature) was significant. This model had a low R^2 and adjusted R^2 values, although the lack of fit F-test was not significant. For the next model, two-parameter interaction terms were considered in addition to the first-order terms. None of these interaction terms were significant, resulting in almost the same R^2 value as before, with lower adjusted R^2 values due to lower term efficiency. After this, the full second-order model was investigated, looking at all first-order and two-pair interaction terms, as well as quadratic terms. In addition to the x_1 term, the quadratic x_2^2 and x_3^3 terms were significant. This model fit the data well, with R^2 value approaching unity and highly insignificant lack of fit F-test p-value. However, there was a large discrepancy between the R^2 and adjusted R^2 values due to the number of insignificant terms in the model. Based on this, a final, truncated second-order model was built using these significant terms (x_1, x_2^2 and x_3^2). Due to conventions with RSM analysis, the first-order forms (x_2 and x_3) of these higher order significant terms were also retained. Relative to the full second-order model, R^2 decreased slightly; however, both adjusted R^2 and LOF F-test were improved. ANOVA output for this final model is presented in Table 10.6 of Appendix C.

Table 5.5: Summary of ANOVA results for average (characteristic) grain width model fitting

Model Type	**Sig. Parameters (p-value ≤ 0.05)**	**Multiple R^2**	**Adjusted R^2**	**LOF p-value**
FO only	x_1	0.6711	0.5536	0.2324
FO + Interactions	x_1	0.6987	0.4795	0.178
Full SO	x_1, x_2^2, x_3^2	***0.9078***	0.7809	0.4755
FO + PQ(x_2,x_3)	x_1, x_2^2, x_3^2	0.8743	***0.8010***	***0.5581***

The coefficients for this grain width model can be converted into natural variables using the coded expressions from Equations 8-10 above. Neglecting the non-significant “BlockFac1” and “BlockFac2” terms, which are dummy variable terms meant to account to block-level differences in the intercept, the linear model has the form

$$
\begin{aligned}
y_{Grain\,Width}\ (\mu m) \\
&= 340\ \mu m + 4.6 \frac{\mu m}{°\mathrm{C}} [T_{Dwell} - 1450°\mathrm{C}] \\
&- 21 \frac{\mu m}{{}^{°\mathrm{C}}/_{hr}} \left[R_{Cool} - 5.5\ {}^{°\mathrm{C}}/_{hr}\right] + 0.3 \frac{\mu m}{°\mathrm{C}} [T_{Cool} - 1150°\mathrm{C}] \\
&+ 14\ \frac{\mu m}{\left({}^{°\mathrm{C}}/_{hr}\right)^2} \left[R_{Cool} - 5.5\ {}^{°\mathrm{C}}/_{hr}\right]^2\ - 0.0012\ \frac{\mu m}{°\mathrm{C}^2} [T_{Cool} - 1150°\mathrm{C}]^2
\end{aligned}
$$

Equation 11

Although the above linear equation is a quantitative description of the resulting response surface for grain width with respect to the growth parameters, a more comprehensive understanding of how these parameters influenced grain width can be obtained through graphical methods. The R is capable of producing a number of different response surface plots, including contour and perspective plots, which can represent a 3-D response, with two parameters as the x and y-axes and the response as the z-axis.

Initial graphical analysis looked at response of grain width against each two-parameter pairing, taken at the -1, 0 and +1 coded levels for the un-plotted parameter, via a 3x3 set of contour plots, presented in Figure 5.11. The most obvious trend was the crystals width dependence on dwell temperature; the crystal width increased monotonically (due to the linear-only dependence in the above model). Trends with cooling rate and cooling temperature were more complex, as these depended on both linear and quadratic terms. Cooling rate was predicted to have a minimum grain width at a cooling rate of 6.3°C/hr; the width more rapidly increased with decreasing cooling rate compared to higher cooling rates. From past experimental study, this predicted grain width increase with increased cooling rates (>10°C/hr) is nonphysical and can be ignored. For cooling temperature, an optimal value of 1130°C was projected from this model, with a slight decrease in grain width for values above and below this. This prediction is sensible, as this temperature should be well below the melting temperature of the Ni-Cr flux. The grain width decreased more rapidly with increasing cooling temperature. Physically, this may be due to the system being quenched prematurely, interrupting growth of crystals in the basal plane direction and potentially producing tapered crystals.

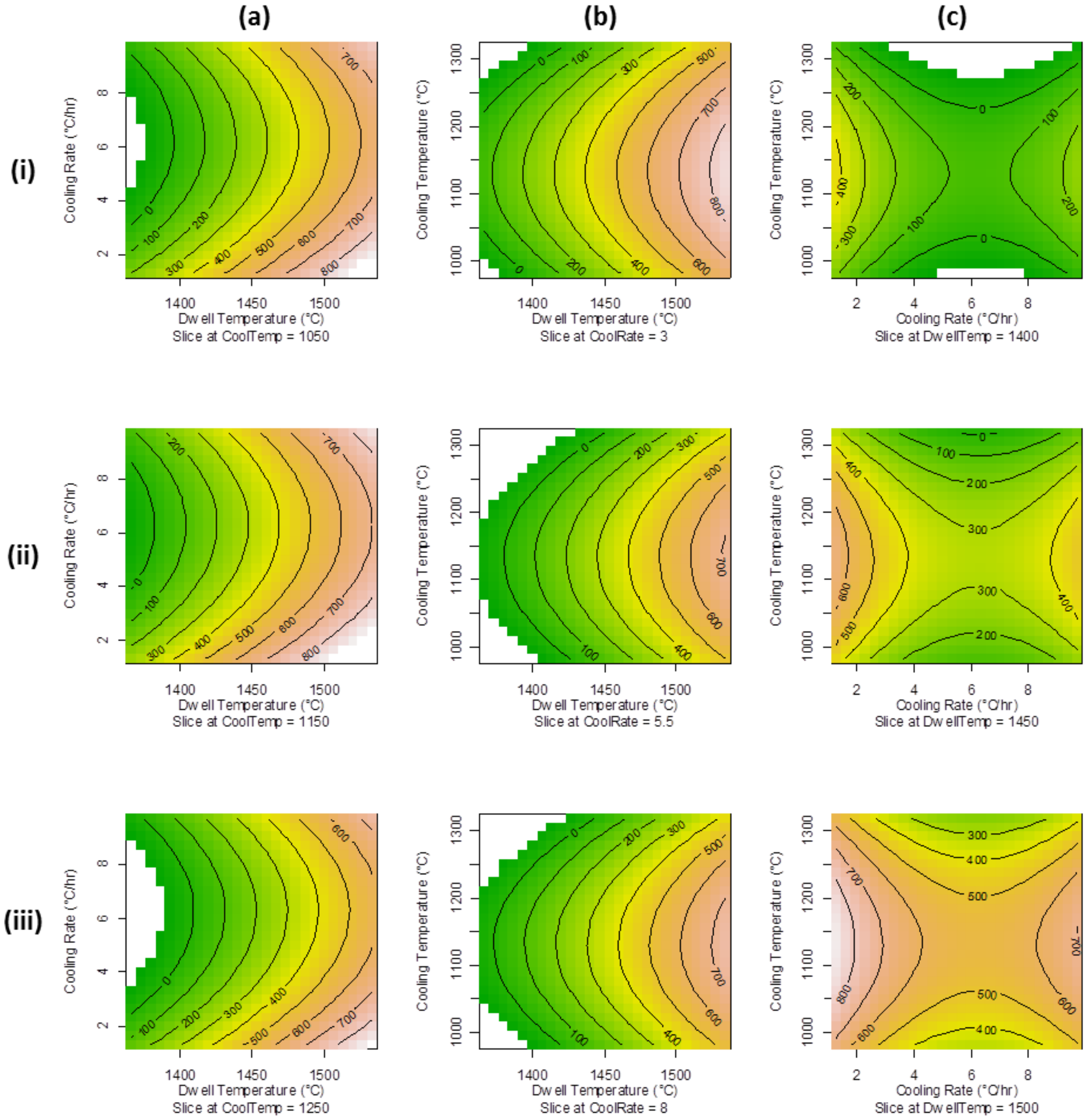

Figure 5.11: Set of contour plots showing response surface for grain width model. Each contour plots the response (represented by color and contour lines) against two of the parameters, with column (a) showing dwell temperature vs cooling rate, column (b) showing dwell temperature vs cooling temperature and (c) showing cooling rate vs cooling temperature. Each parameter pair was projected at a constant value for the third parameter, with row (i) held at the -1 coded value, row (ii) held at the 0 coded value and row (iii) held at the +1 coded value for each parameter.

In addition to modeling grain width within bounds of the experimental runs, the model can be used to predict the response surface beyond this range, so long as the fundamental behavior of the system remains constant in the projected region. Figure 5.12 shows a perspective plot of the response surface with respect to dwell temperature and cooling temperature projected at a cooling rate of 1°C/hr. The trend between grain width and both dwell temperature and cooling temperature illustrated by the contour plots can be seen more clearly here. Most importantly, grain size is predicted to exceed 1000 μm in width at this cooling rate for dwell temperatures ≥1550°C and cooling temperature near 1150°C.

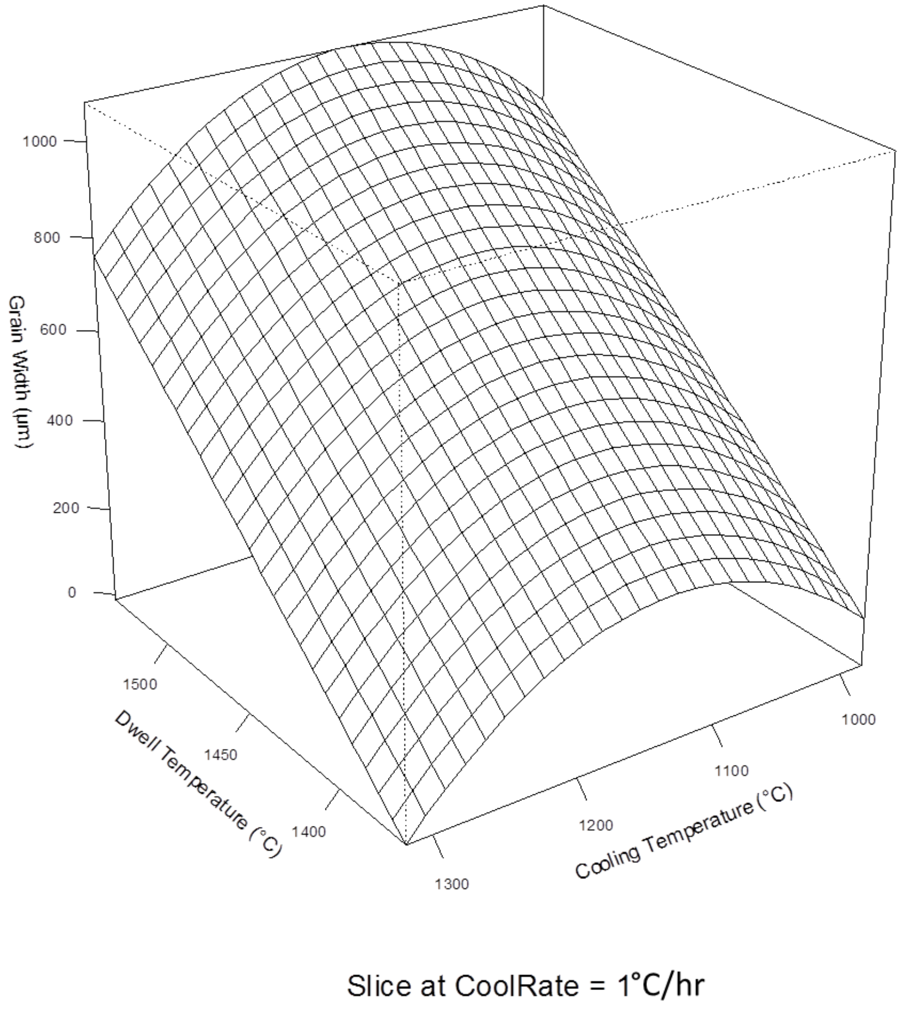

Figure 5.12: Perspective plot showing the prediction of largest characteristic grain width as a function of dwell temperature and cooling temperature, with cooling rate projected at 1°C/hr. Grain width is anticipated to exceed 1000μm for dwell temperatures ≥ 1550°C.

As a final graphical analysis to help show the behavior of the system, perspective plots were modeled with grain width plotted against cooling rate and cooling temperature across a range of four different dwell temperatures (1400°C to 1700°C), illustrated in Figure 5.13. Due to the lack of interaction terms, the shape of this response surface constant for all dwell temperatures; however, the width of the largest grains formed is projected to increase, with a maximum width of 400μm at 1400°C to as wide at a1800μm at 1700°C. Based on these projections, it is clear that increasing the dwell temperature is the most realistic and effective way to increase crystal width. Even at higher cooling rates at 1700°C, grain widths are expected to be greater than 1000 μm.

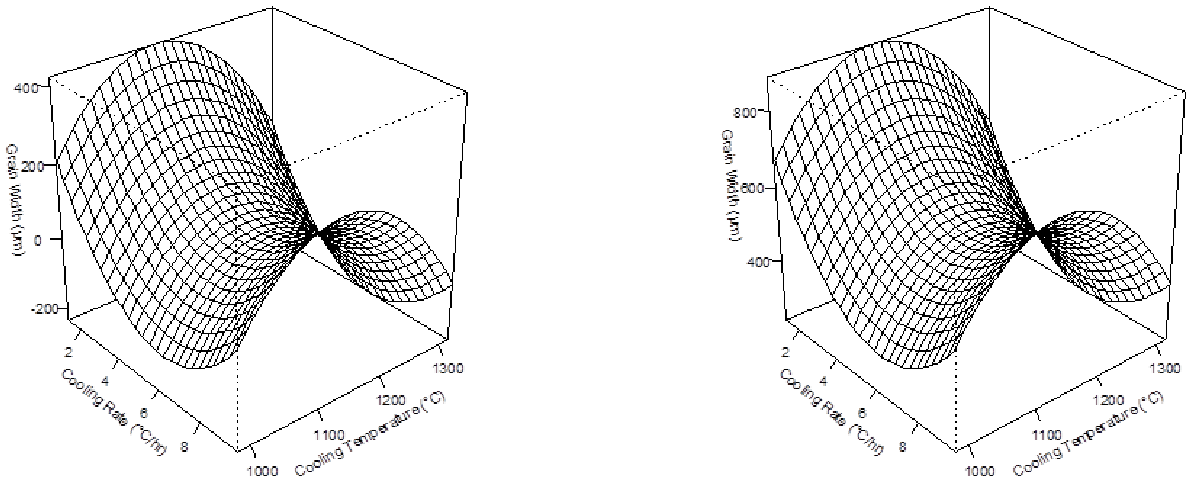

(a) Slice at DwellTemp = 1400°C **(b)** Slice at DwellTemp = 1500°C

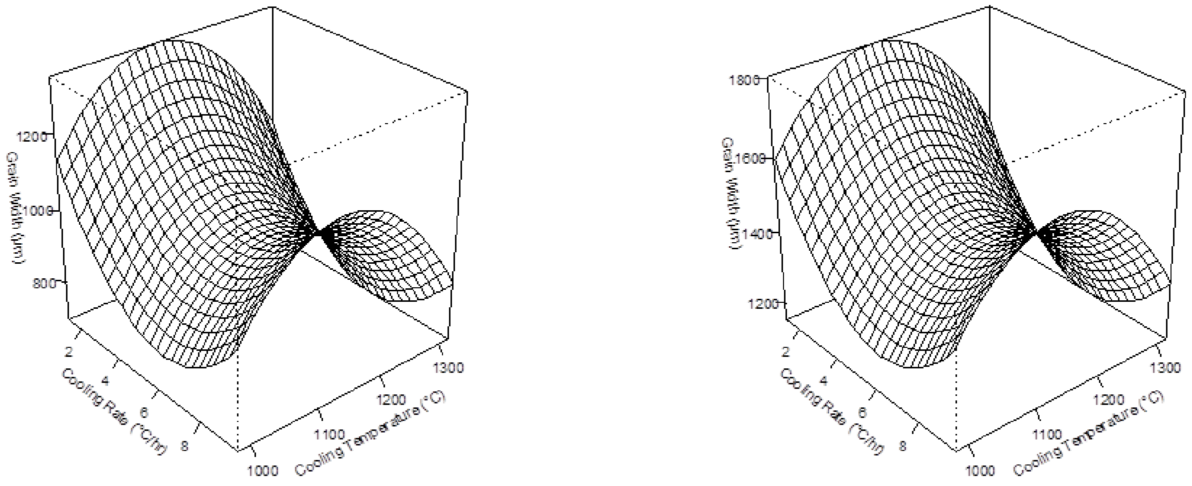

(c) Slice at DwellTemp = 1600°C **(d)** Slice at DwellTemp = 1700°C

Figure 5.13: Perspective plot series predicting the widths of largest characteristic grains formed as a function of cooling rate and cooling temperature, projecting dwell temperature slices at (a) 1400°C, (b) 1500°C, (c) 1600°C and (d) 1700°C. Width is predicted to exceed 1600μm for growth with cooling rate ≥ 2°C/hr and cooling rate of 1150°C at a dwell temperature 1700°C.

The next topic of focus was the crystal layer thickness model. Again, before beginning on model fitting for this response, the raw data collected for experiments with respect to each parameter was plotted to allow for qualitative analysis of trends (Figure 5.13). From these plots, there appear to be linear correlations between thickness and both dwell temperature and cooling rates. Cooling temperature again did not seem to have a strong trend, although all three of these plots appear more complex than in the case of the grain width data. In any case, higher order effects and interaction parameters cannot easily be detected by these plot types. Thus, regression analysis using R must be applied for quantitative analysis of this data.

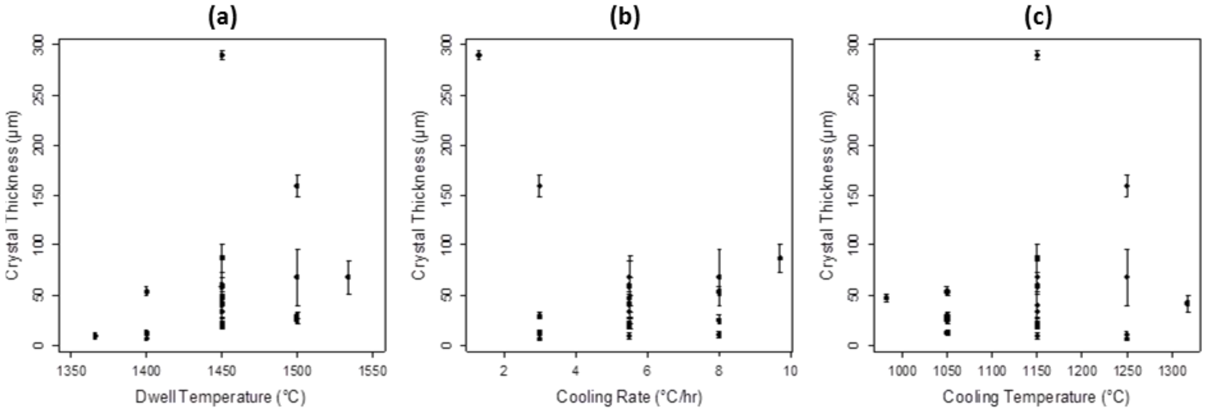

Figure 5.14: Scatterplots showing average crystal layer thickness plotted against (a) dwell temperature, (b) cooling rate and (c) cooling temperature.

Modelling and analysis for the crystal layer thickness response was performed using R (code for main experiments presented in Appendix D), using the same successive model approach as was used in the grain width model to identify significant parameters. Summaries of significant parameters and diagnostic statistics for each of these models are presented in Table 5.5. Unlike the grain width data, the fit for all of the crystal layer thickness models was much less clear-cut, therefore the level of significance for this model fitting was relaxed to $\alpha = 0.1$. The first model looked at the fit of first-order (linear) terms only. Unfortunately, this model had very poor fit, with no terms (other than an intercept) found as significant. Consequently, this model had very low R^2 and adjusted R^2 values and significant lack of fit F-test statistic. The next model, considered two-parameter interaction terms in addition to these first-order terms. Again, none of the terms in this model were significant, with only marginal improvement in diagnostic statistics. Following these two unsuccessful models, the full second-order model was investigated, considering quadratic terms in addition to the first-order and two-pair interaction terms, as well as quadratic terms. The fit for this model was quite different; several terms were significant, including the x_1 and x_2 linear terms, the $x_1{:}x_3$ interaction and the x_2^2 quadratic term. The addition of the second-order terms greatly improved the fit of this model, with increased R^2 value. However, there was a major difference between the R_{-}^2 and adjusted R^2 values due to the number of insignificant terms in the model and the lack of fit F-test statistic was still significant (< 0.1). A final, truncated second-order model was built using the significant x_1, x_2, $x_1{:}x_3$, x_2^2 and x_3^2 terms (as well as the x_3 term due to RSM conventions). Relative to the full second-order model, the R^2 value decreased slightly, however both adjusted R^2 and LOF F-test were improved. ANOVA output for this final model are presented in Table 10.7 of Appendix C. Unfortunately, lack of fit for this truncated model was still significant, requiring the model, and thus any predictions made by it, to be taken with a grain of salt.

Table 5.6: Summary of ANOVA results for crystal layer thickness model fitting

Model Type	**Sig. Parameters (p-value ≤ 0.1)**	**Multiple R^2**	**Adjusted R^2**	**LOF p-value**
FO only	N/A	0.3322	0.09369	0.0095
FO + Interactions	N/A	0.4633	0.07306	0.0084
Full SO	x_1, x_2, $x_1{:}x_3$, x_2^2	***0.8469***	***0.6363***	0.0281
FO +TWI($x_1{:}x_3$)+PQ(x_2)	x_1, x_2, $x_1{:}x_3$, x_2^2	0.7609	0.6214	***0.0323***

The coefficients for this crystal layer thickness model were converted into natural variables using the coded expressions as done for the grain width model. Neglecting the non-significant “BlockFac1” and “BlockFac2” terms, which are dummy variable terms meant to account to block-level differences in the intercept, the linear model has the form

$$\begin{aligned}
&y_{Grain\ Thickness}\ (\mu m)\\
&\quad = 50\ \mu m + 0.43\frac{\mu m}{^{\circ}\mathrm{C}}\left[T_{Dwell} - 1450^{\circ}\mathrm{C}\right]\\
&\quad - 11\frac{\mu m}{{}^{\circ}\mathrm{C}/_{hr}}\left[R_{Cool} - 5.5\ {}^{\circ}\mathrm{C}/_{hr}\right] + 0.08\frac{\mu m}{^{\circ}\mathrm{C}}\left[T_{Cool} - 1150^{\circ}\mathrm{C}\right]\\
&\quad + 0.055\ \frac{\mu m}{^{\circ}\mathrm{C}^2}\left[(T_{Dwell} - 1450^{\circ}\mathrm{C}) \cdot (T_{Cool} - 1150^{\circ}\mathrm{C})\right]\\
&\quad +\ 7.0\frac{\mu m}{\left({}^{\circ}\mathrm{C}/_{hr}\right)^2}\left[R_{Cool} - 5.5\ {}^{\circ}\mathrm{C}/_{hr}\right]^2
\end{aligned}$$

Equation 12

Contour plot analysis was performed again for the crystal layer thickness response against all two-parameter pairs, presented in Figure 5.12 (taken at the -1, 0 and +1 coded levels for the un-plotted parameter). No linear-only trends were observed in these plots, as all parameters displayed either quadratic or two-parameter interaction terms in the model. The most important trend in these plots was the interaction between dwell temperature and cooling temperature. The thickest crystals were predicted to form for the high dwell temperature – high cooling temperature combination, particularly at lower cooling rates. This trend is believed to be caused by two successive events: standard crystal growth (primarily in the basal plane direction) at the high dwell temperature and slow cooling, followed by rapid growth due to quenching resulting from high cooling temperature. These conditions cause the formation of tapered crystal grains. A more detailed plot of this behavior is illustrated in Figure 5.16, a perspective plot of crystal layer thickness plotted against dwell temperature and cooling temperature at a cooling rate of 3°C/hr. However, the fit of this model was significantly worse that for crystal width (LOF F-test p-value was significant), so any predictions made using these projections must be taken with some pause.

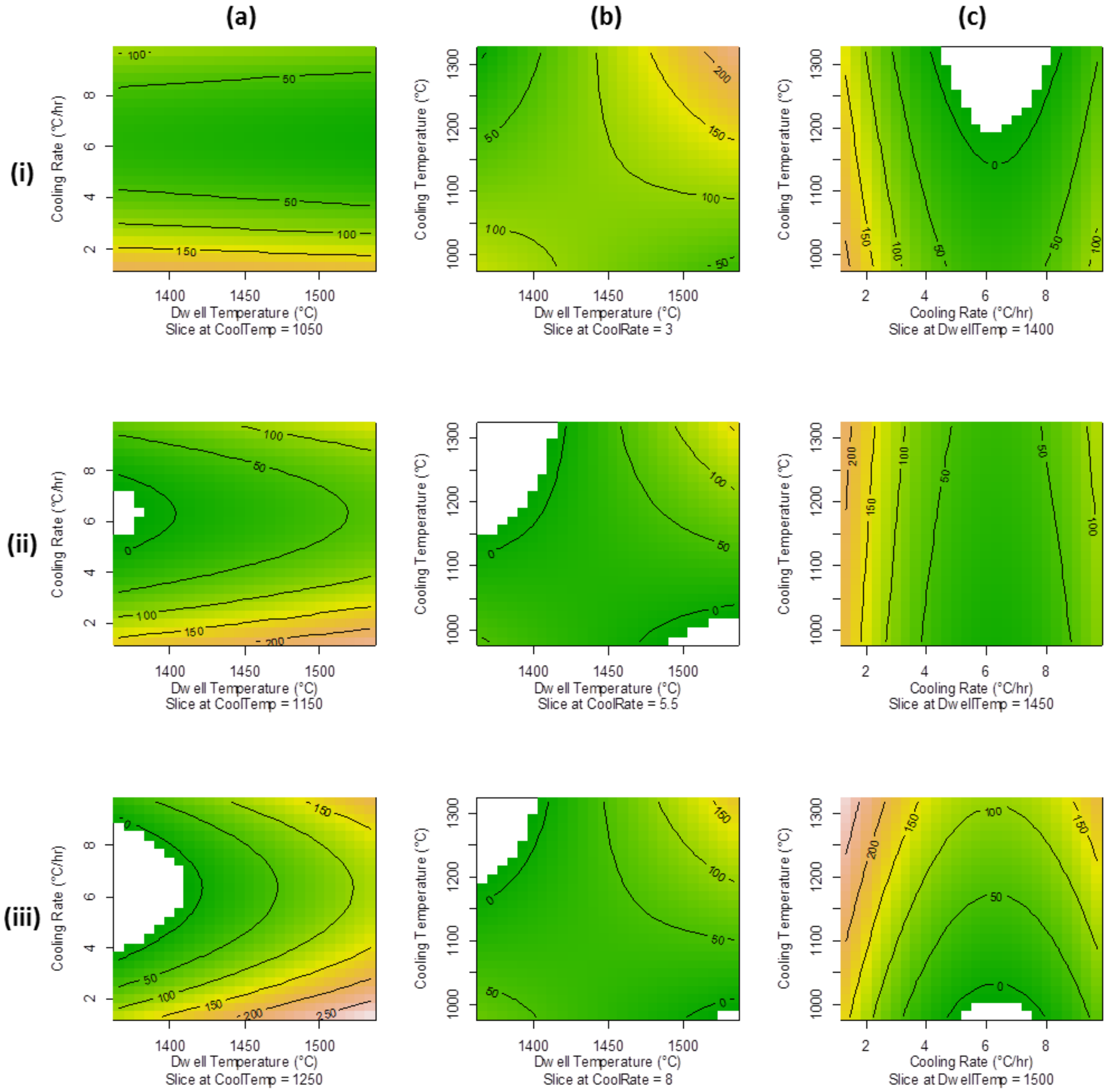

Figure 5.15: Set of contour plots showing response surface for crystal layer thickness model. Each contour plots the response (represented by color and contour lines) against two of the parameters, with column (a) showing dwell temperature vs cooling rate, column (b) showing dwell temperature vs cooling temperature and (c) showing cooling rate vs cooling temperature. Each parameter pair was projected at a constant value for the third parameter, with row (i) held at the -1 coded value, row (ii) held at the 0 coded value and row (iii) held at the +1 coded value for each parameter.

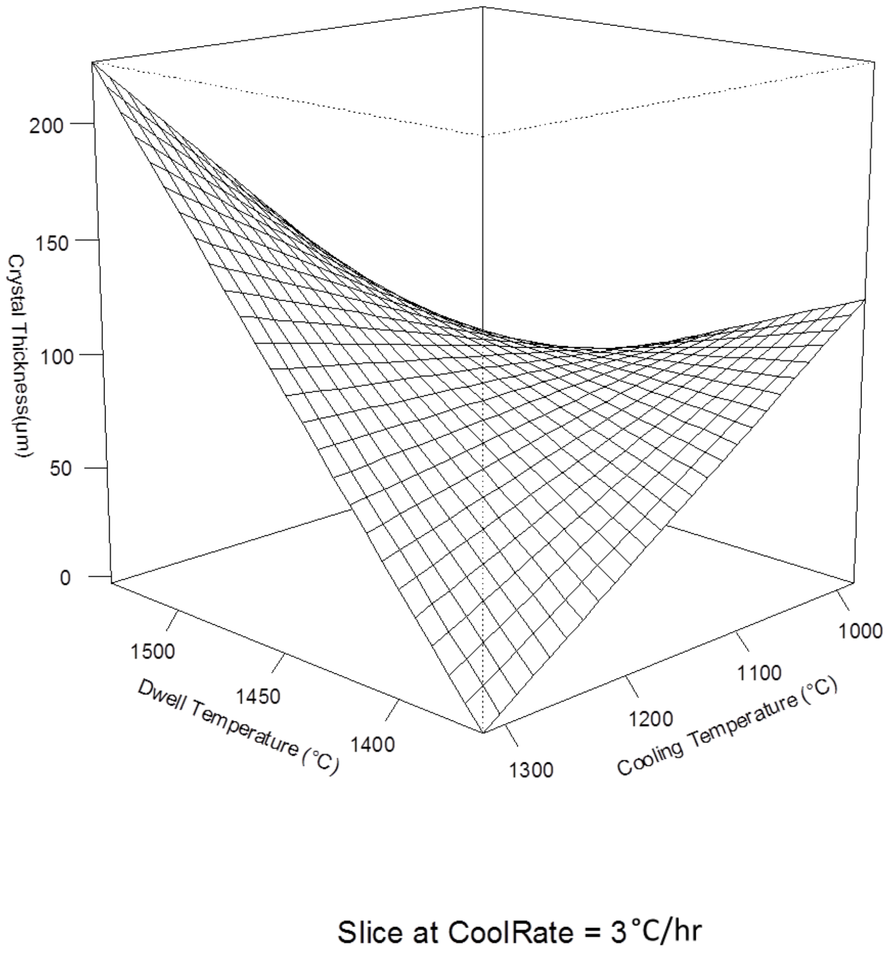

Figure 5.16: Perspective plot for crystal layer thickness model projecting response surface for crystal thickness as a function of dwell temperature and cooling temperature at fixed cooling rate of 3°C/hr. The crystal layer thickness is predicted increase with increasing dwell temperature and cooling temperature (although increased cooling temperature may lead to undesired tapered crystals).

5.5 Relevance of This Work

Based on the findings of this study, it is clear that the single most important parameter for controlling hBN crystal grain size is dwell temperature. Both the grain width and thickness models from this study project improved response with higher dwell temperatures. This is sensible from a thermodynamic standpoint, as the amount of BN that can be dissolved within this flux is dependent on the temperature of that flux. Diffusion rates within the flux should also increase with temperature, helping to accelerate the growth rate. The driving force for solution-based crystal growth methods is the degree of supersaturation that can be achieved for the solute [22]. Therefore, future furnace systems for hBN growth by Ni-Cr flux should be designed with higher dwell temperatures in mind. Assuming that these predictions hold with increasing dwell temperature beyond the range of the experimental region, hBN single-crystal domains as large as 2mm in width should form at a dwell temperature of 1700°C.

For the other two parameters, their effect on crystal width and thickness are more complex. Sensibly, lowering cooling rate should correlate with a decrease in nucleation rate, leading to wider crystal grains. The same conclusion can be drawn from this predictive model, although there does seem to be a practical limit to how low cooling rate can be explored due to exploding experimental runtime. As for cooling temperature, it appears to have the most significant impact on crystal thickness, with thicker crystals being formed at higher cooling temperature (and earlier system quenching). This result suggests that the furnace program could to be altered in order to grow thicker crystals by using two successive cooling stages to form crystals of the desired thickness. The first stage would operate at a slow cooling rate (<4°C/hr) at high temperatures (>1300°C) and promote grain growth in the basal plane direction, followed by a second stage with higher cooling rate (>4°C/hr) down to 1000°C. This second stage could be optimized to promote grain growth in the a-direction, forming wider crystals without degenerating to the formation of an amorphous BN buffer layer.

The modeling performed by this study is largely empirical. The Ni-Cr flux growth process is still a black box, but these models can be used to guide further work the direction of producing wider and thicker grains. Improving the grain size of these bulk hBN crystals should enable the next stage of research in hBN optoelectronic devices and neutron detectors.

Chapter 6 - Isotopically Enriched hBN Growth

Naturally-occurring boron is composed of two isotopes, ^{10}B and ^{11}B, which have respective fractions of approximately 20% and 80% (atomic basis). Due to their relatively low atomic mass, the mass difference between these two isotopes results in a significant change in the hBN crystal lattice behavior. This chapter investigates some of the potential benefits of producing enriched hBN crystals and demonstrates how the Ni-Cr flux growth process could be adapted to grow enriched ^{10}B and ^{11}B crystals. A calibration curve between isotopic concentration and Raman shift was developed and key physical changes (Raman peak shift) were demonstrated to be affected by isotopic concentration.

6.1 Motivation

The enrichment of boron isotopes in hBN is beneficial for several reasons. The efficiency of hBN neutron detectors is predicted to increase with ^{10}B concentration, with up to five-fold increase in neutron absorption for hBN with 100% enrichment in ^{10}B [46]. For comparison, the thermal neutron capture cross-section for ^{10}B is 3800 barns, while the cross section for ^{11}B is only 0.005 barns [42]. Additionally, theory predicts the room temperature thermal conductivity of hBN to increase by 30% for isotopically pure hBN (^{10}B or ^{11}B), due to reduced phonon-isotope scattering in the crystal lattice [120]. Due to this, isotopically enriched hBN crystals may also be capable of long distance propagation of phonon-polariton modes, which may enable the development of phonon-based devices [82].

This work demonstrates that enriched hBN crystals can be grown by reacting enriched boron sources with N_2 gas in a Ni-Cr flux Both ^{10}B and ^{11}B crystals were grown and a calibration curve between Raman shift and the isotopic concentration was established, eliminating the need to perform expensive and destructive mass spectroscopy techniques.

6.2 Methods

Growth of the enriched hBN crystals was performed using standard growth conditions in the CM and Mellen furnaces (dwell temperature of 1500°C, cooling rate of 2°C/hr, and N_2 gas flow only). Unlike in the Ni-Cr flux process, this method added elemental boron to the flux and formed BN by reaction with the N_2 *in situ*. Multiple enriched boron sources were used to achieve a range of concentrations of ^{10}B and ^{11}B. The first sources were a pair of pre-formed Ni-Cr-B alloys (with composition of 46.76 wt.% Cr, 41.47 wt.% Ni and 11.78 wt% B), which were prepared by Ames Laboratories using high purity Ni and Cr sources and two sources of enriched 99.999% purity boron powder from Ceradyne Inc. The isotope concentrations of these enriched high purity boron powders were 99.99 at.% ^{11}B and 92.64 at.% ^{10}B, respectively. The Ni and Cr source materials had low carbon and oxygen impurity concentrations; <75ppm and <35 ppm respectively (measured by glow discharge mass spectroscopy).

The initial experiments used the pre-formed alloy and BN boats. Crystal sizes and habits were analyzed using optical and electron microscopy. While this did successfully produce hBN crystals enriched in ^{10}B and ^{11}B, this procedure had two drawbacks: (1) the Ni-Cr-B alloy pieces did not completely melt during the dwell stage at 1500° and 24 hr and (2) the BN from the boats diffused into the flux, diluting the ^{10}B or ^{11}B enrichment. To achieve the highest isotopic enrichments possible, the growth procedure was changed to form Ni-Cr-B flux by mixing the enriched boron powder with standard Ni and Cr sources (with the same composition as above), and performing growth in an alumina boat. These changes improved the mixing and ingot formation for these materials and prevented diffusion of non-enriched boron into the flux.

Enriched hBN crystals from initial growth experiments using the pre-formed Ni-Cr-B alloy, were submitted (along with an hBN of natural abundance) to Evans Analytic Group for analysis of ^{10}B and ^{11}B isotope concentration by secondary-ion mass spectrometry (SIMS). The isotopic distribution of the three samples was determined via SIMS by calibrating the system with the natural abundance sample defined as 20 at.% ^{10}B. Raman spectroscopy was performed at Kansas State (using the system described in Chp 2), as well as by Dr. Kurt Gaskill, Dr. Josh Caldwell and associates at the U.S. Naval Research Laboratories (NRL). Raman peak measurements for these initial samples were coupled with SIMS data to produce a simple linear calibration curve to estimate the ^{10}B concentration from Raman peak shift. This peak shift phenomenon was analyzed for additional experiments producing a range of enriched ^{10}B and ^{11}B samples. Additionally, peak FWHM was analyzed with respect to peak position (and ^{10}B concentration) to understand this peak narrowing phenomenon.

6.3 Results and Discussion

In this section, experimental results for the growth of enriched hBN crystals by reacting boron with N_2 in Ni-Cr-B flux are discussed. hBN grains were characterized using optical and electron microscopy to identify their size and morphologies and to speculate on how the crystals were formed. The concentrations of ^{10}B and ^{11}B isotopes were measured by SIMS and were correlated to the shift in the E_{2g} Raman peak (occurring at 1366 cm^{-1} for natural abundance hBN) [89] The trends in Raman peak position and FWHM were also highlighted and studied.

6.3.1 Enriched hBN Growth from Ni-Cr-B Alloy

The Ni-Cr-B alloy pieces used in the first experiments did not fully melt, unlike prior Ni-Cr flux growth experiments. Nevertheless, hBN did precipitate and form crystals on the surface of the metal pieces. There were no significant differences in crystal size or habit between the ^{10}B and ^{11}B enriched samples. However, hBN did form by two different mechanisms within samples: standard growth by grain nucleation on the Ni-Cr-B surface, as observed in the Ni-Cr flux method, and a vapor-liquid-solid (VLS) interface growth mechanism. Nucleation of hBN occurred similarly for both samples, producing hexagonal and truncated hexagonal hBN platelets with small domain sizes. SEM images of three hBN crystal platelets formed by this growth mechanism had widths and thicknesses of 20-30 μm and 5 μm, respectively (Figure 6.1).

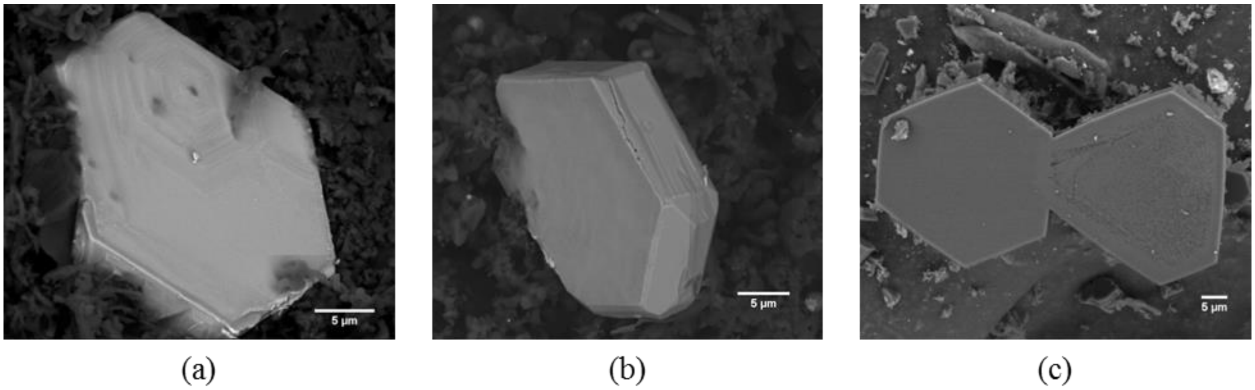

Figure 6.1: SEM images of hBN crystals with platelet-like habit formed by high temperature growth from enriched Ni-Cr-B alloy. (a) Spiral steps on the surface of this ^{10}B enriched hBN crystal was consistent the presence of a screw dislocation. (b) Growth of this ^{10}B enriched hBN crystal produced a platelet-like structure. (c) ^{11}B enriched hBN crystals showed similar growth habit and size as the ^{10}B enriched samples, implying that growth mechanism is independent of isotopic concentration.

Micron-scale hBN filaments appeared to grow as a “tail” forming behind spheres of Ni-Cr-B, consistent with the VLS mechanism, [121]. This growth mechanism had not been previously reported for hBN grown by the Ni-Cr flux and appeared to be similar to hBN nanowire grown from α-FeB particles in N_2 and NH_3, although these filaments were significantly larger in dimension [122]. Observationally, the whisker appeared to have grown as nitrogen is dissolved in the molten metal at its tip, reacting with boron to form hBN. These whiskers had lengths up to 70 μm with diameter of 5 μm (Figure 6.2), several orders of magnitude larger than hBN nanowires from previous studies [122-124]. Again, this mechanism is not expected to show a dependence on isotopic enrichment; however, this growth technique was primarily seen on the ^{10}B-enriched sample.

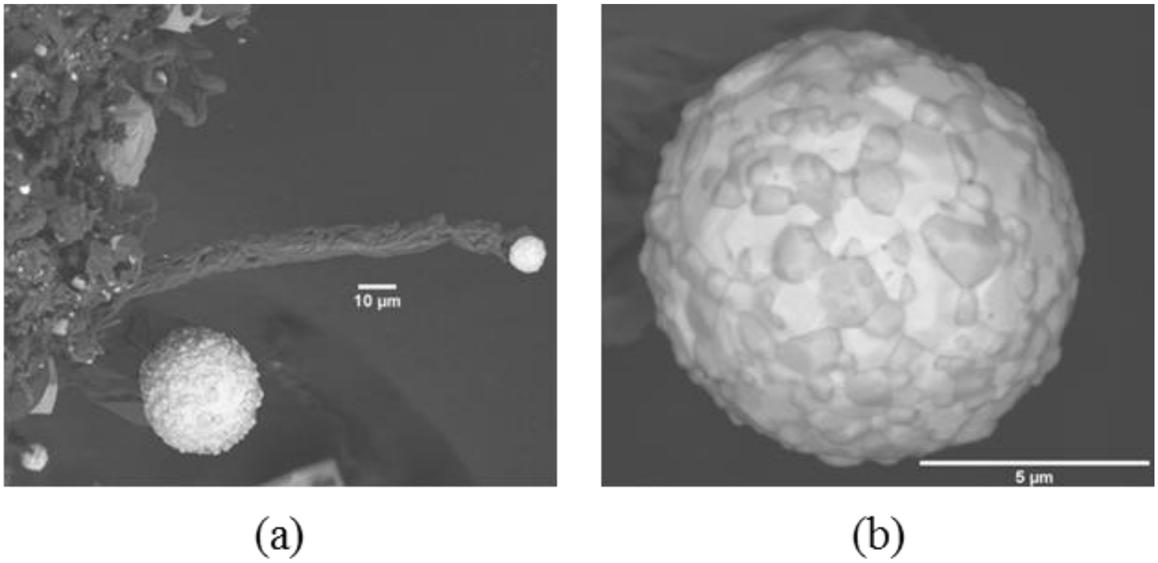

(a) (b)

Figure 6.2: SEM images of (a) an hBN whisker grown via the vapor-liquid-solid interface growth mechanism and (b) Ni-Cr-B metal sphere at the tip of the hBN whisker.

6.3.2 Coupled SIMS-Raman Analysis of Enriched hBN

Enriched ^{10}B and ^{11}B hBN crystals formed from the Ni-Cr-B alloy were collected and submitted to Evans Analytical Group for SIMS analysis. SIMS was calibrated using an hBN crystal with the natural distribution of boron isotopes ("natural abundance"), i.e. 20% ^{10}B and 80% ^{11}B (atomic basis). The majority isotope concentration of the enriched samples was 84.4 at.% for the ^{10}B-rich sample and 93.0 at.% for the ^{11}B-rich sample (with a standard deviation of ±0.01 at.% for each sample). These concentrations were used to determine the enrichment factor (the ratio of majority isotope concentration to concentration of that isotope in natural boron) of each sample, calculated at 4.25 for the ^{10}B-rich sample and 1.16 for the ^{11}B-rich sample. From this analysis, the following conclusions could be drawn: (1) the ^{11}B-rich sample had the highest isotopic enrichment of the two samples and (2) the ^{10}B-rich sample had the larger isotopic deviation from natural abundance.

In addition to SIMS analysis, Raman spectroscopy was performed on the enriched and natural abundance hBN samples to correlate these measurements and to create a calibration curve relating isotopic concentration to corresponding Raman shift peak position. Raman spectra for each sample displayed a similar structure with a single peak corresponding to the E_{2g} vibrational mode between in-plane boron and nitrogen atoms [89]. The peak position for the natural abundance hBN sample matched the value (1366 cm^{-1}) reported in the literature [31]. Table 6.1 provides Raman peak position and FWHM values, while Figure 6.3 shows the Raman spectra for each of the samples, as well as the Raman peak data plotted against SIMS-determined ^{10}B fraction.

Table 6.1: E_{2g} Raman shift peak position and FWHM values for natural abundance and ^{10}B and ^{11}B enriched hBN crystals

Sample	**SIMS ^{10}B Conc. (at %)**	**E_{2g} Raman Shift Peak Position (cm^{-1})**	**Raman Shift Peak FWHM (cm^{-1})**
Natural Abundance	19.9%	1365.6	8.3
^{10}B Enriched Sample 1	84.4%	1390.3	4.5
^{11}B Enriched Sample 1	7.0%	1359.5	3.8

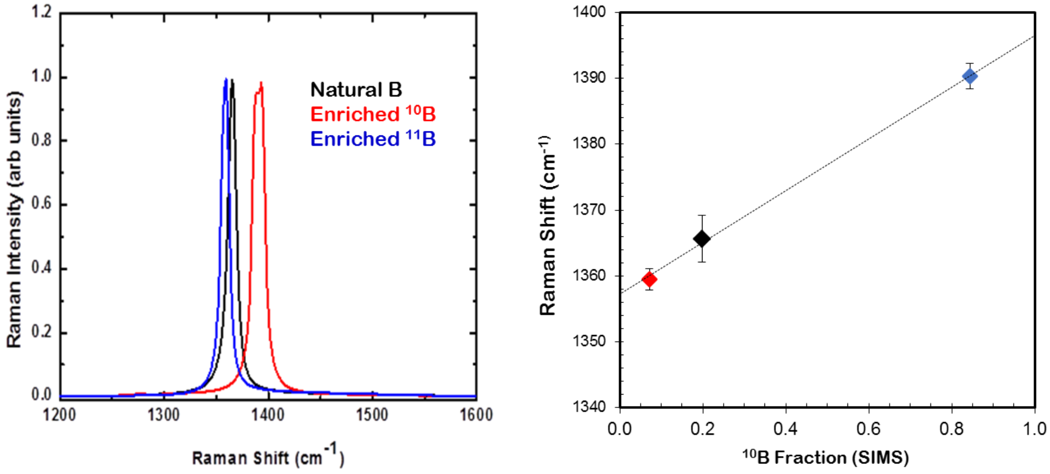

(a) (b)

Figure 6.3: (a) Raman spectra for the enriched and natural abundance hBN samples and (b) Raman shift peak position for E_{2g} mode plotted against its SIMS-determined ^{10}B fraction

The Raman peaks in hBN followed a linear relationship with respect to ^{10}B concentration. The E_{2g} peak shifted to higher wavenumbers with increasing ^{10}B fraction, and shifted to lower values as ^{11}B enrichment approached unity. This change was substantial, 30.8 cm^{-1} between the ^{11}B and ^{10}B enriched samples. The magnitude of this difference in peak position was due to the major difference in atomic mass between the two boron isotopes (10 % change relative ^{10}B), due to their low atomic number.

6.3.3 Additional Experiments using Enriched Boron Powder

Additional experiments were performed to allow for higher isotopic enrichments The HPBN boats were exchanged for alumina boats to prevent dilution of the enriched boron sources. The source materials were changed, as growth from boron powder mixed with Ni and Cr powder source materials produced better results than the pre-formed Ni-Cr-B alloy. Starting from powder source materials resulted in Ni-Cr-B ingots which successfully melted and were covered by enriched hBN crystal sheets (Figure 6.4). The enriched hBN crystal grains grown from these powder sources were also much larger, with flakes on the order of 300 μm compared to <100 μm for the pre-formed Ni-Cr-B ingot samples. Crystals from these samples were extracted and transferred onto sapphire substrates using thermal release tape (Figure 6.5).

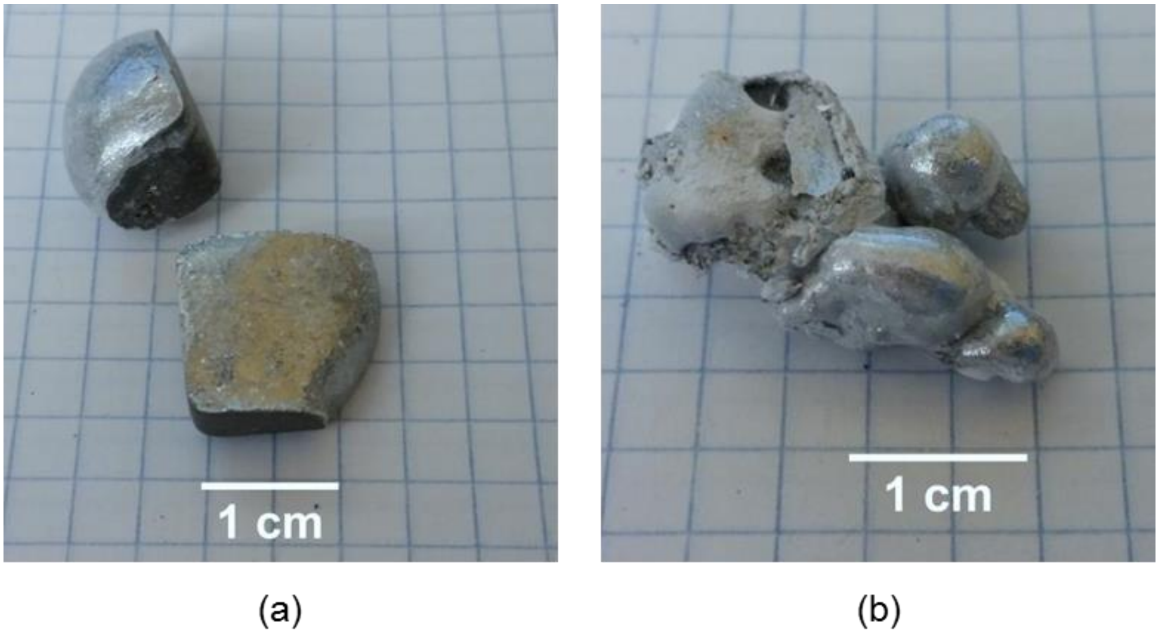

Figure 6.4: Photographs illustrating (a) ^{10}B enriched crystal sheet covering the top surface of the Ni-Cr-B ingot and (b) ^{11}B enriched crystals sheet partially covering the Ni-Cr-B ingot. For both of these samples, enriched powder was mixed with high purity Ni and Cr sources and successfully melted during the growth process.

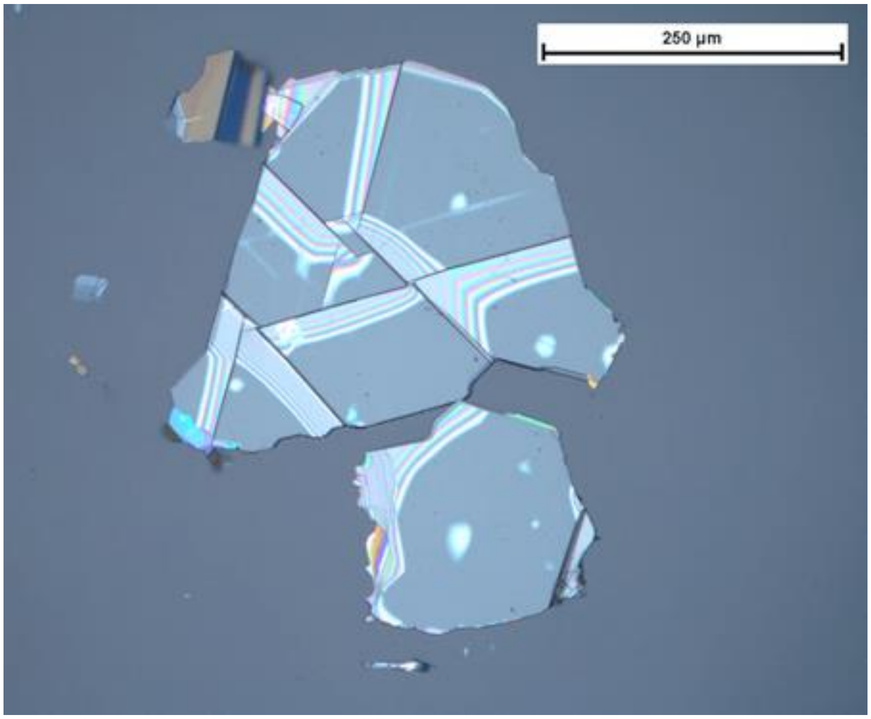

Figure 6.5: Optical micrograph of enriched ^{10}B hBN crystal flake transferred onto sapphire substrate using thermal release tape

SIMS analysis was not performed on these samples; however, isotopic enrichment was expected to be the same as the starting boron powder enrichment due to the lack of external boron sources. Raman spectroscopy was performed on these samples to estimate the isotopic enrichments. The Raman peak positions and FWHMs are presented in Table 6.2. To confirm if these estimates were realistic, the expected enrichment for these experiments were plotted against their Raman shift peak and compared to the SIMS-Raman calibration curve data (Figure 6.6).

Table 6.2: Expected ^{10}B concentration and Raman shift measurements for additional experiments performed in alumina boats using boron powder mixed with Ni and Cr sources

Sample	Source ^{10}B Conc. (at %)	Raman Shift Peak Position (cm^{-1})	Raman Shift Peak FWHM (cm^{-1})
^{10}B Enriched Sample 2	99%	1392.0	3.5
^{11}B Enriched Sample 2	<1%	1356.5	3.6

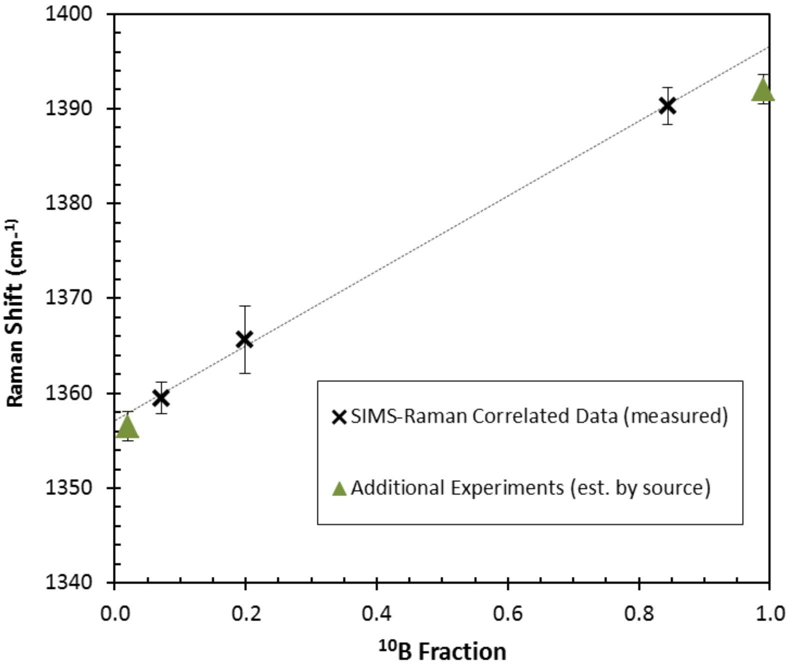

Figure 6.6: Expected ^{10}B fraction vs Raman shift peak position for additional enriched growth experiments, plotted over SIMS-Raman coupled data and linear fit (dashed line). The ^{10}B fraction for the additional experiments was assumed to be equal to that of its boron source material.

The expected ^{10}B fraction (based on the original source isotope concentration) of these additional samples fell slightly below the Raman-^{10}B fraction calibration curve, that either (1) this degree of enrichment was not obtained, (2) the behavior of the Raman shift is not linear as it approaches perfect enrichment or (3) the calibration fit is otherwise imperfect. However, the data does fall reasonably close to the predicted fit of the calibration curve, showing that Raman shift is useful, if imperfect, to quickly evaluate ^{10}B fraction.. Raman shift peak FWHM also showed a significant change with respect to ^{10}B fraction (and peak position). FWHM values for both of the enriched samples were approximately half of that for the natural abundance sample. This peak narrowing demonstrates how enrichment in either isotope results in lowered isotope-phonon scattering.

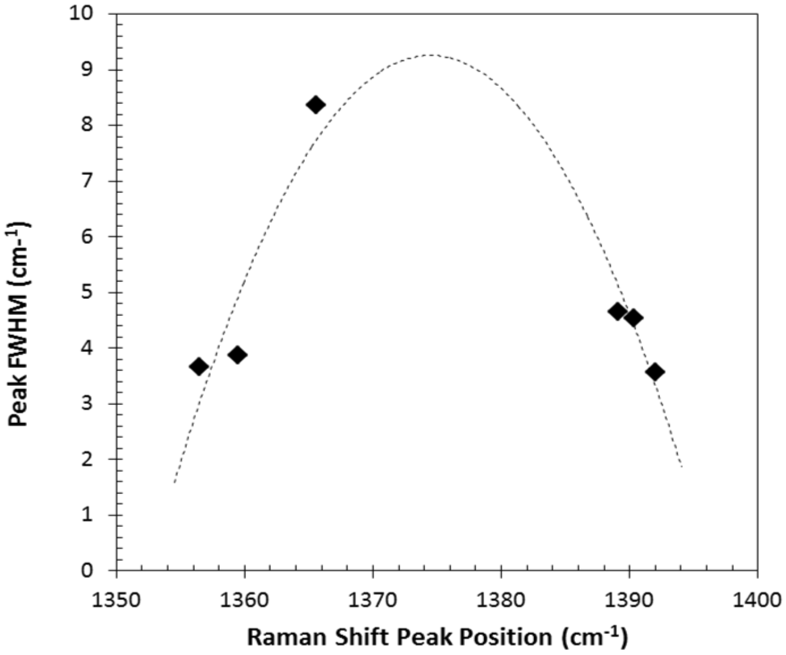

Figure 6.7: Raman shift peak position plotted against FWHM for enriched hBN crystals (and natural abundance standard). Dashed line shows fitted second-order polynomial fit for data predicted from 1st-principles for enriched bulk hBN by Lindsay *et al* [120].

6.4 Relevance of this Work

This study has confirmed that hBN growth by reacting boron in a Ni-Cr-B flux was viable and can produce isotopically enriched hBN crystals. hBN was formed by two mechanisms, nucleated growth and VLS interface growth. Nucleated growth will likely continue to be the primary mechanism of interest, due to the larger crystal dimensions, however, VLS-produced hBN whiskers were of an order of magnitude larger than that of previous studies; therefore if diameter and order of these whiskers can be increased, VLS-based growth may become viable.

Raman spectroscopy was coupled with SIMS data to develop a calibration curve to evaluate the boron isotope concentration of the crystals. Both Raman shift peak position and FWHM changed significantly with the ^{10}B fraction. These results were consisted with predictions for behavior of enriched crystals made by Lindsay *et al* [120]. Notably, narrowing of Raman shift peaks was consistent with predicted decrease in isotope-phonon scattering, important for many transport properties in hBN such as thermal conductivity.

Future work can leverage the growth and analytical techniques enumerated here to produce crystals of sufficient size to fabricate neutron detectors and too test how enrichment of hBN improves neutron capture. hBN enriched in ^{10}B and ^{11}B should be investigated for graphene heterostructure devices, to investigate if reduced isotope-phonon scattering affects the charge carrier mobility of these devices. Finally, isotopic effects, such as phonon-polariton propagation, thermal conductivity and on other physical characteristics of hBN, should be studied to identify any advantages of isotopic enrichment for hBN devices.

Chapter 7 - Defect Selective Etching

This chapter discusses an etching study performed on the hBN crystals grown by the Ni-Cr flux method (discussed in Chp 3&4), using a molten hydroxide salt etchant. The etching process and resulting etch pits are described, as well as the effect of etching temperature on etch pit size and type using optical microscopy, SEM and AFM analysis. Using this data, activation energy for etch pit formation was estimated using the Arrhenius equation. Propagation of the threading dislocations (which produce these etch pits) through the hBN crystal bulk was investigation using cross-sectional TEM imaging.

7.1 Motivation

New applications for hBN have been envisioned, which make use of its structural, optical and electronic properties (discussed in Chp 1). Realizing these applications requires hBN of high structural perfection, as defects such as dislocations create charge traps, scattering centers, and recombination sites that degrade its optical and charge transport properties, such as charge carrier mobility and minority carrier lifetime [31,107-109].

There have been numerous transmission electron microscopy and x-ray diffraction studies to identify defects in hBN [107,108]. Stacking disorder, the imperfect stacking of basal planes, is common, a consequence of the strong bonding within the basal plane layers and weak van der Waals bonding between layers. Delamination voids and misalignment of stacked planes (causing rhombohedral stacking disorder) can be produced in hBN as it is cooled during the growth process due to external strain from the differences in thermal expansion at the hBN-metal interface. Twinning also occurs, as hBN has a limited number of slip systems. A comparison of defects found in hBN to those in graphite are instructive, since both have similar structures planar structure formed by a hexagonal lattice of atoms strongly bonded together in sp2 configuration, with weak interlayer van der Waals [111].

Defect sensitive etching (DSE) is a good method for locating and quantifying the density of non-basal plane defects in hBN crystals. It has been widely employed in the study of defects in AlN, GaN, and SiC single crystals and epitaxial films [109,110]. Wide bandgap semiconductors are etched in molten potassium hydroxide, sodium hydroxide, or a eutectic mixture of the two. Mishima [112] reported one of the few prior studies on the defect sensitive etching of boron nitride, but on the cubic polymorph, i.e. cBN. He etched cBN crystals in molten NaOH at 520 °C to 530 °C for 2 minutes. Hexagonal, triangular, and long, slender pits formed on different crystal planes. This study sought to pursue a similar line of work: investigating the types of features that form on hBN single crystals etched by a molten KOH-NaOH mixture.

7.2 Methods

The bulk hBN crystals used for this etching study were grown using the Ni-Cr flux technique established by Hoffman *et al* [38]. Free-standing crystal flakes were carefully extracted from the metal surface using a release tape transfer technique, minimizing the amount of damage done to the soft hBN layers during the transfer process. After transfer, crystals were sonicated in organic solvents to remove surface impurities, and then heated in air at 500 °C to volatilize any residual carbon contaminants.

Etching was performed on the (0001) surface of hBN crystals using a molten KOH/NaOH mixture (50 wt% mixture) heated resistively by a canister-style furnace (Figure 3.15). The etching mixture was loaded into a vitreous carbon crucible and placed on an alumina pedestal centered in the furnace. The crucible was heated to the desired temperature before the addition of the hBN crystal flake (maintaining the temperature for 5 minutes before etching).

Etching was performed from 425 °C to 525 °C, etching each time for one minute. Immediately after etching, the flakes were quenched in water to stop the etching reaction and dissolve the hydroxide etchant on the surface of the flake. Etched flakes were then soaked in a 10 vol% acetic acid solution overnight to neutralize and remove any residual etchant.

Following the etching and cleaning of these hBN flakes, the resulting etch pits were identified using Nomarski-interference contrast optical microscopy (at 1000x magnification). High resolution images of the etch pits were collected using the SEM FEI Versa3D system at the University of Kansas. Flakes were prepared for SEM imaging by mounting onto SEM stubs and coating a thin metallic layer (10 nm Au) to prevent charging. Using SEM, the morphology, areal density and size distribution of these pits were analyzed across the etching temperature range investigated by this study (425-525°C). The surface topography of the etch pits and the effect of etching temperature on the width and depth of the pits was investigated by atomic force microscopy (AFM) using an Innova AFM system in contact-mode with MSCT cantilevers. Height profiles for different etch pit types were measured for samples etched at 450°C to determine pit depth and topography.

Propagation of threading dislocation types in bulk hBN crystals was investigated by cross-sectional TEM. High-resolution TEM was performed on hBN flakes to identify threading dislocations propagating through the crystal bulk and determine their type (screw, edge or mixed), as done previously for graphite [125-127] and other III-V materials, such as GaN [128]. Sample cross-sections were prepared using focused ion beam (FIB) milling to prepare a thin specimen sliced in the [*0001*] direction (perpendicular to the basal plane). Two diffraction contrast imaging conditions for isolating screw and edge type dislocations, were utilized for dislocation differentiation. Future work aimed to correlated these threading dislocations with etch pit type (screw, edge or mixed); however that work was not able to be complete by the time of writing.

7.3 Results and Discussion

The hBN flakes were etched across five temperatures from 425°C - 525°C, at intervals of 25°C. Three types of hexagonal etch pits were formed on the hBN (0001) surface: flat-bottom pits, pointed-bottom pits and mixed-type pits (which form due to overlap of these first two types). These pits were produced due to imperfections in the crystal lattice resulting from the propagation of threading dislocations through the crystal bulk to the surface. Similar pits types have been identified in GaN etching studies, which correlated with the presence of screw, edge and mixed-type threading dislocations [129].

These etch pits were distributed across the entirety of the flake's surface, with higher concentrations of pits near grain boundaries and line defects. Etch pit size increased with the etching temperature based on optical microscopy and SEM analysis (Figure 7.1 and Figure 7.2, respectfully). Additionally, etch pit type transitioned from non-overlapping flat-bottom and pointed-bottom type pits at etch temperatures of 425°C and 450°C, to an increasing population of overlapping mixed-type pits with increasing etch temperature. At an etching temperature of 525°C, practically all etch pits were mixed-type.

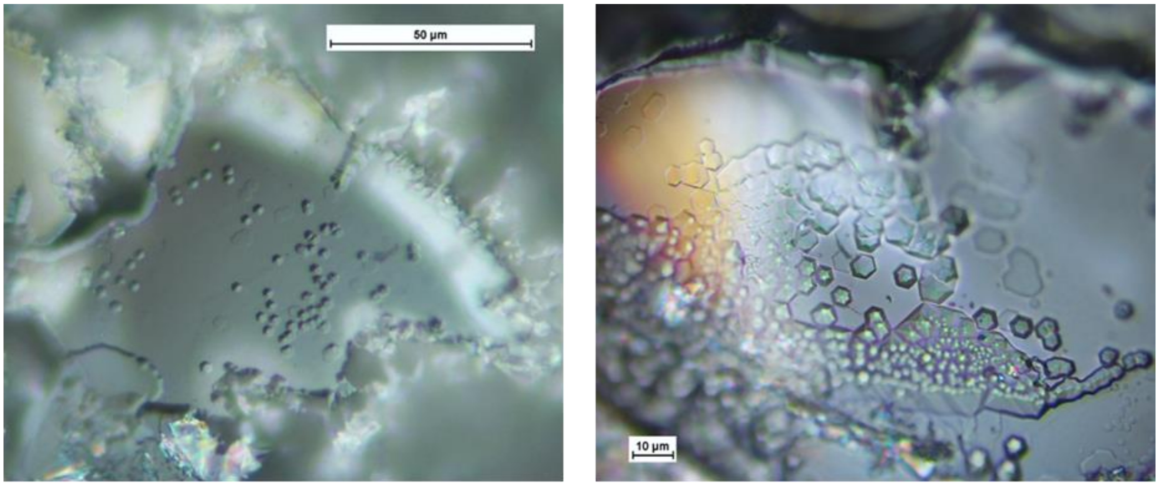

(a) (b)

Figure 7.1: Nomarski interference-contrast optical micrograph of etched hBN flakes taken at 1000x magnification. For the flake etched at 450°C for one minute (a), non-overlapping pointed-bottom and flat-bottom hexagonal etch pits formed on the flake surface. For the flake etched at 525°C for one minute (b), both flat and pointed-bottom pits formed on the flake surface with heavy overlapping.

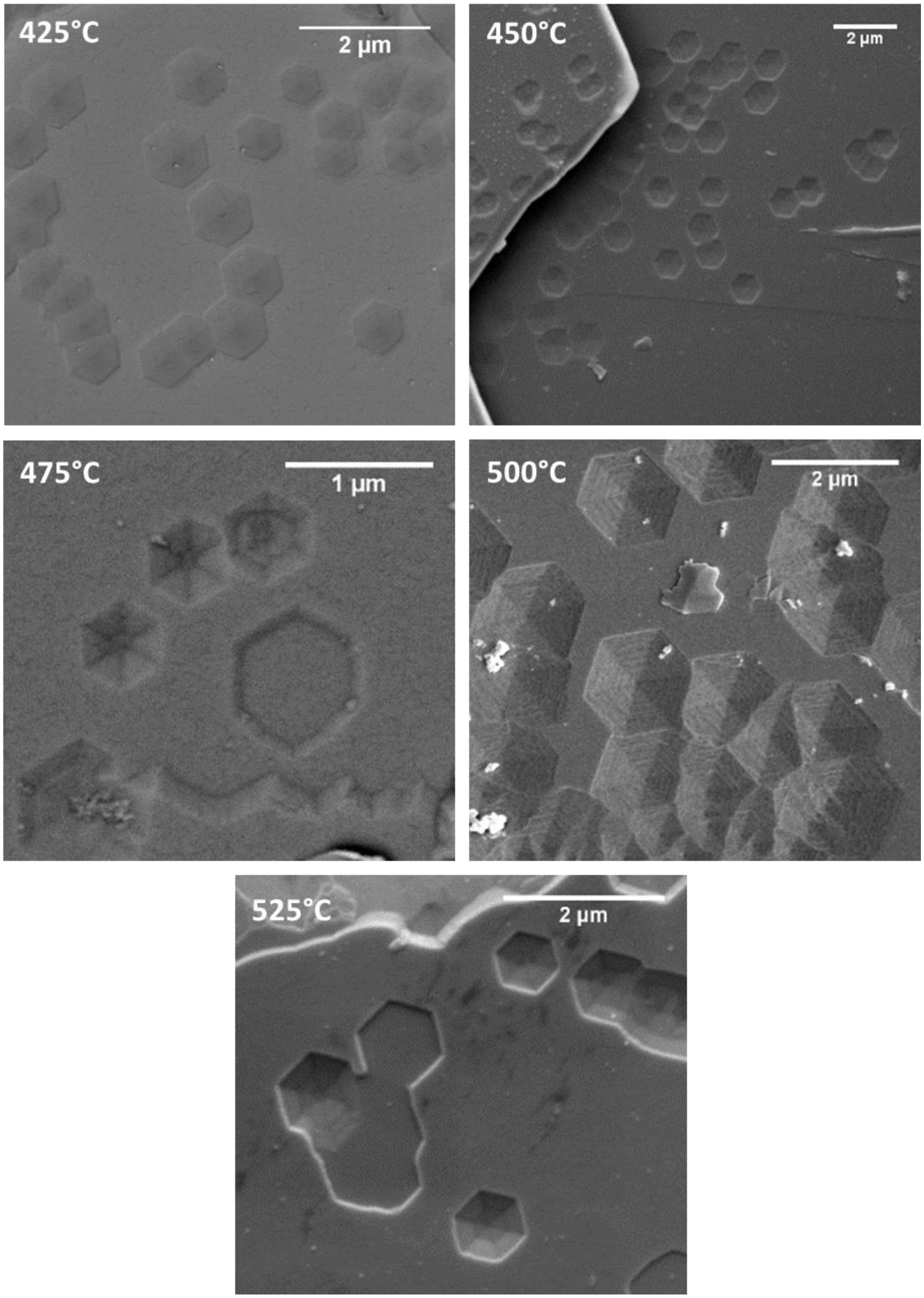

Figure 7.2: SEM Images showing pit shape and distribution on the flakes across all five etching temperatures (425°C to 525°C), showing transition from largely non-overlapping pointed and flat-bottom etch pits, transitioning to fully-overlapping mixed-type pits.

One major goal of this study was to obtain a figure of merit of hBN crystal quality, with which to compare the quality of crystals from run to run and growth method to growth method. Most commonly, the figure used for this is the areal etch pit density. To determine this, etch conditions must be controlled (with respect to etching temperature and time) to forming etch pits which are large enough to easily be counted without overlap. In this study, etching at 450°C for one minute best produced these conditions (Figure 7.2). An estimate of the etch pit density was made for the sample by counting the total number of etch pits in the image and normalizing the area of the image. For the flakes investigated in this study (etched at 450°C/1min), etch pit density was estimated at 5×10^{7} cm^{-2}. For comparison, this was still one or two orders of magnitude higher than that reported for an epitaxial $Al_{0.7}Ga_{0.3}N$ epitaxial film [130].

Based on the size of etch pit formed at each etching temperature, activation energy for this etching process was estimated using a basic Arrhenius equation of the form

$$k = Ae^{\left[{}^{-E_a}/_{RT}\right]} \qquad \textit{Equation 13}$$

with k corresponding with etch rate (in μm/min), A with frequency factor (in μm/min),, E_a as the activation energy (in kJ/mol), T as temperature (in Kelvin) and R as the gas constant [131]. The etch rate was assumed to be proportional to the etch pit width. By substituting etch pit width (W) in for etch rate and taking the natural log of the Arrhenius equation, the linearized form of the equation becomes

$$ln[W] = {}^{-E_a}/_{RT} + C \qquad \textit{Equation 14}$$

where C is an arbitrary constant. Average etch pit width was estimated at each temperature through analysis of the width of measured etch pits collected via SEM imaging of flakes etched at each temperature. The activation energy was estimated by plotting the natural logarithm of the etch pit width against inverse temperature (in K^{-1}), and fitting a line by least squares (Figure 7.3). From this, activation energy was estimated as 60 kJ/mol, which was within an order of magnitude of other III-V materials and typical of a kinetically-controlled reaction [109,110,128].

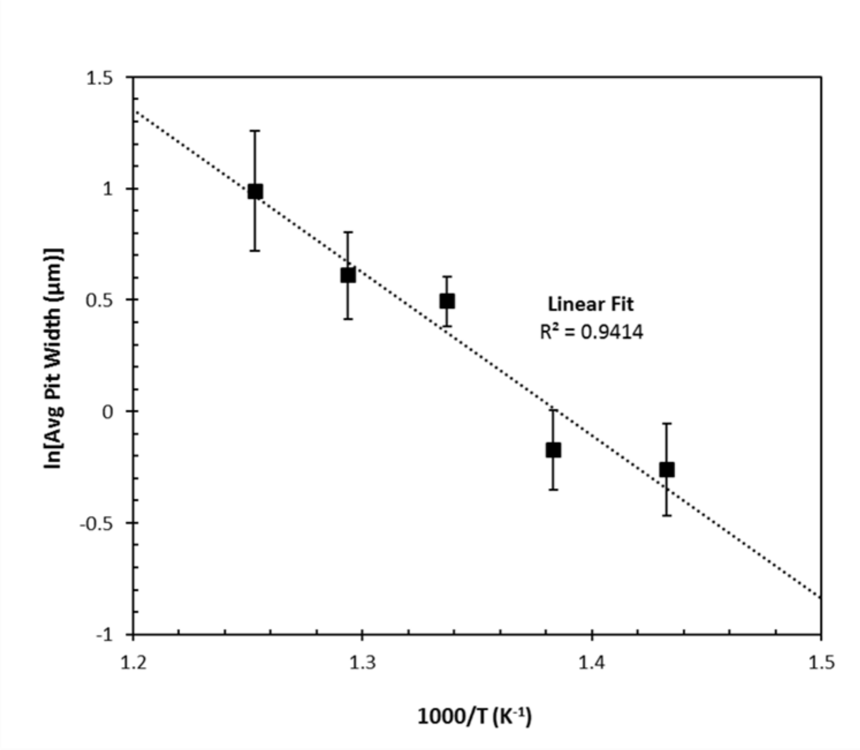

Figure 7.3: Plot of the natural logarithm of the average etch pit width against inverse temperature. The dashed line shows the linear fit for the Arrhenius relationship, with the slope proportional to the etching activation energy. Estimations based on this fit predict an activation energy of approximately 60 kJ/mol.

AFM analysis was performed for samples etched at 450°C and revealed three distinct etch pit surface height profiles (Figure 7.4). The flat-bottom pits had steeply sloping sides and long, flat bottoms. Their height profile quickly dropped and then leveled for most of the pit width, with largely symmetrical shape, with average length and depth of 1.5 μm and of 25nm, respectively. The pointed-bottom pits had approximately 45° sloping sides which formed inverse hexagonal pyramids with pointed bottoms. Their height profile showed linear symmetric sloping walls, with width and depth of approximately 1.5µm and 95 nm, respectively. Finally the mixed-type pits displayed a combination of features from the other two pits and showed the most irregularly shaped depth profile. This profile consisted of asymmetrically sloped pit walls near the outer portion of the wall similar to the pointed-bottom pits, but gently sloped surfaces near the center more like flat-bottom pits. These pits also tended to be wider and much deeper than the other two pit types with a width up to 2.5µm and depth up to 500 nm. To allow direct comparison of the dimensions of these etch pit types, width-to-depth ratio was calculated based on these average width and depth values (Table 7.1).

Table 7.1: Average pit width, depth and width-to-depth ratio for samples etched at 450C and analyzed by AFM surface height profile

Etch Pit Type	Pit Width (um)	Pit Depth (nm)	Width-to-Depth Ratio
Flat-Bottom	1.5	25	60:1
Pointed-Bottom	1.5	95	16:1
Mixed Type	2.5	500	5:1

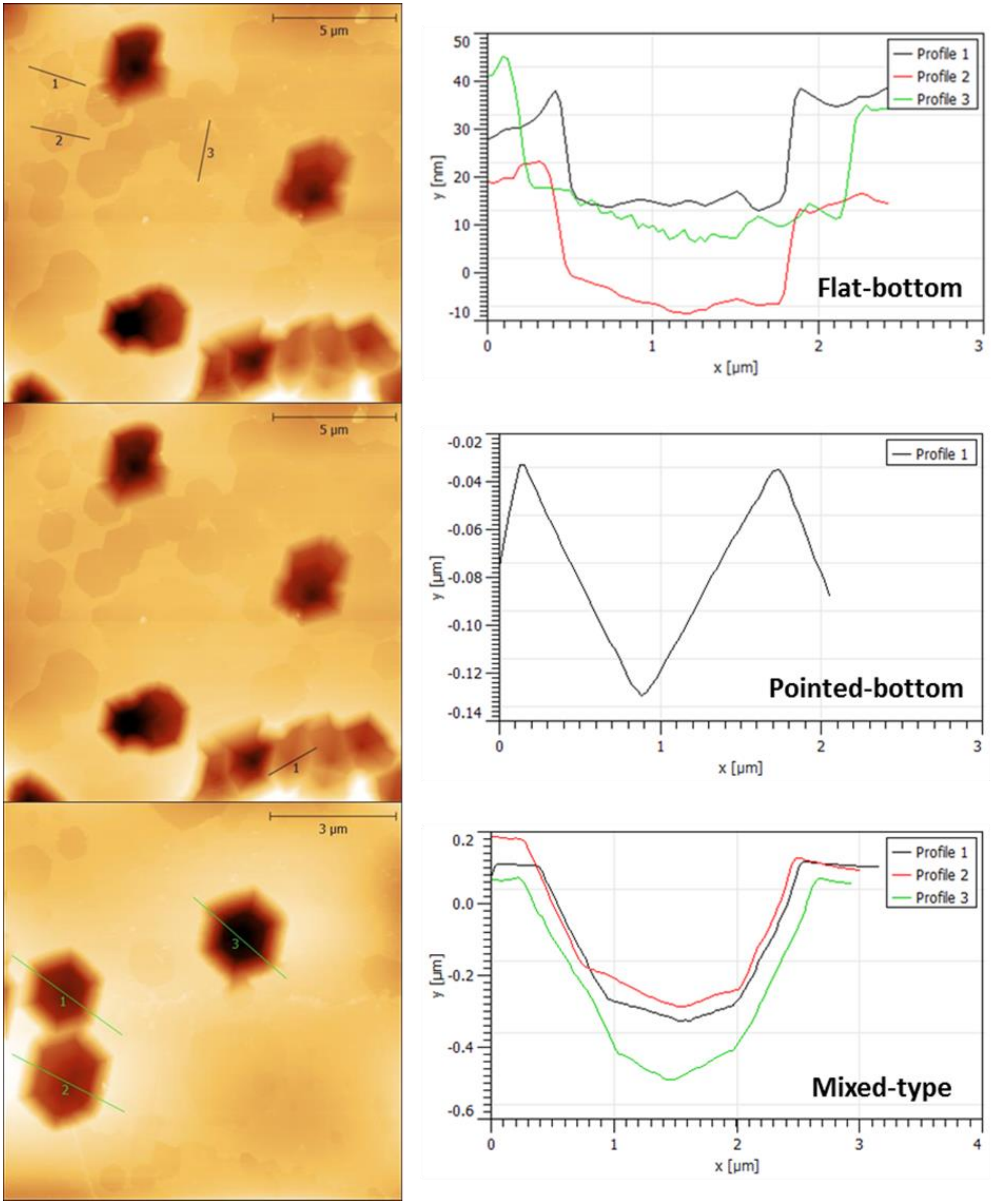

Figure 7.4: AFM images and associated height profiles (from top to bottom) of flat-bottom, pointed bottom and mixed-type etch pits on hBN flakes etched at 450°C for one minute in KOH/NaOH mixture.

The directionality of the Burgers vectors ($\vec{b}$) of different threading dislocations was determined by TEM using two-beam diffraction contrast microscopy. This was achieved by analyzing the sample under multiple diffraction vectors ($\vec{g}$) to evaluate the criteria required for the dislocations to provide no contrast, defined as [125]

$$\vec{b} \cdot \vec{g} = 0, \qquad \textit{Equation 15}$$

meaning that dislocations should disappear (have zero contrast) when its Burgers vector was parallel in diffraction vector. Based on the results in graphite, (which shares the same hexagonal structure and ABAB stacking as hBN), screw dislocations were observed to have Burgers vectors in the [*0001*] direction (perpendicular the basal plane), while edge dislocations had vectors in the [*hkl0*] directions (parallel to the basal plane) [125-127]. Mixed-type dislocations were a combination of these two conditions and had their vector intersect the basal plane in some [*hkli*] direction.

Using these two image conditions both mixed and screw type dislocations were identified in the prepared cross-section (Figure 7.5). Pure edge type dislocations were not seen. The majority of dislocations appear to be mixed-type. At this point, etch pit shapes have not been able to be traced directly to these different dislocation types, but that work is planned for a follow-up study.

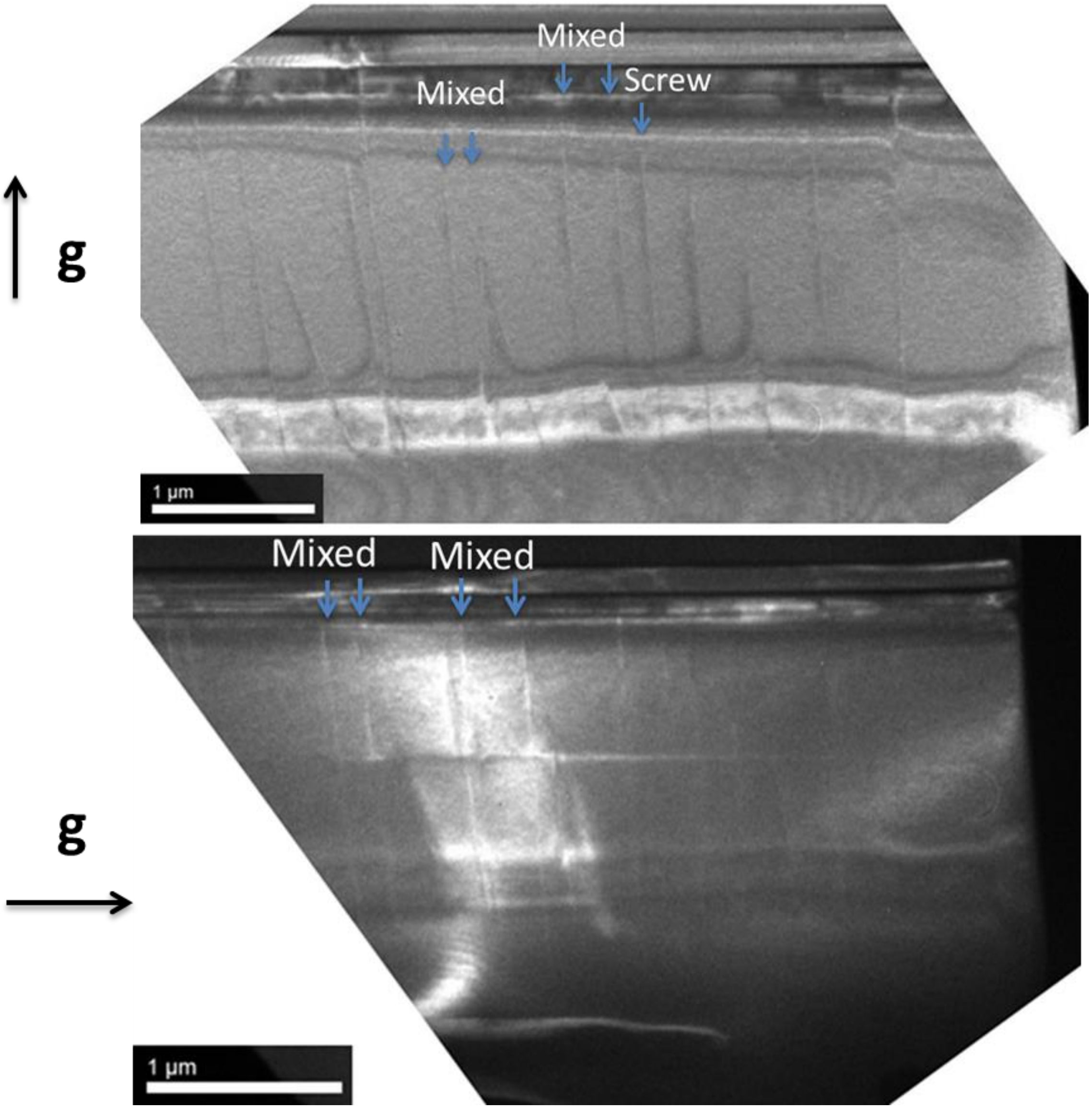

Figure 7.5: Diffraction-contrast TEM images of hBN flake cross sections taken with screw dislocation imaging conditions (top) and edge imaging conditions (bottom). Defects only observed in the top image are screw dislocations, while those only observed in the bottom are edge type. Dislocations present in both are mixed-type, as they have components of both screw and edge dislocations.

7.4 Relevance of This Work

A method for etching bulk hBN crystals using a molten NaOH/KOH mixture was demonstrated. Hexagonal etch pits formed that are similar to those formed with other III-V semiconductors, corresponding to the presence of edge, screw and mixed-type threading dislocations. The etch pit density was approximately 5×10^{7} $cm^{-2}$for hBN grown by current Ni-Cr flux , indicating that these crystals contain a high density of threading dislocations. The activation energy for the etching reaction was 60 kJ/mol, which is slightly lower than that of GaN (88 kJ/mol) [131] and may be due the structural differences in the hexagonal and wurtzite crystal lattices.

Threading dislocations within the hBN crystal bulk were able to be identified using diffraction contrast TEM. Identification of these different threading dislocations is important, as it will give better understanding as to how hBN crystals nucleate and grow from the metal flux. Both screw and mixed-type dislocations were present; however pure edge-type dislocations were not. An additional study will be performed to correlate these threading dislocations with the identified etch pit types revealed by the NaOH-KOH etch by performing diffraction-contrast TEM on etched cross-sections with identified pit shape.

Chapter 8 - hBN Characterization and Applications

This chapter discusses several characterization and application studies performed on the hBN crystals grown by the Ni-Cr (and enriched Ni-Cr-B) flux method. These were performed in collaboration with several researchers, primarily at Kansas State University and the U.S. Naval Research Laboratories (NRL), and included optical and impurity concentration measurements and investigated hBN neutron detectors and as a nanophotonic material. For each study, a brief description of the desired outcomes and methods utilized is discussed, followed by the findings of the study. These studies demonstrate how the improved optical properties and electrical properties of bulk hBN crystals enabled new applications.

8.1 Optical Characterization of Bulk hBN Grown by the Ni-Cr Flux Method

The optical properties of the bulk hBN crystals grown by the Ni-Cr flux method were investigated to measure the optical absorption coefficient as a function of energy and estimate energy bandgap magnitude and type (direct and indirect). An hBN flake was mechanically removed from the metal flux surface and positioned over a 200 μm open aperture in an Au coated surface [132]. Optical micrographs of the flake were collected by confocal microscopy using white light, as well as a 400 nm laser light, to identify individual domains (approximately 100-200 μm in width) within the flake (Figure 8.1).

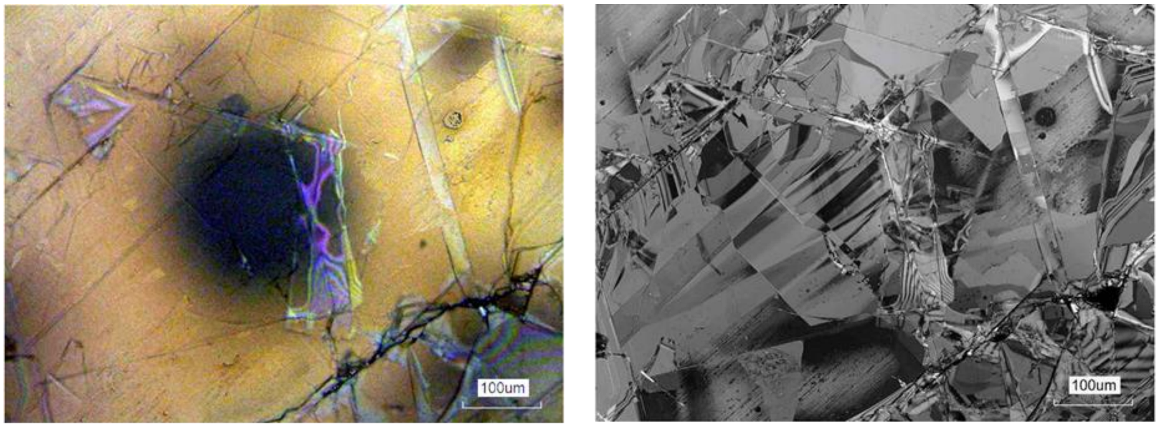

(a) (b)

Figure 8.1: Confocal microscope images of hBN flake mounted on a 200 μm aperture in an Au coated surface using (a) white light and (b) 400 nm laser light. Reproduced with permission from Edgar et al [132].

The optical transmission for the flake was measured from 1 to 6 eV using a Cary 5G spectrophotometer (Figure 8.2a). Band-edge absorption increased sharply at approximately 5.8 eV. The flake thickness was evaluated by fitting the transmission oscillations near 2eV as a Fabry-Perot cavity using 1.85 as the refractive index for hBN (Figure 8.2b) [133]. Based on this fit, the estimated thickness was 6.1 μm. Next, spectral absorption coefficient (α) was evaluated for the bulk hBN as a function of energy (Figure 8.3).

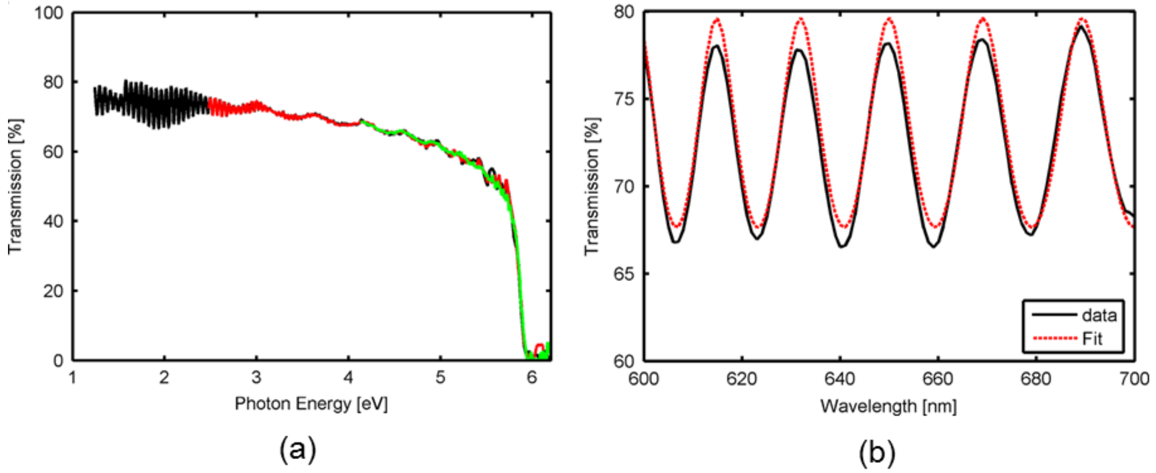

Figure 8.2:(a) Optical transmission spectrum of an hBN flake from 1 to 6 eV, along with (b) a fit to the Fabry-Perot oscillations providing an 6.1 µm estimated thickness. Reproduced with permission from Edgar et al [132].

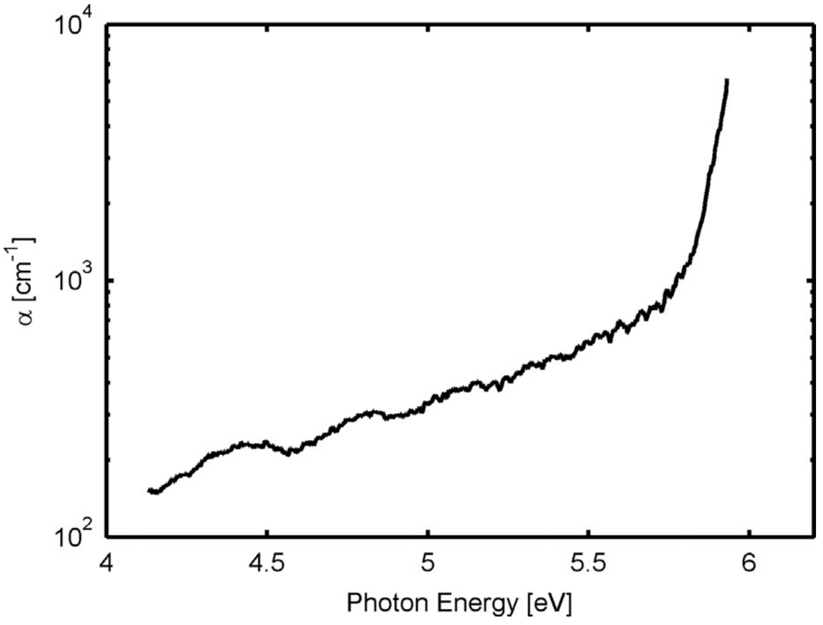

Figure 8.3: Absorption coefficient against photon energy for 6.1µm thick hBN flake. Reproduced with permission from Edgar et al [132].

–After the evaluation of absorption coefficient, energy bandgap (E_g) was evaluated based on the relationship

$$\alpha \propto \left(h\omega - E_g\right)^n \qquad \textit{Equation 16}$$

Where n is ½ and 2 for direct and indirect bandgap materials, respectively. Plotting α^2 and $\alpha^{1/2}$ against the spectral energy allowed the data to be fit to predict the energy bandgap and its type (Figure 8.4). The linear fit for this data indicated that the sample was more consistent with an indirect bandgap at 5.8 eV, compared to a direct bandgap of 5.88 eV. Admittedly, this was not a conclusive measurement, but this does fall in line with the studies by Cassabois [77] and Gao [134] that hBN is an indirect semiconductor. However, there has also been theoretical modeling by Liu *et al* [135] and experimental measurements by Watanabe *et al* [71] that indicate direct bandgap behavior for hBN. Further study is necessary to resolve whether these predictions are in conflict, or if they describe two conditions possible for hBN due to variations in stacking sequence.

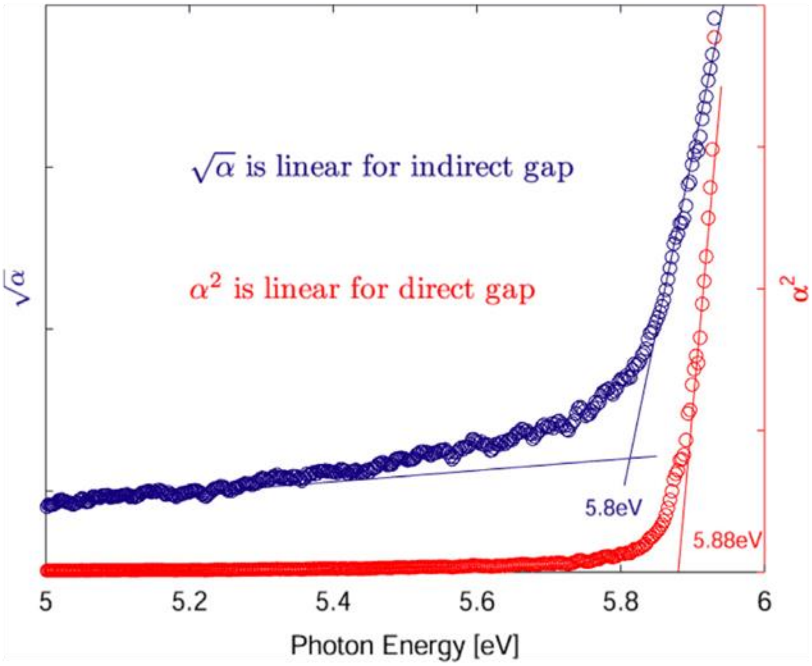

Figure 8.4: Linear fit to spectral data assuming proportionality for α^2 and $\alpha^{1/2}$ to estimate the type of bandgap (direct or indirect) for the hBN flake. Reproduced with permission from Edgar et al [132].

8.2 Major Impurity Concentrations in Bulk hBN Grown by the Ni-Cr Flux Method

To quantify the of major impurity concentrations within hBN grown by the Ni-Cr flux process (using standard purity Ni and Cr sources and N_2 gas flow only), hBN bulk crystals were characterized via secondary-ion mass spectrometry (SIMS) following ion implantation and standardization using artificially-occurring isotopes of carbon, oxygen and silicon. ^{13}C, ^{18}O and ^{29}S (artificially-occurring isotopes) were implanted into the samples by Leonard Kroko, Inc., with the specified energies and doses listed in Table 8.1.

Table 8.1: Details of ions implanted into hBN crystal for impurity concentration analysis

Implanted Ion	**Ion Energy (keV)**	**Implanted Dose (ions/cm²)**
^{13}C	190	1.2×10^{14}
^{18}O	110	5.0×10^{13}
^{29}Si	190	5.0×10^{14}

These isotopes were implanted, as they do not occur naturally but were expected to sputter by SIMS at similar rates compared to the naturally-occurring isotopes of carbon, oxygen and silicon. To obtain quantitative measurements for the impurities, the SIMS measurements were calibrated based on the modeled depth profiles (concentration as a function of depth) of these three artificial isotopes implanted into hBN under their respective conditions (ion energy and dose). The implants were modeled using the SRIM software package [136], which predicted the ion concentration as a function of depth for implantation into hBN at the specified energies and doses.(Figure 8.5). Maximum concentrations for these three isotopes ranged from 10^{19} to 10^{18} ions/cm^3 at depth between 2000Å (0.2 μm) and 5000Å (0.5 μm). These predicted depths profiled were then coupled with the SIMS measurements (performed by Evans Analytical Group) to serve as standards on these samples.

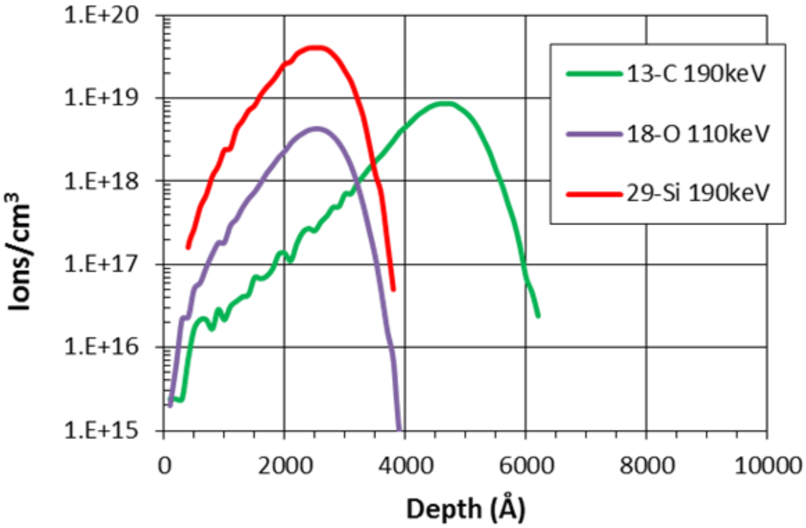

Figure 8.5: Implanted-ion depth profiles predicted using implantation energies and fluxes and TRIM

SIMS analysis was then performed to estimate impurity concentrations of ^{12}C, ^{16}O and ^{30}Si (the majority naturally-occurring isotope of each element) present in these samples (Figure 8.6). Carbon and oxygen were the most significant impurities, with bulk concentrations of approximately 2×10^{20} and 1×10^{19} atoms/cm^3, respectively. The silicon impurity concentration was found to be much lower (10^{17} atoms/cm^3).

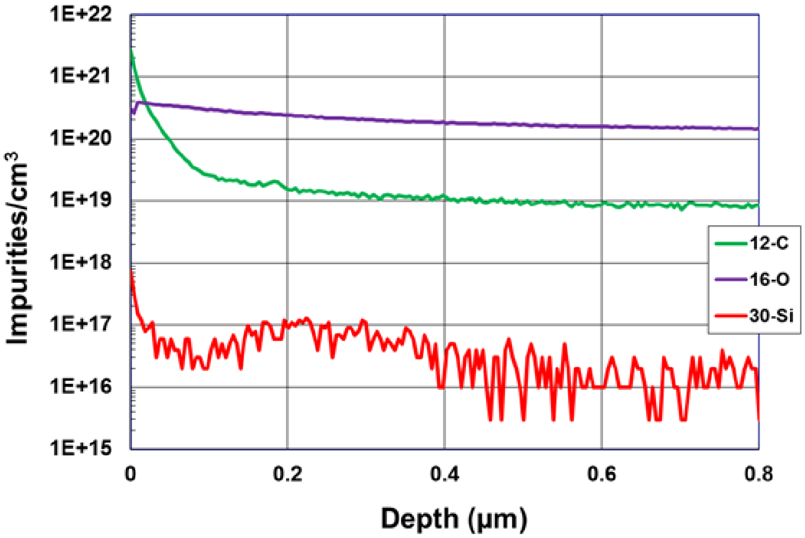

Figure 8.6: SIMS data for hBN crystals grown with N_2 gas only, standardized using ion-implanted samples

Possible sources of these impurities included the Ni and Cr powders in the flux, the HPBN boat, and the N_2 gas. The carbon and oxygen impurities present in these source materials, both in ppm and as an order-of-magnitude estimate of atomic concentration (assuming approximately 10^{23} atoms/cm^3 for solids, 10^{18} atoms/cm^3 for gases) is provided in Table 8.2. Based on this, oxygen impurities likely migrated from the Ni powder and HPBN boat, while carbon impurities may have come from the boat, as well as the Ni and Cr sources. One additional source of impurities may have also been air which leaked into the N_2 gas line or furnace tube or back-diffused through the system exhaust. However, leaks were minimized during operation and back-diffusion was unlikely at the N_2 flowrates used.

Table 8.2: Carbon and oxygen impurity concentrations in source materials for hBN growth, both in ppm and as an order-of-magnitude estimate of atomic concentration

Source Material	**Carbon Concentration (ppm)**	**Carbon Concentration (atoms/cm^3)**	**Oxygen Concentration (ppm)**	**Oxygen Concentration (atoms/cm^3)**
Nickel powder	120	10^{21}	3200	10^{22}
Chromium powder	180	10^{21}	>10	10^{20}
HPBN Boat	320	10^{21}	3000	10^{22}
N_2 gas	<1	10^{14}	<2	10^{14}

This study showed that carbon and oxygen impurities are the main concern for improving the purity of the hBN crystals grown by the Ni-Cr flux method. Ideally, these concentrations should be decreased 1000x to obtain similar concentrations to those in GaN and AlGaN devices ($< 10^{19}$ atoms/cm^3) and obtain intrinsic electrical and optical behavior [137]. These impurities may be reduced by the implementation of forming gas and the use of high-purity Ni and Cr to eliminate carbon and oxygen impurities from doping hBN crystal during the growth process.

8.3 hBN Neutron Detector Testing

One of the main goals of hBN bulk growth for this project was the production of flakes for neutron detection (discussed in Section 1.3.1). A simple hBN neutron detector was fabricated and tested (through collaboration with Tyrel George and Jeffrey Geuther) using the hBN crystal flakes grown by the Ni-Cr flux process and transferred onto a perforated board for the deposition of contacts. The hBN flake was approximately 2.5mm in width and 15µm in thickness, but contained multiple domains and some cracking. Ti/Au top and bottom contacts were deposited on the opposing basal planes of the flake using e-beam deposition, allowing for biasing of the flake in the c-direction (Figure 8.7).

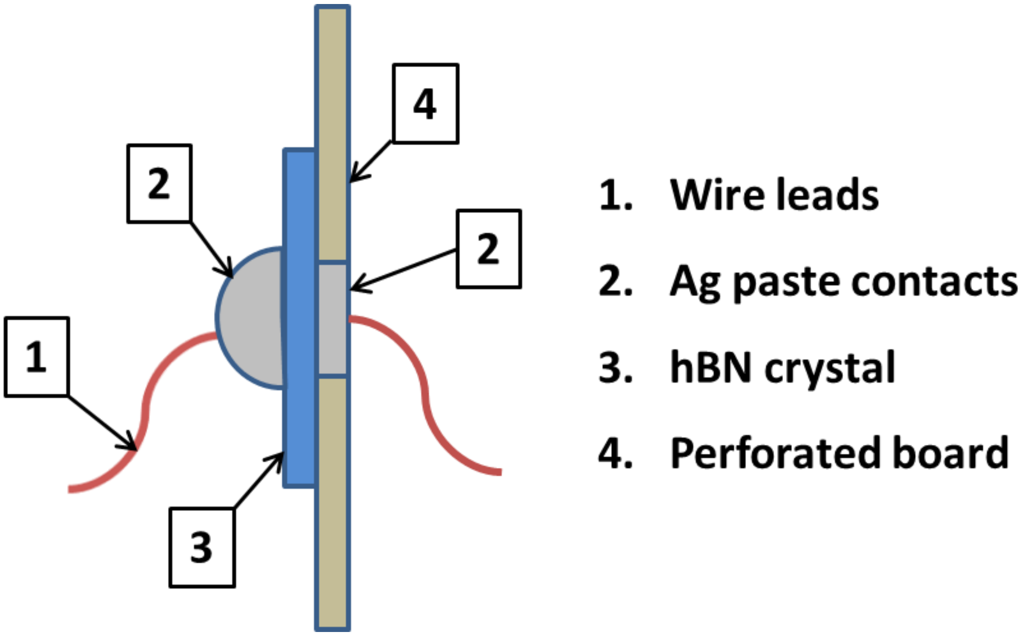

Figure 8.7: Schematic diagram of the simple hBN neutron detector with top and bottom contact geometry (biased in the c-direction) fabricated and tested by Tyrel George. The hBN flake was transferred onto a perforated board to allow for patterning with top and bottom Ti/Au metal contacts by e-beam deposition. Contacts were bonded to wire leads connecting to the pre-amplifier unit using Ag paste.

This device was tested under the diffracted neutron beam at the Kansas State Ward Nuclear Reactor facility. It was connected to an Ortec 142A pre-amplifier unit and biased at +500V during testing. The detector output was processed by multi-channel analyzer (MCA), which recorded counts into energy channels. The device was tested in the diffracted beam port for 20 minute counts under two conditions (Figure 8.8): (1) with the cadmium shutter closed, which blocked all neutrons from the beam and allowed gamma rays only to reach the detector and (2) with the Cd shutter open, allowing both thermal neutrons and gamma rays to reach the detector.

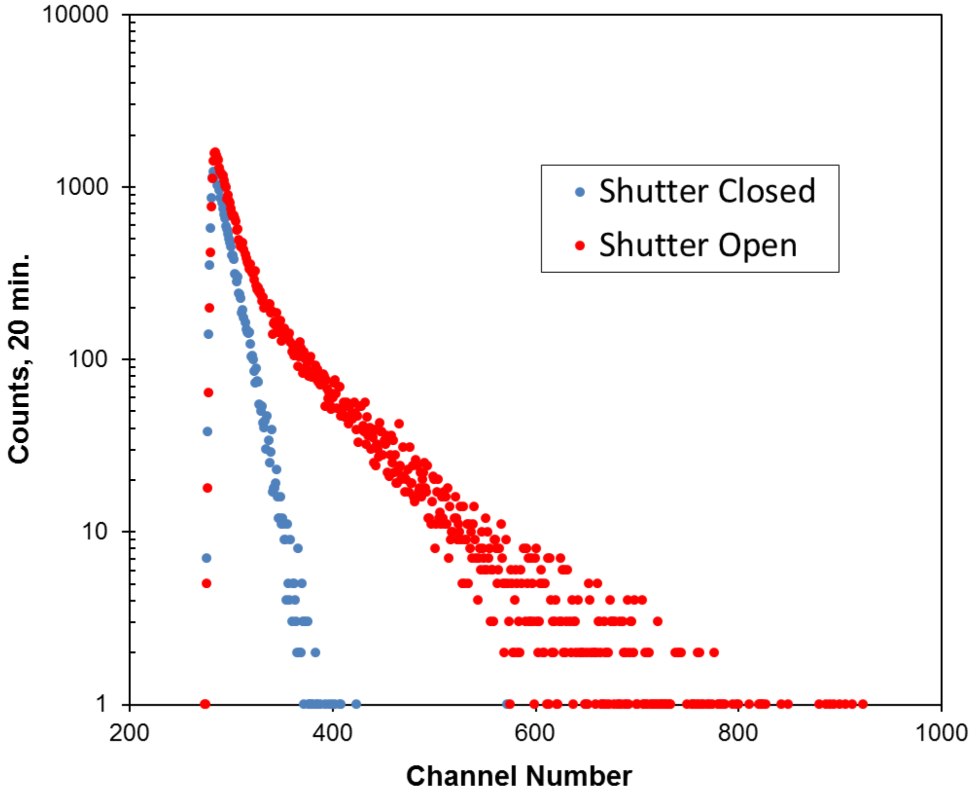

Figure 8.8:20 minute count for hBN neutron detector in the neutron diffraction beam port with the Cd shutter closed (gamma-rays only) and open (gammas and neutrons) at the KSU Ward Reactor (collected by Tyrel George). Event energies reported as channel numbers instead of absolute energies, as the ^{7}Li+α characteristic energy peaks were not able to be resolved for energy calibration.

These measurements showed a definite difference between these two count spectra, with elevated counts at higher energy channels for the shutter-open measurement. It was clear that the detector was able to discriminate between gamma rays and neutrons. Unfortunately, the device resolution was not sufficient to produce the full energy peaks characteristic of the ^{10}B neutron capture reaction [43,48-49]. Due to this, energy channels could not be calibrated to these peak energies.

The device was tested in two more experiments to confirm that it was operating correctly and actually responding to neutrons in the beam. The first test compared the performance of the device under the neutron beam (Cd shutter open) both in air and under vacuum (Figure 8.9a), to demonstrate that the counts measured were not caused due to air ionization. This measurement confirmed that the device performed identically both in air and under vacuum, proving that the device was measuring current collected within the crystal, and thus from nuclear interactions. The second tested compared the device's performance under background conditions and in a 700 mR/hr gamma ray beam (Figure 8.9b). These measurements were nearly identical, showing that the device had minimal gamma response, a highly desired quantity for neutron detectors.

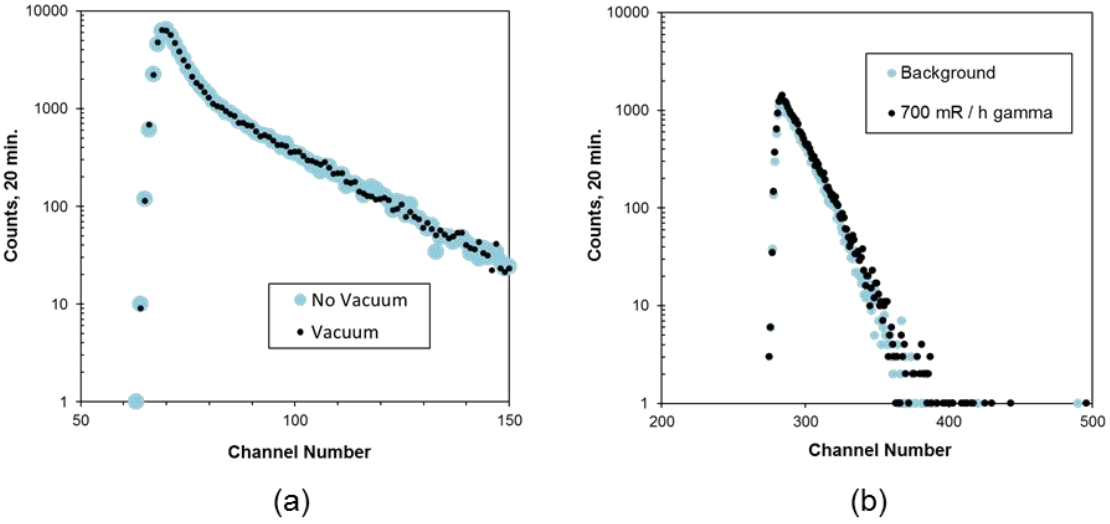

Figure 8.9: (a) 20 minute count comparing the neutron response of the device operating both in air and in vacuum. Lack of deviation between these measurements confirmed that the device was not causing ionization of air. (b) 20 minute count for hBN detector both in background and under gamma ray beam shows that the device had minimal response to gamma rays due to the low atomic number of B and N.

The final test investigated how the device would respond to the modulation of the reactor (Figure 8.10). The count rate for the device was measured in the diffraction beam during the reactor startup, and was able to track the increase in neutron flux in the system, as well as identify the reactor temperature feedback phenomenon during the start-up process. After bringing the reactor to full power, the Cd shutter was cycled between the open and shut positions. The detector was able to differentiate between the shutter being open (50 cps) and closed (15 cps). Finally, the reactor was shut down and the detector response returned to baseline.

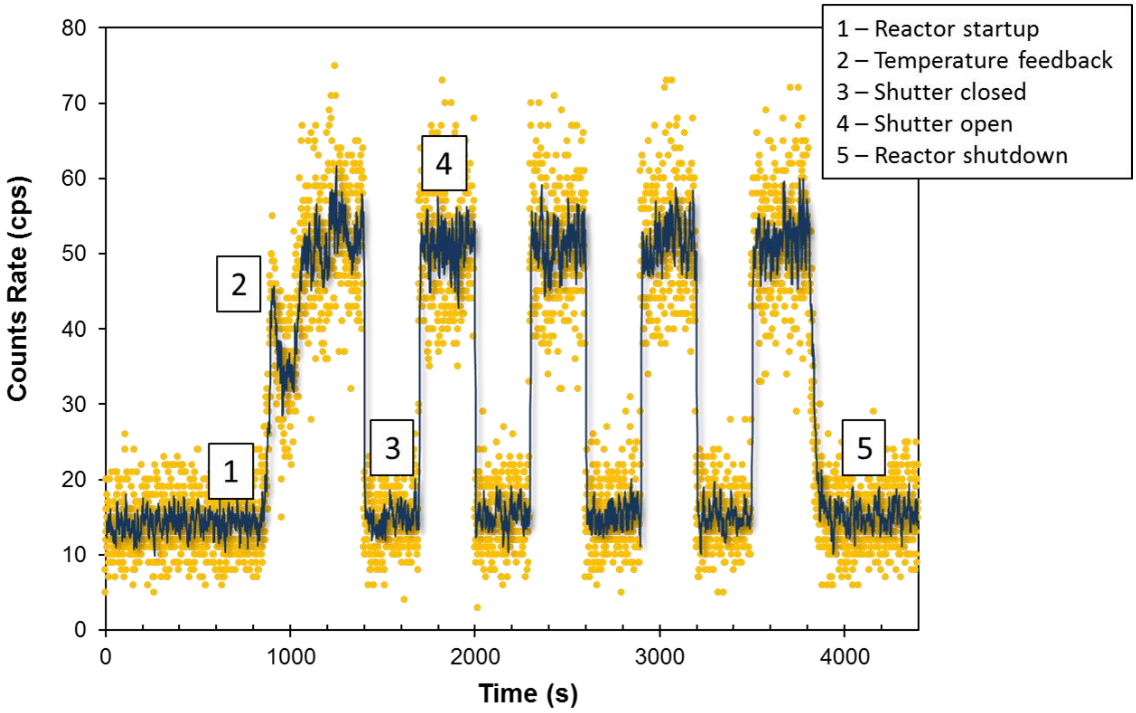

Figure 8.10: Counts per second(cps) vs time plotted for hBN neutron detector sampling Ward reactor neutron beam during furnace startup and Cd shutter cycling (collected by Tyrel George). Yellow dots represent raw data, while blue line represents 7-point rolling average. The detector clearly identified reactor startup (including temperature feedback response) and difference between shutter being closed (gamma rays only) and open (gammas and neutrons).

The performance of this hBN neutron detector demonstrated that an hBN flake grown by the Ni-Cr flux process could show a neutron response above noise while having high gamma ray discrimination. Unfortunately, this device does not fully deliver on the other requirement for a working neutron detector: being able resolve the neutron capture full energy peaks. Cause of this lack in performance can be speculated as the result of a few factors. First, the hBN flake used for this device was grown early in this project (2013) and had smaller domains and more cracking crystals grown after the process improvements discussed in Chapter 3 and 4. Flakes with larger domains may allow contacts to be deposited within a single grain, ensuring that there are no grain boundaries in the device to act as charge traps and recombination sites. As the device was biased in the c-direction, plane-slipping and other basal plane defects may have also degraded device performance. This behavior would explain why the full energy peaks were not resolved, as only small amounts of the ^{7}Li and α-particle energy may have been deposited in the active region. Use of alternative contact geometries, such as side-to-side (a-direction) contacts may improve device performance, by taking advantage of the improved transport properties in the a-direction (in-plane) as opposed to the c-direction (out-of-plane), but will require thicker crystals and sophisticated contact deposition techniques.

8.4 Bulk hBN as an Interference-less Infrared Absorber

Bulk hBN crystals were investigated due to their unique properties as a hyperbolic metamaterial to act as an interference-free perfect absorber (zero reflection) of light wavelengths in the infrared region (approx. 800 cm^{-1}) [132]. For most complete light absorption systems using metamaterial structures, this phenomenon is achieved by destructive light interference, requiring complex multi-pass geometries [139]. For this study, bulk hBN crystals greater than 100μm in thickness were analyzed while still on the Ni-Cr ingot surface and demonstrated perfect absorption of infrared light (around 800 cm^{-1}) in a simplified single-pass geometry.

This behavior was predicted theoretically for hBN and arises from the anisotropic nature of its crystal structure. This results in hyperbolic behavior, with different magnitudes for the in-plane and out-of-plane dielectric functions and permittivity tensor [79,140]. Reflectance spectra for p and s-polarized light were modeled in hBN as a function of incidence angles (θ_0) onto the crystals and light wavenumber. P-polarized light was predicted to have a complex spectrum highly dependent on incidence angles (Figure 8.11a). One dip in reflection occurred at 1650 cm^{-1} for normal incidence (0°), with this feature shifting to higher frequencies with increasing incidence angle. A second absorption dip was predicted near 800 cm^{-1} for incidence angles below 70°. This feature shifted to lower wavenumbers at 70°, then disappeared for 75°. However, the disappearance of this dip at high angle of incidence correlated with new absorption band at 1000 cm^{-1}. S-polarized light reflectance was predicted be independent of incidence angle; it was only dependent on the in-plane permittivity (Figure 8.11b). It showed a singular reflectance dip at 1700 cm^{-1}. To identify the conditions which produced complete absorption, the real and imaginary parts of cos$^2\theta_0$ were plotted as a function of wavenumber (Figure 8.11c). Two points (labeled A and B) were noted at 700 cm^{-1} and 960 cm^{-1}, respectively, where the imaginary part of cos$^2\theta_0$ disappears and the real part is positive and bounded by $0< \cos^2\theta_0<1$, producing a valid incidence angle. These points are conditions where light is predicted to refract in hBN without reflection, being absorbed completely.

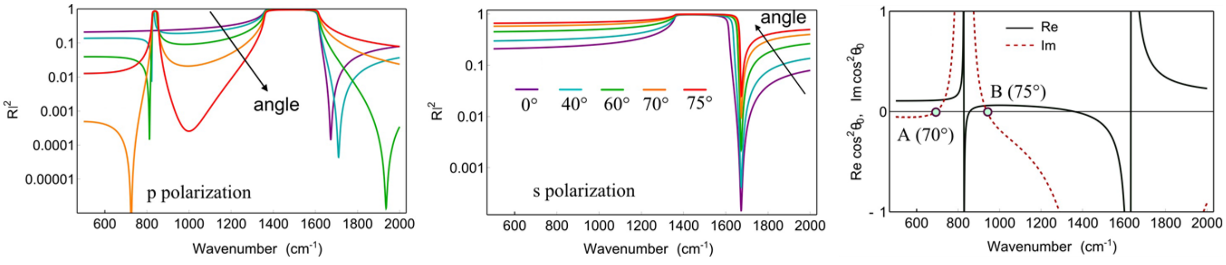

(a) (b) (c)

Figure 8.11: Reflection by a semi-infinite hBN crystal. (a,b) Calculated reflectance (R^2) spectra for p and s polarizations, respectively, for a series of different incidence angles. (c) The real and imaginary parts of squared cosine of the perfect absorption angle θ_0. At two points, denoted by A and B on the graph, $\cos^2\theta_0$ becomes real and positive, corresponding to a real-valued incidence angle. Reproduced with permissions from Baranov et al [132].

To confirm these theoretical models, reflectance spectra were measured for hBN crystals on top of a flat region of the Ni-Cr ingot. These crystal domains were 250-500 μm wide and 200 μm thick, as measured by optical microscopy and SEM analysis. P and s-polarized light reflectivity from Thermoscientific FTIR spectrometer was measured for incidence angles from 0° to 85°, collected in reference to a flat alumina mirror with spectra resolution of 2 cm^{-1}. Data was plotted with reflectivity (R^2) against incidence angle for both light polarizations and compared to calculated predictions (Figure 8.12 and Figure 8.13). These plots show that experimental data was in agreement with the model predictions. Points A and B for the p-polarized light corresponded to conditions for near-perfect absorption. Behavior of s-polarized light was nearly identical to the predicted model.

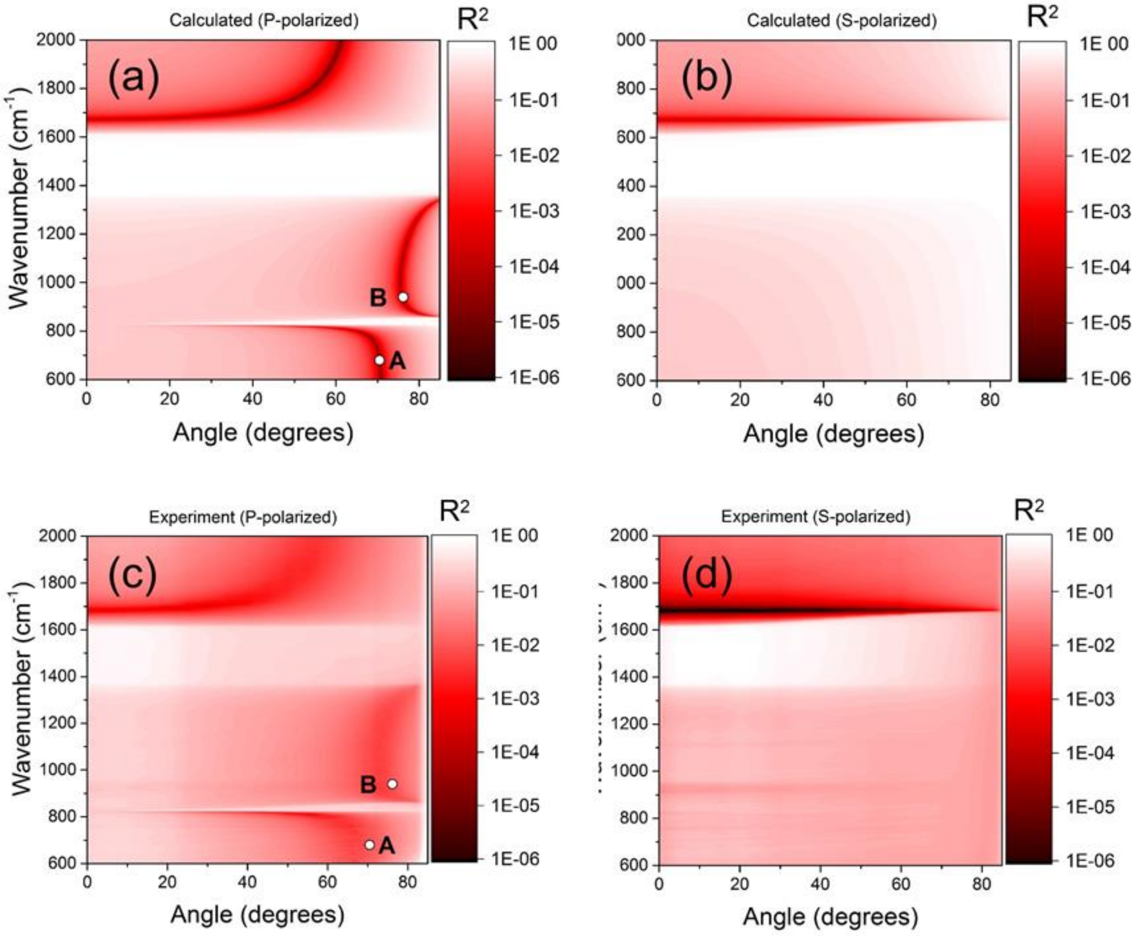

Figure 8.12: (a,b) The calculated reflectivity spectra of a 200 um thick hBN slab on a metal substrate for p and s polarization of incident light, respectively. (c,d) The corresponding measured spectra. The points A and B mark the position of perfect absorption points corresponding to those in Figure 2(c). Reproduced with permissions from Baranov et al [132].

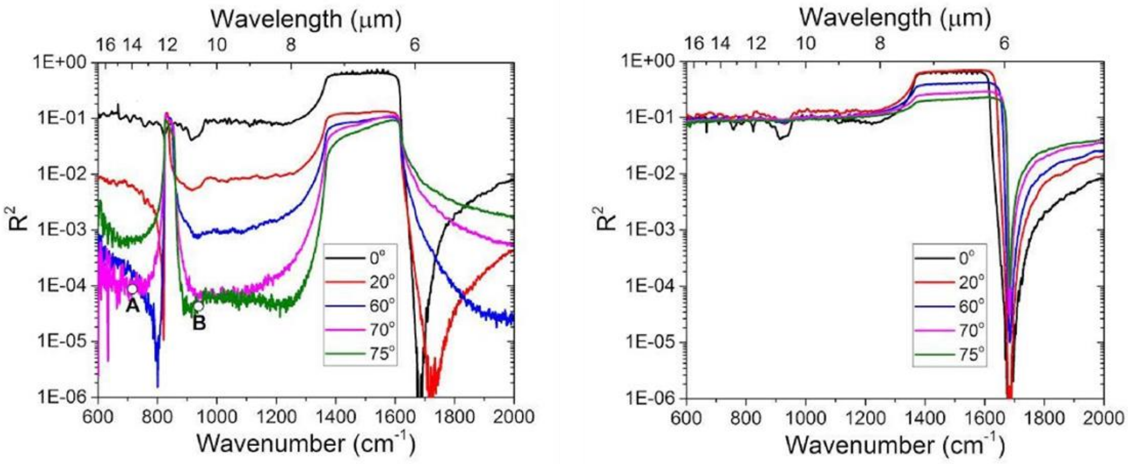

(a) (b)

Figure 8.13: Experimental reflectivity spectra for a series of incidence angles for (a) p and (b) s polarizations. The points A and B mark the position of perfect absorption points. Reproduced with permissions from Baranov et al [132].

This study demonstrated single-pass, interference-free absorption of light using highly anisotropic bulk hBN crystals. Regions of absorption were from 600-1300 cm^{-1} and at 1700 cm^{-1} (mid-infrared), dependent on incidence angle. This method does not depend on destructive interference of light, making it much simpler to implement. These results may lead to new interest in using anisotropic crystals for controlling electromagnetic emissions and may be important for the design of sensing and photovoltaic devices.

8.5 Enriched hBN for Improved Propagation Lengths of Phonon-Polariton Modes

One interesting nanophotonic property of hBN is its ability to produce and sustain hyperbolic phonon-polariton modes [83-84,141-143]. Applications utilizing these properties include hyper-lensing, which allows imaging below the sub-diffraction limit by acting as a negative (refractive) index material [144]. These phonon-polariton modes in hBN have been evaluated using scattering strong near-field optical microscopy (s-SNOM), capable of achieving nanometer spatial resolution and 0.2 cm^{-1} spectral resolution coupled with nano-FTIR spectroscopy [145,146].

One challenge for these nanophotonic applications in hBN has been the limited magnitude and propagation length of these phonon modes. This study (performed in collaboration with Dr. Basov of UCSD and Dr. Caldwell of NRL) investigated if the production and propagation of these modes could be improved by the use of hBN crystals highly enriched in ^{10}B or ^{11}B (grown by Ni-Cr-B flux) due to decreased phonon-isotope scattering [147]. To evaluate this, s-SNOM measurements were performed on hBN bulk crystals with three different boron enrichments: natural abundance (80% ^{11}B), 96% ^{10}B and 98% ^{11}B (Figure 8.14).

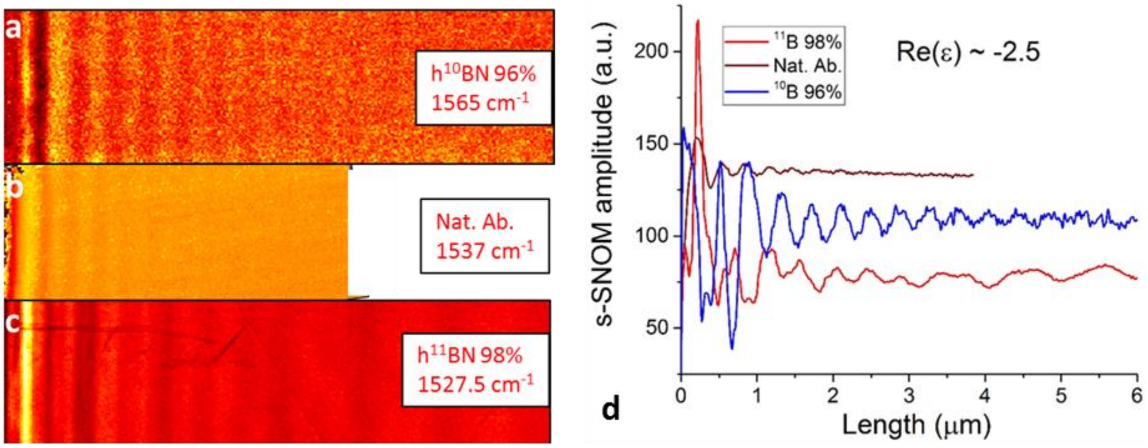

Figure 8.14: (a-c) Spatially-resolved s-SNOM measurements for 96% B-10 enriched hBN flake, natural abundance (80% B-11) hBN flake and 98% B-11 enriched hBN flake, respectively, showing the propagation of these phonon-polariton modes on the surface of these samples. (d) s-SNOM amplitude plotted against length (left-to right) for the three hBN flakes measured in (a-c).

Based on the measurements performed on the three hBN samples, it is clear that a major increase in both the magnitude and propagation length of these phonon modes occurred for the two enriched samples relative to the natural abundance samples. FTIR absorption also shifted up for higher ^{10}B enrichment and shifted lower for higher ^{11}B enrichment (the same trend as identified for Raman shift peak in Chp 5). These results were preliminary and further analysis of higher order polariton-phonon modes is in progress through the use of fast-Fourier transform (FFT). However, there is clear improvement of these phonon modes through the use of enriched (^{10}B or ^{11}B) hBN crystals, potentially opening up new applications for nanophotonic devices.

Chapter 9 - Conclusions and Recommendations

Bulk hBN crystal growth was demonstrated using the Ni-Cr flux process. Large (<5mm), water clear hBN crystal flakes were formed with little cracking and single-crystal domains exceeding 1mm in width and 200 μm in thickness. The hBN crystals were characterized using XRD and photoluminescence, indicating they were high purity and of single-crystal orientation. The process was adapted from the CM furnace system to the larger Mellen system and modified through the addition of an ingot formation cycle and the use of forming gas, which greatly improved the reliability of hBN crystal growth process, suppressed the formation of oxide films on the metal surface and reduced the residual impurity concentrations of the crystals.

The effect of growth parameters on crystal grain size and thickness was modeled using surface response methodology. A set of screening experiments identified the three most important parameters as dwell temperature, cooling rate and cooling temperature. The effects of these three parameters were then investigated using a full factorial design in a central composite design. RSM modeling was performed in R to develop response surfaces for crystal width and thickness. Crystal width had a strong correlation with dwell temperature, with width increasing linearly with dwell temperature. Grain width was predicted to exceed 2mm as dwell temperature was increased to 1700°C. Behavior of crystal thickness was more complex, with strong interactions between the three growth parameters.

Isotopically enriched (^{10}B and ^{11}B) hBN crystals were grown using a Ni-Cr-B flux process adapted from the standard Ni-Cr method. Enrichment of up to 98% ^{11}B and 96% ^{10}B was obtained. ^{10}B concentration was evaluated by SIMS for three samples (7%, 20% and 84%) and coupled with Raman spectroscopy data to allow for rapid and non-destructive means to estimate hBN enrichment. Additionally, Raman shift peak FWHM narrowed with increasing enrichment of either ^{10}B or ^{11}B, indicative of a decrease in phonon-isotope scattering, as predicted in theory. This indicated that enriched hBN flakes may have significantly improved phonon transport properties.

Defect selecting etching was performed on the hBN flakes using a molten KOH/NaOH eutectic mixture at 425-525°C. Three distinct etch pit morphologies were formed, producing an etch pit density of 5×10^7 cm^{-2}. Activation energy for etching was evaluated at approximately 60 kJ/mol using the Arrhenius relationship between etch pit size and etching temperature. Diffraction-contrast TEM imaging was used to identify screw and mixed-type threading dislocations propagating along the c-axis of the crystals.

Several studies were discussed which characterized the hBN flakes grown by the Ni-Cr flux process and utilized them for new applications. These included an optical study of the bulk hBN energy bandgap, a study of majority impurities in the crystals, as well as the fabrication of a simple hBN neutron detector and two nanophotonic studies of hBN. These works illustrate that the unique properties of single crystal hBN enable new applications in physics and engineering.

Based on these findings, a few recommendations can be made on how to further improve hBN growth by the Ni-Cr flux process. RSM modeling of process parameters showed that crystal width had strong dependence on dwell temperature. Higher dwell temperatures (>1500°C) should be investigated for hBN growth to enable reliable growth of hBN single domains >1mm in size. Increasing the hBN grain size is vital for fabricating hBN neutron detectors and performing electrical characterization studies, as a larger domain size will allow the deposition of metal contacts within a single domain. Methods to more efficiently and non-destructively separate the hBN crystals from the Ni-Cr flux should be investigated, ideally to remove crystals during growth to prevent crystal strain and cracking due to thermal and compressive stress. Additionally, means to enable seeded crystal growth of hBN should be pursued, although this may require a complete re-envisioning of the growth process. Means to further reduce residual impurity concentrations in the crystals, as well as control dopant levels, should be investigated. These include the use of forming gas during growth to prevent oxide formation, but may also require use of higher purity materials or materials pre-treatment to eliminate these impurities, particularly carbon and oxygen. These improvements should allow for continued improvement of hBN bulk crystal size and quality and enable further studies of hBN in neutron detectors, nanophotonics and optoelectric devices.

Chapter 10 - References

1. Kubota, Y.; Watanabe, K.; Tsuda, O.; Taniguchi, T. Hexagonal boron nitride single crystal growth at atmospheric pressure Using Ni-Cr solvent. *Chem. Mater.***2008**, *20*, 1661.
2. Haubner, R.; Wilhelm, M.; Weissenbacher, R.; Lux, B. Boron Nitrides - Properties, synthesis and applications. *High Perf Non-oxide Ceram II.* **2002**, *102*, 1-45.
3. Markel, E. J; Leaphart, M. E. In *Nitrides;* Kirk, R. E., Othmer, D. F., Grayson, M. and Eckroth, D., Eds.; Kirt-Othmer Encyclopedia of Chemical Technology; John Wiley & Sons: **1985**, *16*, 1-36.
4. Lipp, A.; Schwetz, K. A.; Hunold, K. Hexagonal boron nitride: Fabrication, properties and applications. *J Eur Ceram Soc.* **1989**, *38*, 1144.
5. Paine, R.T; Narula, C.K. Synthetic routes to boron nitride. *Chem. Rev*. **1990**, *90*, 73-91.
6. Edgar J.H. *Properties of Group III Nitrides*. London: INSPEC, Institution of Electrical Engineers, 1994.
7. Spriggs, G. E. In 13.5: *Properties of diamond and cubic boron nitride*. Beiss, P., Ruthardt, R. and Warlimont, H., Eds.; Landolt-Bornstein - Group VIII Advanced Materials and Technologies; Springer Materials: Vol. A. 91-112.-
8. Solozhenko, V. L.; Turkevich, V. Z.; Holzapfel, W. B. Refined Phase Diagram of Boron Nitride. *J. Phys. Chem*. B **1999**, *103*, 2903-2905.
9. Bundy, F. P.; Wentorf, R. H. Direct transformation of hexagonal boron nitride to denser forms. *The Journal of Chemical Physics* **1963**, *38*, 1144.
10. Corrigan, F. R.; Bundy, F. P. Direct transitions among the allotropic forms of boron nitride at high pressures and temperatures. *J. Chem. Phys*. **1975**, *63*, 3812-3820.
11. Moore, A.W. Characterization of pyrolytic boron nitride for semiconductor-materials processing. *J Cryst Growth*. **1990**, *106*, 6-15.
12. Pierson, H. O. Boron nitride composites by chemical vapor deposition. *J. Compos. Mater*. **1975**, *9*, 228-240.

13. Dean, C. R.; Young, A. F.; Meric, I.; Lee, C.; Wang, L.; Sorgenfrei, S.; Watanabe, K.; Taniguchi, T.; Kim, P.; Shepard, K. L.; Hone, J. Boron nitride substrates for high-quality graphene electronics. *Nat. Nano.* **2010**, *5*, 722-726.

14. Tanaka, T.; Itoh, A.; Yamashita, K.; Rokuta, E.; Oshima, C. Heteroepitaxial system of h-BN/monolayer graphene on Ni(111). *Surf. Rev. Lett.* **2003**, *4*, 697-703.

15. Yang, P.; Prater, J.; Liu, W.; Glass, J.; Davis, R. The formation of epitaxial hexagonal boron nitride on nickel substrates. *J. Electron. Mater.* **2005**, *34*, 1558-1564.

16. Müller, F.; Hüfner, S.; Sachdev, H. One-dimensional structure of boron nitride on chromium (110) - a study of the growth of boron nitride by chemical vapour deposition of borazine. *Surf. Sci.* **2008**, *602*, 3467-3476.

17. Orofeo, C. M.; Suzuki, S.; Kageshima, H.; Hibino, H. Growth and low-energy electron microscopy characterization of monolayer hexagonal boron nitride on epitaxial cobalt. *Nano Res.* **2013**, *6*, 335-347.

18. Roth, S.; Matsui, F.; Greber, T.; Ostenwalder, J. Chemical vapor deposition and characterization of aligned and incommensurate graphene/hexagonal boron nitride heterostack on Cu(111). *Nano Lett.* **2013**, *13*, 2668-2675.

19. Kim, K.K.; Hsu, A; Jia, X.; Kim, S.M.; Shi, Y.; Hofmann, M.; Nezich, D.; Rodrigueznieva, J.F.; Dresselhaus, M.; Palacios, T.; Kong, J. Synthesis of monolayer hexagonal boron nitride thin film by chemical vapor deposition, *Nano Lett.* **2012**, *12,* 161–163.

20. Moore, A. W.; Strong, S. Variations in the structure and morphology of pyrolitic boron nitride. *Ceram. Eng. Sci. Proc.* **1989**, *10*, 846-856.

21. Dreger, L. H.; Dadape, V. V.; Margrave, J. L. Sublimation and decomposition studies on boron nitride and aluminum nitride. *J. Phys. Chem* **1962**, *66*, 1556.

22. Pritula, I.; Sangwal, K. Fundamentals of Crystal Growth from Solutions, In *Handbook of Crystal Growth, 2nd ed.* Rudolph, P., Ed.; Elsevier, **2015**; 1185-1227.

23. Ishii, T.; Sato, T. Growth of single crystals of hexagonal boron nitride. *J. Cryst. Growth* **1983**, *61*, 689-690.

24. Yano, M.; Yap, Y. K.; Okamoto, M.; Onda, M.; Yoshimura, M.; Mori, Y.; Sasaki, T. Na: A new flux for growing hexagonal boron nitride crystals at low temperature. *Jpn. J. Appl. Phys.* **2000**, *39*, L300.

25. Hubáček, M.; Sato, T. The effect of copper on the crystallization of hexagonal boron nitride. *J. Mater. Sci.* **1997**, *32*, 3293.

26. Gu, Y.; Zheng, M.; Liu, Y.; Xu, Z. Low-temperature synthesis and growth of hexagonal boron-nitride in a lithium melt, *J. Am. Ceram. Soc.* **2007**, *90*, 1589-1591.

27. Feigelson, B.N.; Frazier, R.M.; Twigg, M. III-nitride crystal growth from nitride-salt solution, *J. Cryst. Growth* **2007**, *305*, 399-402.

28. Taniguchi, T.; Watanabe, K. Synthesis of high-purity boron nitride single crystals under high pressure by using Ba-BN solvent. *J. Cryst. Growth* **2007**, *303*, 525-529.

29. Taniguchi, T. Growth of cubic boron nitride single crystals using a metal solvent under high pressure. *New Diamond Front. Carbon Technol.* **2004**, *14*, 289-297.

30. Kubota, Y.; Watanabe, K.; Taniguchi, T. Synthesis of cubic and hexagonal boron nitride by using Ni solvent under high pressure. *Jpn. J. Appl. Phys.* **2007**, *46*, 311-314.

31. Kubota, Y.; Watanabe, K.; Tsuda, O.; Taniguchi, T. Deep ultraviolet light-emitting hexagonal boron nitride synthesized at atmospheric pressure, *Science* **2007,** *317*, 932–934.

32. Abdulrahman, R.; Hendry, A. Solubility of nitrogen in liquid nickel-based alloys. *Metall. Mater. Trans. B* **2001**, *32*, 1103-1112.

33. Kowanda, C.; Speidel, M. Solubility of nitrogen in liquid nickel and binary Ni-Xi alloys (Xi = Cr, Mo, W, Mn, Fe, Co) under elevated pressure. *Scripta Mater.* **2003**, *48*, 1073-1078.

34. Nash, P. In *Ni-Cr;* Baker, H., Okamoto, H., Eds.; ASM Handbook, Volume 3 - Alloy Phase Diagrams; ASM International: **1992**, *30*.

35. Liao, P. K.; Spear, K. E. In *B-Ni;* Baker, H., Okamoto, H., Eds.; ASM Handbook, Volume 3 - Alloy Phase Diagrams; ASM International: **1992**, *30*.

36. Bondar, A. In *MSIT B-Cr-Ni (Boron-Chromium-Nickel);* Effenberg, G., Ilyenko, S., Eds.; Landolt-Börnstein New Series IV/11C3; Springer Berlin Heidelberg: Berlin, Heidelberg, **2007**, *11C3*, 153-167.

37. Clubine, B. Synthesis and Characterization of Bulk Single Crystal Hexagonal Boron Nitride from Metal Solvents. Master's Thesis, Kansas State University, Manhattan, KS, 2012.

38. Hoffman, T.B.; Clubine, B.; Zhang, Y.; Snow, K.; Edgar, J.H. Optimization of Ni-Cr Flux Growth for Hexagonal Boron Nitride Single Crystals. *Journal of Crystal Growth* **2014** *393*, 114-118.

39. Liu, Y.; Bhowmick, S.; Yakobson, B.I. BN white graphene and "colorful" edges: the energies and morphology. *Nano Lett.* **2011**, *11*, 3113–3116.

40. Runkle, R. C. Neutron sensors and their role in nuclear nonproliferation. *Nucl. Instrum. Methods Phys. Res.* **2011**, *652*, 37-40.

41. Kouzes, R. T.; Ely, J. H.; Erikson, L. E.; Kernan, W. J.; Lintereur, A. T.; Siciliano, E. R.; Stephens, D. L.; Stromswold, D. C.; Van Ginhoven, R. M.; Woodring, M. L. Neutron detection alternatives to ^{3}He for national security applications. *Nucl. Instrum. Methods Phys Res.* **2010**, *623*, 1035-1045.

42. Crane, T. W.; Baker, M. P. In *Neutron Detectors;* Reilly, D., Ensslin, N., Smith, H. and Kreiner, S., Eds.; Passive Nondestructive Assay of Nuclear Materials; U.S. Nuclear Regulatory Commission: Los Alamos National Laboratory, 1991; pp 379-406.

43. McGregor, D. S.; Hammig, M. D.; Yang, Y. H.; Gersch, H. K.; Klann, R. T. Design considerations for thin film coated semiconductor thermal neutron detectors I: basics regarding alpha particle-emitting neutron reactive films. *Nucl. Instrum. Methods Phys. Res.* **2003**, *500*, 272-308.

44. Kitaguchi, H.; Miyai, H.; Izumi, S.; Kaihara, A. Silicon semiconductor detectors for various nuclear radiations. *IEEE Trans on Nucl Sci.* **1996**, *43*, 1846-1850.

45. Nikolic, R.; Conway, A.; Reinhardt, C.; Graff, R.; Wang, T.; Deo, N.; Cheung, C. Fabrication of Pillar-structured thermal neutron detectors. *NSS '07 IEEE* **2007**, *2*, 1577-1580.

46. Yazbeck, J. Investigations of Hexagonal Boron Nitride as a Semiconductor for Neutron Detection. Master's Thesis, Kansas State University, Manhattan, KS, 2012.

47. Doty, F. P. *Advanced Digital Detectors for Neutron Imaging;* U.S. Department of Energy: Scandia National Laboratories, **2003**

48. McGregor, D. S.; Unruh, T. C.; McNeil, M. J. Thermal neutron detection with pyrolytic boron nitride. *Nucl. Instrum. Methods Phys. Res.* **2008**, *591*, 530.

49. Li, J.; Dahal, R.; Majety, S.; Lin, J. Y.; Jiang, H. X. Hexagonal boron nitride epitaxial layers as neutron detector materials. *Nucl Instrum. Meth Phys Res.* **2011**, *654*, 417-420.

50. Novoselov, K. S.; Fal'ko, V. I.; Colombo, L.; Gellert, P. R.; Schwab, M. G.; Kim, K. A roadmap for graphene. *Nature.* **2013**, *490*, 192-200.

51. Geim, A. K.; Novoselov, K. S. The rise of graphene. *Nat. Mater.* **2007**, *6*, 183-191.

52. Geim, A. K. Graphene: Status and prospects. *Science* **2009**, *19*, 1530-1534.

53. Castro Neto, A. H.; Guinea, F.; Peres, N. M. R.; Nosvoselov, K. S.; Geim, A. K. The electronic properties of graphene. *Rev Mod Phys.* **2009**, *81*, 109-162.

54. Avouris, P. Graphene: Electronic and photonic properties and devices. *Nano Lett.* **2010**, *10*, 4285-4294.

55. Wang, L.; Meric, I.; Huang, P.Y.; Gao, Y.; Tran, H.; Taniguchi, T.; Watanage, K.; Campos, L.M.; Muller, D.A.; Guo, J.; Kim, P.; Hone, J.; Shepard, K.L.; Dean, C.R. One-dimensional electrical contact to a two-dimensional material. *Science*. **2013**, *342,* 614-617.

56. Gannett, W.; Regan, W.; Watanabe, K.; Taniguchi, T.; Crommie, M. F.; Zettl, A. Boron nitride substrates for high mobility chemical vapor deposited graphene. *Appl Phys Lett.* **2011**, *98*, 1-3.

57. Mayorov, A. S.; Gorbachev, R. V.; Britnell, L.; Jalil, R.; Ponomarenko, L. A.; Blake, P.; Novoselov, K. S.; Watanabe, K.; Taniguchi, T.; Geim, A. K. Micrometer-scale ballistic transport in encapsulated graphene at room temperature. *Nano Lett.* **2011**, *11*, 2396-2399.

58. Bolotin, K. I.; Sikes, K. J.; Jiang, Z.; Klima, M.; Fudenberg, G.; Hone, J.; Kim, P.; Stormer, H. L. Ultrahigh electron mobility in suspended graphene. *Solid State Comm.* **2008**, *146*, 351-355.

59. Bolotin, K. I.; Sikes, K. J.; Hone, J.; Stormer, H. L.; Kim, P. Temperature-dependent transport in suspended graphene. *Phys Rev Let.t* **2008**, *100*, 096802.

60. Petrone, N.; Dean, C. R.; Meric, I.; Zan der Zande, A. M.; Huang, P. Y.; Wang, L.; Muller, D.; Shepard, K. L.; Hone, J. Chemical vapor deposition-derived graphene with electrical performance of exfoliated graphene. *Nano Lett.* **2012**, *12*, 2751-2756.

61. Wang, H.; Taychatanapat, T.; Hsu, A.; Watanabe, K.; Taniguchi, T.; Jarillo-Herrero, P.; Palacios, T. BN/Graphene/BN Transistors for RF applications. IEEE *Elect Dev Lett.* **2011**, *32*, 1209-1211.

62. Wang, H.; Hsu, A. L.; Palacios, T. Graphene electronics for RF applications. *IEEE Microwave.* **2012**, *13*, 114-125.

63. Jain, N.; Bansal, T.; Durcan, C.; Yu, B. Graphene-based interconnects on hexagonal boron nitride substrate. IEEE *Elect Dev Lett.* **2012**, *33*, 925-927.

64. Li, Y.; Sun, Q. Q.; Chen, L.; Zhou, P.; Wang, P.; Ding, S.; Zhang, D. W. Hexagonal boron nitride intercalated multi-layer graphene : a possible ultimate solution to ultra-scaled interconnect technology. *AIP Adv.* **2012**, *2*, 012191.

65. Kim, E.; Jain, N.; Xu, Y.; Yu, B. Logic inverter implemented with CVD-assembled graphene FET on hexagonal boron nitride. *IEEE Trans. Nanotechnol.* **2012**, *11*, 1536.

66. Levendorf, M. P.; Kim, C. -.; Brown, L.; Huang, P. Y.; Havener, R. W.; Muller, d. A.; Park, J. Graphene and boron nitride lateral heterostructures for atomically thin circuitry. *Nature* **2012**, *488*, 627-632.

67. Jain, N.; Bansal, T.; Durcan, C. A.; Xu, Y.; Yu, B. Monolayer graphene/hexagonal boron nitride heterostructure. *Carbon* **2013**, *54*, 396-402.

68. Britnell, L.; Gorbachev, R. V.; Jalil, R.; Belle, B. D.; Schedin, F.; Mishchenko, A.; Georgiou, T.; Katsnelson, M. I.; Eaves, L.; Morozov, S. V.; Peres, N. M.; Leist, J.; Geim,

A. K.; Novoselov, K. S.; Ponomarenko, L. A. Field-effect tunneling transistor based on vertical graphene heterostructures. *Science* **2012**, *335*, 947-950.

69. Dean, C. R.; Young, A. F.; Meric, I.; Lee, G; Watanabe, K.; Taniguchi, T.; Shepard, K.; Kim, P.; Hone, J. Graphene based heterostructures. *Solid State Commun.***2012**, *152*, 1275-1282.

70. Pomomarenko, L. A.; Geim, A. K.; Zhukov, A. A.; Jalil, R.; Morozov, S. V.; Novoselov, K. S.; Grigorieva, I. V.; Hill, E. H.; Cheianov, V. V.; Fal'ko, V. I.; Watanabe, K.; Taniguchi, T.; Gorbachev, R. V. Tunable metal-insulator transition in double-layer graphene heterostructures. *Nature Phys.* **2011**, *7*, 958-961.

71. Watanabe, K.; Taniguchi, T.; Kanda, H. Direct-bandgap properties and evidence for ultraviolet lasing of hexagonal boron nitride single crystal. *Nature Materials* **2004**, *3*, 404-409.

72. Watanabe, K.; Taniguchi, T. Hexagonal boron nitride as a new ultraviolet luminescent material and its application. *Int. J. Appl. Ceram. Technol.* **2011**, *8*, 977-989.

73. Majety, S.; Cao, X.K.; Dahal, R.; Lin, J.Y.; Jiang, H.X. Band-edge transitions in hexagonal boron nitride epilayers. *Appl. Phys. Lett.* **2012**, *101*, 051110.

74. Ikeda, M.; Uchida, S. Blue-violet laser diodes suitable for Blu-ray Disk. *Physica Status Solidi (A)* **2002**, *194*, 407-413.

75. Hecht, J. Materials are a tough challenger for ultraviolet diode lasers. *Laser Focus World* **2008**, *44*, 67-71.

76. Lister, G.G.; Lawler, J.E.; Lapatovich, W.P.; Godyak, V.A. The physics of discharge lamps. *Rev. Mod. Phys.* **2004**, *76*, 541-598.

77. Cassabois, G.; Valvin, P.; Gil, B. Hexagonal boron nitride is an indirect bandgap semiconductor. *Nat. Photonics*, **2016**, *10*, 262-266.

78. Xia, F.; Wang, H,; Xiao, D.; Dubey, M.; Ramasubramaniam, A. Two-dimensional material nanophotonics. *Nat. Photonics* **2014**, *8*, 899-907.

79. Poddubny, A.; Iorsh, I.; Belov, P.; Kivshar, Y. Hyperbolic metamaterials. *Nat. Photonics,* **2013**, *7*, 948-957.

80. Caldwell, J.D.; Lindsay, L.; Giannini, V.; Vurgaftman, I.; Reinecke, T.L.; Maier, S.A.; Glembocki, O.J. Low-loss, infrared and terahertz nanophotonics using surface phonon polaritons. *Nanophotonics* **2015**, *4*, 44-68.

81. L. Novotny, B. Hecht, *Principles of Nano-Optics*, 2nd ed; Cambridge Univ. Press: Cambridge, **2012**.

82. Dai, S.; Fai, Z.; Ma, Q.; Rodin, A.S.; Wagner, M.; McLeod, A.S.; Liu, M.K.; Gannett, W.; Regan, W.; Watanage, K.; Taniguchi, T.; Thiemens, M.; Dominguez, G.; Castro Neto, A.H.; Zettl, A.; Keilmann, F.; Jarillo-Herrero, P.; Fogler, M.M.; Basinov, D.N. Tunable phonon polaritons in atomically thin van der Waals crystals of boron nitride. *Science* **2014**, *343*, 1125-1129.

83. Jacob, Z. Hyperbolic phonon-polaritons. *Nat. Mater.* **2014**, *13*, 1081-1083.

84. Li, P.; Lewin, M.; Kretinin, A.V.; Caldwell, J.D.; Novoselov, K.S.; Taniguchi, T.; Watanabe, K.; Gaussmann, F.; Taubner, T. Hyperbolic phonon-polaritons in boron nitride for near-field optical imaging and focusing. *Nat. Communications* **2014**, *6*, 1-9.

85. Capper, P. Bulk *Crystal Growth of Electronic, Optical & Optoelectronic Materials*. Chichester: John Wiley & Sons, **2005**.

86. Yu, P.Y.; Cardona, M. *Fundamentals of Semiconductors. Physics and Materials Properties*; Springer: New York, **2005**.

87. Balint, M.G.; Petrescu, M.I. Crystallographic features of hBN as a precursor in the cBN high-temperature high-press synthesis. *Y.P.B. Sci. Bull.*, **2007**, *69*, 79-90.

88. Schimpf, C.; Motylenko, M.; Rafaja, D. Quantitative description of microstructure defects in hexagonal boron nitrides using X-ray diffraction analysis. *Mater Charact*. **2013**, *86*, 190-199.

89. Geick, R.; Perry, C.H.; Rupprecht, G. Normal modes in hexagonal boron nitride, *Phys Rev*. **1966**, *146*, 543–547.

90. Caldwell, J.D.; Anderson, T.J.; Culbertson, J.C.; Jernigan, G.G.; Hobart, K.D.; Kub, F.J.; Tadjer, M.J.; Tedesco, J.L.; Hite, J.K.; Mastro, M.A.; Myers-Ward, R.L.; Eddy, C.R.;

Campben, P.M.; Gaskill, D.K. Technique for the Dry Transfer of Epitaxial Graphene onto Arbitrary Substrates. *ACS Nano*. **2010**, *4*, 1108-1114.

91. Schroder, R. R.; Muller, M. B1.17 Microscopy: Electron (SEM and TEM). In *Encyclopedia of Chemical Physics and Physical Chemistry, Vol II*; Moore, J. H.; Spencer, N. D., Eds. **2001.**

92. Goodhew, P.J.; Humphreys, F.J.; Beanland, R. *Electron Microscopy and Analysis, 3rd ed*., CRC Press, **2000**

93. Haugstad, G. *Atomic Force Microscopy: Understanding Basic Modes and Advanced Applications*. Wiley: Hoboken, NJ, **2012**.

94. Gorbachev, R.V.; Riaz, I.; Nair, R.R.; Jalil, R.; Britnell, L.; Belle, B.D.; Hill, E.W.; Novoselov, K.S.; Watanabe, K.; Taniguchi, T.; Geim, A.K.; Blake, P. Hunting for monolayer boron nitride: optical and raman signatures. *Small.* **2011**, *7*, 465-68.

95. Cullity, B.D. *Elements of X-ray Diffraction*, 3rd ed., Prentice Hall, **2001**.

96. Pease, R.S. An X-ray study of boron nitride, *Acta Cryst.* **1952**, *5*, 356-361.

97. Smith, E.; Dent, G. *Modern Raman Spectroscopy: A Practical Approach,* Wiley: Hoboken, **2005**.

98. Brundle, C.R.; Evans, C.A; Wilson, S. "Raman Spectroscopy." *Encyclopedia of Materials Characterization: Surfaces, Interfaces, Thin Films*. Boston: Butterworth-Heinemann, **1992**. 428-41.

99. Reich, S.; Ferrari, A.C.; Arenal, R.; Leiseau, A.; Bello, I.; Robertson, J. Resonant Raman scattering in cubic and hexagonal boron nitride. *Phys Rev.* **2005**, *71*, 205201.

100. Parker, J.H.; Feldman, D.W.; Ashkin, M. Raman scattering by silicon and germanium. *Phys. Rev.* **1967** *155*, 712-714.

101. Wang, Z. 16.3.5 Photoluminescence Spectroscopy. In *Handbook of Deposition Technologies for Films and Coatings, 3rd Ed.*; Martin P., Ed.; Elsevier: Oxford, **2010**; 780-786.

102. Yacobi, B.G. Cathodoluminescence. In *Encyclopedia of Materials Characterization – Surfaces, Interfaces and Thin Films*. Brundle, C.R., Ed.; Reed Publishing: Stoneham, MA, **1992**; 149-160.

103. Museur, L.; Brasse, G.; Pierret, A.; Maine, S.; Attal-Tretout, B.; Ducastelle, F.; Loiseau, A.; Barjon, J.; Watanabe, K.; Taniguchi, T.; Kanaev, A. Exciton and interband optical transitions in hBN single crystal. *Phys. Status Solidi-R*, **2011**, *5*, 214-216.

104. Watanabe, K.; Taniguchi, T. Jahn-Teller effect on exciton states in hexagonal boron nitride single crystal. *Physical Review B* **2009**, *79*, 1-4.

105. Jin, M.-S.; Kim, N.-O. Photoluminescence of Hexagonal Boron Nitride (h-BN) Film. *Journal of Electrical Engineering and Technology* **2010**, *5*, 637-639.

106. Tran, T.T.; Bray, K.; Ford, M.J.; Toth, M.; Aharonovich, I. Quantum emission from hexagonal boron nitride monolayers. *Nat. Nanotechnology Lett.* **2015**, *242*, 1-6.

107. Huang, J.; Zhu, Y.T. Advances in the synthesis and characterization of boron nitride, *Defects and Diffusion Forum*, 2000,*186-187,* 1-32 (2).

108. Turan, S.; Knowles, K.M. High resolution transmission electron microscopy of the defect structure of boron nitride, *Phys. Status Sol. A*, **1995**, *150*, 227-237.

109. Weyher, J.L. Characterization of wide-band-gap semiconductors (GaN, SiC) by defect-selective etching and complementary methods. *Superlattice Microst*. **2006**, *40*, 270-288.

110. Zhuang, D.; Edgar, J.H. Wet etching of GaN, AlN, and SiC: a review. *Mater Sci Eng, R.* **2005**, *48*, 1-46.

111. S.B. Austerman, S.M. Myron, and J.W. Wagner, Growth and characterization of graphite single crystals, *Carbon*, **1967**, *5*, 549-557.

112. O. Mishima, Growth and polar properties of cubic boron nitride, in *Applications of Diamond Films and Related Materials*, Y. Tzeng, M. Yoshikawa, M. Murakawa, and A. Feldman eds., Elsevier, **1991**, *73*, 647-651.

113. Myers, R.H.; Montgomery, D.C.; Anderson-Cool, C.M. *Response Surface Methodology: Process and Product Optimization Using Designed Experiment*. 3rd ed. Wiley: Hoboken, NJ, **2009**.

114. Gopaladasu, P.; Cecchi, J.L.; Malloy, K. J.; Kaspik, R. Response Surface Modeling of the Composition of $AlAs_ySb_{1-y}$ Alloys Grown by Molecular Beam Epitaxy. *J Cryst Growth*, **2001**, *225,* 556-60.

115. Yu, H.; Sui, Y.; Wang, J.; Zhang, F.; Dai, X. Optimal control of oxygen concentration in a Magnetic Czochralski crystal growth by response surface methodology. *J Mater Sci Technol*, **2006**, *22***,** 173-178.

116. *The R Project for Statistical Computing*. Vers. 3.0.1. http://www.r-project.org/

117. Lenth, R.V. *Package 'rsm'*. Vers. 2.07. **2014**. http://cran.r-project.org/web/packages/rsm/index.html.

118. Lenth, R.V. "Response-Surface Methods in R, Using Rsm." **2012**. Univerisity of Iowa, Iowa City: IA.

119. Lenth, R.V. "Surface Plots in the Rsm Package." **2012**. University of Iowa, Iowa City: IA.

120. L. Lindsay, L.; Broido, D.A. Enhanced thermal conductivity and isotope effect in single-layer hexagonal boron nitride. *Phys. Rev. B.* 2011, *84* 155421(2011).

121. Wagner, R.S.; Ellis, W.C. Vapor-liquid-solid mechanism of single crystal growth. *Appl. Phys. Lett.* **1964**, *4*, 89.

122. Hou, K.F.; Hu, Z.; Chen, F.; Fu, J.J.; Chen, Y.; Liu, B.H.; Ding, J.; Dong, L.; White, T. Synthesis of boron nitride nanowires. *Appl. Phys. Lett.* **2002**, *80*, 3611-3613.

123. Deepak, F.L.; Vinod, C.P.; Mukhopadhyay, K.; Govinadaraj, A.;C.N.R. Rao, C.N.R. Boron nitride nanotubes and nanowires. *Chem. Phys. Lett.* **2002**, *353*, 345-352.

124. Ishii, T.; Sato, T.; Sekikawa, Y.; Iwata, M. Growth of whiskers of hexagonal boron nitride. *J. Cryst. Growth.* **1981**, *52*, 285-289.

125. Amelinckx, S.; Delavignette, P.; Heerschap, M. Dislocations and Stacking Faults in Graphite, In *Chemistry and Physics of Carbon: A Series of Advances*. Walker, P.L, Ed.. Dekker: New York, **1965**; Vol. 1; 1-71.

126. Thomas, J.M; Roscoe, C. Nonbasal Dislocations in Graphite, In *Chemistry and Physics of Carbon: A Series of Advances*. Walker, P.L, Ed.. Dekker: New York, **1965**; Vol. 3; 1-44.

127. Williamson, G.K. Electron microscope studies of dislocation structures in graphite. *Proceedings of the Royal Society of London A*, **1960**,*257*, 457-463.

128. Ponce, F.A.; Cherns, D.; Young, W.T.; Steeds, J.W. Characterization of dislocations in GaN by transmission electron diffraction and microscopy techniques. *Appl. Phys. Lett.*, **1996**, *69*, 770-772.

129. L. Lu, Z. Y. Gao, B. Shen, F. J. Xu, Z. L. Miao, Y. Hao, Z. J. Yang, G. Y. Zhang, X. P. Zhang, J. Xu, D. P. Yu, Microstructure and origin of dislocation etch pits in GaN epilayers grown by metal organic chemical vapor deposition, *J. Appl. Phys*., **2008**, *104*, 123525.

130. M. Moseley, A. Allerman, M. Crawford, J.J. Wierer, Jr., M. Smith, and L. Biedermann, Electrical current leakage and open-core threading dislocations in AlGaN-based deep ultraviolet light-emitting diodes, *J. Appl. Phys*., **2014**, *116*, 053104.

131. Stocker, D.A.; Schubert, E.F.; Redwing, J.M. Crystallographic wet chemical etching of GaN. *Appl. Phys. Lett.*, **1998**, *73*, 2654-2656.

132. Edgar, J.H.; Hoffman, T.B.; Clubine, B.; Currie, M.; Du, X.Z.; Lin, J.Y.; Jiang, H.X. Characterization of bulk hexagonal boron nitride single crystals grown by the metal flux technique. *J. Cryst. Growth*. **2014** *404*, 110-113.

133. Stenzel, O.; Hahn, J.; Roeder, M.; Ehrlich, A.; Prause, S.; Richter, F. The optical constants of cubic and hexagonal boron nitride thin films and their relation to the bulk optical constants. *Phys. State Solidi A*, **1996**, *158*, 281–287.

134. Gao, S.-P. Crystal structures and band gap characters of h-BN polytypes predicted by the dispersion corrected DFT and GW methods. *Solid State Commun.*, **2012**, *152***,** 1817-1820

135. Liu, L.; Feng, Y.P.; Shen, Z.X. Structure and electronic properties of h-BN. *Phys. Rev. B*, **2003,** *68*, 104102.

136. *SRIM*, version 2010; James F. Ziegler. http://www.srim.org/ (accessed April 2015).

137. Pearton, S.J.; Zolper, J.C.; Shul, R.J.; Ren, F. GaN: Processing, defects and devices. *J Appl. Phys.* **1999**, *86*, 1-78.

138. Baranov, D.G.; Edgar, J.H.; Hoffman, T.B.; Bassim, N.; Caldwell, J.D. Perfect interference-less absorption at infrared frequencies by a van der Waal's crystal. *Phys Rev. B.* **2015**, *92*, 201405.

139. Chen, H.T. Interference theory of metamaterial perfect absorbers. *Opt. Express*, **2012**, *20*, 7165.

140. Geim, A.K.; Grigorieva, I.V. Van der Waals heterostructures. *Nature*, **2013**, *499*, 419-425.

141. Caldwell, J.D.; Kretinin, A.V.; Chen, Y.; Giannini, V.; Fogler, M.M.; Francescato, Y.; Ellis, C.T.; Tischler, J.G.; Woods, C.R.; Giles, A.J.; Hong, M.; Watanabe, K.; Taniguchi, T.; Maier, S.A.; Novoselov, K.S. Sub-diffractional volume-confined polaritons in the natural hyperbolic material hexagonal boron nitride. *Nat. Commun.* **2014**, *5*, 5221.

142. Dai, S.; Ma, Q.; Anderson, T.; Mcleod, A.S.; Fei, Z.; Liu, M.K.; Wagner, M.; Watanabe, K.; Taniguchi, T.; Thiemens, M.; Keilmann, F.; Jarillo-Herrero, P.; Fogler, M.M.; Basov, D.N. Subdiffractional focusing and guiding of polaritonic rays in a natural hyperbolic material. *Nat. Commun.* **2014**, *6*, 6963.

143. Dai, S.; Ma, Q.; Anderson, T.; Fei, Z.; Goldflam, M.D.; Wagner, M.; Watanabe, K.; Taniguchi, T.; Thiemens, M.; Keilmann, F.; Janssen, G.C.A.M.; Zhu, S-E.; Jarillo-Herrero, P.; Fogler, M.M.; Basov, D.N. Graphene on hexagonal boron nitride as a tunable hyperbolic metamaterial. *Nat. Nanotechnol.* **2015**, *10*, 682-686.

144. Hoffman, A.J.; Alekseyev, L.; Howard, S.S.; Franz, K.J.; Wasserman, D.; Podolskiy, V.A.; Narimanov, E.E.; Sivco, D.L.; Gmachl, C. Negative refraction in semiconductor metamaterials. *Nat. Mater.*, **2007**, *6*, 946-950.

145. Pollard, B.; Muller, E.A.; Hinrichs, K.; Raschke, M.B. Vibrational nano-spectroscopic imaging correlating structure with intermolecular coupling and dynamics. *Nat. Commun.*, **2014**, *5*, 3587.

146. Huth, F.; Govyadinov, A.; Amarie, S.; Naunsing, W.; Keilmann, F.; Hillenbrand, R. Nano-FTIR absorption spectroscopy of molecular fingerprints at 20nm special resolution. *Nano Lett.*, **2012**¸***12*,** 3973-3978.

147. Giles, A.J.; Dai, S.; Hoffman, T.B.; Vurgaftman, I.; Fogler, M.; Reinecke, T.; Lindsey, L.; Edgar, J.H.; Basov, D.; Caldwell, J.D. Enhanced Hyperbolic Polariton Propagation through Isotopic Enrichment. *In Preparation.*

Appendix A - Successful Experiment Summary

Table 10.1: Table listing details for successful Ni-Cr experiments

Experiment	Exp Date	Furnace	Gas	Ni Source	Cr Source	Pre-melt Cycle	Dwell Time (hr)	Dwell Temp (°C)	Cool Rate (°C/hr)	Cool Temp (°C)	Crystal Morphology	Crystal Shape	Crystal Width (µm)
CM-B 25	3/20/13	CM	N2	Acros Org	Sigma Aldrich	Yes (reused)	24	1525	2	1325	crystal sheet	Triangular/Irregular	450
CM-B 27	4/4/2013	CM	N2	reused (Acros)	reused (Aldrich)	reused	24	1525	2	1325	crystal sheet	Triangular/Irregular	300-500
CM-B 29	4/12/2013	CM	N2	reused (Acros)	reused (Aldrich)	reused	24	1525	2	1325	crystal sheet	triangular	400-500
CM-B 41	6/5/2013	CM	N2	Aesar powder, 99.7%	Aesar powder, 99%	No	24	1525	2	1325	crystal sheet	irregular	100
CM-BN 1a	11/22/2013	CM	N2	reused	reused	No	24	1525	2	1200	embedded sheet	irregular	400
CM-BN 2a	11/26/2013	CM	N2	Aesar powder, 99.7%	Aesar powder, 99%	No	24	1525	2	1200	sheet on top of buffer layer	triangular/irregular	400
CM-BN 3b	1/9/2014	CM	N2	Aesar powder, 99.7%	Aesar powder, 99%	No	24	1525	4	1200	platelets in buffer layer	hex/mod hex	275
CM-Melt 2a	2/17/2014	CM	N2	Aesar powder, 99.7%	Aesar powder, 99%	Yes	24	1525	4	1200	crystal sheet w/ some pillars	irregular/mod hexagon	500
CM-Melt 3(a&b)	2/28/2014	CM	N2	Aesar powder, 99.7%	Aesar powder, 99%	Yes	24	1525	4	1200	platelets in buffer layer	hexagons	375
CM-Melt 5b	3/13/2014	CM	N2	Aesar powder, 99.7%	Aesar powder, 99%	Yes	24	1525	4	1200	platelets in buffer layer	irregular/ hexagonal	800\100
CM-Dwell 1(a&b)	3/29/2014	CM	N2	Aesar powder, 99.7%	Aesar powder, 99%	Yes	12	1525	quench	N/A	clear platelets with slight taper	hexagonal	100
CM-Dwell 2(a&b)	4/6/2014	CM	N2	Aesar powder, 99.7%	Aesar powder, 99%	Yes	12	1525	4 (quench)	1200	crystal sheet	rounded irregular grains	1000
CM-Dwell 3b	4/14/2014	CM	N2	Aesar powder, 99.7%	Aesar powder, 99%	Yes	12	1525	4 (quench)	1200	"floating" platelets w/ taper	modified hexagonal	100
CM-Dwell 5a	5/11/2014	CM	N2	Aesar powder, 99.7%	Aesar powder, 99%	Yes	48	1525	4	1200	platelets	hexagonal/rounded	550
CM-DD 1a	5/27/2014	CM	N2	Aesar powder, 99.7%	Aesar powder, 99%	Yes	24	1525	2	1475	platelets (slight taper)	hexagonal	75
CM-DD 3b	7/1/2014	CM	N2	Aesar powder, 99.7%	Aesar powder, 99%	Yes	24	1525	2	1325	platelets (slight taper)	hexagonal	N/A
CM-NIST 9b	10/1/2014	CM	N2	reused (Aesar)	reused (Aesar)	No	24	1525	5	1425	platelets (slight taper)	irregular/hexagonal	125-150
CM-NIST 10a	10/30/2014	CM	N2	Aesar powder, 99.7%	Aesar powder, 99%	Yes	24	1525	5	1025	platelets	hexagonal	30
CM-NIST 11	11/26/2014	CM	N2	reused (Aesar)	reused (Aesar)	No	24	1500	5	1100	platelets	Truncated hex (rounded)	75-80
CM-NIST 12	12/15/2015	CM	N2	reused (Aesar)	reused (Aesar)	No	24	1500	5	1100	crystal sheet (on buffer layer)	triangular/irregular	250
CM-TEST6	3/10/2015	CM	N2	Aesar powder, 99.7%	Aesar powder, 99%	Yes	18	1450	6.5	1150	crystal sheet	triangular/irregular	100-175
CM-Test 10a	3/30/2015	CM	N2	Aesar powder, 99.7%	Aesar powder, 99%	Yes	18	1450	6.5	1150	crystal sheet	triangular/irregular	135

CM-Slow 1a	7/16/2015	CM	N2	reused	reused	No	18	1500	1 (quench)	1400	platelets (tapered)	hexagonal	225
CM-Slow 2b	8/7/2015	CM	N2	reused	reused	no	18	1500	1 (quench)	1340	platelets (tapered)	hexagonal	250
M-BN 1	6/24/2013	Mellen	N2	Aesar powder, 99.7%	Aesar powder, 99%	No	24	1525	4	1225	crystal sheet	triangular/irregular	170-230
M-BN 6	8/30/2013	Mellen	N2	Aesar powder, 99.7%	Aesar powder, 99%	No	36	1500	2	1200	platelets/needles	hexagonal	50-75
M-BN 8b	10/28/2013	Mellen	N2	Aesar powder, 99.7%	Aesar powder, 99%	No	36	1525	4	1200	platelets	hexagonal	300-500
M-BN 12a	3/19/2014	Mellen	N2	Aesar shot, 99.95%	Aesar Chunks, 99.2%	No	24	1525	4	1200	crystal sheet	triangular	400-500
M-BLT 3b	4/28/2014	Mellen	N2	Aesar shot, 99.95%	Aesar Chunks, 99.2%	Yes	48	1425	4	1025	platelets	hexagonal	40
M-BLT 5b	5/13/2014	Mellen	N2	reused	reused	No	24	1425	2	1225	platelets	hexagonal	200-1000
M-NIST 3b	8/24/2014	Mellen	N2	Aesar shot, 99.95%	Aesar Chunks, 99.2%	Yes	24	1425	4	1225	crystal sheet	triangular	300-400
M-NIST 5a	9/9/2014	Mellen	N2	Aesar shot, 99.95%	Aesar Chunks, 99.2%	Yes	24	1425	4	1225	crystal sheet	triangular/irregular	300
M-NIST 5b	9/9/2014	Mellen	N2	Aesar shot, 99.95%	Aesar Chunks, 99.2%	Yes	24	1425	4	1225	crystal sheet	triangular/hexagonal	200
M-NIST 6a	11/3/2014	Mellen	N2	Aesar shot, 99.95%	Aesar Chunks, 99.2%	Yes	24	1500	5	1000	crystal sheet	triangular	350-650
M-NIST 6b	11/3/2014	Mellen	N2	Aesar shot, 99.95%	Aesar Chunks, 99.2%	Yes	24	1500	5	1000	crystal sheet	triangular/hex/irregular	500
M-NIST 8a	11/26/2014	Mellen	N2	Aesar shot, 99.95%	Aesar Chunks, 99.2%	Yes	24	1500	5	1200	crystal sheet and platelets	Triangular /hexagonal	400
M-NIST 9b	12/3/2014	Mellen	N2	reused	reused	No	24	1500	5	1000	crystal sheet	Triangular/irregular	200
M-NIST15b	4/14/2015	Mellen	N2	reused	reused	No	12	1450	4	1150	crystal sheet	Triangular	275
M-Prod 2	11/25/2015	Mellen	N2	reused (Aesar shot)	reused (Aesar chunks)	No	18	1500	5	1200	crystal sheet	Triangular/irregular	400-500
M-Prod 4a	12/7/2015	Mellen	N2	Aesar shot, 99.95%	Aesar Chunks, 99.2%	Yes	18	1500	5	1000	crystal sheet	Triangular/irregular	250-475
M-Prod 4b	12/7/2015	Mellen	N2	reused (Aesar shot)	reused (Aesar chunks)	No	18	1500	5	1000	crystal sheet	Irregular/triangular	450
M-Prod 5	1/19/2016	Mellen	N2 + Forming	Aesar shot, 99.95%	Aesar Chunks, 99.2%	Yes	18	1500	5	1150	crystal sheet	Triangular/irregular	200-300
M-Prod 9	3/2/2016	Mellen	N2 + Forming	ESPI Ni powder	ESPI Cr chunks	No	12	1500	200	N/A	crystal sheet	Triangular	650
M-Prod 10	3/4/2016	Mellen	N2 + Forming	ESPI Ni powder	ESPI Cr chunks	No	12	1500	200	N/A	crystal sheet	Triangular	250-750
M-Prod 11	3/8/2016	Mellen	N2 + Forming	ESPI Ni powder	ESPI Cr chunks	No	12	1500	5	1200	crystal sheet	Triangular	500
M-Prod 13	3/28/2016	Mellen	N2 + Forming	reused (ESPI Ni)	reused (ESPI Cr)	No	12	1500	5	1200	platelets	Rounded/Hexagonal	375-500
M-Prod 14	3/28/2016	Mellen	N2 + Forming	reused (ESPI Ni)	reused (ESPI Cr)	No	12	1500	5	1200	platelets	Hexagonal	450
M-Prod 17	4/12/2016	Mellen	N2 + Forming	Alfa Aesar High Purity Ni	Alfa Aesar High Purity Cr	No	12	1500	5	1200	platelets	Truncated Hexagonal	450-600

Appendix B - Data from Response Surface Methodology Experiments

Screening Experiments Raw Data:

Table 10.2: Average grain width measurements for screening run experiments

Run Order	Standard Order	Dwell Temperature (°C)	Dwell Time (hr)	Cooling Rate (°C/hr)	Cooling Temperature (°C)	Quench Rate (°C/hr)	Average Grain Width (μm)	Grain Size Standard Deviation (μm)
1	4	1500	12	9	1250	70	336	69
2	7	1500	12	4	1250	150	496	77
3	5	1500	24	4	1050	150	525	79
4	3	1400	24	4	1250	70	238	68
5	1	1400	12	4	1050	70	21	10
6	10	1450	18	6.5	1150	110	142	36
7	6	1400	12	9	1050	150	31	6
8	2	1500	24	9	1050	70	278	89
9	8	1400	24	9	1250	150	98	53
10	9	1450	18	6.5	1150	110	264	44

Main Experiments Raw Data:

Table 10.3: Average grain width and crystal thickness measurements for screening run experiments

Overall Order	Block	Run Order	Standard Order	Dwell Temperature (°C)	Cooling Rate (°C/hr)	Cooling Temperature (°C)	Average Grain Width (µm)	Grain Size Standard Deviation (µm)	Average Crystal Layer Thickness (µm)	Crystal Layer Thickness Standard Deviation (µm)
1	Fac1	1	2	1500	8	1050	445.2	94.3	25.7	5.0
2	Fac1	2	4	1400	8	1250	10.4	2.0	11.0	3.2
3	Fac1	3	1	1400	3	1050	8.2	1.0	12.6	1.8
4	Fac1	4	5	1450	5.5	1150	326.3	41.7	58.1	31.4
5	Fac1	5	3	1500	3	1250	348.2	52.3	159.3	10.3
6	Fac1	6	6	1450	5.5	1150	273.0	45.4	33.8	5.6
7	Fac2	1	6	1450	5.5	1150	122.2	41.8	17.8	1.8
8	Fac2	2	2	1400	8	1050	158.9	52.1	54.0	4.9
9	Fac2	3	5	1450	5.5	1150	395.3	99.7	22.1	2.0
10	Fac2	4	1	1500	3	1050	841.6	115.9	29.0	3.1
11	Fac2	5	3	1400	3	1250	140.7	63.3	6.7	1.2
12	Fac2	6	4	1500	8	1250	569.6	79.9	68.0	28.6
13	Axial 1	1	6	1450	5.5	1318	43.6	4.4	41.7	8.4
14	Axial 1	2	8	1450	5.5	1150	359.7	61.2	39.9	18.7
15	Axial 1	3	2	1534	5.5	1150	756.1	238.7	68.3	17.1
16	Axial 1	4	3	1450	1.3	1150	732.8	143.0	289.8	4.6
17	Axial 1	5	4	1450	9.7	1150	395.3	93.0	87.0	14.3
18	Axial 1	6	1	1366	5.5	1150	5.7	0.9	9.7	2.9
19	Axial 1	7	7	1450	5.5	1150	339.4	46.0	60.5	7.0
20	Axial 1	8	5	1450	5.5	982	76.7	15.0	47.0	3.8

Appendix C - R ANOVA Output for RSM Experiments

Screening Experiment R ANOVA Output

Table 10.4: ANOVA results produced by R for total screening run model considering all five parameters

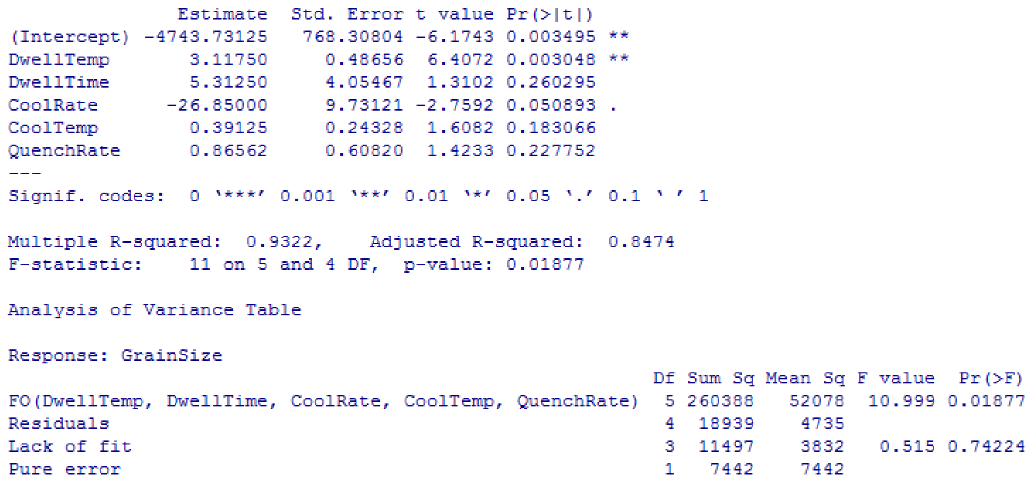

```
               Estimate  Std. Error t value Pr(>|t|)
(Intercept) -4743.73125   768.30804 -6.1743 0.003495 **
DwellTemp       3.11750     0.48656  6.4072 0.003048 **
DwellTime       5.31250     4.05467  1.3102 0.260295
CoolRate      -26.85000     9.73121 -2.7592 0.050893 .
CoolTemp        0.39125     0.24328  1.6082 0.183066
QuenchRate      0.86562     0.60820  1.4233 0.227752
---
Signif. codes:  0 ‘***’ 0.001 ‘**’ 0.01 ‘*’ 0.05 ‘.’ 0.1 ‘ ’ 1

Multiple R-squared:  0.9322,    Adjusted R-squared:  0.8474
F-statistic:    11 on 5 and 4 DF,  p-value: 0.01877

Analysis of Variance Table

Response: GrainSize
                                                          Df Sum Sq Mean Sq F value  Pr(>F)
FO(DwellTemp, DwellTime, CoolRate, CoolTemp, QuenchRate)  5 260388   52078  10.999 0.01877
Residuals                                                 4  18939    4735
Lack of fit                                               3  11497    3832   0.515 0.74224
Pure error                                                1   7442    7442
```

Table 10.5: ANOVA results produced by R for reduced screening run model considering only significant parameters (and cooling temperature)

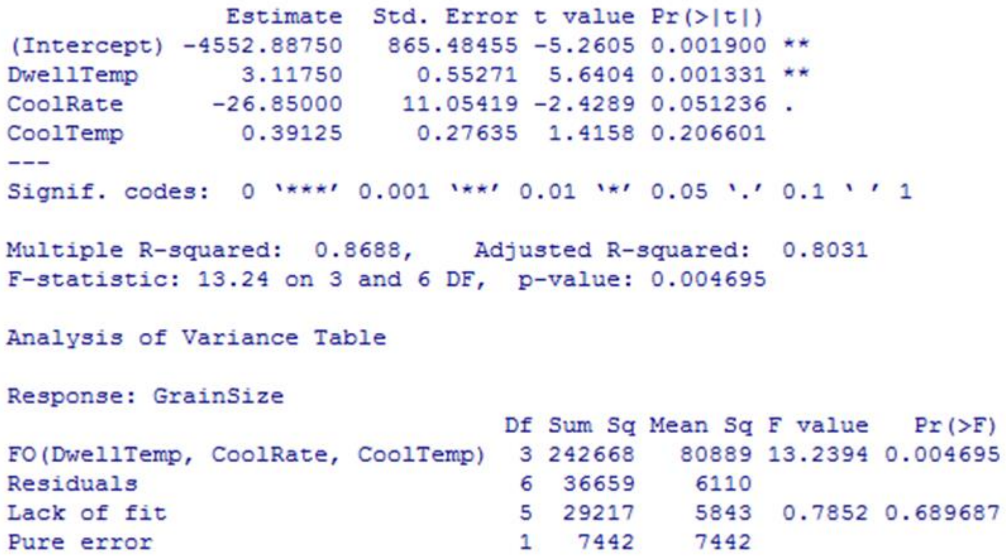

```
               Estimate  Std. Error t value Pr(>|t|)
(Intercept) -4552.88750   865.48455 -5.2605 0.001900 **
DwellTemp       3.11750     0.55271  5.6404 0.001331 **
CoolRate      -26.85000    11.05419 -2.4289 0.051236 .
CoolTemp        0.39125     0.27635  1.4158 0.206601
---
Signif. codes:  0 ‘***’ 0.001 ‘**’ 0.01 ‘*’ 0.05 ‘.’ 0.1 ‘ ’ 1

Multiple R-squared:  0.8688,    Adjusted R-squared:  0.8031
F-statistic: 13.24 on 3 and 6 DF,  p-value: 0.004695

Analysis of Variance Table

Response: GrainSize
                                  Df Sum Sq Mean Sq F value   Pr(>F)
FO(DwellTemp, CoolRate, CoolTemp)  3 242668   80889 13.2394 0.004695
Residuals                          6  36659    6110
Lack of fit                        5  29217    5843  0.7852 0.689687
Pure error                         1   7442    7442
```

Main Experiment R ANOVA Output

Table 10.6: ANOVA table produced by R for main run final model for grain width, with first-order terms for dwell temperature (x_1), cooling rate (x_2) and cooling temperature (x_3) and quadratic terms for cooling rate and cooling temperature. Coefficient estimates are for coded variable form.

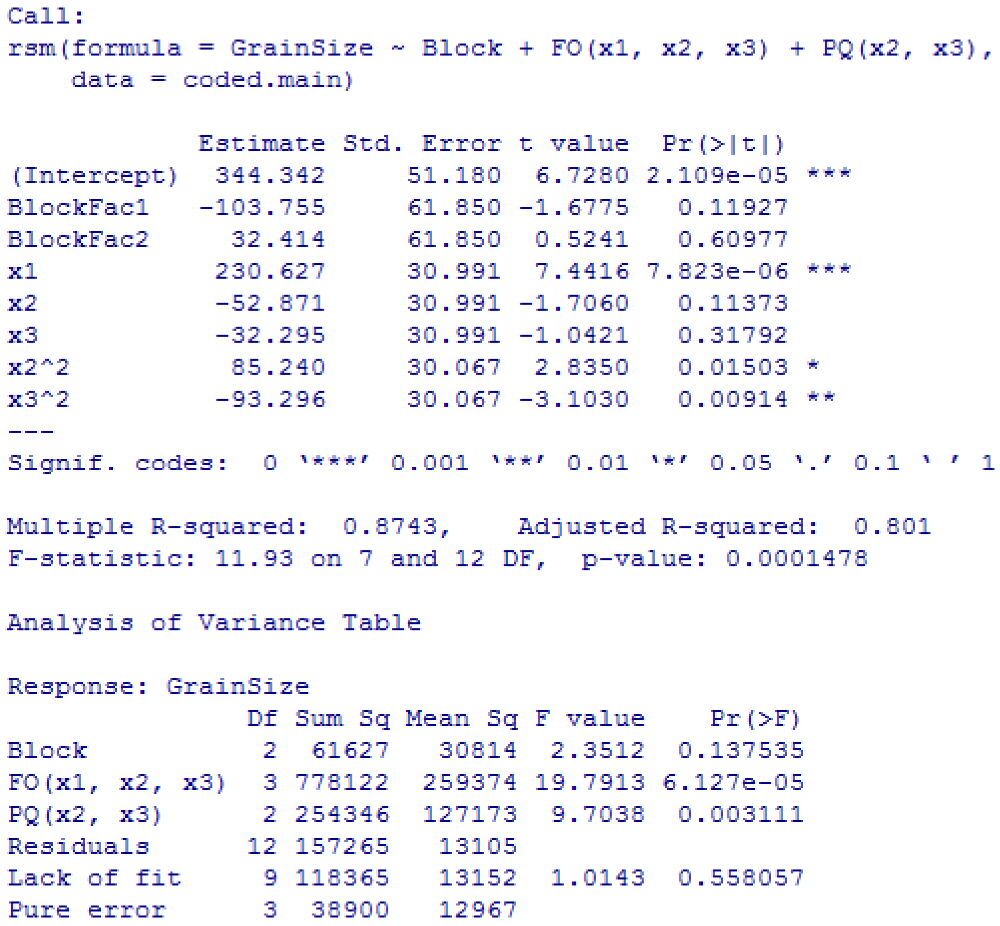

```
Call:
rsm(formula = GrainSize ~ Block + FO(x1, x2, x3) + PQ(x2, x3),
    data = coded.main)

            Estimate Std. Error t value  Pr(>|t|)
(Intercept)  344.342     51.180  6.7280 2.109e-05 ***
BlockFac1   -103.755     61.850 -1.6775   0.11927
BlockFac2     32.414     61.850  0.5241   0.60977
x1           230.627     30.991  7.4416 7.823e-06 ***
x2           -52.871     30.991 -1.7060   0.11373
x3           -32.295     30.991 -1.0421   0.31792
x2^2          85.240     30.067  2.8350   0.01503 *
x3^2         -93.296     30.067 -3.1030   0.00914 **
---
Signif. codes:  0 ‘***’ 0.001 ‘**’ 0.01 ‘*’ 0.05 ‘.’ 0.1 ‘ ’ 1

Multiple R-squared:  0.8743,    Adjusted R-squared:  0.801
F-statistic: 11.93 on 7 and 12 DF,  p-value: 0.0001478

Analysis of Variance Table

Response: GrainSize
               Df Sum Sq Mean Sq F value    Pr(>F)
Block           2  61627   30814  2.3512  0.137535
FO(x1, x2, x3)  3 778122  259374 19.7913 6.127e-05
PQ(x2, x3)      2 254346  127173  9.7038  0.003111
Residuals      12 157265   13105
Lack of fit     9 118365   13152  1.0143  0.558057
Pure error      3  38900   12967
```

Table 10.7: ANOVA table produced by R for main run final model for crystal layer thickness, with first-order terms for dwell temperature (x_1), cooling rate (x_2) and cooling temperature (x_3), dwell temperature by cooling temperature interaction term (x_1:x_3) and quadratic term for cooling rate (x_2^2).

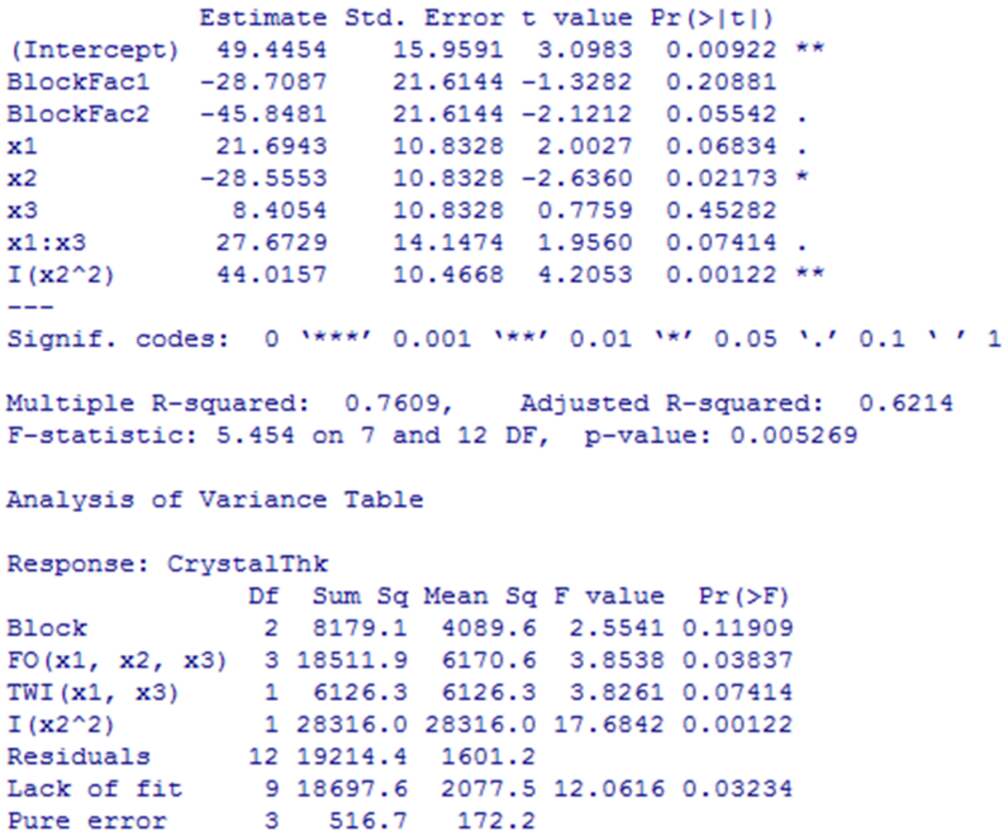

```
             Estimate Std. Error t value Pr(>|t|)
(Intercept)   49.4454    15.9591  3.0983  0.00922 **
BlockFac1    -28.7087    21.6144 -1.3282  0.20881
BlockFac2    -45.8481    21.6144 -2.1212  0.05542 .
x1            21.6943    10.8328  2.0027  0.06834 .
x2           -28.5553    10.8328 -2.6360  0.02173 *
x3             8.4054    10.8328  0.7759  0.45282
x1:x3         27.6729    14.1474  1.9560  0.07414 .
I(x2^2)       44.0157    10.4668  4.2053  0.00122 **
---
Signif. codes:  0 '***' 0.001 '**' 0.01 '*' 0.05 '.' 0.1 ' ' 1

Multiple R-squared:  0.7609,    Adjusted R-squared:  0.6214
F-statistic: 5.454 on 7 and 12 DF,  p-value: 0.005269

Analysis of Variance Table

Response: CrystalThk
               Df  Sum Sq Mean Sq F value   Pr(>F)
Block           2  8179.1  4089.6  2.5541  0.11909
FO(x1, x2, x3)  3 18511.9  6170.6  3.8538  0.03837
TWI(x1, x3)     1  6126.3  6126.3  3.8261  0.07414
I(x2^2)         1 28316.0 28316.0 17.6842  0.00122
Residuals      12 19214.4  1601.2
Lack of fit     9 18697.6  2077.5 12.0616  0.03234
Pure error      3   516.7   172.2
```

Appendix D - R Program Code for RSM Experiments

Screening Run Analysis Code and Raw Output:

```
R Console Page 1
> #---------------------------------------------------------------------------
> #Starting with the coding of the main-effects model (linear 1st order only)
for the
> # set of screening experiments (CM-Screen).
> #
> #1st order of business is to load in the rsm library and be able to call in
the Excel datasheet
containing the
> #sample measurements of grain size, XRD peak, Raman peak, ...
>
> library(rsm)
>
> #This time doing it with the natural data and then going to coded data
> screen.data <- read.csv("E:/Dropbox/BN project/CM Design of Experiments
Study/CM-Screen Analysi
s and Modeling/Natural Variable Analysis.csv",
+ header=TRUE, row.names = 1)
>
> Coded<-coded.data(screen.data, x1 ~ (DwellTemp - 1450)/50, x2 ~ (DwellTime
- 18)/6,
+ x3~(CoolRate - 6.5)/2.5, x4~(CoolTemp - 1150)/100, x5 ~ (QuenchRate -
110)/40)
>
> #This reads in the experiment data with coded variables and measured data
> #Now that the datafile is in R, we can begin with modeling and analysis
>
> #First I'm going to plot the avg grain size measurement agains the run
order
> RunOrder <- seq(1,10,1)
> plot(GrainSize ~ RunOrder, data = screen.data, type="p", main = "Run order
vs Grain Size",
+ xlab = "Run order", ylab = "Avg Grain Size(um)")
> check<-lm(GrainSize~RunOrder, data=screen.data)
> summary(check)
Call:
lm(formula = GrainSize ~ RunOrder, data = screen.data)
Residuals:
Min 1Q Median 3Q Max
-237.56 -76.90 -41.56 135.94 203.78
Coefficients:
Estimate Std. Error t value Pr(>|t|)
(Intercept) 415.20 107.57 3.860 0.00481 **
RunOrder -31.33 17.34 -1.807 0.10838
---
Signif. codes: 0 ‘***’ 0.001 ‘**’ 0.01 ‘*’ 0.05 ‘.’ 0.1 ‘ ’ 1
Residual standard error: 157.5 on 8 degrees of freedom
Multiple R-squared: 0.2899, Adjusted R-squared: 0.2011
F-statistic: 3.265 on 1 and 8 DF, p-value: 0.1084
```

```
> #From this, there is an R-squared value of 0.29 for the Run order vs Grain
size, so there is ba
sically no correlation
> #between the Grain size and order of experiments (a test to make sure there
is not systemic iss
ues with the exp set)
>
> grain.model <- rsm (GrainSize
~FO(DwellTemp,DwellTime,CoolRate,CoolTemp,QuenchRate), data=scree
n.data)
> #We start with our model building with the grain size measurements. These
avg measurements had
a wide spread and relatively
> #low measurement to measurement deviation.
>
> summary(grain.model)
Call:
rsm(formula = GrainSize ~ FO(DwellTemp, DwellTime, CoolRate,
CoolTemp, QuenchRate), data = screen.data)
Estimate Std. Error t value Pr(>|t|)
(Intercept) -4743.73125 768.30804 -6.1743 0.003495 **
DwellTemp 3.11750 0.48656 6.4072 0.003048 **
DwellTime 5.31250 4.05467 1.3102 0.260295
CoolRate -26.85000 9.73121 -2.7592 0.050893 .
R Console Page 2
CoolTemp 0.39125 0.24328 1.6082 0.183066
QuenchRate 0.86562 0.60820 1.4233 0.227752
---
Signif. codes: 0 ‘***’ 0.001 ‘**’ 0.01 ‘*’ 0.05 ‘.’ 0.1 ‘ ’ 1
Multiple R-squared: 0.9322, Adjusted R-squared: 0.8474
F-statistic: 11 on 5 and 4 DF, p-value: 0.01877
Analysis of Variance Table
Response: GrainSize
Df Sum Sq Mean Sq F value Pr(>F)
FO(DwellTemp, DwellTime, CoolRate, CoolTemp, QuenchRate) 5 260388 52078
10.999 0.01877
Residuals 4 18939 4735
Lack of fit 3 11497 3832 0.515 0.74224
Pure error 1 7442 7442
Direction of steepest ascent (at radius 1):
DwellTemp DwellTime CoolRate CoolTemp QuenchRate
0.11310100 0.19273426 -0.97410162 0.01419431 0.03140435
Corresponding increment in original units:
DwellTemp DwellTime CoolRate CoolTemp QuenchRate
0.11310100 0.19273426 -0.97410162 0.01419431 0.03140435
> #From this model, we see that dwell temperature has strong correlation with
the data, cooling r
ate has lower (but reasonable)
> #correlation (p-value very close to 0.05). The next closest factor would be
cooling temperature
, which has a higher p-value but
> #is the next best candidate for the CCD model factor.
>
> #We can redefine the model taking only into account these three parameters,
this will slightly
change linear parameters
> #and will change p-values slightly
```

```
> grain.lm <- rsm (GrainSize ~FO(DwellTemp,CoolRate,CoolTemp),
data=screen.data)
> summary(grain.lm)
Call:
rsm(formula = GrainSize ~ FO(DwellTemp, CoolRate, CoolTemp),
data = screen.data)
Estimate Std. Error t value Pr(>|t|)
(Intercept) -4552.88750 865.48455 -5.2605 0.001900 **
DwellTemp 3.11750 0.55271 5.6404 0.001331 **
CoolRate -26.85000 11.05419 -2.4289 0.051236 .
CoolTemp 0.39125 0.27635 1.4158 0.206601
---
Signif. codes: 0 '***' 0.001 '**' 0.01 '*' 0.05 '.' 0.1 ' ' 1
Multiple R-squared: 0.8688, Adjusted R-squared: 0.8031
F-statistic: 13.24 on 3 and 6 DF, p-value: 0.004695
Analysis of Variance Table
Response: GrainSize
Df Sum Sq Mean Sq F value Pr(>F)
FO(DwellTemp, CoolRate, CoolTemp) 3 242668 80889 13.2394 0.004695
Residuals 6 36659 6110
Lack of fit 5 29217 5843 0.7852 0.689687
Pure error 1 7442 7442
Direction of steepest ascent (at radius 1):
DwellTemp CoolRate CoolTemp
0.11532112 -0.99322282 0.01447294
Corresponding increment in original units:
DwellTemp CoolRate CoolTemp
0.11532112 -0.99322282 0.01447294
R Console Page 3
>
> #Now we can plot Dwell Temp vs Avg grain size
> plot(GrainSize ~ DwellTemp, data = screen.data, type="p", main = "Dwell
Temperature vs Grain Si
ze",
+ xlab = "Dwell Temperature (C)", ylab = "Avg Grain Size(um)", pch=20)
>
> #Repeat above for Cooling Rate vs Avg grain size
> plot(GrainSize ~ CoolRate, data = screen.data, type="p", main = "Cooling
Rate vs Grain Size",
+ xlab = "Cooling Rate (C/hr)", ylab = "Avg Grain Size(um)", pch=20)
>
> #Repeat above for Cooling Temp vs Avg grain size
> plot(GrainSize ~ CoolTemp, data = screen.data, type="p", main = "Cooling
Temperature vs Grain S
ize",
+ xlab = "Cooling Temperature (C)", ylab = "Avg Grain Size(um)", pch=20)
> local({fn<-choose.files(filters=Filters[c('R','txt','All'),],index=4)
+ file.show(fn,header=fn,title='')})
```

Main Run Analysis Code and Raw Output:

```
R Console Page 1
> #---------------------------------------------------------------------------
> #This program looks to analyze the results of the CM-Main Experiments using
the package rsm mod
el.
> #Goal of this is to develop a full second order model and identify
significant terms (linear, i
nteraction and potentially quadratic)
> #to describe the hBN crystals formed by these results.
>
> #1st order of business is to load in the rsm library and be able to call in
the Excel datasheet
containing the
> #sample measurements of grain width and thicknesses
>
> library(rsm); library(Hmisc)
> #Everytime we start a program using programs from 'package rsm', we must
load the library.
> #The Hmisc library also adds some useful plotting tool, such as allowing
the addition of error
bars
>
> main.data <- read.csv("E:/Dropbox/BN project/Dissertation/RSM Grain Size
Data/CM-Main R Workboo
k (Natural variables).csv",
+ header=TRUE, row.names = 1)
>
> #This calls in the datafile including the parameter details and grain size
measurement data
> #From this, we can use this data to build our model
>
> names(main.data)
[1] "Block" "Run.Order" "StdOrder" "DwellTemp"
[5] "CoolRate" "CoolTemp" "GrainSize" "SizeError"
[9] "CrystalThk" "CrystalError" "TotalThk" "TotalError"
[13] "PerThk" "PerError" "EffGrowthTime" "DeltaT"
[17] "EffGrowthRate" "EGRErr"
>
> #Next, we need to transpose this data in its natural variable form into
coded variables (-1,0,1
,etc).
> #This allows all factor levels to be normalize so that the difference in
level value for each f
actor is equal.
>
> coded.main <- coded.data(main.data, x1~(DwellTemp-1450)/50, x2~(CoolRate-
5.5)/2.5,
+ x3~(CoolTemp-1150)/100,block = "Block")
> coded.main
Block Run.Order StdOrder DwellTemp CoolRate CoolTemp GrainSize SizeError
1 Fac1 1 2 1500 8.0 1050 445.216667 94.3269712
2 Fac1 2 4 1400 8.0 1250 10.414286 2.0194294
3 Fac1 3 1 1400 3.0 1050 8.228571 1.0258562
```

```
4 Fac1 4 5 1450 5.5 1150 326.255556 41.7376961
5 Fac1 5 3 1500 3.0 1250 348.178571 52.2509638
6 Fac1 6 6 1450 5.5 1150 273.000000 45.4399604
7 Fac2 1 6 1450 5.5 1150 122.242857 41.7518406
8 Fac2 2 2 1400 8.0 1050 158.943333 52.1351431
9 Fac2 3 5 1450 5.5 1150 395.277778 99.6809131
10 Fac2 4 1 1500 3.0 1050 841.577778 115.8962335
11 Fac2 5 3 1400 3.0 1250 140.688889 63.3009369
12 Fac2 6 4 1500 8.0 1250 569.581429 79.8530134
13 Axial1 1 6 1450 5.5 1318 43.600000 4.3512450
14 Axial1 2 8 1450 5.5 1150 359.747778 61.2445552
15 Axial1 3 2 1534 5.5 1150 756.070000 238.6827468
16 Axial1 4 3 1450 1.3 1150 732.755556 142.9904552
17 Axial1 5 4 1450 9.7 1150 395.314286 92.9804716
18 Axial1 6 1 1366 5.5 1150 5.728571 0.9232448
19 Axial1 7 7 1450 5.5 1150 339.371429 45.9994462
20 Axial1 8 5 1450 5.5 982 76.671429 14.9573521
CrystalThk CrystalError TotalThk TotalError PerThk PerError
1 25.66667 4.997333 168.46667 3.696395 0.15235457 0.029851393
2 11.03333 3.189566 93.00000 14.346777 0.11863799 0.038874180
3 12.63333 1.778576 103.20000 12.011245 0.12241602 0.022361095
4 58.10000 31.445349 405.66667 87.608751 0.14322103 0.083458371
5 159.25000 10.253048 203.43333 76.870432 0.78281173 0.300060558
6 33.80000 5.565070 166.86667 18.072447 0.20255693 0.039918907
7 17.83333 1.789786 266.96667 45.682856 0.06679985 0.013251638
8 53.96667 4.885011 92.66667 28.814811 0.58237410 0.188606818
R Console Page 2
9 22.14667 1.984070 209.70000 49.200305 0.10561119 0.026523679
10 29.03333 3.134220 385.10000 14.764484 0.07539167 0.008636754
11 6.70000 1.153256 72.50000 10.114841 0.09241379 0.020475949
12 67.96667 28.620680 67.96667 28.620680 1.00000000 0.595523601
13 41.70000 8.364807 41.70000 8.364807 1.00000000 0.283684025
14 39.93333 18.717461 39.93333 18.717461 1.00000000 0.662866946
15 68.29000 17.050493 190.86667 145.367958 0.35778903 0.286768456
16 289.80000 4.635731 289.80000 4.635731 1.00000000 0.022622199
17 87.03333 14.287874 87.03333 14.287874 1.00000000 0.232165125
18 9.70000 2.858321 9.70000 2.858321 1.00000000 0.416729545
19 60.53333 7.011657 134.03333 22.490961 0.45162895 0.092085978
20 47.03333 3.843609 118.63333 11.460512 0.39645968 0.050165456
EffGrowthTime DeltaT EffGrowthRate EGRErr
1 56.25000 450 0.4562963 0.08884147
2 18.75000 150 0.5884444 0.17011020
3 116.66667 350 0.1082857 0.01524494
4 54.54545 300 1.0651667 0.57649807
5 83.33333 250 1.9110000 0.12303658
6 54.54545 300 0.6196667 0.10202628
7 54.54545 300 0.3269444 0.03281274
8 43.75000 350 1.2335238 0.11165740
9 54.54545 300 0.4060222 0.03637461
10 150.00000 450 0.1935556 0.02089480
11 50.00000 150 0.1340000 0.02306512
12 31.25000 250 2.1749333 0.91586177
13 24.00000 132 1.7375000 0.34853364
14 54.54545 300 0.7321111 0.34315345
15 69.81818 384 0.9781120 0.24421279
16 230.76923 300 1.2558000 0.02008817
17 30.92784 300 2.8140778 0.46197458
```

```
18 39.27273 216 0.2469907 0.07278133
19 54.54545 300 1.1097778 0.12854704
20 85.09091 468 0.5527422 0.04517062
Data are stored in coded form using these coding formulas ...
x1 ~ (DwellTemp - 1450)/50
x2 ~ (CoolRate - 5.5)/2.5
x3 ~ (CoolTemp - 1150)/100
>
> #Based on the conventions of this coding, we have now defined new coded
variables to take the p
lace of the natural variables
> #for analysis. These are as follows
> # x1 = (DwellTemp-1450)/50 - This is the coded variable for Dwell
Temperature
> # x2 = (CoolRate-5.5)/2.5 - This is the coded variable for Cooling Rate
> # x3 = (CoolTemp-1150)/100 - This is the coded variable for Cooling
Temperature
> #For the models we will be building, we will be referring to these coded
variables for the rsm
functions.
> #However, the rsm function will automatically also produce model details
for these natural vari
ables
> #by using these coded functions
>
> #Now that we have entered the dataset into R and have coded it, we are
ready for our rsm analys
is of
> #both crystal width and thickness with respect to the experimental factors
> #--------------------------------------------------------------------------
>
> #Part 1: Crystal Width Analysis
>
> #Section A: Model Building
>
> #Our first set on analyses is going to be looking at crystal width as a
function of these param
eters
> #Based on the results of the screening runs, we are anticipating to see a
strong dependence on
dwell temperature
>
> #Before we do any modeling, it is worthwhile to plot our raw data (with
error bars) against
> #each parameter. We can do this using the errbar function
> par(mfrow = c(1,3))
R Console Page 3
>
> #1st plot - Dwell Temperature
> errbar(main.data$DwellTemp,main.data$GrainSize,
+ main.data$GrainSize+main.data$SizeError, main.data$GrainSize-
main.data$SizeError,
+ cap=0.015, main = NULL, sub=NULL, xlim = c(1350, 1550), cex.lab = 1.5,
cex.axis=1.2,
+ xlab="Dwell Temperature (°C)", ylab = "Grain Width (µm)", pch=16)
>
> #2nd plot - Cooling Rate
```

```
> errbar(main.data$CoolRate,main.data$GrainSize,
+ main.data$GrainSize+main.data$SizeError, main.data$GrainSize-
main.data$SizeError,
+ cap=0.015, main = NULL, sub=NULL, cex.lab = 1.5, cex.axis=1.2,
+ xlab="Cooling Rate (°C/hr)", ylab = "Grain Width (μm)", pch=16)
>
> #3rd plot - Cooling Temperature
> errbar(main.data$CoolTemp,main.data$GrainSize,
+ main.data$GrainSize+main.data$SizeError, main.data$GrainSize-
main.data$SizeError,
+ cap=0.015, main = NULL, sub=NULL, cex.lab = 1.5, cex.axis=1.2,
+ xlab="Cooling Temperature (°C)", ylab = "Grain Width (μm)", pch=16)
>
> #To start out looking at models, we want to look at a first-order-only
(linear) model. Likely,
this model is not going
> #to sufficiently fit the data. However, we can use this as a baseline for
comparison
>
> width.rsm1 <- rsm (GrainSize ~ Block + FO(x1,x2,x3), data=coded.main)
> summary(width.rsm1)
Call:
rsm(formula = GrainSize ~ Block + FO(x1, x2, x3), data = coded.main)
Estimate Std. Error t value Pr(>|t|)
(Intercept) 338.657 60.623 5.5863 6.707e-05 ***
BlockFac1 -103.442 92.603 -1.1171 0.2827769
BlockFac2 32.728 92.603 0.3534 0.7290360
x1 230.627 46.419 4.9684 0.0002063 ***
x2 -52.871 46.419 -1.1390 0.2738170
x3 -32.295 46.419 -0.6957 0.4979825
---
Signif. codes: 0 '***' 0.001 '**' 0.01 '*' 0.05 '.' 0.1 ' ' 1
Multiple R-squared: 0.6711, Adjusted R-squared: 0.5536
F-statistic: 5.712 on 5 and 14 DF, p-value: 0.004463
Analysis of Variance Table
Response: GrainSize
Df Sum Sq Mean Sq F value Pr(>F)
Block 2 61627 30814 1.0481 0.376574
FO(x1, x2, x3) 3 778122 259374 8.8220 0.001556
Residuals 14 411611 29401
Lack of fit 11 372711 33883 2.6131 0.232440
Pure error 3 38900 12967
Direction of steepest ascent (at radius 1):
x1 x2 x3
0.9657598 -0.2214015 -0.1352382
Corresponding increment in original units:
DwellTemp CoolRate CoolTemp
48.2879905 -0.5535037 -13.5238217
> #From this FO model, we see the same strong dependence on dwell temperature
(wider grains at hi
gher dwell temp)
> #is still observed for this dataset. The other terms have low p-values, but
this does not mean
they are to be rejected yet.
>
> #Lack of fit (LOF) has a fairly low p-value, indicating that this model is
not adequately fitting the data. Additionally,
```

```
> #both the R-squared (0.6711) and adj. R-squared (0.5536) terms are low
(>0.7), showing that the
fit is inadequate and ineffient (x2 and x3 terms
R Console Page 4
> #are only marginally improving the fit).
>
> #For our attempt, we will fit a model including both the FO linear terms
and all x1-x3 interact
ion terms
> width.rsm2 <- rsm(GrainSize ~ Block + FO(x1,x2,x3) + TWI(x1,x2,x3),
data=coded.main)
> summary(width.rsm2)
Call:
rsm(formula = GrainSize ~ Block + FO(x1, x2, x3) + TWI(x1, x2,
x3), data = coded.main)
Estimate Std. Error t value Pr(>|t|)
(Intercept) 338.657 65.461 5.1735 0.0003069 ***
BlockFac1 -103.442 99.993 -1.0345 0.3231138
BlockFac2 32.728 99.993 0.3273 0.7495828
x1 230.627 50.124 4.6012 0.0007635 ***
x2 -52.871 50.124 -1.0548 0.3141246
x3 -32.295 50.124 -0.6443 0.5325769
x1:x2 -24.425 65.461 -0.3731 0.7161480
x1:x3 -44.121 65.461 -0.6740 0.5142230
x2:x3 42.097 65.461 0.6431 0.5333444
---
Signif. codes: 0 ‘***’ 0.001 ‘**’ 0.01 ‘*’ 0.05 ‘.’ 0.1 ‘ ’ 1
Multiple R-squared: 0.6987, Adjusted R-squared: 0.4795
F-statistic: 3.188 on 8 and 11 DF, p-value: 0.0393
Analysis of Variance Table
Response: GrainSize
Df Sum Sq Mean Sq F value Pr(>F)
Block 2 61627 30814 0.8989 0.434942
FO(x1, x2, x3) 3 778122 259374 7.5662 0.005082
TWI(x1, x2, x3) 3 34523 11508 0.3357 0.799923
Residuals 11 377088 34281
Lack of fit 8 338189 42274 3.2602 0.179954
Pure error 3 38900 12967
Stationary point of response surface:
x1 x2 x3
3.056270 3.970374 3.029211
Stationary point in original units:
DwellTemp CoolRate CoolTemp
1602.81349 15.42593 1452.92109
Eigenanalysis:
$values
[1] 37.19844 -12.19262 -25.00583
$vectors
[,1] [,2] [,3]
x1 0.5533356 -0.68202121 0.4781911
x2 -0.5403531 -0.73081061 -0.4170544
x3 -0.6339071 0.02762098 0.7729158
>
> #The ANOVA results for this second model shows that none of the interaction
terms are significa
nt. Basically the same fit
```

```
> #as the FO only model (x1 is significant), but major drop in adjusted R-
squared
>
> #Next model to look at is the full second order model. This just adds the
quadratic terms in ad
dition to those in model 2.
> width.rsm3 <- rsm(GrainSize ~ Block + SO(x1,x2,x3), data=coded.main)
> summary(width.rsm3)
Call:
rsm(formula = GrainSize ~ Block + SO(x1, x2, x3), data = coded.main)
R Console Page 5
Estimate Std. Error t value Pr(>|t|)
(Intercept) 325.247 60.014 5.4195 0.0006311 ***
BlockFac1 -102.702 64.911 -1.5822 0.1522607
BlockFac2 33.468 64.911 0.5156 0.6200770
x1 230.627 32.517 7.0925 0.0001027 ***
x2 -52.871 32.517 -1.6260 0.1426080
x3 -32.295 32.517 -0.9932 0.3497039
x1:x2 -24.425 42.466 -0.5752 0.5809974
x1:x3 -44.121 42.466 -1.0390 0.3292047
x2:x3 42.097 42.466 0.9913 0.3505726
x1^2 22.589 31.702 0.7125 0.4963802
x2^2 87.476 31.702 2.7593 0.0247015 *
x3^2 -91.060 31.702 -2.8724 0.0207536 *
---
Signif. codes: 0 ‘***’ 0.001 ‘**’ 0.01 ‘*’ 0.05 ‘.’ 0.1 ‘ ’ 1
Multiple R-squared: 0.9078, Adjusted R-squared: 0.7809
F-statistic: 7.158 on 11 and 8 DF, p-value: 0.004878
Analysis of Variance Table
Response: GrainSize
Df Sum Sq Mean Sq F value Pr(>F)
Block 2 61627 30814 2.1358 0.1806155
FO(x1, x2, x3) 3 778122 259374 17.9781 0.0006487
TWI(x1, x2, x3) 3 34523 11508 0.7976 0.5289885
PQ(x1, x2, x3) 3 261671 87224 6.0458 0.0187584
Residuals 8 115417 14427
Lack of fit 5 76518 15304 1.1802 0.4755482
Pure error 3 38900 12967
Stationary point of response surface:
x1 x2 x3
-4.6001643 -0.5357111 0.8132852
Stationary point in original units:
DwellTemp CoolRate CoolTemp
1219.991785 4.160722 1231.328523
Eigenanalysis:
$values
[1] 93.08131 22.97890 -97.05521
$vectors
[,1] [,2] [,3]
x1 0.2102449 0.9626710 -0.1704747
x2 -0.9681636 0.2292461 0.1005262
x3 -0.1358543 -0.1439123 -0.9802208
>
> #We see that the quadratic x2 and x3 terms are significant. This is nice!
Probably not a great
first-principles model,
```

```
> #but shows there is some optimal conditions for grow, possibly within the
experimental region.
Major increase in R-squared
> #values (up to 0.9078). This value is probably too high, as we are
overfitting the model with t
he interaction terms.
> #LOF p-values very high, we are almost there.
>
> #We can now build our final model. From the first three, we see that the
significant terms are
the linear x1 and
> #the quadratic x2 and x3 terms. For rsm models, we must also include the
lower order (linear) x
2 and x3 terms as well.
> #This makes our model FO(x1,x2,x3) + PW(x2,x3)
> width.rsm.final <- rsm(GrainSize ~ Block + FO(x1,x2,x3) + PQ(x2,x3),
data=coded.main)
> summary(width.rsm.final)
Call:
R Console Page 6
rsm(formula = GrainSize ~ Block + FO(x1, x2, x3) + PQ(x2, x3),
data = coded.main)
Estimate Std. Error t value Pr(>|t|)
(Intercept) 344.342 51.180 6.7280 2.109e-05 ***
BlockFac1 -103.755 61.850 -1.6775 0.11927
BlockFac2 32.414 61.850 0.5241 0.60977
x1 230.627 30.991 7.4416 7.823e-06 ***
x2 -52.871 30.991 -1.7060 0.11373
x3 -32.295 30.991 -1.0421 0.31792
x2^2 85.240 30.067 2.8350 0.01503 *
x3^2 -93.296 30.067 -3.1030 0.00914 **
---
Signif. codes: 0 ‘***’ 0.001 ‘**’ 0.01 ‘*’ 0.05 ‘.’ 0.1 ‘ ’ 1
Multiple R-squared: 0.8743, Adjusted R-squared: 0.801
F-statistic: 11.93 on 7 and 12 DF, p-value: 0.0001478
Analysis of Variance Table
Response: GrainSize
Df Sum Sq Mean Sq F value Pr(>F)
Block 2 61627 30814 2.3512 0.137535
FO(x1, x2, x3) 3 778122 259374 19.7913 6.127e-05
PQ(x2, x3) 2 254346 127173 9.7038 0.003111
Residuals 12 157265 13105
Lack of fit 9 118365 13152 1.0143 0.558057
Pure error 3 38900 12967
Stationary point of response surface:
x1 x2 x3
0.0000000 0.3101326 -0.1730803
Stationary point in original units:
DwellTemp CoolRate CoolTemp
1450.000000 6.275332 1132.691970
Eigenanalysis:
$values
[1] 85.23995 0.00000 -93.29577
$vectors
[,1] [,2] [,3]
x1 0 1 0
x2 1 0 0
```

```
x3 0 0 1
>
> #Here we see ther results of our final model. Very high significance for x1
and x2^2 and x3^2 t
erms.
> #R-squared (0.8743) and adjusted R-squared(0.8010) values are in a nice
place and p-value for L
OF is high (0.5581).
> #Looking further, the stationary point listed here is somewhat unclear. Due
to the signs of the
eigenvalues,
> #this stationary point appears to be a saddle point. Will need to look at
contour plots and ste
epest slope
> #analysis to see if I can evaluate what optimal conditions would be.
>
>
> #Section B: Contour and Perspective Plots
>
> #Following from the development of our model, we can now use graphical
techniques available in
R, such as contour
> #and perspective plots to show what our response surface looks like and
where our region for op
timal grain
> #width is located.
>
> #We can start with contour plots, we will do one plot for each parameter
pair combination, with
R Console Page 7
the contour slice
> #taken at the 0 coded value (Dwell Temp = 1450 C, Cooling Rate = 5.5 C/hr,
Cooling Temp = 1150
C). This will show
> #the directionality of where we should be pushing the process to improve
crystal size.
>
> #Going to make a 3x3 of contour plots, looking at each plot at -1,0, and 1
of each parameter
> par(mfrow = c(3,3))
>
> #First countour plot: -1 values for each plot
> contour(width.rsm.final,~x1+x2+x3,decode=TRUE,
+ xlabs = c("Dwell Temperature (°C)", "Cooling Rate (°C/hr)", "Cooling
Temperature (°C)"),
+ zlim =c(-100,900), zlab="Grain Width (µm)",lty = 1, lwd = 1.2, methods =
"flattest",
+ at = c(x1=-1, x2=-1,x3=-1), atpos=1, image=TRUE,
img.col=terrain.colors(2560, alpha=1))
There were 36 warnings (use warnings() to see them)
>
> #Contour 2: 0 values for each plot
> contour(width.rsm.final,~x1+x2+x3,decode=TRUE,
+ xlabs = c("Dwell Temperature (°C)", "Cooling Rate (°C/hr)", "Cooling
Temperature (°C)"),
+ zlim =c(-100,900), zlab="Grain Width (µm)", lty = 1, lwd = 1.2, methods =
"flattest",
```

```
+ at = c(x1=0, x2=0,x3=0), atpos=1, image=TRUE, img.col=terrain.colors(2560,
alpha=1))
There were 36 warnings (use warnings() to see them)
>
> #Contour 3: 1 values for each plot
> contour(width.rsm.final,~x1+x2+x3,decode=TRUE,
+ xlabs = c("Dwell Temperature (°C)", "Cooling Rate (°C/hr)", "Cooling
Temperature (°C)"),
+ zlim =c(-100,900), zlab="Grain Width (µm)", lty = 1, lwd = 1.2, methods =
"flattest",
+ at = c(x1=1, x2=1,x3=1), atpos=1, image=TRUE, img.col=terrain.colors(2560,
alpha=1))
There were 36 warnings (use warnings() to see them)
>
> #We can do more than look within the plot area, we can also look slightly
outside of it. In thi
s plot, I predict
> #the grain width at a cooling rate of 1C/hr as a function of Dwell and
Cooling Temp
>
> par(mfrow = c(1,1))
> persp(width.rsm.final,~x1+x3,decode=TRUE,
+ xlabs = c("Dwell Temperature (°C)", "Cooling Temperature (°C)"),
+ at = c(x2=-1.8), atpos=3, theta = 235, phi = 25, r=8,
+ zlab="Grain Width (µm)", cex.axis = 0.75, cex.lab= 1, cex.sub=1.5)
>
> #We can push this prediction a little further, here I am going to do a
series of prediction for
Dwell Temp slices
> #going from 1400C to 1700C,
> par(mfrow = c(2,2))
>
> #Plot 1 - 1400C: x1=-1
> persp(width.rsm.final,~x2+x3,decode=TRUE, at = c(x1=-1),
+ xlabs = c("Cooling Rate (°C/hr)", "Cooling Temperature (°C)"),
+ atpos=3, theta = 50, phi = 30, r=8,
+ zlab="Grain Width (µm)", cex.axis = 0.7, cex.lab= 0.7, cex.sub=1.2)
>
> #Plot 2 - 1500C: x1 = 1
> persp(width.rsm.final,~x2+x3,decode=TRUE, at = c(x1=1),
+ xlabs = c("Cooling Rate (°C/hr)", "Cooling Temperature (°C)"),
+ atpos=3, theta = 50, phi = 30, r=8,
+ zlab="Grain Width (µm)", cex.axis = 0.7, cex.lab= 0.7, cex.sub=1.2)
>
> #Plot 3 - 1600C: x1 = 2
> persp(width.rsm.final,~x2+x3,decode=TRUE, at = c(x1=3),
+ xlabs = c("Cooling Rate (°C/hr)", "Cooling Temperature (°C)"),
+ atpos=3, theta = 50, phi = 30, r=8,
+ zlab="Grain Width (µm)", cex.axis = 0.7, cex.lab= 0.7, cex.sub=1.2)
>
> #Plot 4 - 1700C: x1 = 5
> persp(width.rsm.final,~x2+x3,decode=TRUE, at = c(x1=5),
+ xlabs = c("Cooling Rate (°C/hr)", "Cooling Temperature (°C)"),
+ atpos=3, theta = 50, phi = 30, r=8,
+ zlab="Grain Width (µm)", cex.axis = 0.7, cex.lab= 0.7, cex.sub=1.2)
>
```

```
> #Its important to note here that our predictions for 1700C or even 1600C
may not actually be ac
R Console Page 8
curate.
> #These are projections assuming that the system is going to be operating in
the same way
> #(chemically, physically,etc) outside the exp region as inside. This may
not be the case due to
> #temperature problems with equipment or physical changes, such as higher
chromium vapor pressur
e
> #or higher reactivity causing problems, etc. More experiments will be
needed to look confirm th
at
> #this trend holds
>
> #---------------------------------------------------------------------------
>
> #Part 2: Crystal Thickness Analysis
>
> #Section A: Model Fitting
>
> #Like the grain width section, we start this off by plotting the raw
thickness data
> #with respect to each parameter
> par(mfrow = c(1,3))
>
> #1st plot - Dwell Temperature
> errbar(main.data$DwellTemp,main.data$CrystalThk,
+ main.data$CrystalThk+main.data$CrystalError, main.data$CrystalThk-
main.data$CrystalError,
+ cap=0.015, main = NULL, sub=NULL, xlim = c(1350, 1550), cex.lab = 1.5,
cex.axis=1.2,
+ xlab="Dwell Temperature (°C)", ylab = "Crystal Thickness (µm)", pch=16)
>
> #2nd plot - Cooling Rate
> errbar(main.data$CoolRate,main.data$CrystalThk,
+ main.data$CrystalThk+main.data$CrystalError, main.data$CrystalThk-
main.data$CrystalError,
+ cap=0.015, main = NULL, sub=NULL, cex.lab = 1.5, cex.axis=1.2,
+ xlab="Cooling Rate (°C/hr)", ylab = "Crystal Thickness (µm)", pch=16)
>
> #3rd plot - Cooling Temperature
> errbar(main.data$CoolTemp,main.data$CrystalThk,
+ main.data$CrystalThk+main.data$CrystalError, main.data$CrystalThk-
main.data$CrystalError,
+ cap=0.015, main = NULL, sub=NULL, cex.lab = 1.5, cex.axis=1.2,
+ xlab="Cooling Temperature (°C)", ylab = "Crystal Thickness (µm)", pch=16)
>
> #We start working for the crystals thickness model exactly in the same was
as the width model;
> #looking at a FO model then building until we find conditions which
minimize LOF and maximize
> #adjusted R-squared values.
> thk.rsm1 <- rsm (CrystalThk ~ Block + FO(x1,x2,x3), data=coded.main)
> summary(thk.rsm1)
Call:
```

```
rsm(formula = CrystalThk ~ Block + FO(x1, x2, x3), data = coded.main)
Estimate Std. Error t value Pr(>|t|)
(Intercept) 80.5029 21.8878 3.6780 0.002483 **
BlockFac1 -30.4224 33.4342 -0.9099 0.378266
BlockFac2 -47.5618 33.4342 -1.4225 0.176765
x1 21.6943 16.7596 1.2944 0.216458
x2 -28.5553 16.7596 -1.7038 0.110500
x3 8.4054 16.7596 0.5015 0.623794
---
Signif. codes: 0 '***' 0.001 '**' 0.01 '*' 0.05 '.' 0.1 ' ' 1
Multiple R-squared: 0.3322, Adjusted R-squared: 0.09369
F-statistic: 1.393 on 5 and 14 DF, p-value: 0.2858
Analysis of Variance Table
Response: CrystalThk
Df Sum Sq Mean Sq F value Pr(>F)
Block 2 8179 4089.6 1.067 0.370413
FO(x1, x2, x3) 3 18512 6170.6 1.610 0.231816
Residuals 14 53657 3832.6
Lack of fit 11 53140 4830.9 28.047 0.009528
R Console Page 9
Pure error 3 517 172.2
Direction of steepest ascent (at radius 1):
x1 x2 x3
0.5889848 -0.7752557 0.2282005
Corresponding increment in original units:
DwellTemp CoolRate CoolTemp
29.449242 -1.938139 22.820052
>
> #From this FO model, we see that the only term of any significance
(although p<0.05 still) is t
he x2 term (CoolRate)
> #However, the R-squared values are very high for this model and the LOF p-
value is quite signif
icant, showing that
> #this model does not sufficiently fit the data. We need to keep adding
terms to see if the fit
improves.
>
> #Next step, we will add in the interaction terms to the FO model to see if
this improves the fi
t
>
> thk.rsm2 <- rsm(CrystalThk ~ Block + FO(x1,x2,x3) + TWI(x1,x2,x3),
data=coded.main)
> summary(thk.rsm2)
Call:
rsm(formula = CrystalThk ~ Block + FO(x1, x2, x3) + TWI(x1, x2,
x3), data = coded.main)
Estimate Std. Error t value Pr(>|t|)
(Intercept) 80.5029 22.1356 3.6368 0.00391 **
BlockFac1 -30.4224 33.8127 -0.8997 0.38754
BlockFac2 -47.5618 33.8127 -1.4066 0.18716
x1 21.6943 16.9493 1.2799 0.22690
x2 -28.5553 16.9493 -1.6847 0.12016
x3 8.4054 16.9493 0.4959 0.62971
x1:x2 -17.5396 22.1356 -0.7924 0.44490
x1:x3 27.6729 22.1356 1.2502 0.23719
```

```
x2:x3 -15.6146 22.1356 -0.7054 0.49522
---
Signif. codes: 0 '***' 0.001 '**' 0.01 '*' 0.05 '.' 0.1 ' ' 1
Multiple R-squared: 0.4633, Adjusted R-squared: 0.07306
F-statistic: 1.187 on 8 and 11 DF, p-value: 0.3858
Analysis of Variance Table
Response: CrystalThk
Df Sum Sq Mean Sq F value Pr(>F)
Block 2 8179 4089.6 1.0433 0.384696
FO(x1, x2, x3) 3 18512 6170.6 1.5742 0.251276
TWI(x1, x2, x3) 3 10538 3512.6 0.8961 0.473754
Residuals 11 43119 3919.9
Lack of fit 8 42602 5325.2 30.9172 0.008425
Pure error 3 517 172.2
Stationary point of response surface:
x1 x2 x3
-0.6169378 -0.5550624 -1.1357630
Stationary point in original units:
DwellTemp CoolRate CoolTemp
1419.153109 4.112344 1036.423700
Eigenanalysis:
$values
[1] 20.532633 -6.644318 -13.888314
$vectors
[,1] [,2] [,3]
R Console Page 10
x1 0.6209009 0.2921820 0.72740067
x2 -0.4960045 0.8649934 0.07593353
x3 0.6070104 0.4079412 -0.68199880
>
> #Just are for crystal width, we don't see any significant interaction terms
here. LOF p-value i
s only increased a
> #very small amount, so this model is not going to cut it.
>
> #Next, we should look at the full second order model to see if the addition
of quadratic terms
improves the model
> thk.rsm3 <- rsm(CrystalThk ~ Block + SO(x1,x2,x3), data=coded.main)
> summary(thk.rsm3)
Call:
rsm(formula = CrystalThk ~ Block + SO(x1, x2, x3), data = coded.main)
Estimate Std. Error t value Pr(>|t|)
(Intercept) 64.4068 19.5937 3.2871 0.011070 *
BlockFac1 -29.5342 21.1924 -1.3936 0.200928
BlockFac2 -46.6737 21.1924 -2.2024 0.058776 .
x1 21.6943 10.6163 2.0435 0.075264 .
x2 -28.5553 10.6163 -2.6898 0.027506 *
x3 8.4054 10.6163 0.7917 0.451343
x1:x2 -17.5396 13.8647 -1.2651 0.241455
x1:x3 27.6729 13.8647 1.9959 0.081026 .
x2:x3 -15.6146 13.8647 -1.1262 0.292723
x1^2 -10.6775 10.3503 -1.0316 0.332430
x2^2 42.2638 10.3503 4.0833 0.003518 **
x3^2 -8.7743 10.3503 -0.8477 0.421224
---
Signif. codes: 0 '***' 0.001 '**' 0.01 '*' 0.05 '.' 0.1 ' ' 1
```

```
Multiple R-squared: 0.8469, Adjusted R-squared: 0.6363
F-statistic: 4.022 on 11 and 8 DF, p-value: 0.02918
Analysis of Variance Table
Response: CrystalThk
Df Sum Sq Mean Sq F value Pr(>F)
Block 2 8179.1 4089.6 2.6593 0.13018
FO(x1, x2, x3) 3 18511.9 6170.6 4.0125 0.05153
TWI(x1, x2, x3) 3 10537.9 3512.6 2.2841 0.15583
PQ(x1, x2, x3) 3 30816.0 10272.0 6.6795 0.01432
Residuals 8 12302.7 1537.8
Lack of fit 5 11786.0 2357.2 13.6853 0.02813
Pure error 3 516.7 172.2
Stationary point of response surface:
x1 x2 x3
-4.622476 -1.614098 -5.374138
Stationary point in original units:
DwellTemp CoolRate CoolTemp
1218.876201 1.464755 612.586196
Eigenanalysis:
$values
[1] 45.5795929 0.8467017 -23.6142769
$vectors
[,1] [,2] [,3]
x1 -0.1962997 0.6479750 0.73593128
x2 0.9623143 0.2713593 0.01775714
x3 -0.1881956 0.7116829 -0.67682334
>
R Console Page 11
> #This improves the fit somewhat, although LOF is still significant, which
is problematic.
> #For some reason, the x1:x3 interaction term and the x2 linear term are
suddenly now significan
t,
> #as is the added the x2^2 term. We can build our final model for crystal
thickness from the sig
nificant
> #terms of the SO model: FO(x1,x2,x3) + TWI(x1,x3) + PQ(x2)
>
> thk.rsm.final <- rsm(CrystalThk ~ Block + FO(x1,x2,x3) +TWI(x1,x3)+
I(x2^2), data=coded.main)
> summary(thk.rsm.final)
Call:
rsm(formula = CrystalThk ~ Block + FO(x1, x2, x3) + TWI(x1, x3) +
I(x2^2), data = coded.main)
Estimate Std. Error t value Pr(>|t|)
(Intercept) 49.4454 15.9591 3.0983 0.00922 **
BlockFac1 -28.7087 21.6144 -1.3282 0.20881
BlockFac2 -45.8481 21.6144 -2.1212 0.05542 .
x1 21.6943 10.8328 2.0027 0.06834 .
x2 -28.5553 10.8328 -2.6360 0.02173 *
x3 8.4054 10.8328 0.7759 0.45282
x1:x3 27.6729 14.1474 1.9560 0.07414 .
I(x2^2) 44.0157 10.4668 4.2053 0.00122 **
---
Signif. codes: 0 ‘***’ 0.001 ‘**’ 0.01 ‘*’ 0.05 ‘.’ 0.1 ‘ ’ 1
Multiple R-squared: 0.7609, Adjusted R-squared: 0.6214
F-statistic: 5.454 on 7 and 12 DF, p-value: 0.005269
```

```
Analysis of Variance Table
Response: CrystalThk
Df Sum Sq Mean Sq F value Pr(>F)
Block 2 8179.1 4089.6 2.5541 0.11909
FO(x1, x2, x3) 3 18511.9 6170.6 3.8538 0.03837
TWI(x1, x3) 1 6126.3 6126.3 3.8261 0.07414
I(x2^2) 1 28316.0 28316.0 17.6842 0.00122
Residuals 12 19214.4 1601.2
Lack of fit 9 18697.6 2077.5 12.0616 0.03234
Pure error 3 516.7 172.2
Stationary point of response surface:
x1 x2 x3
-0.3037410 0.0000000 -0.7839546
Stationary point in original units:
DwellTemp CoolRate CoolTemp
1434.813 5.500 1071.605
Eigenanalysis:
$values
[1] 13.83646 0.00000 -13.83646
$vectors
[,1] [,2] [,3]
x1 -0.7071068 0 0.7071068
x2 0.0000000 -1 0.0000000
x3 -0.7071068 0 -0.7071068
>
> #Able to get this function working now using the I(x2^2) as the pure
quadratic term.
> #From this we see that the model has a R-squared value of 0.7609 and an
adjusted
> #R-squared value of 0.6214. This is not as good as the width model, but
still pretty good
> #for our 20 experiment set.
>
> #Section D: Contour and Perspective Plots
>
> #Following the same pattern as the grain width model, we can now move on to
the development of
R Console Page 12
contour and
> #perspective plots to understand how crystal thickness is affected by each
parameter.
>
> #Our first course of action is to reproduce the 3x3 plot from above for
each parameter combinat
ion at -1,0 and 1.
> par(mfrow = c(3,3))
>
> #First countour plot: -1 values for each plot
> contour(thk.rsm.final,~x1+x2+x3,decode=TRUE,
+ xlabs = c("Dwell Temperature (°C)", "Cooling Rate (°C/hr)", "Cooling
Temperature (°C)"),
+ zlim = c(-10,300),
+ zlab="Crystal Thickness (μm)",lty = 1, lwd = 1.2, methods = "flattest",
+ at = c(x1=-1, x2=-1,x3=-1), atpos=1, image=TRUE,
img.col=terrain.colors(2560, alpha=1))
There were 36 warnings (use warnings() to see them)
>
```

```
> #Contour 2: 0 values for each plot
> contour(thk.rsm.final,~x1+x2+x3,decode=TRUE,
+ xlabs = c("Dwell Temperature (°C)", "Cooling Rate (°C/hr)", "Cooling
Temperature (°C)"),
+ zlab="Crystal Thickness (μm)", lty = 1, lwd = 1.2, methods = "flattest",
+ zlim = c(-10,300),
+ at = c(x1=0, x2=0,x3=0), atpos=1, image=TRUE, img.col=terrain.colors(2560,
alpha=1))
There were 36 warnings (use warnings() to see them)
>
> #Contour 3: 1 values for each plot
> contour(thk.rsm.final,~x1+x2+x3,decode=TRUE,
+ xlabs = c("Dwell Temperature (°C)", "Cooling Rate (°C/hr)", "Cooling
Temperature (°C)"),
+ zlab="Crystal Thickness (μm)", lty = 1, lwd = 1.2, methods = "flattest",
+ zlim = c(-10,300),
+ at = c(x1=1, x2=1,x3=1), atpos=1, image=TRUE, img.col=terrain.colors(2560,
alpha=1))
There were 36 warnings (use warnings() to see them)
>
> #Figured out how to use the rsm function, so these are now in their natural
variable form
>
> #Finally for this section, the most interesting to consider is the x1*x3
perspective plot. Lets
evaluate it at
> #a few x2 = -1, which is the best condition within the operating region for
producing thick cry
stals
>
> persp(thk.rsm.final,~x1+x3,decode=TRUE, at = c(x2=-1),
+ xlabs = c("Dwell Temperature (°C)", "Cooling Temperature (°C)"),
+ atpos=3, theta = 225, phi = 15, r=8,
+ zlab="Crystal Thickness(μm)", cex.axis = 1, cex.lab= 1, cex.sub=1.5)
>
> #------------------------------------------------------------------------
>
> #Part 3: Alternative Parameter Analysis
>
> #For this final part, I want to look if there is any significance for some
of the
> #alternative parameters/responses resulting from the data collected
>
> #These include: DeltaT (Dwell Temp-Cooling Temp), Effective Growth Time
(DeltaT/CoolRate)
> #and Effective Growth Rate(Crystal Thickness/Eff Growth Time)
>
> #First, I want to plot Width and Thickness vs Delta T and Eff Growth Time
> par(mfrow = c(2,2))
>
> #1st plot - DeltaT vs Width
> errbar(main.data$DeltaT,main.data$GrainSize,
+ main.data$GrainSize+main.data$SizeError, main.data$GrainSize-
main.data$SizeError,
+ cap=0.015, main = NULL, sub=NULL, cex.lab = 1.5, cex.axis=1.2,
+ xlab="Delta T (°C)", ylab = "Grain Width (μm)", pch=16)
>
```

```
> #2st plot - DeltaT vs Thickness
> errbar(main.data$DeltaT,main.data$CrystalThk,
+ main.data$CrystalThk+main.data$CrystalError, main.data$CrystalThk-
main.data$CrystalError,
+ cap=0.015, main = NULL, sub=NULL, cex.lab = 1.5, cex.axis=1.2,
+ xlab="Delta T (°C)", ylab = "Crystal Thickness (µm)", pch=16)
>
R Console Page 13
> #3rd plot - Eff Growth Time vs Width
> errbar(main.data$EffGrowthTime,main.data$GrainSize,
+ main.data$GrainSize+main.data$SizeError, main.data$GrainSize-
main.data$SizeError,
+ cap=0.015, main = NULL, sub=NULL, cex.lab = 1.5, cex.axis=1.2,
+ xlab="Effective Growth Time (hr)", ylab = "Grain Width (µm)", pch=16)
>
> #4th plot - Eff Growth Time vs Thickness
> errbar(main.data$EffGrowthTime,main.data$CrystalThk,
+ main.data$CrystalThk+main.data$CrystalError, main.data$CrystalThk-
main.data$CrystalError,
+ cap=0.015, main = NULL, sub=NULL, cex.lab = 1.5, cex.axis=1.2,
+ xlab="Effective Growth Time (hr)", ylab = "Crystal Thickness (µm)", pch=16)
>
> #There appears to be a trend between DeltaT and width here, as well as
maybe for EGT
> #and both width and thickness
>
> #Going to go a linear model for each of these to see if there is any
significance
> #We will ignore things like block and other factors, basically only looking
at a
> #single linear parameter
>
> lm.DeltaT.Width<-lm(GrainSize ~ FO(DeltaT), data=main.data)
> summary(lm.DeltaT.Width)
Call:
lm(formula = GrainSize ~ FO(DeltaT), data = main.data)
Residuals:
Min 1Q Median 3Q Max
-439.16 -146.22 4.59 80.85 415.31
Coefficients:
Estimate Std. Error t value Pr(>|t|)
(Intercept) -36.8174 180.3523 -0.204 0.8405
FO(DeltaT) 1.1809 0.5746 2.055 0.0547 .
---
Signif. codes: 0 '***' 0.001 '**' 0.01 '*' 0.05 '.' 0.1 ' ' 1
Residual standard error: 237.3 on 18 degrees of freedom
Multiple R-squared: 0.1901, Adjusted R-squared: 0.1451
F-statistic: 4.224 on 1 and 18 DF, p-value: 0.05466
> #Not really any fit here, p value = 0.1. This is not very good for fitting
anything
>
> lm.EGT.Width<-lm(GrainSize ~ FO(EffGrowthTime), data=main.data)
> summary(lm.EGT.Width)
Call:
lm(formula = GrainSize ~ FO(EffGrowthTime), data = main.data)
Residuals:
Min 1Q Median 3Q Max
```

```
-439.66 -157.38 -9.75 124.76 433.39
Coefficients:
Estimate Std. Error t value Pr(>|t|)
(Intercept) 136.093 87.563 1.554 0.1375
FO(EffGrowthTime) 2.673 1.053 2.538 0.0206 *
---
Signif. codes: 0 ‘***’ 0.001 ‘**’ 0.01 ‘*’ 0.05 ‘.’ 0.1 ‘ ’ 1
Residual standard error: 226.3 on 18 degrees of freedom
Multiple R-squared: 0.2635, Adjusted R-squared: 0.2226
F-statistic: 6.44 on 1 and 18 DF, p-value: 0.02063
> #Very similar to DeltaT, this does not have a major correlation with
crystal width
> #Probably, because parameters effective width are quite complex
>
> lm.EGT.Thk<-lm(CrystalThk ~ FO(EffGrowthTime), data=main.data)
> summary(lm.EGT.Thk)
R Console Page 14
Call:
lm(formula = CrystalThk ~ FO(EffGrowthTime), data = main.data)
Residuals:
Min 1Q Median 3Q Max
-100.067 -23.765 -4.271 19.249 89.910
Coefficients:
Estimate Std. Error t value Pr(>|t|)
(Intercept) -2.3656 19.3240 -0.122 0.9039
FO(EffGrowthTime) 0.8764 0.2324 3.771 0.0014 **
---
Signif. codes: 0 ‘***’ 0.001 ‘**’ 0.01 ‘*’ 0.05 ‘.’ 0.1 ‘ ’ 1
Residual standard error: 49.94 on 18 degrees of freedom
Multiple R-squared: 0.4413, Adjusted R-squared: 0.4103
F-statistic: 14.22 on 1 and 18 DF, p-value: 0.001399
> #Very strong correlation with crystal thickness, although it can be argued
that
> #cooling rate is the dominant factor in this term. I need more reasons to
talk about this
>
> #There isn't really enough here to talk about EGT. I think the final thing
I want to
> #do is present Effective Growth Rate (EGR) as a rsm function of the three
parameters
>
> par(mfrow = c(1,3))
>
> #1st plot - DwellTemp vs EGR
> errbar(main.data$DwellTemp,main.data$EffGrowthRate,
+ main.data$EffGrowthRate+main.data$EGRErr, main.data$EffGrowthRate-
main.data$EGRErr,
+ cap=0.015, main = NULL, sub=NULL, cex.lab = 1.5, cex.axis=1.2,
+ xlab="Dwell Temperature (°C)", ylab = "Eff Growth Rate ( μm/hr)", pch=16)
>
> #2nd plot - CoolRate vs EGR
> errbar(main.data$CoolRate,main.data$EffGrowthRate,
+ main.data$EffGrowthRate+main.data$EGRErr, main.data$EffGrowthRate-
main.data$EGRErr,
+ cap=0.015, main = NULL, sub=NULL, cex.lab = 1.5, cex.axis=1.2,
+ xlab="Cooling Rate(°C)", ylab = "Eff Growth Rate (μm/hr)", pch=16)
>
```

```
> #3rd plot - CoolTemp vs EGR
> errbar(main.data$CoolTemp,main.data$EffGrowthRate,
+ main.data$EffGrowthRate+main.data$EGRErr, main.data$EffGrowthRate-
main.data$EGRErr,
+ cap=0.015, main = NULL, sub=NULL, cex.lab = 1.5, cex.axis=1.2,
+ xlab="Cooling Temperature (°C)", ylab = "Eff Growth Rate (μm/hr)", pch=16)
>
> #Going to do a final rsm model looking at the EGR as a function of the
parameters
>
> EGR.rsm1 <- rsm(EffGrowthRate ~ Block + FO(x1,x2,x3), data=coded.main)
> summary(EGR.rsm1)
Call:
rsm(formula = EffGrowthRate ~ Block + FO(x1, x2, x3), data = coded.main)
Estimate Std. Error t value Pr(>|t|)
(Intercept) 1.17839 0.21716 5.4264 8.927e-05 ***
BlockFac1 -0.38691 0.33171 -1.1664 0.26294
BlockFac2 -0.43356 0.33171 -1.3070 0.21227
x1 0.28581 0.16628 1.7189 0.10766
x2 0.34623 0.16628 2.0822 0.05615 .
x3 0.35230 0.16628 2.1187 0.05248 .
---
Signif. codes: 0 ‘***’ 0.001 ‘**’ 0.01 ‘*’ 0.05 ‘.’ 0.1 ‘ ’ 1
Multiple R-squared: 0.4989, Adjusted R-squared: 0.3199
F-statistic: 2.788 on 5 and 14 DF, p-value: 0.05966
Analysis of Variance Table
Response: EffGrowthRate
Df Sum Sq Mean Sq F value Pr(>F)
R Console Page 15
Block 2 0.8143 0.40717 1.0793 0.36651
FO(x1, x2, x3) 3 4.4439 1.48129 3.9264 0.03166
Residuals 14 5.2817 0.37726
Lack of fit 11 5.1080 0.46436 8.0211 0.05644
Pure error 3 0.1737 0.05789
Direction of steepest ascent (at radius 1):
x1 x2 x3
0.5008186 0.6066952 0.6173344
Corresponding increment in original units:
DwellTemp CoolRate CoolTemp
25.040929 1.516738 61.733437
> #A little bit going on here, but not very good fit, should just go straight
to SO model
>
> EGR.rsm2 <- rsm(EffGrowthRate ~ Block + SO(x1,x2,x3), data=coded.main)
> summary(EGR.rsm2)
Call:
rsm(formula = EffGrowthRate ~ Block + SO(x1, x2, x3), data = coded.main)
Estimate Std. Error t value Pr(>|t|)
(Intercept) 0.977145 0.141381 6.9114 0.0001231 ***
BlockFac1 -0.375808 0.152917 -2.4576 0.0394660 *
BlockFac2 -0.422455 0.152917 -2.7627 0.0245740 *
x1 0.285810 0.076603 3.7311 0.0057790 **
x2 0.346232 0.076603 4.5198 0.0019504 **
x3 0.352303 0.076603 4.5991 0.0017575 **
x1:x2 -0.131626 0.100042 -1.3157 0.2247251
x1:x3 0.506931 0.100042 5.0672 0.0009684 ***
x2:x3 -0.083700 0.100042 -0.8366 0.4270737
```

```
x1^2 -0.135816 0.074684 -1.8185 0.1064891
x2^2 0.368148 0.074684 4.9294 0.0011503 **
x3^2 0.052878 0.074684 0.7080 0.4990362
---
Signif. codes: 0 '***' 0.001 '**' 0.01 '*' 0.05 '.' 0.1 ' ' 1
Multiple R-squared: 0.9392, Adjusted R-squared: 0.8557
F-statistic: 11.24 on 11 and 8 DF, p-value: 0.001036
Analysis of Variance Table
Response: EffGrowthRate
Df Sum Sq Mean Sq F value Pr(>F)
Block 2 0.8143 0.40717 5.0853 0.0375737
FO(x1, x2, x3) 3 4.4439 1.48129 18.5004 0.0005878
TWI(x1, x2, x3) 3 2.2505 0.75016 9.3691 0.0053779
PQ(x1, x2, x3) 3 2.3906 0.79688 9.9526 0.0044723
Residuals 8 0.6405 0.08007
Lack of fit 5 0.4669 0.09337 1.6129 0.3682751
Pure error 3 0.1737 0.05789
Stationary point of response surface:
x1 x2 x3
-0.5887523 -0.6959818 -1.0599925
Stationary point in original units:
DwellTemp CoolRate CoolTemp
1420.562385 3.760046 1044.000754
Eigenanalysis:
$values
[1] 0.3997229 0.1987659 -0.3132789
$vectors
[,1] [,2] [,3]
x1 -0.2533972 0.5071163 0.82378573
x2 0.9208710 0.3872785 0.04485494
R Console Page 16
x3 -0.2962878 0.7699665 -0.56512397
> #Now this is looking like an actual model, will build a final truncated
model
> #from these significant terms
>
> EGR.rsm.final <- rsm(EffGrowthRate ~ Block + FO(x1,x2,x3)+ TWI(x1,x3) +
I(x2^2), data=coded.mai
n)
> summary(EGR.rsm.final)
Call:
rsm(formula = EffGrowthRate ~ Block + FO(x1, x2, x3) + TWI(x1,
x3) + I(x2^2), data = coded.main)
Estimate Std. Error t value Pr(>|t|)
(Intercept) 0.913353 0.124201 7.3538 8.808e-06 ***
BlockFac1 -0.372288 0.168213 -2.2132 0.0470097 *
BlockFac2 -0.418935 0.168213 -2.4905 0.0284058 *
x1 0.285810 0.084305 3.3902 0.0053663 **
x2 0.346232 0.084305 4.1069 0.0014544 **
x3 0.352303 0.084305 4.1789 0.0012790 **
x1:x3 0.506931 0.110102 4.6042 0.0006065 ***
I(x2^2) 0.375617 0.081457 4.6112 0.0005992 ***
---
Signif. codes: 0 '***' 0.001 '**' 0.01 '*' 0.05 '.' 0.1 ' ' 1
Multiple R-squared: 0.8896, Adjusted R-squared: 0.8252
F-statistic: 13.81 on 7 and 12 DF, p-value: 7.048e-05
Analysis of Variance Table
```

```
Response: EffGrowthRate
Df Sum Sq Mean Sq F value Pr(>F)
Block 2 0.8143 0.40717 4.1985 0.0414653
FO(x1, x2, x3) 3 4.4439 1.48129 15.2743 0.0002124
TWI(x1, x3) 1 2.0558 2.05583 21.1987 0.0006065
I(x2^2) 1 2.0621 2.06209 21.2633 0.0005992
Residuals 12 1.1637 0.09698
Lack of fit 9 0.9901 0.11001 1.9002 0.3248244
Pure error 3 0.1737 0.05789
Stationary point of response surface:
x1 x2 x3
-0.6949733 0.0000000 -0.5638040
Stationary point in original units:
DwellTemp CoolRate CoolTemp
1415.251 5.500 1093.620
Eigenanalysis:
$values
[1] 0.2534654 0.0000000 -0.2534654
$vectors
[,1] [,2] [,3]
x1 -0.7071068 0 0.7071068
x2 0.0000000 -1 0.0000000
x3 -0.7071068 0 -0.7071068
> #Final model is interesting, need to look at what the contour plots
> #actually look like.
>
> par(mfrow = c(3,3))
>
> #First countour plot: -1 values for each plot
> contour(EGR.rsm.final,~x1+x2+x3,decode=TRUE,
+ xlabs = c("Dwell Temperature (°C)", "Cooling Rate (°C/hr)", "Cooling
Temperature (°C)"),
+ zlab="Eff Growth Rate (µm/hr)",lty = 1, lwd = 1.2, methods = "flattest",
R Console Page 17
+ at = c(x1=-1, x2=-1,x3=-1), atpos=1, image=TRUE,
img.col=terrain.colors(2560, alpha=1))
There were 36 warnings (use warnings() to see them)
>
> #Contour 2: 0 values for each plot
> contour(EGR.rsm.final,~x1+x2+x3,decode=TRUE,
+ xlabs = c("Dwell Temperature (°C)", "Cooling Rate (°C/hr)", "Cooling
Temperature (°C)"),
+ zlab="Eff Growth Rate (µm/hr)", lty = 1, lwd = 1.2, methods = "flattest",
+ at = c(x1=0, x2=0,x3=0), atpos=1, image=TRUE, img.col=terrain.colors(2560,
alpha=1))
There were 36 warnings (use warnings() to see them)
>
> #Contour 3: 1 values for each plot
> contour(EGR.rsm.final,~x1+x2+x3,decode=TRUE,
+ xlabs = c("Dwell Temperature (°C)", "Cooling Rate (°C/hr)", "Cooling
Temperature (°C)"),
+ zlab="Eff Growth Rate (µm/hr)", lty = 1, lwd = 1.2, methods = "flattest",
+ at = c(x1=1, x2=1,x3=1), atpos=1, image=TRUE, img.col=terrain.colors(2560,
alpha=1))
There were 36 warnings (use warnings() to see them)
>
```

```
> #My thoughts from this is that we see large effective growth rate for
different reasons
> #due to each parameter
> #DwellTemp- highest growth rate at high dwell temp - higher driving force
for growth
>
> #CoolRate - Highest growth rate at higher rate - (tapered crystals?), seems
to also
> #increase after going below 4C/hr, maybe transitioning to better quality
here
>
> #CoolTemp - Better at higher temps - this is likely due to formation of
tapered crystals
> # when you quench at >1300C, likely to form tapered crystals.
>
> #Final plot - perspective: want to look at cases for when coolTemp is lower
(-1)
> #This will tell us what to do to make thicker crystals that are not tapered
>
> persp(EGR.rsm.final,~x1+x2,decode=TRUE, at = c(x3=-1),
+ xlabs = c("Dwell Temperature (°C)", "Cooling Temperature (°C)"),
+ atpos=3, theta = (295-180), phi = 24, r=8,
+ zlab="Eff Growth Rate(μm/hr)", cex.axis = .8, cex.lab= 1, cex.sub=1.5)
```